Precision meets sustainability at the LHC: extraction of fundamental parameters of the Standard Model and machine learning techniques in the simulation

Dissertation
zur Erlangung des Doktorgrades an der Fakultät
für Mathematik und Naturwissenschaften
Fachbereich Physik
der Bergische Universität Wuppertal

vorgelegt von

Valentina Guglielmi

Hamburg, 2025

Eidesstattliche Versicherung / Declaration on oath

Hiermit versichere ich an Eides statt, dass ich die vorliegende Dissertationsschrift selbst verfasst und keine anderen als die angegebenen Hilfsmittel und Quellen benutzt habe. Die eingereichte schriftliche Fassung entspricht der auf dem elektronischen Speichermedium. Die Dissertation wurde in der vorgelegten oder einer ähnlichen Form nicht schon einmal in einem früheren Promotionsverfahren angenommen oder als ungenügend beurteilt.

I hereby declare, on oath, that I have written the present dissertation by my own and have not used any resources and aids other than those acknowledged. The written version submitted corresponds to the one stored electronically. The dissertation presented in this form, has not already been accepted in an earlier doctoral procedure or assessed as unsatisfactory.

Hamburg, 26 March, 2025

Valentina Guglielmi

Gutachter der Dissertation:	Prof. Dr. Katerina Lipka
Zusammensetzung der Prüfungskommission:	Prof. Dr. Katerina Lipka
	Prof. Dr. Wolfgang Wagner
	Prof. Dr. Dirk Lützenkirchen-Hecht
	Prof. Dr. Sven-Olaf Moch
	Prof. Dr. Harrison Prosper

Abstract

This thesis presents precise determinations of two fundamental parameters of the standard model (SM), the strong coupling constant $\alpha_S(m_\mathrm{Z})$ and the top quark mass m_t along with its width Γ_t. These contribute importantly to constraints on the stability of the SM electroweak vacuum.

For the determination of $\alpha_S(m_\mathrm{Z})$, CMS inclusive jet measurements using LHC proton-proton (pp) collisions at centre-of-mass energies $\sqrt{s} = 2.76,\ 7,\ 8$, and 13 TeV are analysed together, for the first time. This has been made possible by detailed studies of the correlations between the different data sets. The CMS jet data are combined with HERA deep inelastic scattering measurements to extract the parton distribution functions (PDFs) and $\alpha_S(m_\mathrm{Z})$, simultaneously. This approach properly accounts for the correlation between PDFs and $\alpha_S(m_\mathrm{Z})$. The resulting value, $\alpha_S(m_\mathrm{Z}) = 0.1176^{+0.0014}_{-0.0016}$, is the most precise value of $\alpha_S(m_\mathrm{Z})$ from jet rates to date and has been achieved through a comprehensive QCD analysis at next-to-next-to-leading order. Further, the running of α_S up to an energy scale of 1.6 TeV is probed.

The measurement of the top quark mass parameter in the Monte Carlo (MC) simulation m_t^MC and Γ_t from the unfolded differential cross section of top quark-antiquark ($\mathrm{t\bar{t}}$) and single top quark production in association with a W boson (tW) is performed. This analysis uses LHC pp collision data at $\sqrt{s} = 13$ TeV, collected by the CMS experiment during 2017–2018. Events in the dilepton decay channel are selected. The differential cross section as a function of the invariant mass of the lepton and b quark, $m_{\ell\mathrm{b}}$, is unfolded to the particle level. This analysis is the first of its kind using CMS data, employing the state-of-the-art event generator bb4l, which simulates $\mathrm{pp} \to \mathrm{b\bar{b}}\ell^+\ell^-\nu\bar{\nu}$ final states and takes into account the interference between $\mathrm{t\bar{t}}$ and tW production. The precision of this measurement is estimated using Asimov pseudo-data, resulting in $m_\mathrm{t}^\mathrm{MC} = 172.61^{+0.41}_{-0.44}$ GeV and $\Gamma_\mathrm{t} = 1.36^{+0.24}_{-0.28}$ GeV. The m_t^MC result is as precise as the most accurate single-experiment direct m_t^MC measurement and will present the first determination of m_t^MC from the combined $\mathrm{t\bar{t}}$ and tW cross sections from the CMS Collaboration once the analysis is unblinded. Further, this analysis promises improved precision as compared to direct measurements of Γ_t obtained with the bb4l method.

Finally, a machine learning (ML) technique is presented, developed to reweight MC simulations obtained with a particular set of model parameters to simulations with alternative values of these parameters, or to simulations based on an entirely different model. The reweighting is performed at the generator level by applying the output of the ML algorithm, stored as weights, to the nominal MC simulation. As a result, detailed detector simulation and event reconstruction are not needed for alternative MC samples, significantly reducing computational costs by up to 75%. The performance of the method is studied in simulated $t\bar{t}$ production and results are presented for reweighting to model variations and higher-order calculations. This ML-based reweighting is already used by the CMS experiment and will facilitate precision measurements at the High-Luminosity LHC.

Zusammenfassung

In dieser Arbeit werden zwei fundamentale Parameter des Standardmodells (SM) präzise bestimmt: die starke Kopplungskonstante $\alpha_S(m_Z)$ und die Masse des Top-Quarks m_t sowie dessen Breite Γ_t. Diese tragen wesentlich dazu bei, die Stabilität des elektroschwachen Vakuums des SM zu bestimmen.

Die inklusiven Jet-Messungen von CMS mit LHC Proton-Proton (pp) Kollisionen bei Schwerpunktsenergien $\sqrt{s} = 2,76,\ 7,\ 8$ und 13 TeV werden zum ersten Mal gemeinsam ausgewertet. Ermöglicht wurde dies durch detaillierte Untersuchungen der Korrelationen zwischen den verschiedenen Datensätzen. Die CMS Jet-Daten werden mit HERA Messungen der tief-inelastischen Streuung kombiniert, um die Partonverteilungsfunktionen (PDFs) und $\alpha_S(m_Z)$ gleichzeitig zu extrahieren. Dieser Ansatz berücksichtigt die Korrelation zwischen PDFs und $\alpha_S(m_Z)$ in korrekter Weise. Der sich daraus ergebende Wert, $\alpha_S(m_Z) = 0,1176^{+0,0014}_{-0,0016}$, ist der bisher genaueste Wert für $\alpha_S(m_Z)$ aus Jetproduktionsraten und wurde durch eine umfassende QCD Analyse in nächst-zu-nächst-führender Ordnung erreicht. Außerdem wird der Verlauf von α_S bis zu einer Energie von 1,6 TeV untersucht.

Die Messung des Top-Quark-Massenparameters in der Monte-Carlo (MC) Simulation m_t^{MC} und Γ_t wird mit dem entfalteten differentiellen Wirkungsquerschnitt der Top-Quark-Anti-Quark Paarproduktion ($t\bar{t}$) und der Produktion von einzelnen Top-Quarks, gemeinsam mit einem W-Boson, durchgeführt. Diese Analyse verwendet LHC pp Kollisionsdaten bei $\sqrt{s} = 13$ TeV, die vom CMS Experiment während 2017-2018 gesammelt wurden. Es werden Ereignisse im dileptonischen Zerfallskanal ausgewählt. Der differentielle Wirkungsquerschnitt als Funktion der invarianten Masse des Leptons und des b-Quarks, $m_{\ell b}$, wird auf die Teilchenebene entfaltet. Diese Analyse ist die erste ihrer Art mit CMS Daten, die den Ereignisgenerator bb4l verwendet, der $pp \to b\bar{b}l^+l^-\nu\bar{\nu}$ Endzustände simuliert und die Interferenz zwischen $t\bar{t}$ und tW Produktion berücksichtigt. Unter Verwendung von Asimov-Pseudodaten erhält man die Werte $m_t^{MC} = 172,61^{+0,41}_{-0,44}$ GeV und $\Gamma_t = 1,36^{+0,24}_{-0,28}$ GeV. Das Ergebnis von m_t^{MC} ist so genau wie die genaueste direkte m_t^{MC} Messung an einem einzelnen Experiment und wird die erste Bestimmung von m_t^{MC} aus einer kombinierten $t\bar{t}$ und tW Messung innerhalb der CMS Kollaboration darstellen sobald die interne Begutachtung der Analyse abgeschlossen ist. Darüber hinaus verspricht diese Analyse eine verbesserte Präzision

im Vergleich zu direkten Messungen von Γ_t, die mit der bb4l-Methode erhalten wurden.

Schließlich wird eine Technik des maschinellen Lernens (ML) vorgestellt, die entwickelt wurde, um MC Simulationen, die mit einem bestimmten Satz von Modellparametern erhalten wurden, gegenüber Simulationen mit alternativen Werten dieser Parameter oder gegenüber Simulationen, die auf einem völlig anderen Modell basieren, neu zu gewichten. Die Neugewichtung erfolgt auf Generatorebene durch Anwendung der als Gewichte gespeicherten Ergebnisse des ML-Algorithmus auf die nominale MC Simulation. Infolgedessen sind für alternative MC Samples keine detaillierte Detektorsimulation und Ereignisrekonstruktion erforderlich, was den Rechenaufwand um bis zu 75% reduziert. Die Leistung der Methode wird in einer simulierten $t\bar{t}$-Produktion untersucht, und es werden Ergebnisse für die Neugewichtung bei Modellvariationen und Berechnungen höherer Ordnung vorgestellt. Diese ML-basierte Neugewichtung wird bereits vom CMS Experiment verwendet und wird Präzisionsmessungen en am High-Luminosity LHC ermöglichen.

Contents

Introduction

The Standard Model (SM) of particle physics is a quantum field theory developed in the 1970s that describes three of the four fundamental forces (electromagnetic, strong and weak forces) of nature and classifies all known elementary particles. It is defined by 26 free parameters, including the strengths of the interactions (fundamental couplings) and the masses of elementary particles. Many of these parameters are not constant but depend on the energy scale at which the interaction is probed, a property known as *running*. While the model predicts how these parameters depend on the energy scale and are related to each other, their actual values at a specific energy scale must be determined from measurements. Despite its success in describing particle physics, the SM has known limitations. It does not include gravity or explain matter-antimatter asymmetry, dark matter, or dark energy, indicating the need for new physics. Validity tests of the SM and searches for new physics are subject of experimental investigations in high-energy particle colliders.

The Large Hadron Collider [1] at CERN is the facility at the frontier of collision energy. To date, the LHC has successfully accomplished Run1 (2010–2012) and Run2 (2015–2018), while Run3 (2022-2026) is ongoing at a centre-of-mass energy $\sqrt{s} = 13.6$ TeV and will continue until 2026. Thereafter, the accelerator complex will undergo upgrades to prepare for its High Luminosity (HL–LHC) phase, with operations set to resume in 2030. The LHC was designed as a discovery machine for the observation of the Higgs boson and establishing its properties. Along with the successful accomplishment of this task, it has also demonstrated ability for highly precise measurements of the SM parameters, which may reveal tiny deviations from the SM predictions, probing indirectly new physics. Significant insights can be gained from already collected data at the LHC (Run1+Run2) and the comprehensive interpretation of different measurements.

One of the most stringent tests of the SM is the proof of stability of the SM electroweak vacuum, driven by the values of the top quark mass m_t, strong coupling constant $\alpha_S(m_\mathrm{Z})$ and, to a smaller extent, the Higgs boson mass. This is the main topic of this thesis, where precise determinations of $\alpha_S(m_\mathrm{Z})$ and m_t with the LHC data have been performed. Furthermore, the novel strategy to measure the top quark width Γ_t strongly correlated to the value of m_t has been implemented in the analysis of the LHC data, reducing the uncertainty of available results.

In the SM, the processes produced in proton-proton (pp) collisions at the LHC are primarily driven by the strong interaction, as described by quantum chromodynamics (QCD). The strength of this interaction is governed by the fundamental coupling α_S, which is an energy-scale dependent parameter. At high energy scales, the strong force becomes increasingly weak, a phenomenon known as *asymptotic freedom*, where quarks can be considered asymptotically free. At low energy scales, the strong force becomes increasingly strong, leading to the property of *confinement*, preventing quarks from being observed as free particles. When a quark or gluon (commonly referred to as partons) is kicked out from a proton, such as in pp collisions at the LHC, it forms a collimated spray of particles, called a *jet*. The jets preserve the flavour, momentum and direction of the original parton, with its production rate being directly proportional to the value of α_S. Jets are abundantly produced at the LHC and jet production is a standard-candle process to test the QCD dynamics up to the highest accessible energy scales. A challenge in the determination of α_S from jet production in pp collisions comes from the structure of the protons themselves, encoded in the parton distribution functions (PDFs). As a result, the theoretical predictions of the jet cross sections are affected by both α_S and PDFs, so that variation of one parameter would be compensated by the variation of another. To account for the correlation between $\alpha_S(m_\mathrm{Z})$ and PDFs, both should be extracted simultaneously in a comprehensive QCD analysis. In this thesis, the most precise determination of $\alpha_S(m_\mathrm{Z})$ from the jet rates measured by the CMS experiment at the LHC is presented. This analysis uses the CMS inclusive jet measurements in pp collisions at $\sqrt{s} = 2.76,\ 7,\ 8$ and 13 TeV, produced during Run1 and Run2 of the LHC. For the first time, all these measurements are analysed together, accurately estimating the correlations of the systematic uncertainties across the different measurements. The aforementioned correlation between the PDFs and $\alpha_S(m_\mathrm{Z})$ is mitigated in this comprehensive QCD analysis at NNLO, based on CMS jet production measurements together with the inclusive deep inelastic

ep scattering cross sections at HERA. Furthermore, the running of α_S is demonstrated up to 1.6 TeV.

Within the SM, the relationship between m_{t} and Γ_{t} is known to N3LO [2–5] in QCD with an uncertainty of a few percent. While m_{t} has been determined with sub-percent precision [6], the most precise extraction of Γ_{t} remains at the 10% level [7]. Further, the latter relies on indirect techniques that assume the SM and are based on measurements of the branching fraction of the top quark decay $B(\mathrm{t} \to \mathrm{Wb})$. Alternatively, direct measurements of kinematic distributions sensitive to Γ_{t} provide a less model-dependent approach that probes non-SM couplings, though with a lower precision. While the differential cross section for $\mathrm{t\bar{t}}$ production is measured with high precision at the LHC, the theoretical predictions and Monte Carlo (MC) simulations often rely on the narrow-width approximation for top quark decay into a b quark and a W boson. In this case, the single top quark production in association with a W boson (tW) is treated as a separate process, though both $\mathrm{t\bar{t}}$ and tW processes are characterised by the same final states (WWbb) and interfere. Conventional approaches for modelling $\mathrm{t\bar{t}}+\mathrm{tW}$ interference [8–11] introduce significant uncertainties, which can become a limiting factor in precision measurements of Γ_{t}. In dileptonic decays, the invariant mass of the lepton and b quark, $m_{\ell\mathrm{b}}$, is demonstrated to be sensitive to both m_{t} and Γ_{t}. Theoretically, it was found to be a robust observable [12] for the extraction of m_{t}. The measurement of $m_{\ell\mathrm{b}}$ avoids the need for the full top-quark reconstruction, suffering from kinematic ambiguities caused by the neutrinos. This thesis presents the extraction of m_{t} and Γ_{t} using $\mathrm{t\bar{t}}+\mathrm{tW}$ events, for the first time in CMS experiment, by incorporating the interference between $\mathrm{t\bar{t}}$ and tW production using a state-of-the-art event generator, which simulates $pp \to b\bar{b}l^{+}l^{-}\nu\bar{\nu}$ [13, 14], and employing the $m_{\ell\mathrm{b}}$ distribution. This measurement is based on data obtained in LHC pp collision at $\sqrt{s} = 13$ TeV, collected by the CMS experiment in 2017-2018.

Precision measurements at the LHC rely on accurate modelling uncertainty estimation, which often requires generating additional MC samples. These simulations come at a high computational cost, with over 75% of the total CPU resources allocated to modelling the detector response and the event reconstruction [15, 16]. However, limited computing resources constrain the size of the MC samples, posing a challenge for precision analyses. This thesis addresses this issue by applying a machine learning (ML) technique [17] to reweight the MC simulations obtained with a particular set of

model parameters to simulations with alternative values of these parameters, or based on an entirely different model. The reweighting is performed by applying the output of the ML algorithm, stored as weights, to the nominal MC simulation. As a result, detailed detector simulation and event reconstruction are not needed for alternative MC samples, significantly reducing computational costs. In this thesis, the method is applied for the case of $\mathrm{t\bar{t}}$ production at the LHC, for the first time, and is extensively tested for variations of model parameters of the MC simulation in CMS, as well as applying an alternative simulation model.

The thesis is structured as follows. Chapter 1 introduces the SM of particle physics and its parameters, while Chapter 2 describes the phenomenology of hadronic collisions, with a focus on the role of jets and the top quark within the SM. Chapter 3 provides an overview of the LHC and the CMS experiment, along with a description of the CMS event reconstruction. Chapter 4 presents the ML method used to reweight MC samples in CMS. The measurement of the top quark mass and width from $\mathrm{t\bar{t}}+\mathrm{tW}$ events is discussed in Chapter 5. In Chapter 6, the comprehensive QCD analysis of CMS inclusive jets performed at NNLO is presented. The Chapter 7 concludes the thesis.

Chapter 1

The Standard Model and its parameters

This Chapter deals with the theoretical framework relevant to the research presented in this thesis. Section 1.1 introduces the Standard Model of particle physics, which classifies elementary particles and their interactions. In Section 1.2, the theory of quantum chromodynamics is discussed, followed by the electroweak (EW) theory in Section 1.3, while Section 1.4 focuses on the Brout-Englert-Higgs mechanism. Lastly, Section 1.5 addresses the issue of the stability of the EW vacuum.

1.1 Standard Model of particle physics

The Standard Model (SM) of particle physics is a quantum field theory [18], developed in the 1960s and 1970s, which aims to explain three of the four fundamental forces of nature and classifies all known elementary particles. The SM is formulated using the Lagrangian formalism. Its Lagrangian is built on the principle of *local gauge symmetry* and is invariant under the gauge group $SU(2) \otimes U(1) \otimes SU(3)$. The group $SU(2) \otimes U(1)$ represents the unified electroweak sector, which combines the electromagnetic and weak interactions. The $SU(3)$ group corresponds to the gauge symmetry of quantum chromodynamics (QCD), which describes the strong force. The concept of local gauge invariance asserts that the laws of physics should remain unchanged under local (i.e., position-dependent) transformations of the symmetry groups. This symmetry requirement leads to the introduction of field excitations – the particles which transmit the interactions. Furthermore, as a Lorentz-invariant theory, the SM remains unchanged under the combined transformations of charge conjugation (C),

parity (P), and time reversal (T), a property known as CPT invariance. However, the three individual symmetries or a combination of two of them are not necessarily conserved.

The particle content of the SM is illustrated in Figure 1.1. Based on their spin, particles are classified into fermions and bosons. Bosons are characterised by integer spin and follow the Bose-Einstein statistics. In contrast, fermions have half-integer spin and obey the Dirac statistics. The fundamental blocks of matter, leptons and quarks, are fermions, while their interactions are transmitted by bosons. The photon γ is responsible for the electromagnetic interactions, while the $W^{\pm}$ and Z bosons mediate the charged- and neutral- current weak interactions, respectively. Finally, the gluons g carry the strong force. The Higgs boson (H) mediates a special interaction as the only scalar boson of the SM. The fermions and the W and Z bosons acquire their masses by interacting with the Higgs field through the Higgs–Brout–Englert mechanism [19, 20]. The Lagrangian density $\mathcal{L}$ of the SM can be expressed as a sum of the contributions from the different interactions:

$$\mathcal{L} = \mathcal{L}_{QCD} + \mathcal{L}_{EW} + \mathcal{L}_{Higgs}.$$

For each fermion, there is a corresponding antiparticle with identical mass and spin but opposite electric charge and other quantum numbers. The leptons encompass charged particles as electron e, muon μ, and tau τ and neutral particles as neutrinos (ν_e, ν_μ, ν_τ). Every charged lepton is paired with its corresponding neutrino in the charged-current weak interaction.

The quarks are classified into up-type and down-type quarks, with electric charge $+2/3e$ and $-1/3e$, respectively. The up-type quarks consist of the up (u), charm (c) and top (t) quarks, while the down-type are called down (d), strange (s) and bottom (b). While the lepton flavour is conserved in all interactions, the quark flavour is changed by the weak interaction referred to as *flavour mixing*.

In the SM, leptons and quarks are organised into three generations, as shown in Figure 1.1. Each generation of particles exhibits similar quantum properties with the exception of their masses, which increase progressively from one generation to the other. The number of generations is not explained by the SM. Experimentally, mea-

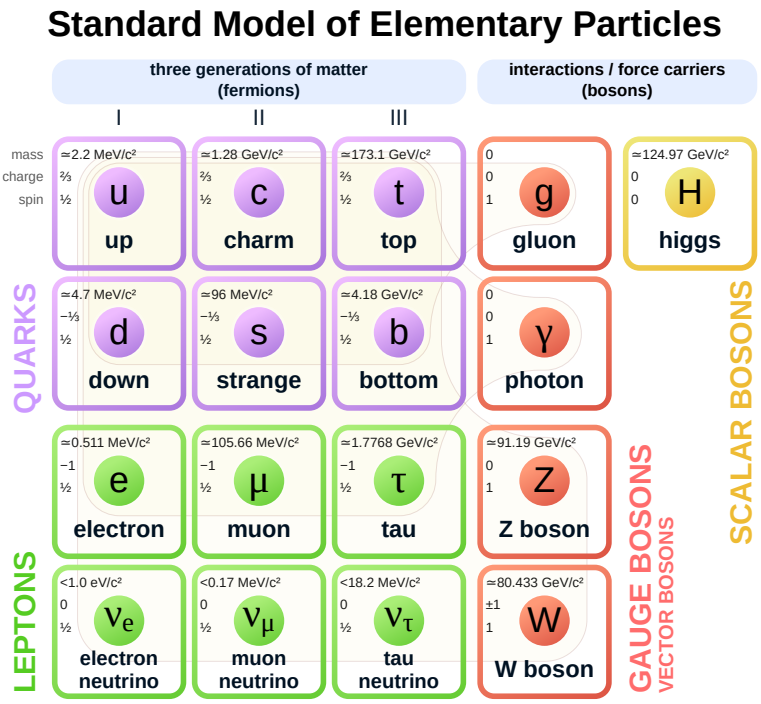

Figure 1.1: Summary of the elementary particles described by the SM and their main properties. Figure taken from Ref. [21].

surements of Z boson width at CERN LEP collider [22] have confirmed the existence of 3 light neutrino flavours, and, in turn, 3 lepton generations.

The SM operates with 26 free parameters, which are related to the strengths of the interactions (fundamental couplings) and masses of the elementary particles. Many of these are not constant but depend on the energy scale at which the interaction is probed. While the model predicts how these parameters depend on the energy scale and are related to each other, their actual values at a specific energy scale must be determined from measurements. The SM has been extensively studied and validated in high-energy scattering experiments, mostly realised at particle colliders. Despite its remarkable success in explaining a wide range of particle physics phenomena, the SM has known limitations. For instance, it neither accounts for gravitation nor explains the origin of the matter-antimatter asymmetry and the existence of dark matter and dark energy. These open questions suggest the presence of physics beyond the SM (BSM). Precision measurements of the SM are particularly promising, as they may

reveal subtle deviations from SM predictions, thereby providing indirect evidence of new physics.

1.2 Quantum chromodynamics

Quantum chromodynamics (QCD) is a Yang-Mills [23] theory based on the SU(3) symmetry group, describing the strong interaction between quarks and gluons. The conserved charge of $SU(3)_C$ is the *colour charge*, with each quark appearing in a colour state red, green, or blue, while an antiquark takes the respective anti-colour state. The quark fields q transform as colour triplets $q = (q_a, q_b, q_c)^T$ under $SU(3)_C$ transformations. The colour charge was proposed to explain how three quarks, despite having identical quantum properties, can combine to form baryons without violating Pauli's exclusion principle. This is, for instance, the case of the baryon Δ^{++} [24–26] – a fermion, which contains three up quarks, all with the same spin and therefore appearing with an identical quantum state. The introduction of an additional degree of freedom via totally antisymmetric colour contribution to the total wave function solves the issue.

The $SU(3)_C$ group has $N^2 - 1 = 8$ generators (t_a), represented in the *fundamental representation* by the Gell-Mann matrices. The gluons are the corresponding eight gauge fields G^a_μ. The $SU(3)_C$ of QCD is an exact symmetry, and the masses of quarks in each colour state are identical. The dynamics of the quark q, antiquark $\bar{q}$ and gluon fields are described by the QCD Lagrangian density, where the mass term is included explicitly:

$$\mathcal{L}_{\text{QCD}} = -\frac{1}{4} F^a_{\mu\nu} F^{\mu\nu}_a + \sum_{flavours} \overline{q}(i\gamma^\mu D_\mu - m_q)q, \tag{1.1}$$

Here, the sum accounts for the quark flavours. The covariant derivative and the field strenght tensor $F^a_{\mu\nu}$ are given by:

$$D_\mu = \partial_\mu - i g_s t_a G^a_\mu(x), \tag{1.2}$$

$$F^a_{\mu\nu} = \partial_\mu G^a_\nu - \partial_\nu G^a_\mu + g_s f^{abc} G^b_\mu G^c_\nu, \tag{1.3}$$

where g_s is a dimensionless real parameter representing the coupling strength and f^{abc} are the antisymmetric structure constants of the $SU(3)$ group. The structure constants obey to the commutation relation $[t_a, t_b] = i f^{abc} t_c$ of its eight generators

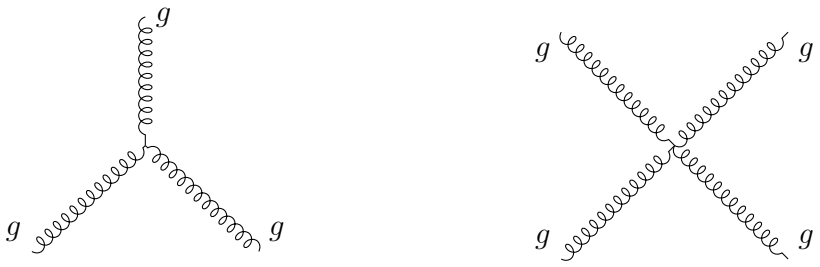

Figure 1.2: Feynman diagram representations of the trilinear (left) and the quartic (right) gluon self-interaction vertices.

$(a, b, c = 1...8)$. Due to the non-Abelian structure of $SU(3)_C$, the kinetic term of the gluon fields results in the gluon self-interaction vertices, as illustrated in Figure 1.2. The gluon coupling to quarks is defined by the colour factor and the strong coupling g_s, expressed by the strong coupling parameter $\alpha_S = g_s^2/(4\pi)$. One of the fundamental properties of QCD is the flavour-independence of the coupling.

A significant milestone in confirming QCD came in 1979 when the TASSO experiment, and the other PETRA experiments, observed three-jet events in e^+e^- collisions at the DESY PETRA storage ring. This result provided the first experimental evidence of gluons [27–30]. Subsequently, the LEP experiments exploited the angular distribution of four-jets to confirm the existence of trilinear gluon coupling, thus providing proof of QCD's non-Abelian structure [31].

The potential between two quarks at leading order (LO), as a function of their distance r, is given by:

$$V(r) = \frac{1}{2} C_F \frac{\alpha_S}{r} + \sigma \cdot r, \tag{1.4}$$

where the colour factor C_F is $\frac{4}{3}$ for a colour-singlet and the *string tension* σ is approximately $\sigma \approx 0.9$ GeV/fm. The first term is Coulomb-like, while at large distances ($r \gg 1$ fm) the potential increases linearly as $V(r) \sim r$, thereby preventing the observation of isolated quarks. The lines of force squeeze into a "string", which stores potential energy until it becomes energetically favourable to create a quark-antiquark ($q\bar{q}$) pair. This phenomenon, known as *confinement*, is responsible for hadronisation, ensuring that quarks are always confined within colour-neutral bound states called hadrons.

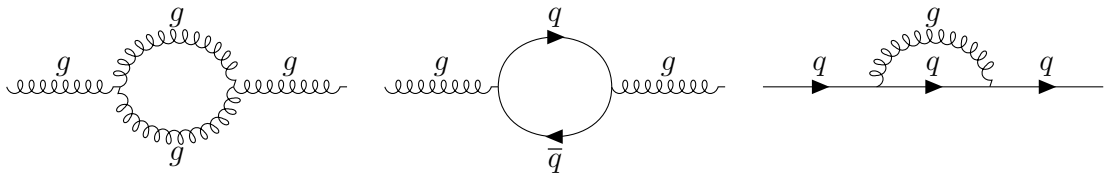

Figure 1.3: Feynman diagram representations of one-loop corrections to the gluon (left and middle) and quark propagators (right).

Corrections to the gluon and quark propagators, as illustrated in Figure 1.3, introduce logarithmic ultraviolet divergences in the cross section calculations when considering higher order in perturbation theory. These infinities at each order in perturbation theory can be subtracted and absorbed into the definitions of the bare (i.e. tree-level) parameters of the Lagrangian [32], a procedure known as *renormalisation*. The choice of the renormalisation scheme, and hence the definition of the QCD parameters, is not unique. Nevertheless, the results of calculations of physical observables should be independent of the chosen renormalisation scheme when considering all orders in perturbation theory. One of the most widely used renormalisation procedures is the *modified minimal subtraction* ($\overline{\text{MS}}$) scheme. Renormalisation introduces a *renormalisation scale* μ_r at which ultraviolet divergences are subtracted. Considering a physical dimensionless observable O that depends on an energy scale Q, the μ independence of O can be mathematically expressed as [33]:

$$\left[\mu^2\frac{\partial}{\partial\mu^2} + \beta(\alpha_S)\frac{\partial}{\partial\alpha_S} - \gamma_m(\alpha_S)m\frac{\partial}{\partial m}\right] O(Q^2/\mu^2, \alpha_S, m/Q) = 0, \tag{1.5}$$

known as *renormalisation group equations* (RGEs) for the strong coupling α_S and the quark mass m, defined as:

$$\beta(\alpha_S) = \mu^2\frac{\partial\alpha_S}{\partial\mu^2}, \quad -\gamma_m(\alpha_S)m = \mu^2\frac{\partial m}{\partial\mu^2}, \tag{1.6}$$

where $\beta(\alpha_S)$ is the QCD β function and $\gamma_m(\alpha_S)$ is the mass anomalous dimension [33]. The resulting energy-scale dependence of the strong coupling and quark masses, governed by the QCD RGE, is also referred to as *running*. In the limit of $\alpha_S \ll 1$, the β and γ_m functions can be expanded in perturbation series:

$$\beta(\alpha_S) = -\alpha_S^2\sum_{n=0}^{\infty}\beta_n\alpha_S^n, \quad \gamma_m(\alpha_S) = \alpha_S\sum_{n=0}^{\infty}c_n\alpha_S^n, \tag{1.7}$$

where the coefficients β_n and c_n contain the n+1-loop corrections to the propagators and vertices. At 1-loop precision, the solutions for β and γ functions correspond to:

$$\alpha_S(\mu^2) = \frac{\alpha_S(\mu_0^2)}{1 + \beta_0 \alpha_S(\mu_0^2) \ln\left(\frac{\mu^2}{\mu_0^2}\right)}, \tag{1.8}$$

$$m_q(\mu) = m_q(\mu_0) \left[1 - c_0 \alpha_S(\mu) \ln\left(\frac{\mu^2}{\mu_0^2}\right)\right], \tag{1.9}$$

where μ_0 represents the initial scale at which α_S and m_q are evaluated. The values of $\alpha_S(\mu_0)$ and $m(\mu_0)$ at a particular scale μ_0 need to be determined experimentally. In Eqs. (1.8) and (1.9), $\beta_0 = (33 - 2n_f)/12\pi$ and $c_0 = 1/\pi$ with n_f being the number of active flavours with masses $m_q^2 \ll \mu^2$. The two contributions to β_0 arise from the following effects:

- *colour screening* ($2n_f/12\pi$): creation of virtual $q\bar{q}$ pairs that increase the effective charge as a function of Q, similarly to the vacuum polarisation in QED, and
- *colour anti-screening* ($33/12\pi$): emission and self-coupling of gluons, which reduces the effective colour charge for a distance smaller than the reach of the strong interaction ($\sim$ 1 fm).

The anti-screening effect is dominant if the number of flavours is smaller than 16. As a result, the effective charge becomes smaller at high energies (short distances). This property is known as *asymptotic freedom* [34,35], and implies that only for large Q can the quarks be considered as asymptotically free. In this limit, the strong force tends to zero, enabling the application of perturbative calculations. On the other hand, α_S increases with growing distance (decreasing energy) in the confinement regime. The scale μ at which $\alpha_S(\mu)$ diverges is denoted as Λ_{QCD}. For $n_f = 5$, $\Lambda_{\mathrm{QCD}} = 213$ MeV [36]. This range is probed by means of lattice QCD [37]. The running of α_S was illustrated by many experiments, as presented in Figure 1.4.

The running of quark masses is usually treated in the $\overline{\mathrm{MS}}$ scheme [38], with the typical energy scale chosen as the quark mass itself, $m(m)$. Another renormalisation scheme is the quark pole mass scheme, where the quark mass would correspond to the pole of the quark propagator in the approximation of a quark as a free particle [39]. The colour of the quark does not prevent its definition as an asymptotic state in perturbation theory, and hence the pole mass $m_{\mathrm{q}}^{\mathrm{pole}}$ can be formally defined at any order [40, 41].

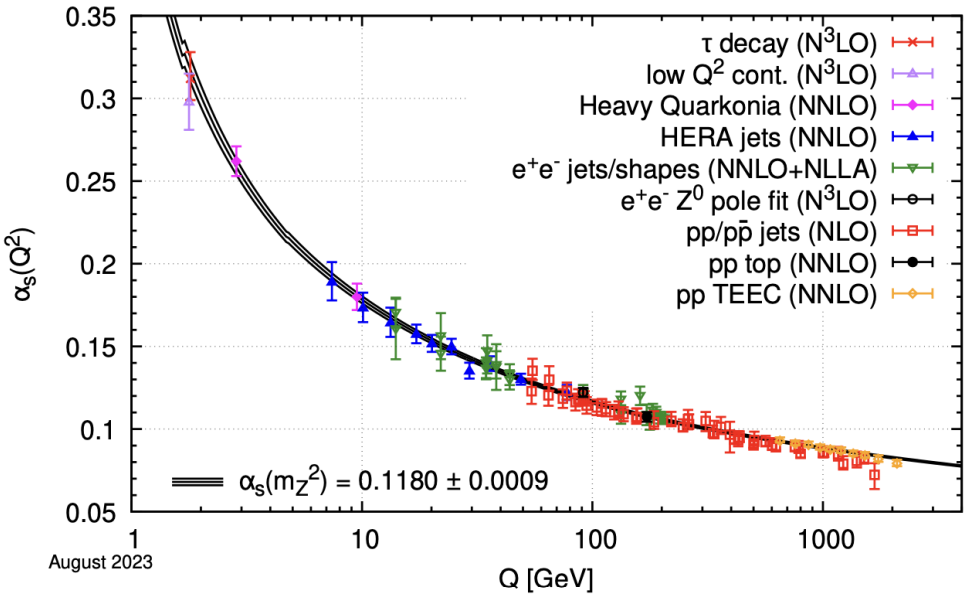

Figure 1.4: State-of-the-art determinations of α_S as a function of the energy scale Q compared to the running of the coupling computed at five loops taking as an input the current PDG average, $\alpha_S(m_Z) = 0.1180 \pm 0.0009$. Figure taken from Ref. [6].

However, the concept of an asymptotic "quark particle" is not physically meaningful as it assumes that virtual QCD self-energy quantum corrections (absorbed into the mass) can be separated from the real radiation effects at arbitrarily small scales μ. As a result, the definition of m_q^{pole} has an intrinsic *renormalon ambiguity* [42–44] of 110–250 MeV [45, 46]. An alternative short-distance mass definition is the MSR mass [47], which reduces the infrared renormalon ambiguity by introducing a variable scale R. This scale permits the split of the infrared and ultraviolet contributions. As a result, the mass definition is less sensitive to the non-perturbative effects.

The pole mass is related to the $\overline{\text{MS}}$ and MSR masses at each order in perturbation theory. When including QCD corrections, the m_q^{pole} differs from the $\overline{\text{MS}}$ mass, e.g., for top quark this difference is about 9 GeV [39]. In the particular case of the top quark, the renormalon-free mass schemes MSR and $\overline{\text{MS}}$ can be converted to each other with a precision of about 10–20 MeV [47] regardless of the selected renormalisation scales. Finally, the MSR mass converges to $\overline{\text{MS}}$ mass at $R = m(m)$ and to the pole mass definition when $R \to 0$. However, this limit is purely formal, as the MSR mass is only

applicable for R scales that remain in the realm of perturbation theory.

1.3 Unified electroweak theory

The unified theory of electromagnetic and weak interactions was formulated by Glashow, Salam, and Weinberg [48–50]. This is a local gauge theory based on the symmetry group $SU(2)_L \otimes U(1)_Y$ where the conserved charges are the weak isospin T and the hypercharge Y, respectively. The fermion fields are categorised into left-handed and right-handed components, defined by their chirality. Chirality for a Dirac fermion Ψ is defined through the operator γ^5, which has eigenvalues ± 1. Any Dirac field can thus be projected into its left- or right-handed component by applying the projection operators $\frac{1}{2}(1-\gamma^5)$ or $\frac{1}{2}(1+\gamma^5)$, respectively. In the SM, left-handed fermions and right-handed antifermions are organised into $SU(2)_L$ weak isospin doublets as eigenstates of γ^5 with eigenvalue -1, having weak isospin quantum numbers $(T, T_3) = (1/2, \pm 1/2)$. On the other hand, right-handed fermions and left-handed antifermions transform as weak isospin singlets with eigenvalue $+1$ under γ^5, having isospin quantum numbers $T = T_3 = 0$. The weak interaction is observed to be maximal parity violating [51], implying that only fermions with left chirality participate in weak interactions.

Below an energy scale of about 246 GeV, which corresponds to the EW vacuum scale, the EW theory falls back to the charge symmetry of electromagnetism $U(1)_{em}$. The conserved charges of the group $SU(2)_L \otimes U(1)_Y$ are related to the electric charge Q via the Gell–Mann–Nishijima formula [52]:

$$Q = \frac{Y}{2} + T_3. \tag{1.10}$$

Here, T_3 is the eigenvalue of the third component of the weak isospin operator. From Eq. (1.10), the hypercharge of right-handed neutrinos is 0, indicating that they can not participate in any SM interactions.

The gauge-invariant Lagrangian for the EW sector can be written as:

$$\mathcal{L}_{\mathrm{EW}} = i\bar{L}\gamma^\mu D_\mu L + \bar{R} i\gamma^\mu D_\mu R - \frac{1}{4} B^{\mu\nu} B_{\mu\nu} - \frac{1}{4} W_a^{\mu\nu} W^a_{\mu\nu}, \tag{1.11}$$

where γ_μ are the four Dirac matrices. The first and second terms represent the fermion kinematic sector associated with the left-handed doublets L and the right-handed

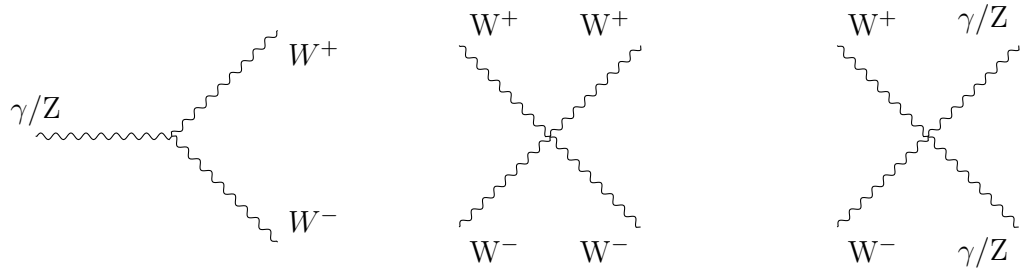

Figure 1.5: Feynman diagram representations of possible trilinear (left) and quartic (middle and right) EW boson self-interaction vertices.

singlet R. The remaining parts describe the interactions of the gauge bosons: B_μ associated with the $U(1)_Y$ group and the three fields W^i_μ (with i running from 1 to 3) corresponding to the $SU(2)_L$ group. The gauge covariant derivative D_μ reads:

$$D_\mu = \partial_\mu - i\frac{g'}{2}YB_\mu - igT_iW^i_\mu. \tag{1.12}$$

Here, g and g' are real dimensionless parameters representing the coupling strengths of the interactions. When acting on an isospin doublet, the T_i operators are represented by $\sigma_i/2$, where σ_i are the three Pauli's matrices. The field strength tensors for the Abelian $U(1)_Y$ and the non-Abelian $SU(2)_L$ gauge groups are given by:

$$U(1)_Y : B_{\mu\nu} = \partial_\mu B_\nu - \partial_\nu B_\mu, \tag{1.13}$$

$$SU(2)_L : W^i_{\mu\nu} = \partial_\mu W^i_\nu - \partial_\nu W^i_\mu - g\,\epsilon^{ijk}W^j_\mu W^k_\nu, \tag{1.14}$$

where $\epsilon^i{}_{jk}$ is the structure constant of $SU(2)_L$ group. The non-Abelian structure of the $SU(2)_L$ symmetry group results in the self-interactions of the gauge bosons, as shown in Figure 1.5.

The invariance under the local gauge symmetry of the group $SU(2)_L \otimes U(1)_Y$ implies that all particles should be massless. However, experimental observations demonstrated that fermions and weak bosons possess finite masses, indicating that $SU(2)_L \otimes U(1)_Y$ symmetry is spontaneously broken by the Higgs field, which leads to the mixing of the fields W^i_μ and B_μ and results in three massive weak bosons ($\mathrm{W}^+, \mathrm{W}^-, \mathrm{Z}$) and one massless electromagnetic photon (γ). The new mass eigenstates of the W bosons are defined as:

$$W^\pm_\mu = \frac{1}{\sqrt{2}}(W^1_\mu \mp iW^2_\mu). \tag{1.15}$$

The electromagnetic field A^μ and the neutral current field Z^μ, corresponding to the photon and the Z boson, can be derived from a rotation of the original massless fields:

$$\begin{pmatrix} A_\mu \\ Z_\mu \end{pmatrix} = \begin{pmatrix} \cos\theta_W & \sin\theta_\mathrm{W} \\ -\sin\theta_\mathrm{W} & \cos\theta_W \end{pmatrix} \begin{pmatrix} B_\mu \\ W^3_\mu \end{pmatrix}. \tag{1.16}$$

Here, the parameter θ_W is referred to as the *Weinberg angle* or *electroweak mixing angle*. These relations are valid under the condition $g \sin\theta_\mathrm{W} = g' \cos\theta_\mathrm{W} = e$.

At LO, the EW mixing angle relates the masses of the W and Z bosons as $\sin^2\theta_\mathrm{W} = 1 - m^2_\mathrm{W}/m^2_\mathrm{Z}$. At higher orders, the effective weak mixing angle $\sin^2\theta_\mathrm{eff} = k_f \cdot \sin^2\theta_\mathrm{W}$ is introduced, where k_f is a flavour-dependent effective scaling factor absorbing higher order corrections. Currently, the most precise effective leptonic electroweak mixing angle $\sin^2\theta^l_\mathrm{eff}$ values are 0.23221 ± 0.00029 from b quark forward-backward asymmetry results at the CERN LEP experiments, and 0.23098 ± 0.00026 from left-right asymmetry data at the SLD experiment at SLAC [53]. These two values differ by 3.2 standard deviations. A recent CMS measurement [54] presents a $\sin^2\theta^l_\mathrm{eff}$ obtained with a precision that exceeds that of all previous hadron collider measurements [55, 56], is comparable to that of the LEP and SLD results [53] and is in perfect agreement with the SM.

1.4 EW symmetry breaking and mass generation

The Higgs–Brout–Englert mechanism [19, 20] introduces the masses of elementary particles through the spontaneous breaking of the EW symmetry. The corresponding term of the SM Lagrangian featuring the new scalar field ϕ (Higgs field) reads:

$$\mathcal{L}_\mathrm{Higgs} = (D^\mu\phi)^\dagger (D_\mu\phi) - V(\phi). \tag{1.17}$$

The Higgs potential $V(\phi)$, dependent on the real parameters μ and λ, is defined such that it is invariant under the symmetry group $SU(2)_L \otimes U(1)_Y$:

$$V(\phi) = -\mu^2|\phi|^2 + \lambda|\phi^4|. \tag{1.18}$$

While the parameter λ drives the stability of the EW vacuum [58], the parameter μ represents the minimum of the potential $V(\phi)$ for a given value of λ. If $\mu^2 < 0$, the

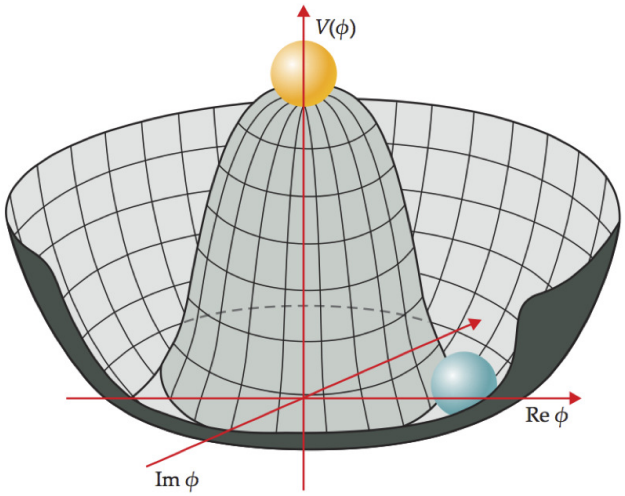

Figure 1.6: The Higgs potential for $\mu^2 > 0$: the local minimum corresponds to $\phi \equiv 0$, while the lowest energy state is degenerate and defined by $|\phi^2| = \mu^2/2\lambda$. Figure taken from Ref. [57].

only solution for the minimum of $V(\phi)$ is obtained for $\phi = 0$, which preserves the symmetry. In contrast, when $\mu^2 > 0$, the potential presents a degenerate minimum, as illustrated in Figure 1.6. The ground state of the potential has infinitely many degenerate solutions for the field ϕ corresponding to:

$$|\phi|^2 = \frac{\mu^2}{2\lambda} \equiv \frac{v^2}{2}, \tag{1.19}$$

where v is a non-zero vacuum expectation value. Through a gauge transformation of the scalar field ϕ, a particular minimum can be fixed, and the Higgs doublet can now be written as:

$$\phi = \begin{bmatrix} \phi_1 \\ \phi_2 \end{bmatrix} \rightarrow \frac{1}{\sqrt{2}} \begin{bmatrix} 0 \\ v + h \end{bmatrix}. \tag{1.20}$$

This choice breaks the EW symmetry and introduces the mass terms for the W and Z fields:

$$m_{\mathrm{W}} = gv/2, \qquad m_{\mathrm{Z}} = m_{\mathrm{W}}/\cos\theta_{\mathrm{W}}. \tag{1.21}$$

The vacuum expectation value defines the natural scale of the EW interactions and corresponds to $v \approx 246$ GeV [59]. Here, the field excitations h about the vacuum value v manifest as a physical scalar field whose excitation is the Higgs boson. The Higgs boson attains a mass $m_{\mathrm{H}} = \sqrt{2\lambda}v$, and its interactions with the weak vector bosons

are naturally generated. In addition, expanding the potential around the minimum of ϕ results in trilinear and quartic self-interaction terms of the field h with coupling strengths proportional to μ^2/v and λ. The Higgs boson was observed at the LHC by the ATLAS [60] and CMS Collaborations [61] in 2012 and is being studied in detail since then [62, 63].

While the Higgs kinetic term in Eq. (1.17) introduces the masses and couplings to h for the weak bosons via the non-zero vacuum expectation value, the fermion mass terms and Higgs couplings arise from the Yukawa interaction. The Lagrangian of the Yukawa sector reads:

$$\mathcal{L}_{\text{Yukawa}} = -\overline{Q_L^i} Y_{ij}^{'(u)} \phi_c u_R^j - \overline{Q_L^i} Y_{ij}^{'(d)} \phi d_R^j - \overline{L_L^i} Y_{ij}^{(l)} \phi \ell_R^j + \text{h.c.}, \tag{1.22}$$

where the three terms refer to the u-type, d-type quark and lepton fermions, respectively, $\phi_c = i\sigma^2\phi^*$ and *h.c.* denotes the hermitian conjugate. Here, the Yukawa matrices Y_{ij} are complex matrices with dimensionality equal to the number of generations. The elements of the Yukawa matrices are the Yukawa couplings y_f, which are proportional to the fermion's mass m_f:

$$y_f = \sqrt{2} m_f / v. \tag{1.23}$$

In the quark sector of Eq. (1.22), real diagonal mass matrices are obtained only by a change from the original flavour basis to the mass eigenstates ($Y_{ij}^{'}$), which is responsible for the flavour mixing, described by the Cabibbo-Kobayashi-Maskawa (CKM) matrix [36]. In the SM, the CKM matrix is a complex unitary matrix that can be parametrised in terms of three mixing angles and one CP-violating phase [59]. The parameters of the CKM matrix can be determined experimentally [59].

Similarly, the flavour mixing in the leptonic sector can be introduced. However, if neutrinos were massless, as predicted by the SM, the flavour and mass states would naturally coincide, and no mixing would be needed. Consequently, the charged-current interactions between leptons should be diagonal in the flavour. However, the neutrino oscillations are an experimental proof of the non-zero neutrino mass [64–68]. In this case, the SM Lagrangian in Eq. (1.22) can be extended to include the mass terms of the neutrinos, along with the leptonic equivalent of the CKM matrix, known as the Pontecorvo-Maki-Nakagawa-Sakata (PMNS) matrix [69, 70]. Currently, only upper

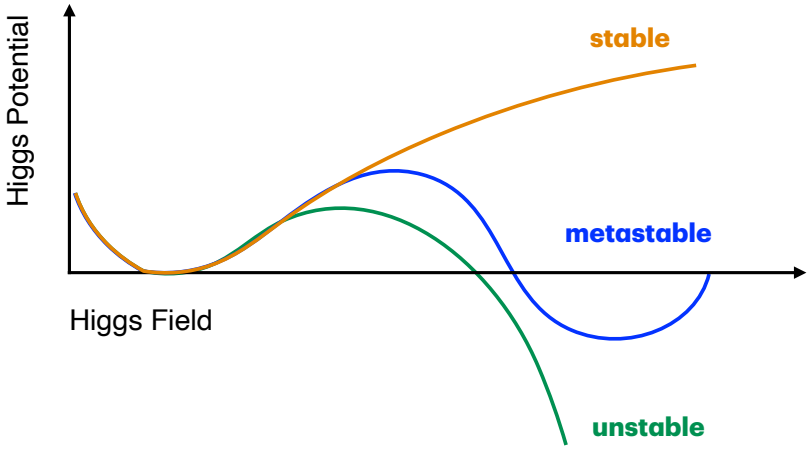

Figure 1.7: The Higgs potential in different stability scenarios of the EW vacuum.

limits on neutrino masses have been established. For instance, the effective electron antineutrino mass is constrained to $m_\nu < 0.8$ eV/c^2 at a 90% confidence level [71].

1.5 The stability of the electroweak vacuum

The stability of the SM EW vacuum is a fundamental proof of the validity of the SM and is linked to the properties of the Higgs field and its potential. If the Universe lies in the global minimum of the potential, it is stable. However if this minimum is only local, the Universe might tunnel out into a true vacuum state. So, the fate of the Universe is determined by the slope of the curve as shown in Figure 1.7, which features the stable, metastable and unstable scenarios. This slope is defined by a sign of the Higgs quartic coupling λ. A condition for the EW vacuum stability is that the Higgs quartic coupling parameter λ should always be positive. However, the analysis of the potential implies a possibly vanishing λ around the Planck scale, as shown in Figure 1.8 (left). Among the SM fields, those associated with the most massive particles exhibit the largest coupling to the Higgs field. As a result, loops involving top quarks contribute the most significant corrections to the parameters of the Higgs potential.

The evolution of λ as a function of the energy scale depends on the values of the top

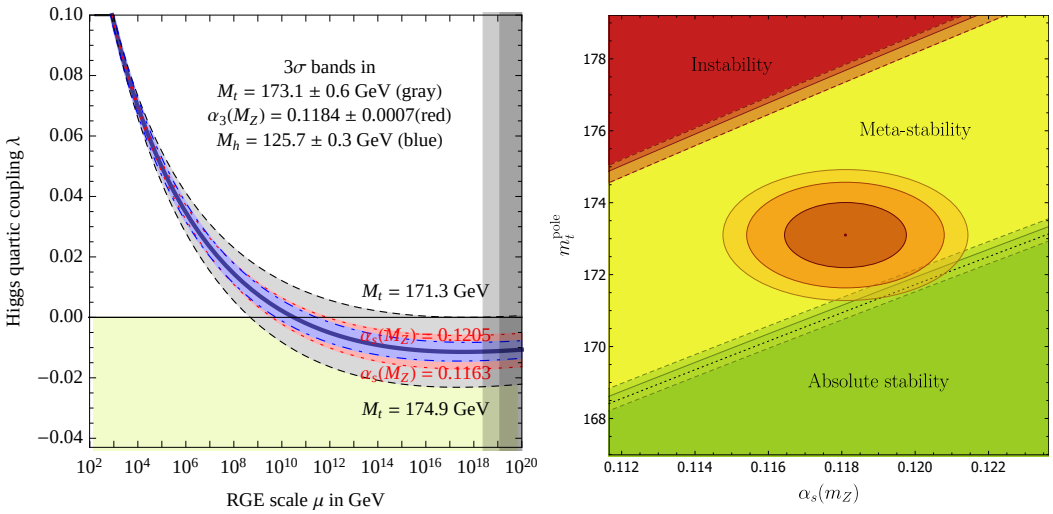

Figure 1.8: *Left*: The evolution of the Higgs quartic coupling λ as a function of RGE scale μ, including the $\pm 3\sigma$ uncertainty in the values of $\alpha_S(m_Z)$, m_t^{pole}, and the Higgs boson mass. Figure taken from Ref. [58]. *Right*: The regions of stability, metastability and instability as a function of the values of $\alpha_S(m_Z)$ and m_t^{pole}. The values $m_t^{pole} = 173.1 \pm 0.6\,\text{GeV}$ and $\alpha_S(m_Z) = 0.1181 \pm 0.0011$ are assumed, with the ellipses indicating the 68%, 95% and 99% confidence levels. Figure taken from Ref. [75].

quark mass m_t, $\alpha_S(m_Z)$, and (to a lesser extent) m_H [58, 72–74]. Predicted regions of instability, metastability and stability of the EW vacuum for different assumed values of $\alpha_S(m_Z)$ and m_t are shown in Figure 1.8 (right). With the values of m_t, $\alpha_S(m_Z)$ and m_H considered in Ref. [75], only the unstable vacuum hypothesis can be firmly rejected. Any non-stable result for the EW vacuum would suggest the presence of new physics at the scale where λ becomes negative, necessary to stabilise the vacuum. In Ref. [76], several new physics models were investigated in this context. The work of Ref. [76] also estimates that reducing the current uncertainties in m_t and $\alpha_S(m_Z)$ by a factor of two to three would be necessary to prove that the SM predicts vacuum stability at the 5σ level. As a result, precise experimental determinations of $\alpha_S(m_Z)$ and m_t are crucial in probing the stability of the EW vacuum.

Chapter 2

Phenomenology of hadronic collisions

This Chapter describes the theoretical aspects related to the physics analyses presented in this thesis. Section 2.1 discusses the QCD factorisation, followed by a discussion of the proton structure and its determination in Section 2.2. The modelling of proton-proton collisions through Monte Carlo (MC) simulations is described in Section 2.3. The phenomenology of jet and top quark production is presented in Sections 2.4 and 2.5, respectively, with a particular focus on the methods to determine the strong coupling constant $\alpha_S(m_{\mathrm{Z}})$, the top quark mass m_{t}, and its width Γ_{t}.

2.1 Physics at hadron colliders

The cross section of particle production in proton-proton (pp) collisions at high energies can be computed using a master formula known as the QCD *factorisation theorem* [77]. This theorem states that the parton dynamics can be factorised into short-distance and long-distance interactions at factorisation scale μ_{f}, which separates the perturbative and non-perturbative regimes, respectively. The cross section for a given process, $\sigma_{\mathrm{pp}} \to ab + X$, can be formulated as the convolution of the parton distribution functions (PDFs) of the proton $\mathrm{f}_i(x, \mu_{\mathrm{f}})$ with the partonic cross section $\hat{\sigma}_{ij\to ab}$:

$$\sigma_{\mathrm{pp}\to ab+X} = \int dx_1 \int dx_2 \sum_{ij} \mathrm{f}_i(x_1\,, \mu_{\mathrm{f}})\ \mathrm{f}_j(x_2\,, \mu_{\mathrm{f}}) \hat{\sigma}_{ij\to ab}\left(x_1, x_2, \alpha_S(\mu), \mu_{\mathrm{r}}, \mu_{\mathrm{f}}\right). \quad (2.1)$$

The PDFs represent the probability density function of finding a parton i, carrying a fraction x of the proton momentum, inside the proton, as resolved at μ_{f}. They

are considered *universal*, meaning these are intrinsic properties of the nucleon and, therefore, do not depend on the particular process. The $\hat{\sigma}_{ij\to ab}$ can be calculated perturbatively.

Beyond leading order (LO) in perturbation theory, the scale μ_f is introduced to subtract infrared divergences that arise from hard collinear initial-state radiation. This scale corresponds to the minimum transverse momentum at which a collinear splitting of an interacting parton can be resolved while the remaining infrared divergences are absorbed into the PDFs. In this way, the dependence on the scale μ_f from the PDFs and $\hat{\sigma}_{ij}$ cancel out when considering all orders in perturbation theory. However, at a fixed order prediction (e.g. next-to-LO (NLO)), a residual dependence remains and has to be evaluated.

The relevant RGEs for evolving the PDFs as a function of the scale μ_f are the Dokshitzer-Gribov-Lipatov-Altarelli-Parisi (DGLAP) equations [78–84], formulated in 1977. For the gluon g and the singlet Σ, the DGLAP reads:

$$\mu\frac{d}{d\mu}\begin{bmatrix}\mathrm{f}_\Sigma(x,\mu^2)\\ \mathrm{f}_g(x,\mu^2)\end{bmatrix} = \int_x^1 \frac{d\xi}{\xi}\begin{bmatrix}P_{qq}\left(\frac{x}{\xi},\alpha_S(\mu^2)\right) & P_{qg}\left(\frac{x}{\xi},\alpha_S(\mu^2)\right)\\ P_{gq}\left(\frac{x}{\xi},\alpha_S(\mu^2)\right) & P_{gg}\left(\frac{x}{\xi},\alpha_S(\mu^2)\right)\end{bmatrix}\begin{bmatrix}\mathrm{f}_\Sigma(\xi,\mu^2)\\ \mathrm{f}_g(\xi,\mu^2)\end{bmatrix}, \tag{2.2}$$

where the singlet $\mathrm{f}_\Sigma(x,\mu^2)$ is defined as $\sum_{i=1}^{N_f}\left(q_i(x,\mu^2)+\bar{q}_i(x,\mu^2)\right)$ [83] and i runs over the number of active quark flavours in the nucleon. The non-singlet evolution equations for the valence distributions q_v and the non-singlet quark flavour asymmetries $q_\pm$ are given by:

$$\mu\frac{d}{d\mu}\mathrm{f}_{q_i}^{\mathrm{NS}}(x,\mu^2) = \int_x^1 \frac{d\xi}{\xi}P_{q_iq_i}^{\mathrm{NS}}\left(\frac{x}{\xi},\alpha_S(\mu^2)\right)\mathrm{f}_{q_i}^{\mathrm{NS}}(\xi,\mu^2), \quad i\in[\mathrm{v},\pm]. \tag{2.3}$$

In Eq. (2.2) and (2.3), the functions $P_{ij}(z)$ are the Altarelli-Parisi splitting functions, which can be calculated perturbatively. The corresponding Feynman diagrams at LO are shown in Figure 2.1.

At LO, the splitting functions can be interpreted as the probability that a parton i emits a parton j with a fraction x of its longitudinal momentum in the collinear approximation. This implies that they are positive definite for $z<1$, and they satisfy

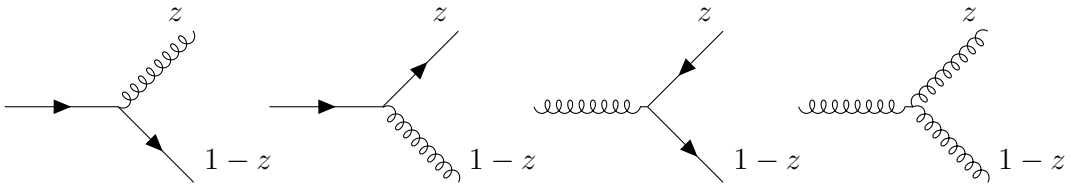

Figure 2.1: The Feynman diagram representations at LO for the processes corresponding to the Altarelli-Parisi splitting functions $P_{qg}(z)$, $P_{qq}(z)$, $P_{gq}(z)$, and $P_{gg}(z)$ (from left to right).

the *sum rules*:

$$\begin{cases} \int_0^1 dz P_{ns}(z) = 0, \\ \int_0^1 dz z \left(P_{qq}(z) + P_{gq}(z)\right) = 0, \\ \int_0^1 dz z \left(2n_f P_{qg}(z) + P_{gg}(z)\right) = 0, \end{cases} \tag{2.4}$$

corresponding to the conservation of quark number and momentum [33]. Here, the quark flavour indices have been omitted. Similarly, the PDFs satisfy a set of sum rules [33, 85]. The conservation of the number of up- and down-quarks in the proton and the conservation of momentum is given by:

$$\begin{cases} \int_0^1 dx[\mathrm{u}(x) - \overline{\mathrm{u}}(x)] = 2, \\ \int_0^1 dx[\mathrm{d}(x) - \overline{\mathrm{d}}(x)] = 1, \\ \sum_j \int_0^1 dx \mathrm{f}_j(x) x = 1. \end{cases} \tag{2.5}$$

While the scale dependence (evolution) of the PDFs can be calculated in perturbative QCD using the DGLAP equations, their x dependence can not yet be calculated from the first principles and needs to be extracted from the experimental data. The PDFs are typically parametrised in the form of a polynomial at a chosen starting scale Q_0. Then, they are evolved to the kinematic regions of the measurements using the DGLAP equations. Finally, the PDFs are extracted by comparing the theory predictions to data in a χ^2 minimisation procedure. The phenomenology groups, such as ABMP [86], MSHT [87], CTEQ [88], and NNPDF [89], combine many data from several experiments and processes to interpret those in terms of PDFs (and in some cases also quark masses, $\alpha_S(m_\mathrm{Z})$, or other parameters), in a procedure known as a *global QCD analysis*. Differences in the results arise from the selection of data, theory assumptions and different parametrisations of the functional forms.

2.2 Constraining PDFs from experimental data

Precise knowledge of PDFs is essential to accurately describe the initial state in pp collisions. Currently, the uncertainties in the PDFs are the limiting factor for many high-precision interpretations of the LHC measurements. For instance, recent CMS results on e.g. the mass of the W boson [90] and the effective electroweak mixing angle [54] depend on the choice of the PDFs. Uncertainties in the PDFs represent the dominant uncertainties in these measurements, ∼21% and ∼50% of the total uncertainty in m_{W} and $\sin^2\theta^l_{\mathrm{eff}}$, respectively, highlighting the need for continuous improvements in understanding the parton dynamics by incorporating high-precision collider data.

The PDFs can be determined using dedicated measurements, such as Deep Inelastic Scattering (DIS), or in hadronic collisions. The main constraints on the PDFs are imposed by the DIS data, collected in $e^{\pm}p$ collisions at HERA [91]. The DIS process at energies above the Z boson mass proceeds either through exchange of a virtual photon or a Z boson (*Neutral Current*, NC) or a $W^{\pm}$ boson (*Charged Current*, CC). These processes are illustrated in Figure 2.2 for the $e^{-}p$ interaction.

The kinematics of DIS $e^{\pm}p$ scattering is described by the following variables [33]:

$$\begin{cases} Q^2 = -q^2 = -(k-k')^2, \\ x = \dfrac{Q^2}{2P\cdot q}, \\ y = \dfrac{P\cdot q}{k\cdot P}, \end{cases} \tag{2.6}$$

where P is the proton's momentum, $k(k')$ the momentum of the incoming (outcoming) lepton, and q the momentum transferred from the incoming particle to the target. Here, Q^2 represents the virtuality of the boson; x is a *scaling* variable; and y corresponds to the momentum fraction of the lepton taken by the hadronic final state in the proton rest frame. The *inclusive* cross sections for the NC and CC contributions, where inclusive means that the cross sections are integrated over all possible hadronic final states, are given respectively by:

$$\frac{d^2\sigma^{\mathrm{NC}}_{e^{\pm}p}}{dxdQ^2} = \frac{2\pi\alpha^2}{xQ^4}\left[Y_+\tilde{F}_2(x,Q^2) \mp Y_- x\tilde{F}_3(x,Q^2) - y^2\tilde{F}_L(x,Q^2)\right], \tag{2.7}$$

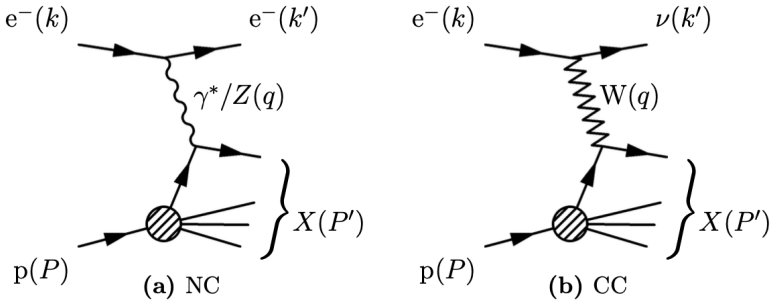

Figure 2.2: NC (a) and CC (b) processes in e^-p collisions. The hadronic final state is labelled as X, and the four momenta are shown in brackets.

$$\frac{d^2\sigma^{\mathrm{CC}}_{e^+p}}{dxdQ^2} = \frac{G_F^2}{2\pi x}\left(\frac{M_{\mathrm{W}}^2}{Q^2+M_{\mathrm{W}}^2}\right)^2\left[Y_+\tilde{W}_2^{\pm}(x,Q^2) \mp Y_- x\tilde{W}_3^{\pm}(x,Q^2) + y^2\tilde{W}_L^{\pm}(x,Q^2)\right], \tag{2.8}$$

where α is the electromagnetic coupling constant, G_F the Fermi coupling constant and $Y_\pm = 1 \pm (1-y)^2$. Here, $\tilde{F}_i(x,Q^2)$ and $\tilde{W}_i^{\pm}(x,Q^2)$ with $i = 2,3,L$ are generalised structure functions for the NC and CC, respectively.

The combination of NC and CC measurements are sensitive to light quarks at low and medium x and to the gluon PDF via scaling violations. It is worthwhile noticing that the inclusive DIS is only indirectly sensitive to the gluon distribution. Production of jets and heavy quarks in DIS, instead, while probing the gluon distribution directly [92], is statistically limited in particular at high x. High-energy pp collision at the LHC provide valuable information on the PDFs in particular at high x. However, the LHC data alone are not sufficient to constrain the PDFs, since the momentum fractions x_1 and x_2 of two colliding protons, carried by the interacting partons, cannot be disentangled. Therefore, the DIS data are always used for PDF extraction. At the LHC, different processes in pp collisions can be used to provide additional constraints on different PDFs. Heavy quark pair production probes the gluon distribution in a wide range of x: while the forward c and b quark production provides key information about the gluon at very low x [93,94], the top-quark pair production gives information about the gluon at high x [95–98]. The Drell-Yan processes probe the valence distribution and contribute to flavour decomposition of the sea [54], while associated W+c production probes directly the strange quark distribution [99–102]. The production of jets is sensitive to the valence quark distributions and the high-x range of the gluon

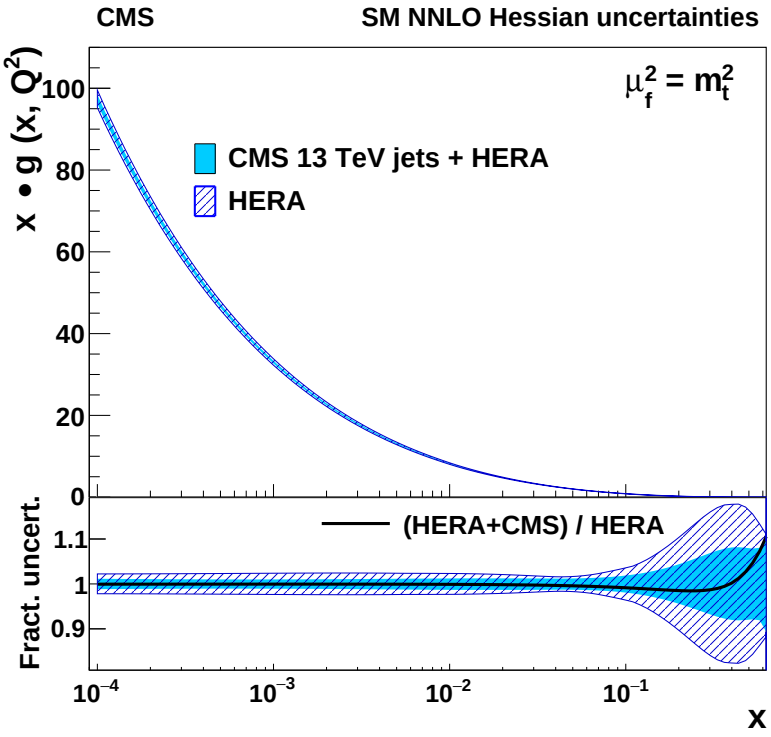

Figure 2.3: The gluon PDF distribution shown as a function of x at the scale $\mu_f^2 = m_t^2$. The filled (hatched) band shows the results of a fit using HERA DIS and CMS inclusive jet cross section data at $\sqrt{s} = 13$ TeV (HERA DIS data only) with their total uncertainty. The lower panel displays a comparison of the relative PDF uncertainties for each distribution. The line represents the ratio of the central PDF values of the two variants of the fit. Figure taken from Ref. [106].

distribution [103–108]. In Figure 2.3, the gluon distribution derived from the CMS jet production measurements at a centre-of-mass energy $\sqrt{s}$ of 13 TeV [106] combined with DIS data are compared to those obtained using only DIS data. The inclusion of jet production data notably enhances the gluon distribution at high x.

In this thesis, the simultaneous extraction of $\alpha_S(m_Z)$ and PDFs is performed using jet data measured by CMS at multiple $\sqrt{s}$, combined with DIS data.

2.3 Monte Carlo simulations

The MC event generators, paired with a detailed simulation of the experimental apparatus, are essential to compare data to theoretical predictions at the LHC. The gen-

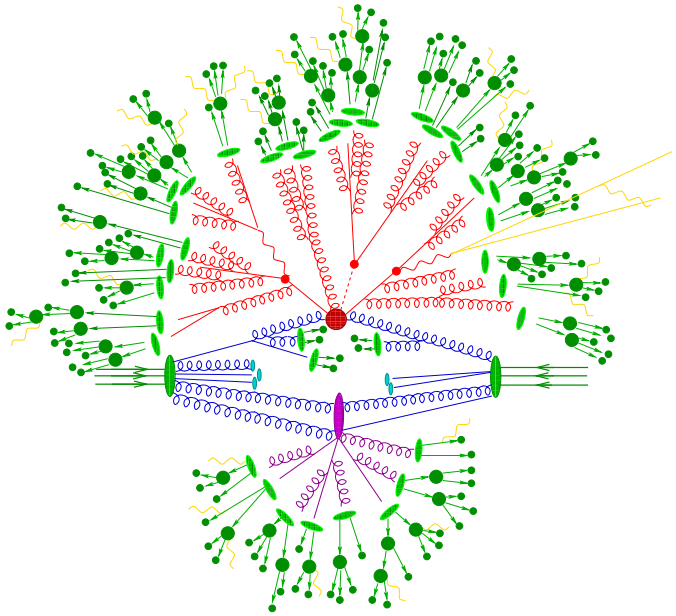

Figure 2.4: A schematic representation of the MC simulation of a pp collision. Partons from the colliding protons contribute to the hard interaction (red circle in the centre), surrounded by parton branchings simulated by the PS. A secondary scattering event (purple circle) is illustrated, representing multiple-parton interactions. The hadronisation process (light green circles), together with the decays of final state hadrons (dark green circles), are also shown. Figure taken from Ref. [109].

eration of MC-simulated events is factorised into a number of steps, each addressed with different techniques, depending on the typical energies involved. An illustration of a typical pp collision event generated in MC simulation is presented in Figure 2.4. After the hard interaction, the final-state partons can further fragment with the emission of soft and collinear partons simulated by parton shower (PS). While the hard interaction, and partially fragmentation, can be computed in perturbation theory, soft processes such as multiple parton interactions (MPI), hadronisation, and hadron decays into stable particles rely on phenomenological methods. The different steps of the MC event generation, along with the simulation of the detector response, are detailed below.

Matrix Element (ME): The partonic cross section is calculated by evaluating the probability of the hard interaction. MC generators at NLO in QCD used at the LHC experiments include POWHEG [110–113] and MG5_AMC@NLO [114]. In the POWHEG method, infrared singularities are handled by cancelling soft and collinear real emis-

sions with their corresponding virtual corrections. This results in a fraction of events with negative weights, typically around 1% at NLO accuracy and increasing to ∼10% at NNLO accuracy. Similarly, in MG5_AMC@NLO, negative weights arise from the subtraction method used to regulate divergences, though their fraction depends on the process and phase-space region.

Parton shower: PS models imply the same splitting functions presented in Section 2.1 within the framework of PDFs. For any hard process generating a parton i, the cross section for a hard configuration with cross section σ_0, accompanied by a parton j carrying a momentum fraction z, is given by [115]:

$$d\sigma \approx \sigma_0 \sum_{partons,j,i} \frac{\alpha_S}{2\pi} \frac{d\theta^2}{\theta^2} P_{ji}(z) dz, \tag{2.9}$$

where $P_{ji}(z)$ are the splitting functions, and θ is the angle of the emission. Equation (2.9) is solved through an iterative process, starting from the ME of the hard scattering and incorporating a final-state branching at each step. The divergences in the limit $\theta \to 0$ can be removed by setting a shower cutoff Q_0, which defines the scale below which a splitting is not resolved. By using k as an ordering variable, the Sudakov form factor describes the probability of no resolvable branchings occurring with $k^2 > q^2$ [115, 116]:

$$\Delta_i(Q^2, q^2) = \exp\left[-\sum_j \int_{q^2}^{Q^2} \frac{dk^2}{k^2} \frac{\alpha_S}{2\pi} \int_{Q_0^2/k^2}^{1-Q_0^2/k^2} P_{ji}(z) dz \right]. \tag{2.10}$$

Here, q is the virtuality of the emitted parton. In the PS implementation, a random number r is selected, and the equation $\Delta_i(Q^2, q^2) = r$ is solved for q^2. If $q^2 > Q_0^2$, a resolvable branching with $k^2 = q^2$ is generated according to $P_{ji}(z)$; otherwise, the evolution stops. The shower algorithm numerically carries out the all-order summation embedded in the exponentiation of Eq. (2.9). By summing the terms with the greatest number of logs of Q_0^2 at each order of α_S, it is referred to as a *leading collinear logarithmic parton shower algorithm* [115]. Another key factor is the running of the strong coupling α_S, which increases as q^2 decreases. This leads to higher branching probabilities and a faster development of the shower. Consequently, the shower cutoff scale Q_0 must be set significantly above Λ_{QCD} to preserve the validity of perturbation theory. As a result, Q_0 strongly affects the final observable distributions of the

PS. A similar method applies to initial-state showers, with Eq. (2.9) modified to include PDF evolution and correct momentum fraction for each interacting parton [115].

ME-PS matching: To prevent double counting, real emissions present in both the fixed-order ME calculation and the PS must be carefully handled. This is done by subtracting overlapping terms when matching the PS to the ME calculation, correcting the hardest emission from the parton shower. One widely used matching procedure is the POWHEG method [110–113], which applies appropriate corrections to the Sudakov form factor. The value of the scale at which the matching is performed, known as the *resummation* scale (h_{damp}) [117], is tuned using experimental data. This procedure ensures that both the NLO accuracy of the ME calculation and the leading-logarithmic resummation properties of the PS are preserved. Alternatively, the matching scheme FxFx [118] is used in MG5_AMC@NLO. Generating and matching to next-to-NLO (NNLO) predictions is an ongoing area of development. An example is the POWHEG MiNNLO [119–122] event generator.

Underlying Event: All the interactions that are not linked to the hard scattering (e.g. beam remnants and multiple parton-parton interactions) are collectively referred to as the *underlying event*. This process is simulated using phenomenological models, where dedicated tunes are derived by fitting the model parameters to the experimental data [123]. Furthermore, the interference between the hard-interaction partons and final-state radiation due to colour correlations have to be accounted for [124]. Several colour reconnection models are available [125–127] for LHC analyses.

Hadronisation: At energy scales below Λ_{QCD} and the PS cutoff, coloured objects recombine to form colour-neutral hadrons. This process is described by hadronisation models, with two main classes being the *string* model [128] as used in, e.g., PYTHIA [129] generator, and the *cluster* model as implemented in, e.g., HERWIG [130]. The string model assumes that $q\bar{q}$ pairs are subject to a linearly rising potential compressed in a string. As the distance between the quarks increases, the potential energy rises until it becomes energetically favourable to break the string and produce a new $q\bar{q}$ pairs. The fragmentation process continues until stable hadrons are formed. In this framework, the gluons are modelled as kinks in the strings, influencing the kinematic properties of the hadrons. The Bowler–Lund parametrisation [131] extends the string model by incorporating the effects of the heavy quark mass on the string po-

tential. This parametrisation describes the distribution of the momentum fraction of the heavy quark carried by the associated hadron. Alternatively, the Peterson fragmentation function can be used [132]. The Lund string model has been employed in this thesis. Otherwise, the cluster model of hadronisation is based on clustering quarks and antiquarks at the hadronisation scale. In the first step, gluons are split into $q\bar{q}$ pairs. Then, the surrounding quarks and antiquarks are combined and form colour-neutral clusters, which subsequently decay into hadrons.

Simulation of the detector response: At the CMS experiment, a comprehensive simulation of the detector is carried out using the GEANT4 package [133]. Particles produced at "generator level" in MC event generators are propagated through the detector simulation and undergo modifications based on various detector effects, such as scattering in detector materials and bremsstrahlung. This simulation is tuned on real collision data to ensure a reliable description of the detector [39]. The resulting "detector-level" objects can then be processed in the same way as real collision data, serving as inputs for the particle reconstruction and identification algorithms described in Section 3.3. This step in the simulation is the most CPU- and storage-intensive.

2.4 Jets and α_S

The particles produced by fragmentation and hadronisation and originating from the same initial parton form collimated sprays called *jets*, which conserve the properties of the original parton, such as its flavour, direction, and momentum. Jet production was observed for the first time in 1975 by the SPEAR experiment in e^+e^- collisions at SLAC at $\sqrt{s} = 3 - 7.4$ GeV, illustrating the confinement property of QCD [31]. Since then, jet measurements have been used for the fundamental tests of QCD properties [31, 134, 135]. While there are several processes from which to extract $\alpha_S(m_Z)$ at the LHC (e.g., top quark pair production cross section [106, 136–138], W/Z bosons cross sections [139, 140] and Z boson p_T distribution [141]), jet production is a standard candle process to determine $\alpha_S(m_Z)$ at high energy scales. A summary of the latest determination of $\alpha_S(m_Z)$ at the LHC, with at least NNLO accuracy in QCD, is presented in Figure 2.5.

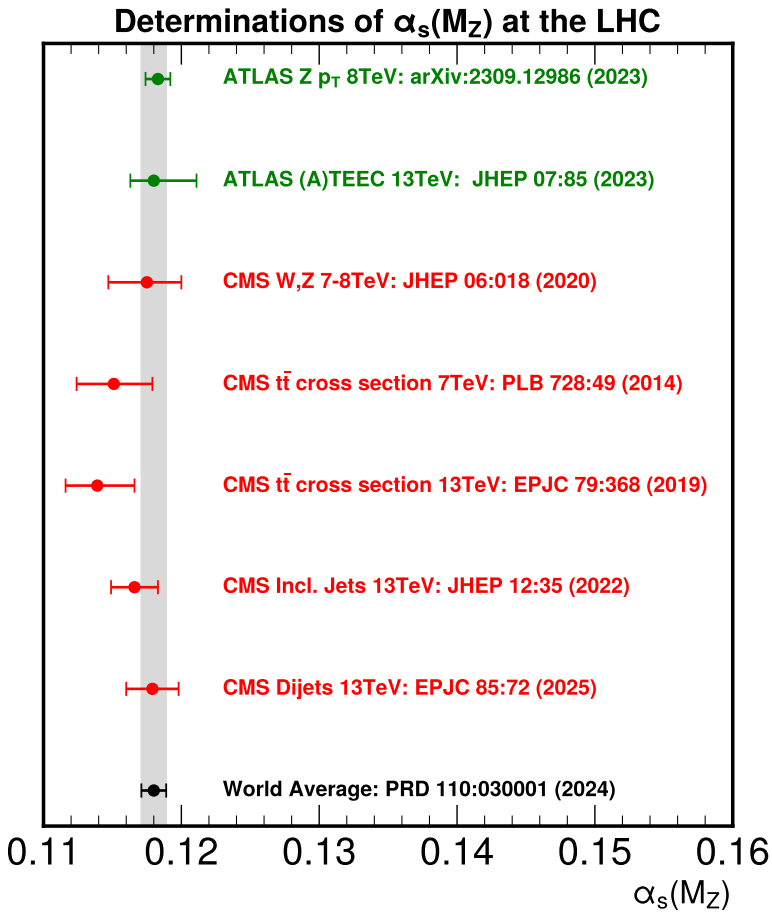

Figure 2.5: Summary of $\alpha_S(m_Z)$ determinations from ATLAS (green) and CMS (red) collaborations at least at NNLO in QCD. The results are compared to the world average $\alpha_S(m_Z) = 0.118 \pm 0.0009$ [6] (black).

Jet definition

The definition of a jet is not unique and depends on the clustering algorithm used. A jet is defined as a cone of radius R around an axis that (ideally) aligns with the direction of the initial parton. The clustering algorithm should have some desirable features, including easy implementation from theoretical and experimental perspectives. An essential requirement is the *infrared-collinear* safe property, i.e. the algorithm must be robust against the emission of additional soft or collinear radiation.

This feature is crucial to ensure the renormalisation of the theory. A category of jet algorithms largely used at the LHC is the *sequential-recombination algorithms*, which reconstruct the "history" of the jet and is theoretically robust. This class of algorithms uses a metric that searches for the minimum value within the set of distances between pairs of particles i and j, and between each particle i and the beam B (d_{iB}):

$$\begin{cases} d_{ij} \equiv \min\left(k_{\mathrm{T}i}^{2p}, k_{\mathrm{T}j}^{2p}\right) \dfrac{\Delta y_{ij}^2 + \Delta\phi_{ij}^2}{R^2}, \\ d_{iB} \equiv k_{\mathrm{T}i}^{2p}. \end{cases} \tag{2.11}$$

Here, p is a parameter defining the type of jet algorithm, k_{T} is the transverse momentum of the particle, R is the cone radius parameter, and $\Delta\phi_{ij}^2$ and Δy_{ij}^2 are the squared differences between the azimuthal angles ϕ and rapidities y of i and j particles. The rapidity y is defined as:

$$y = \frac{1}{2}\frac{E + p_z}{E - p_z}, \tag{2.12}$$

where E represents the object's energy, and p_z is the momentum component along the beam direction. The algorithm proceeds iteratively by checking if $d_{ij} < d_{iB}$. If this condition is satisfied, particles i and j are merged into a jet by summing their momenta. Otherwise, particle i is assigned as a new jet. If any particles remain unclustered, the process is repeated. Based on the power parameter p, different subsets of sequential-recombination algorithms are defined, as shown in Table 2.1. The jets obtained from the three different clustering algorithms are illustrated in Figure 2.6.

Power Parameter p	**Algorithm**
$p = 1$	k_{T} [142]
$p = 0$	Cambridge-Aachen [143]
$p = -1$	anti-k_{T} [144]

Table 2.1: Sequential-recombination algorithms defined by the power parameter p.

In this thesis, the anti-k_{T} [144] algorithm is used, which starts clustering from the highest p_{T} object and progressively accumulates softer particles around it. The process stops when no particles are found within a radius R around the hard centre. The resulting jets are almost well-defined cones, an important feature for calibrating jets in pp collisions and minimising noise effects from pileup and MPI. However, this algorithm is not ideal for substructure studies. In such cases, reclustering with the

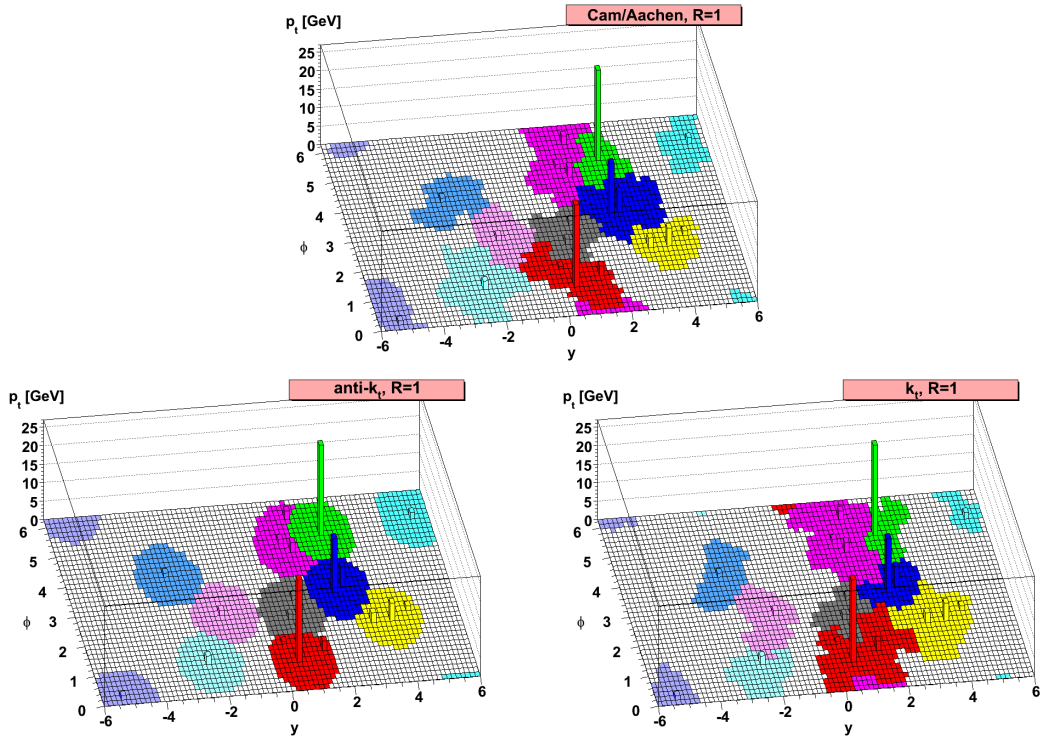

Figure 2.6: Jets clustered by using different jet algorithms. Figures taken from Ref. [144].

Cambridge-Acheen algorithm is typically applied. The jet cone radius R is a crucial parameter in jet analyses. On one hand, R should be large enough to contain all partons, minimising any out-of-cone losses. However, if R is too large, the contamination from pileup, initial-state radiation, and hadronisation effects increases. For QCD interpretation studies, a larger radius is typically used.

Probing QCD with inclusive jets

The production of *inclusive jets*, denoted as pp $\rightarrow$ jet + X, refers to events that feature at least one jet in the final state with reconstructed p_{T} above a given threshold, where "inclusive" means that no constraints are imposed on the total number of jets in the event. This is a standard candle process to test the QCD dynamics up to the highest accessible energy scales. In pp collisions at the LHC, inclusive jet production has been extensively studied by the CMS [103–106, 148, 149] and ATLAS [150–155] Col-

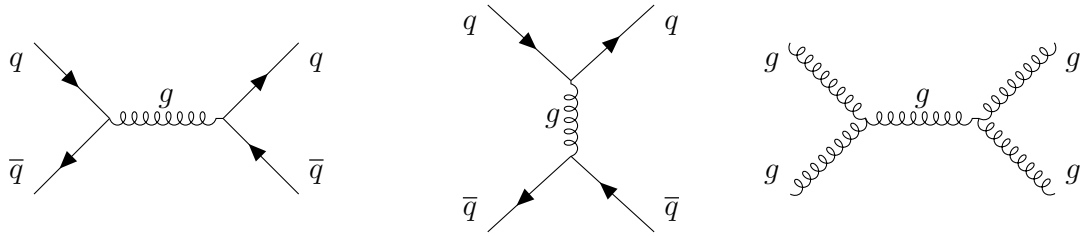

Figure 2.7: The Feynman diagram representations for jet production at LO in hadronic collisions. The first two diagrams show the quark-antiquark annihilation production mode in the s-channel (left) and t-channel (middle), respectively, while the third diagram (right) represents the gluon-gluon fusion production mode.

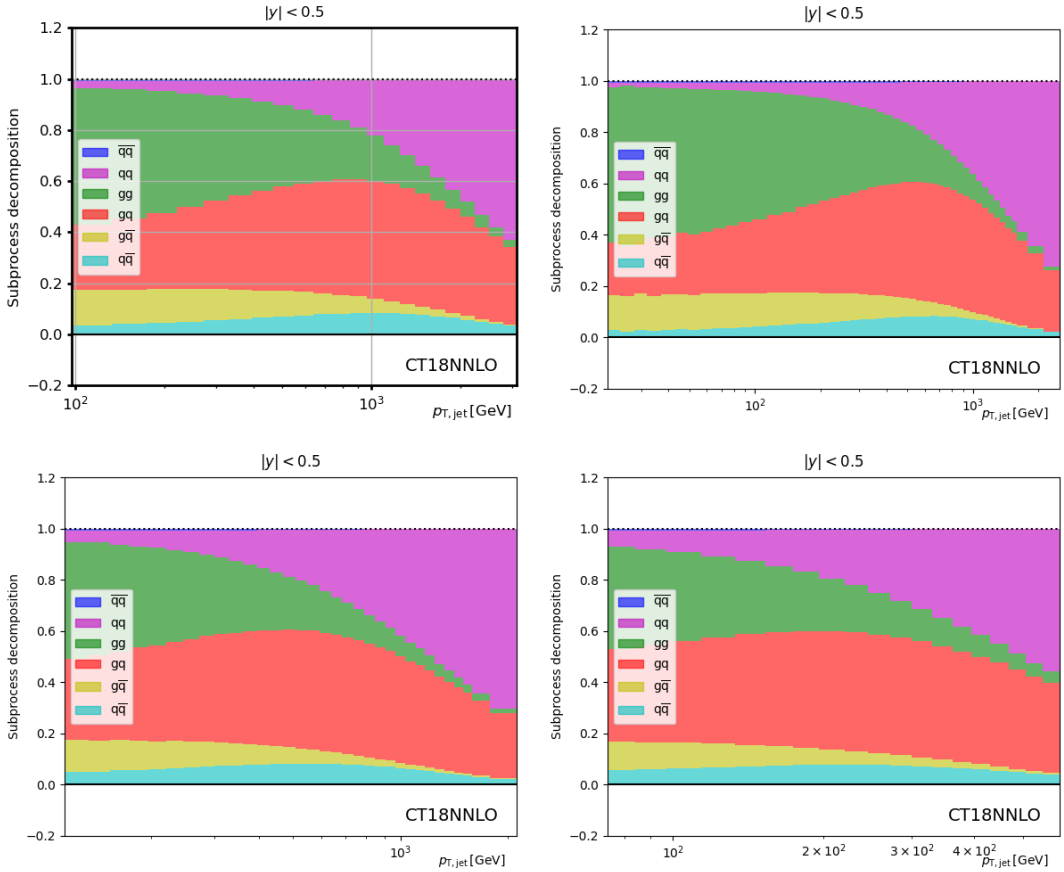

Figure 2.8: The inclusive jet production modes at the LHC at NNLO. The most central rapidity bin of the CMS inclusive jet measurement at $\sqrt{s}$ =13 (upper left), 8 (upper right), 7 (lower left) and 2.76 (lower right) TeV are shown. Figures produced using the fastNLO program and the fastNLO interpolation grids [145–147].

laborations at several $\sqrt{s}$ over a wide kinematic range. The Feynman diagrams of jet productions at LO are shown in Figure 2.7. In hadronic collisions at $\sqrt{s} = 13$ TeV, jets are predominantly produced through the gluon-gluon fusion process at low to medium p_{T}, whereas quark-quark and quark-gluon interactions become dominant at higher p_{T} values. As $\sqrt{s}$ decreases, the contribution from quark-gluon becomes more significant at low/medium p_{T}, while at high p_{T}, quark-quark contributions become larger, as illustrated in Figure 2.8. As a result, jets are particularly sensitive to the gluon and valence PDF distributions. At the same time, jet production is driven by the value of $\alpha_S(m_{\mathrm{Z}})$. Consequently, the theoretical predictions of the jet cross sections is affected both by $\alpha_S(m_{\mathrm{Z}})$ and PDFs, so that variation of one parameter would be compensated by the variation of another. To account for the correlation between α_S and PDFs, both should be extracted simultaneously. Several comprehensive QCD analyses were performed at HERA and at the LHC experiments [91,104–108,156] using the inclusive and multi-jet production for determination of PDFs and $\alpha_S(m_{\mathrm{Z}})$. Further, high-p_{T} jet production can also probe models beyond the SM, e.g. Contact Interactions, usually modelled by means of Effective Field Theory [157]. Recent simultaneous determination of PDFs, strong coupling, and the effective couplings of New Physics [106, 158] account for the correlations between the QCD and EFT parameters and start to be most commonly used for the BSM interpretations of the jet data.

This thesis presents the most precise determination of $\alpha_S(m_{\mathrm{Z}})$ ever obtained by using the jet production measurements. The $\alpha_S(m_{\mathrm{Z}})$ together with PDFs is extracted in a comprehensive QCD analysis at NNLO combining CMS inclusive jet measurements at several $\sqrt{s}$. Moreover, the running of α_S as a function of the energy scale is illustrated at NNLO, up to ∼2 TeV. The details and results of this analysis are presented in Chapter 6.

2.5 The top quark mass and width

The existence of the top quark was suggested already by Kobayashi and Maskawa in 1973 [159] before its direct measurement. Following the discovery of the b quark at Fermilab in 1977 [160], the search for its expected isospin partner began. Although initial searches at e^+e^- colliders were unsuccessful, the top quark was eventually discovered by the CDF and D0 Collaborations at Fermilab at $\sqrt{s} = 1.8$ TeV [161,162]. The top quark is the most massive elementary particle known with a $m_{\mathrm{t}}^{\mathrm{pole}}$ mass of

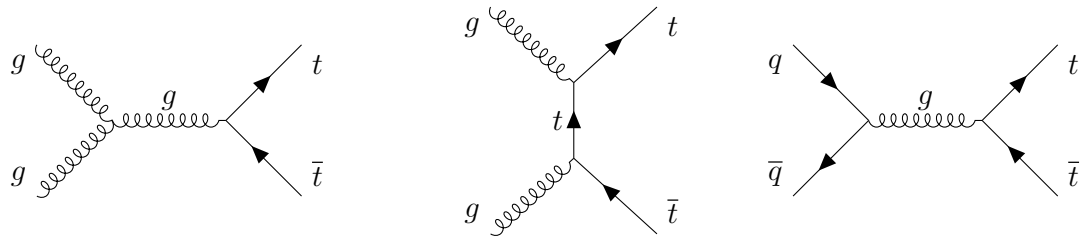

Figure 2.9: The Feynman diagram representations for $t\bar{t}$ production at LO in hadronic collisions. The first two diagrams show the gluon-gluon fusion production mode in the s-channel (left) and t-channel (middle), respectively. The third diagram (right) shows the quark-antiquark annihilation production mode.

about 172.4 ± 0.7 GeV [6]. Its total decay width, assuming $|V_{\mathrm{tb}}| = 1$ and neglecting the b quark mass, can be expressed as [163]:

$$\Gamma_{\mathrm{t}}^{\mathrm{LO}} = \frac{G_F m_t^3}{8\pi\sqrt{2}} \left(1 - \frac{m_W^2}{m_t^2}\right)^2 \left(1 + 2\frac{m_W^2}{m_t^2}\right), \tag{2.13}$$

where m_{t} refers to $m_{\mathrm{t}}^{\mathrm{pole}}$. The top quark decay width is predicted up to N3LO, with the analytic calculation yielding 1.3120 ± 0.0038 GeV [2]. However, the total decay width is highly sensitive to the value of $m_{\mathrm{t}}^{\mathrm{pole}}$ assumed in the calculations. To take this effect into account in Ref. [2], the PDG uncertainty in m_t^{pole} derived from cross section measurements ($\Delta m_t = \pm 0.7$ GeV) is included and the overall uncertainty increases to ± 0.0194 GeV. The top quark lifetime is $\tau_{\mathrm{t}} \approx 5 \times 10^{-25}$ s, which is much smaller than the hadronisation time scale of $1/\Lambda_{\mathrm{QCD}} \approx 3 \times 10^{-24}$ s. As a result, the top quark decays before forming top-flavoured hadrons and is an ideal candidate for studying the properties of an unconfined quark, such as its charge and polarisation.

In pp collisions, top quarks can be produced either in top quark-antiquark ($t\bar{t}$) pairs via the strong interaction or as single top quarks through the EW interaction. At the LHC, $t\bar{t}$ pair production dominates with a cross section approximately four times higher than that of single top production. Experiments at the LHC and Tevatron have studied this process across a wide range of energies and found that it is well described by perturbative QCD, as shown in Figure 2.10. In pp collisions, about 90% of the $t\bar{t}$ pairs are produced via the gluon-gluon fusion process [164], followed by the $q\bar{q}$ annihilation. The Feynman diagrams of $t\bar{t}$ production at LO are illustrated in Figure 2.9.

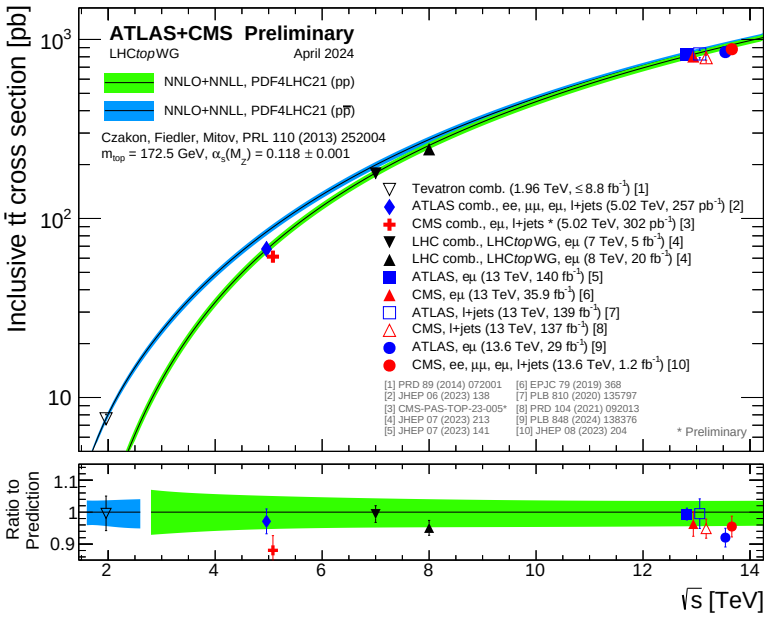

Figure 2.10: Summary of the $t\bar{t}$ production cross section measurements from LHC and Tevatron as a function of $\sqrt{s}$. These results are compared to NNLO QCD predictions complemented with NNLL resummation (top++2.0). The theory uncertainty band accounts for variations in μ_r, μ_f, PDFs and $\alpha_S(m_Z)$. Measurements performed at the same $\sqrt{s}$ are slightly offset for clarity. Figure taken from Ref. [165].

The top quark decays via the charged-current weak interaction, mainly in a b quark and a W boson. The branching ratio for its primary decay channel, $t \to Wb$, is determined by the elements of the CKM matrix [59]:

$$B(t \to Wb) = \frac{|V_{tb}|^2}{|V_{tb}|^2 + |V_{ts}|^2 + |V_{td}|^2}. \tag{2.14}$$

Here, V_{tq} is the CKM element that controls the $t \to Wq$ vertex. In particular $V_{tb} = 0.998$ [166].

The top quark decays are named following W decays, so that in practice, the $t\bar{t}$ events are classified as *fully hadronic*, *semileptonic*, and *dileptonic*. In the fully hadronic channel, both W bosons decay in a $q\bar{q}$ pair. In the semileptonic channel, one W boson decays hadronically, while the other decays into a lepton and a neutrino. Finally, both W bosons decay leptonically in the dileptonic channel. The corresponding branching ratios for each channel are shown in Figure 2.11. While the fully hadronic channel accounts for nearly half of the $t\bar{t}$ decays, the dileptonic channel provides the cleanest

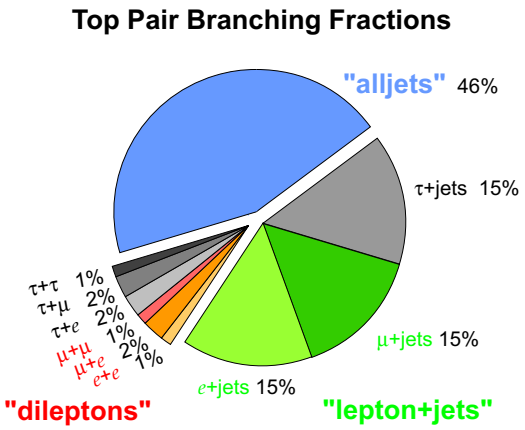

Figure 2.11: The branching ratios of the various decay channels of $t\bar{t}$ production. The label *lepton+jets* refers to the semileptonic channels, while *alljets* denotes the fully hadronic channel. Figure taken from Ref. [167].

signature. The semileptonic channel has intermediate properties, with sizeable statistics and moderate background contamination.

Measurement of top quark mass

To perform a measurement of m_t, the distributions of the events observed in data are compared with MC simulations or theoretical predictions across a range of assumed m_t values. A fitting procedure is then applied to extract the best-fit m_t. Detector-level distributions can be employed via a 'template fit'. Otherwise, distributions corrected for experimental effects through unfolding can be compared to theoretical predictions. The measurements of m_t performed so far in CMS are based mainly on $t\bar{t}$ pair production. However, this process interferes with single top production tW, an effect that has not yet been accounted for. In current measurements, tW is typically treated as a background.

The top quark mass can be determined in different ways at the LHC. One approach implies reconstruction of the invariant mass of its decay products. This method is often referred to as a *direct measurement* and recent results [168] report its precision of less than 0.4 GeV. However, these measurements are strongly dependent on distributions obtained from MC simulations and thus on the model assumptions of the

state-of-the-art MC generators [115, 169, 170], such as details of the PS and hadronisation simulation. Therefore, the result of direct measurements corresponds to the m_{t} parameter in the MC simulation, $m_{\mathrm{t}}^{\mathrm{MC}}$, used for its extraction. The relation of $m_{\mathrm{t}}^{\mathrm{MC}}$ and $m_{\mathrm{t}}^{\mathrm{pole}}$ is investigated in Ref. [170], for the most clear topology of e^+e^- collisions, and currently has an uncertainty of about 0.5 GeV. Analogous studies show that the value of $m_{\mathrm{t}}^{\mathrm{MC}}$ is close to the MSR mass with a similar uncertainty for the scale R set close to the MC shower cutoff scale [47].

Several observables relevant for the m_{t} determination at LO and NLO QCD were investigated in Ref. [12], and their sensitivity to input parameters was explored. One of the most promising observables to measure $m_{\mathrm{t}}^{\mathrm{MC}}$ is the invariant mass of the lepton and the b-jet, $m_{\ell\mathrm{b}}$, in dilepton $\mathrm{t\bar{t}}$ events. This choice is motivated by the fact that using $m_{\ell\mathrm{b}}$ eliminates the need for full top quark reconstruction, which typically requires the reconstruction of multiple jets (e.g. in semileptonic and hadronic decays) or neutrinos. Experimentally, leptons are measured with excellent resolution and efficiency and b-jets are reliably identified through b-tagging techniques. Theoretically, fully-off shell corrections at NLO in QCD are available for the $m_{\ell\mathrm{b}}$ observable [13, 14] as detailed in Chapter 5. Considering the top quark decay $\mathrm{t} \to \mathrm{bW}$ with the W boson decaying leptonically at LO and neglecting the masses of leptons and b quarks, $m_{\ell\mathrm{b}}$ can be defined as [39]:

$$m_{\ell\mathrm{b}}^2 = \frac{m_{\mathrm{t}}^2 - m_{\mathrm{W}}^2}{2}(1 - cos\theta_{lb}), \tag{2.15}$$

where θ_{lb} is the angle between the lepton and the b quark in the W boson rest frame. The relation between $m_{\ell\mathrm{b}}$ and m_{t} is well established for a fixed value of W boson mass m_{W} and its upper bound asymptotically reaches $\sqrt{m_{\mathrm{t}}^2 - m_{\mathrm{W}}^2}$.

As an alternative to the direct measurements, the value of the top quark mass can be determined in a well-defined renormalisation scheme, such as pole mass or $\overline{\mathrm{MS}}$. In this method, the measured observables sensitive to m_{t} are compared to fixed-order theoretical predictions. Typical observables include the inclusive $\mathrm{t\bar{t}}$ cross-section or differential cross sections as a function of a m_{t}-sensitive variable, e.g. the invariant mass of the $\mathrm{t\bar{t}}$ pair or that of the $\mathrm{t\bar{t}}$+1 jet system [171]. Finally, a complementary experimental approach is to measure m_{t} from boosted high-energy top quarks. The top decay products are detected in a single jet clustered in a small area of the detector, which significantly reduces the issue of combinatorial background. Because of the

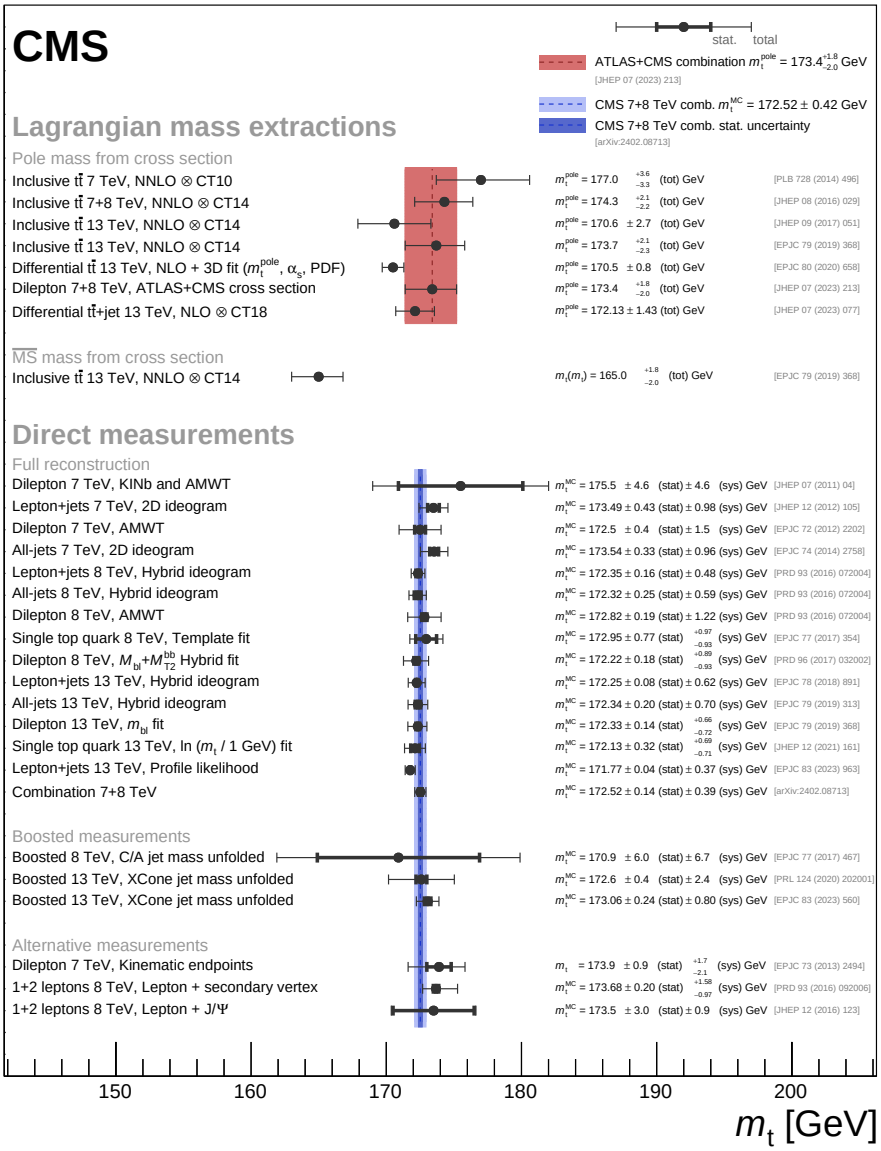

Figure 2.12: Overview of the top quark mass CMS measurements, including results from a combination with ATLAS. The markers show the measured value, while the statistical and total uncertainties are displayed as horizontal error bars. Figure taken from Ref. [39].

higher energy required to produce these boosted top quarks, their rates are relatively low. However, with increasing energy and integrated luminosity, the three CMS results obtained using boosted top quarks have improved the measurement precision by almost a factor of ten (as illustrated in Figure 2.12), with promising prospects for the

future High-Luminosity LHC [39]. An overview of all the top quark mass measurements performed by CMS, together with the combination results with ATLAS, are summarised in Figure 2.12.

Measurement of top quark width

Within the SM, the relationship between m_{t} and Γ_{t} is known to N3LO in QCD with an uncertainty of a few percent [2–5]. Improving the precision of Γ_{t} can, therefore, lead to a stringent test of the SM. Furthermore, a precise determination of Γ_{t} provides a constraint on the branching ratios of invisible or semi-visible decay modes of the top quark. For instance, flavour-changing neutral current decays involving weakly interacting particles are particularly challenging to detect at the LHC [172, 173]. A specific example is the decay $\mathrm{t} \to \mathrm{u} + X$, where X is an invisible particle.

Indirect techniques assume the SM and rely on measurements of the branching fraction $B(\mathrm{t} \to \mathrm{Wb})$ to determine Γ_{t}. The most precise determination of Γ_{t} is obtained by the CMS collaboration [7] via an indirect technique. Otherwise, direct measurements of kinematic distributions sensitive to Γ_{t} can be performed. Although less precise with a total uncertainty of a few hundred MeV, this class of measurements does not require an a priori assumption of the SM. As a result, non-SM couplings or decays of the top quark can be probed, manifesting themselves as deviations from the expected SM Γ_{t} value. Direct measurements, based on template fits to invariant mass spectra that peak near m_{t}, were made by the CDF [174] and ATLAS [175, 176] Collaborations. Owing to their cleaner event signatures, the most sensitive observable in dilepton and semileptonic decays from $t\bar{t}$ production is $m_{\ell b}$, as defined in Eq. (5.1). While the peak position of $m_{\ell \mathrm{b}}$ is linearly sensitive to m_{t}, the measured width around the peak depends only weakly on Γ_{t}, as it is mostly affected by undetected neutrinos and b quark fragmentation. A novel approach [177] exploits events in the tails of the $m_{\ell \mathrm{b}}$ distribution, which is linearly sensitive to Γ_{t}. This technique is also followed in Ref. [178] and provides the most precise direct measurements of the top quark width.

For the first time in CMS, this thesis presents the extraction of $m_{\mathrm{t}}^{\mathrm{MC}}$ and Γ_{t}, incorporating the interference between tW and $\mathrm{t\bar{t}}$ production while leveraging the $m_{\ell \mathrm{b}}$ observable. The details of this measurement are presented in Chapter 5.

Chapter 3

CMS at the LHC

This Chapter provides an introduction to the Large Hadron Collider (LHC) accelerator and the Compact Muon Solenoid (CMS) detector. The LHC and CMS are discussed in Sections 3.1 and 3.2. The event reconstruction process in CMS is detailed in Section 3.3. The High Luminosity LHC (HL–LHC) upgrade is outlined in Section 3.4. Finally, Section 3.5 addresses the sustainability challenges associated with the computational demands of the simulations.

3.1 The Large Hadron Collider

The LHC [1] is a circular synchrotron collider, operating with protons or heavy ions, located at the CERN laboratories in Geneva at the forefront of addressing fundamental questions in high-energy physics. In this thesis, data produced from pp collision have been used. The LHC features a 27-km ring of superconducting magnets and accelerate protons up to 7 TeV and focus proton beams circulating in opposite directions. The designed centre-of-mass energy of the LHC is $\sqrt{s} = 14$ TeV. Situated 100 m underground, it has been built in the tunnel that previously hosted the LEP accelerator. A powerful system of staged accelerators, including previous machines (LINAC, PS, SPS), accelerates and boosts the two proton beams up to 450 GeV before they are injected into the main ring, where they reach their final energy. A complex system of magnets focuses the beam and holds the beam's orbit on a circle. In Figure 3.1, a schematic view of the CERN accelerator complex is illustrated. Proton or heavy-ion bunches collide at four interaction points, each hosting one of the main experiments:

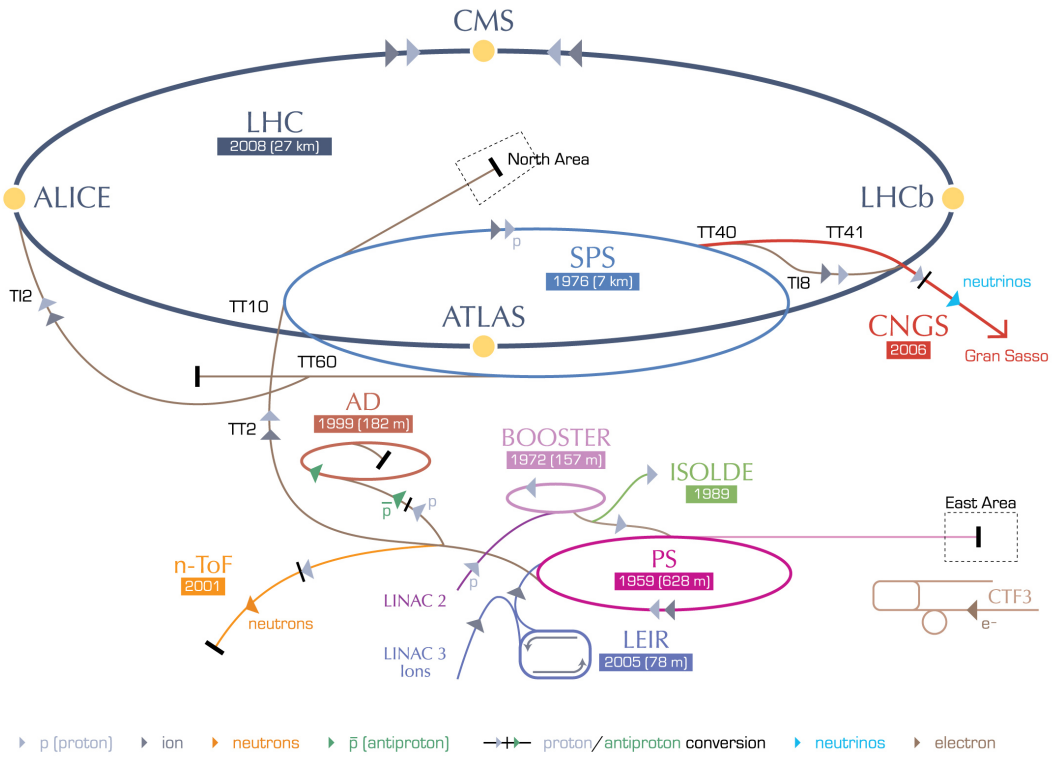

Figure 3.1: The CERN accelerator complex located in Geneva. The different accelerators and detectors are shown. Figure taken from Ref. [183].

two general-purpose detectors ATLAS [179] and CMS [180], ALICE [181] for heavy-ion collisions and LHCb [182] specialised in b physics.

The *instantaneous luminosity* changes over time and can be expressed in terms of the accelerator parameters as [184]:

$$\mathcal{L} = \frac{n_b N_b^2 f F}{4\pi\sigma_x\sigma_y}, \tag{3.1}$$

where f is the revolution frequency, n_b the number of bunches in each beam, N_b the number of protons per bunch, and σ_x and σ_y the widths of Gaussian distributed beam profiles in the $x-$ and $y-$ directions. Finally, F is a geometrical factor accounting for several effects [184], including the crossing angle of the beam, the collision offset, the Hourglass effect, and the non-Gaussian beam profiles. The LHC was designed to reach an instantaneous luminosity of 10^{34} cm^{-2}s^{-1}. The integral over time of the

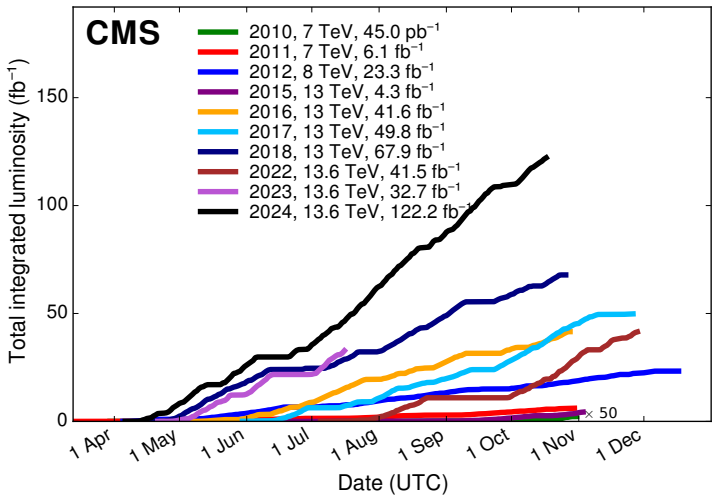

Figure 3.2: Integrated luminosity delivered to the CMS experiment per year of data taking. Figure taken from Ref. [185].

instantaneous luminosity is called *integrated luminosity*:

$$\mathcal{L}_{\text{int}} \equiv \int dt\mathcal{L} = \frac{N}{\sigma}, \tag{3.2}$$

where N is the total number of events recorded of a given process with a cross section σ. In Figure 3.2, the integrated luminosity delivered to the CMS experiment over various years of data taking is illustrated.

At the LHC, a "Run" denotes a specific data-taking period defined by distinct beam energies and intensities. Run1, conducted between 2010 and 2012, marked the LHC's first operational phase, colliding protons at $\sqrt{s} = 7$ TeV (2010–2011) and $\sqrt{s} = 8$ TeV (2012). After a two-year shutdown, the LHC resumed pp collisions in 2015 with Run2, operating at a record centre-of-mass energy of $\sqrt{s} = 13$ TeV and spanning the period from 2015 to 2018. Low-luminosity runs were also carried out at $\sqrt{s} = 2.76$ in Run1 (2010) and 5.02 TeV in Run2 (2015), respectively. The accelerator underwent a second three-year shutdown in 2019, during which the injector complex was upgraded to produce brighter and lower-emittance beams. The current running period (Run3) at 13.6 TeV began in 2022 and will continue until 2026. A third long shutdown, lasting approximately four years, will be necessary to upgrade the accelerator. The LHC is

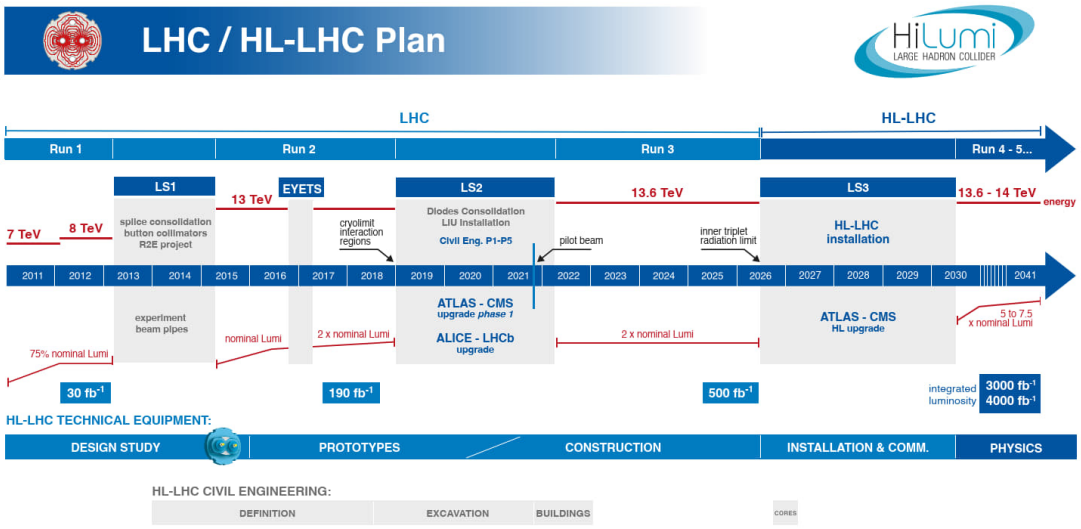

Figure 3.3: The LHC schedule and the plan for the HL–LHC. Figure taken from Ref. [186].

expected to resume operations for the High-Luminosity (HL) phase of the LHC in 2030. The schedule of the LHC is shown in Figure 3.3.

A high instantaneous luminosity results in a high number of simultaneous collisions within the same bunch crossing, referred to as *pileup* (PU). These additional collisions create significant challenges for the event reconstruction, as contributions from different interactions overlap. At the end of Run1, the average PU was ~ 20, while in Run2, it reached ~ 40. Currently, during Run3, it has increased to ~ 60 simultaneous collisions. In Figure 3.4, the PU distributions over various years of data taking are illustrated.

The data analysed in this thesis were collected by the CMS detector during Run1 and Run2. Specifically, part of the Run2 data (2017–2018) is used in Chapter 5 for the measurement of the top quark mass and width with the data collected at $\sqrt{s} = 13$ TeV. In Chapter 6, inclusive jet measurements from Run1 at $\sqrt{s} = 2.76$, 7 and 8 TeV together with 2016 data-taking period from Run2 at $\sqrt{s} = 13$ TeV are combined for the determination of the strong coupling.

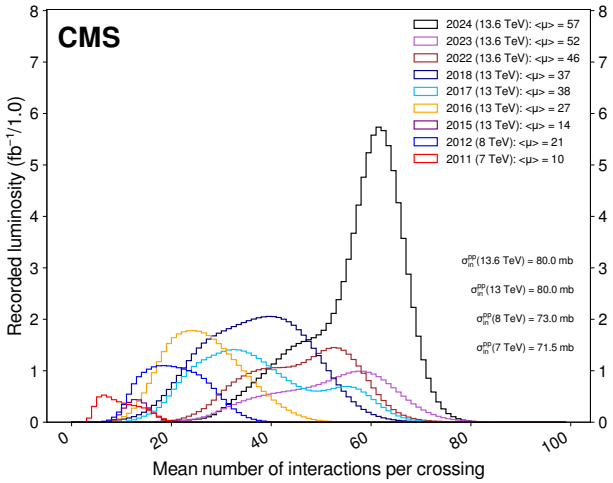

Figure 3.4: Pileup per year of data taking. Figure taken from Ref. [185].

3.2 The Compact Muon Solenoid experiment

The CMS [180] experiment is a general-purpose detector with a broad physics program, conducting precision tests of the SM and searches for BSM physics [187]. Stable particles produced in collisions are detected by measuring their momenta and energies, thereby reconstructing the collision event. Before discussing the structure of the CMS detector, it is helpful to introduce the coordinate system [188] used by the experiment. The origin of the coordinate system is set to the nominal collision point inside the detector, with the beam direction aligned along the z-axis, the x-axis pointing towards the centre of the LHC ring, and the y-axis perpendicular to the (x, z) plane, pointing outwards from the surface. Owing to the cylindrical symmetry of the collisions around the beam axis, a cylindrical coordinate system is preferred (r, ϕ, θ). Here, r is the distance from the interaction point $r = \sqrt{x^2 + y^2}$, ϕ the azimuthal angle in the (x, y) plane, while θ the polar angle measured with respect to the z-axis. The kinematics of the particles are defined by the transverse momentum $p_{\mathrm{T}} = \sqrt{p_x^2 + p_y^2}$ and rapidity y, as defined in Eq. (2.12). The p_{T} and differences in rapidity Δy are Lorentz-invariant under boosts along the beam axis. The pseudorapidity η is another important quantity that quantifies how centrally a particle is produced:

$$\eta = -\log\left(\tan\left(\frac{\theta}{2}\right)\right). \tag{3.3}$$

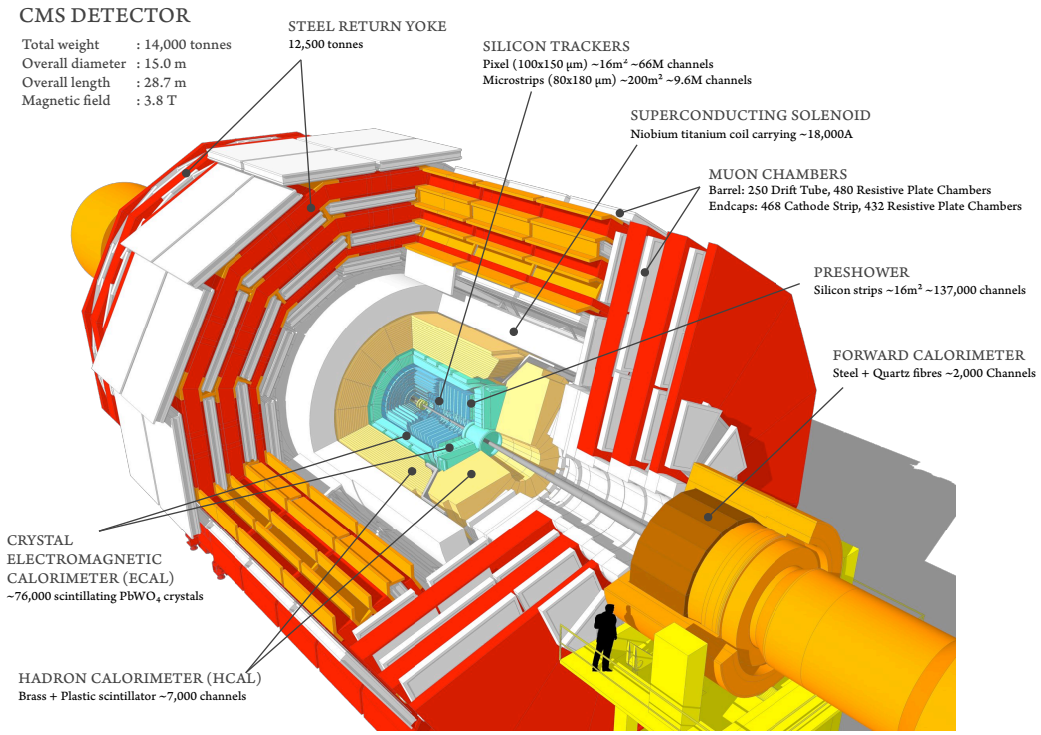

Figure 3.5: Illustration of the CMS detector. Figure taken from Ref. [189].

When the particle is aligned with the transverse plane ($\theta = 90°$), $\eta = 0$, and η increases towards infinity as the particle's trajectory moves closer to the beamline direction ($\theta = 0°$). In the relativistic limit, where the momentum of the particle is much larger than its mass, η and y become approximately the same. While the y is used in theory and measurements, η is often preferred in detector studies where detector coverage is typically expressed as a function of η.

The CMS experiment consists of several subdetector layers, as illustrated in Figure 3.5. The major feature of the detector is a superconducting solenoid, measuring 12.5 meters in length and 6.3 meters in diameter. It generates a uniform magnetic field of 3.8 T. The solenoid volume encompasses a silicon pixel and strip tracker, a lead-tungstate crystal electromagnetic calorimeter (ECAL), and a brass and scintillator hadronic calorimeter (HCAL). Finally, the muon chambers are embedded in the steel flux-return yoke outside the solenoid. The design of the detector includes a central cylindrical structure called *barrel* and two *endcap* disks arranged perpendicular to the beam axis.

3.2.1 The tracking system

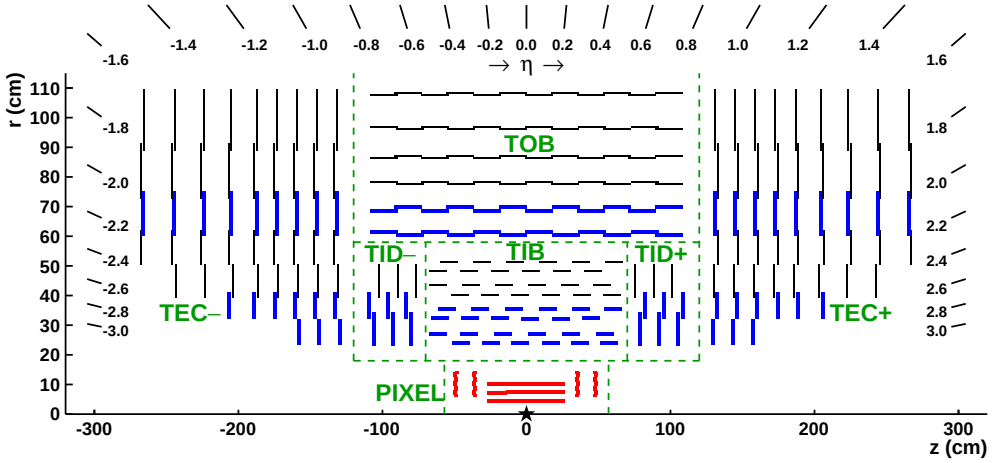

Figure 3.6: A schematic view of a quarter of the tracker before the upgrade in 2016. It comprises the inner pixel (red) and the strip detectors (blue). Figure taken from Ref. [190].

The tracking volume is housed within a cylinder of 5.8 m in length and 2.6 m in diameter. The CMS tracking system employs advanced silicon technologies to precisely measure the tracks of charged particles and reliably associate each track with its corresponding interaction vertex. Additionally, it can reconstruct secondary vertices, which are essential for identifying heavy-flavour jets, as explained in Section 3.3.3.

The CMS tracker consists of an inner pixel detector and an outer strip detector, as illustrated in Figure 3.6. The silicon pixel tracker comprises three barrel layers and two disks in the endcaps. During the LHC shutdown between the 2016 and 2017 data-taking periods, an upgraded version of the pixel detector was installed. The new detector features an additional pixel layer in the barrel region and an extra endcap disk on each side [191]. These are mounted closer to the beam pipe, enhancing the precision of the interaction vertex reconstruction. The silicon strip detector is divided into the tracker inner barrel (TIB), the tracker outer barrel (TOB), the tracker inner disks (TID) and the tracker endcap (TEC). The CMS tracker covers a $|\eta| < 2.5$ range and comprises 66 million pixels and 10 million strip sensors. Position measurements with a resolution between 10 and 20 μm [191] can be achieved in the pixel detector. In the strip tracker, performance varies: the innermost layer has resolutions ranging

from 23 to 34 μm in the $r - \phi$ direction and 23 μm in the z direction, while the outermost layer has resolutions between 35 and 53 μm in $r - \phi$ and 52 μm in the z direction [192].

3.2.2 The electromagnetic calorimeter

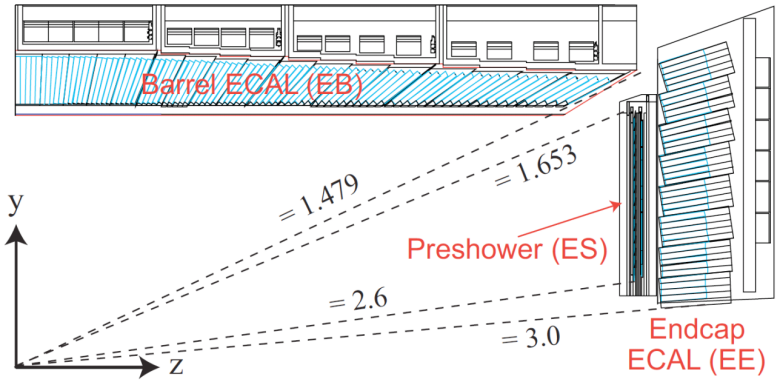

Figure 3.7: A schematic view of one quarter of the ECAL. Figure taken from Ref. [193].

The ECAL is a hermetic and homogeneous calorimeter composed of approximately 75000 lead tungstate ($PbWO_4$) crystals, and it is designed to measure the energy of photons and electrons with excellent precision. The properties of $PbWO_4$ crystals, such as high density (8.28 g/cm^3), short radiation length (0.89 cm), and small Molière radius (2.2 cm), enable fine granularity and a compact calorimeter design. Additionally, it is a fast material emitting about 80% of the light within 25 ns [194]. The ECAL spans up to $|\eta| = 3$ in pseudorapidity and is divided into three subsystems: the electromagnetic barrel (EB) calorimeter ($|\eta| < 1.479$), the electromagnetic endcap (EE) calorimeters ($1.479 < |\eta| < 3.0$), and the preshower detector ($1.653 < |\eta| < 2.60$). Scintillation light is detected by silicon avalanche photodiodes in the EB and vacuum photodiodes in the EE. The preshower detector is a fine-granularity sampling calorimeter that enhances the identification of photon pairs from $\pi^0 \to \gamma\gamma$ decays against prompt photons and improves the position resolution for photons and electrons. It is composed of alternating layers of lead absorbers to initiate electromagnetic showers and silicon strip detectors to capture the resulting signals [188]. A schematic representation of the ECAL structure is provided in Figure 3.7.

3.2.3 The hadron calorimeter

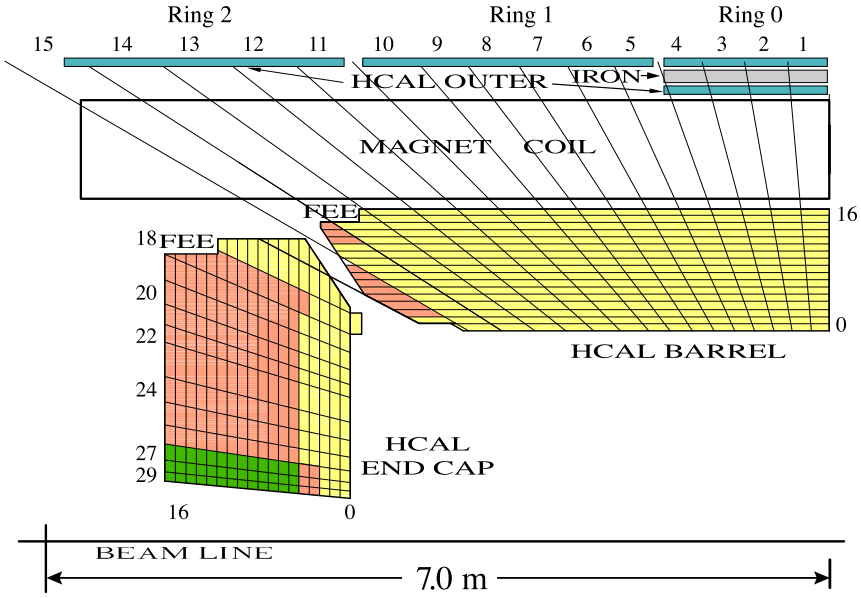

Figure 3.8: A schematic view of one quarter of the HCAL. Figure taken from Ref. [195].

The HCAL is a sampling calorimeter that measures the energy of charged and neutral hadrons. It is divided into several sections: the central barrel (HB: $|\eta| < 1.4$), the endcaps (HE: $1.3 < |\eta| < 3$); the outer calorimeter (HO: $|\eta| < 1.26$); the forward calorimeter (HF: $3 < |\eta| < 5.2$). The layers are staggered to eliminate gaps through which particles could escape, ensuring hermetic coverage. The barrel and endcap components comprise alternating layers of brass absorbers and plastic scintillators. The HO is located outside the magnetic volume and uses the solenoid coil and the steel of the return yoke as absorber materials. To withstand the harsher radiation conditions in the forward regions, the HF employs steel as an absorber and Cherenkov radiating quartz fibres as the sensitive material. The average energy deposit is 760 GeV in this component, while is expected to be 100 GeV in the rest of the detector.

3.2.4 The muon detector system

The reconstruction of muons begins with measuring their momenta and positions in the tracking system. As minimum-ionising particles, muons pass through the calorimeters with minimal energy deposition before reaching the muon detector system. The

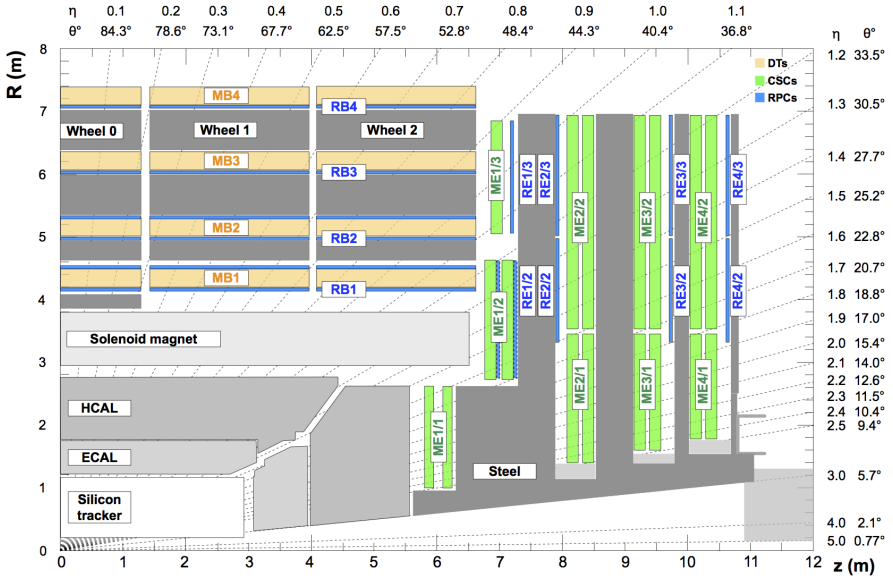

Figure 3.9: A schematic view of one quarter of the CMS muon system. The DT stations are labelled as MB (muon barrel), and the CSCs as ME (muon endcap). The RPCs are mounted in the barrel and the endcaps, labelled RB and RE, respectively. Figure taken from Ref. [196].

latter consists of multiple chambers embedded within the iron yoke and is optimised for efficient muon identification and precise trajectory measurement. The muon system incorporates three types of gaseous detectors: drift tube chambers (DTs) in the barrel region ($0.9 < |\eta| < 1.2$), cathode strip chambers (CSCs) in the endcap sections ($|\eta| < 2.4$), and resistive plate chambers (RPCs) present in both regions ($|\eta| < 1.6$). DTs and CSCs work with the tracker to reconstruct muon tracks, while RPCs enhance the trigger performance due to their exceptional time resolution of about 1 ns. When combining the muon detector system and tracker information, the transverse momentum resolution is approximately 1–3% for muons with $p_{\mathrm{T}} < 100$ GeV and around 10% for muons with p_{T} in the TeV range [196].

3.2.5 The trigger system

At design luminosity, the LHC bunch crossing rate is 40 MHz [188]. As a result, approximately 10^9 interactions per second are produced. However, the rate at which collision data can be stored on disk for offline analysis is limited. A two-tiered trigger system, the *Level 1 Trigger* (L1) and the *High-Level Trigger* (HLT), enables the re-

duction of collision frequencies from 40 MHz to an event recording rate of about 1 kHz.

The L1 trigger is a hardware-based system designed to lower the event rate to about 100 kHz [197]. Given the 25 ns bunch spacing, particles from one event may not fully exit the detector when new particles are produced in the next collision. The data are temporarily stored in a "pipeline" to manage this overlap. In this way, the system can process information from multiple interactions. The L1 trigger must be extremely fast, operating with a fixed latency of 3.2 μs [198], and rely on detectors with excellent time resolution. At this stage, only information from the muon detectors and calorimeters are used. The selection relies on candidate objects with properties above predefined thresholds that indicate the presence of physics objects (e.g., electrons, muons, photons, jets) with p_{T} above a given threshold. Global event characteristics such as transverse missing energy $\vec{\not{E}}_T$ are also taken into account [198].

Subsequently, the software-based HLT refines the event selection and reduces the output rate to a few kHz using a complex offline-quality reconstruction algorithm. At this stage, data from all subdetectors are synchronised to fully reconstruct events through a predefined sequence of steps called the HLT-path. Finally, events passing the HLT selection are saved for offline analysis. The output rates of L1 and HLT can be regulated by applying prescales, which reduce the number of accepted events by selecting only a fixed fraction of those passing specific criteria.

3.3 The event reconstruction in CMS

As different types of particles interact differently with the subdetector material, they leave distinct characteristic signatures of their type, as depicted in Figure 3.10. These signatures enable particle identification and measurement of their direction and energy. Interaction vertices are identified around the pp interaction points. The vertices and trajectories of charged particles are reconstructed from hits in the tracking system, and the momenta are measured from the curvature of the particles in the magnetic field. Electrons and charged hadrons are absorbed in the ECAL and HCAL, respectively, where the energy of the particles is determined from calorimeter deposits. Photons and neutral hadrons do not leave signals in the tracker system but are identified based on the energy deposits in the calorimeters. Muons, being minimum-ionising particles, penetrate the calorimeters and are detected in the muon chambers. Here,

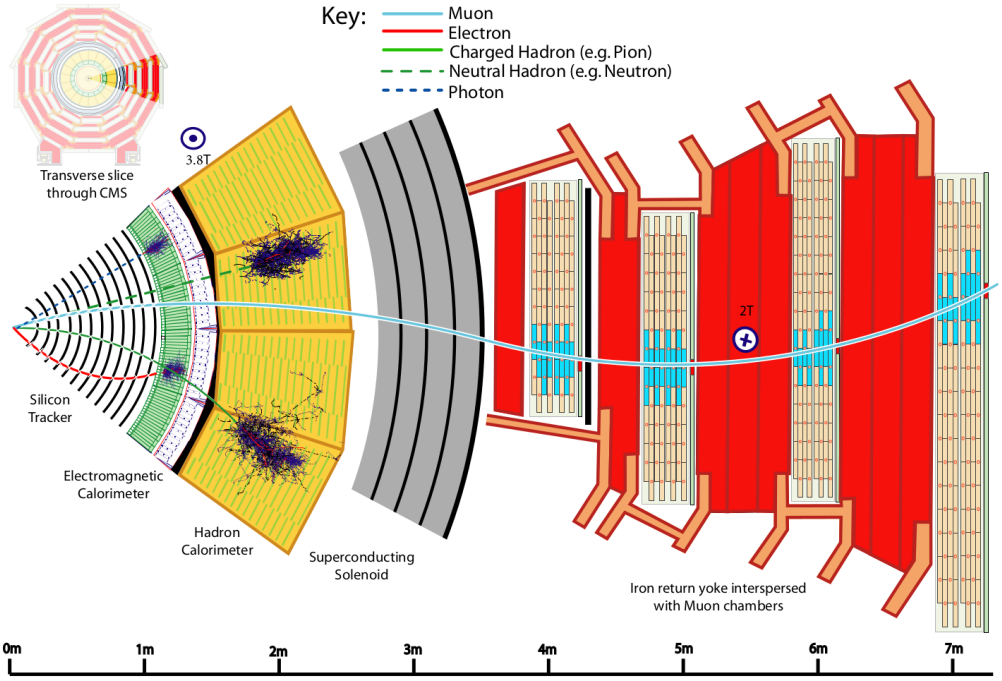

Figure 3.10: The signatures of various particles travelling through the CMS detector, from the beam interaction point to the muon detector system. Figure taken from Ref. [199].

additional tracking layers outside the solenoid enhance their momentum measurement. Neutrinos, which do not interact with the detector material, remain undetected but can be inferred through $\vec{\not{E}}_T$.

3.3.1 The particle flow algorithm

The particle-flow (PF) algorithm [200] aims to reconstruct and identify each particle in the event by combining information from various elements of the CMS detector. The algorithm involves two steps: first, the reconstruction of the PF elements (i.e., charged tracks, muon tracks, and calorimeter clusters), followed by the matching of the reconstructed elements. As a result, particle candidates are classified as photons, electrons, muons, charged hadrons, or neutral hadrons, as illustrated in Figure 3.11.

The process starts with an iterative tracking algorithm designed to optimise the track-finding efficiency while keeping a low fake rate, meaning the proportion of spurious tracks incorrectly reconstructed from random or misassigned detector hits. Then, the

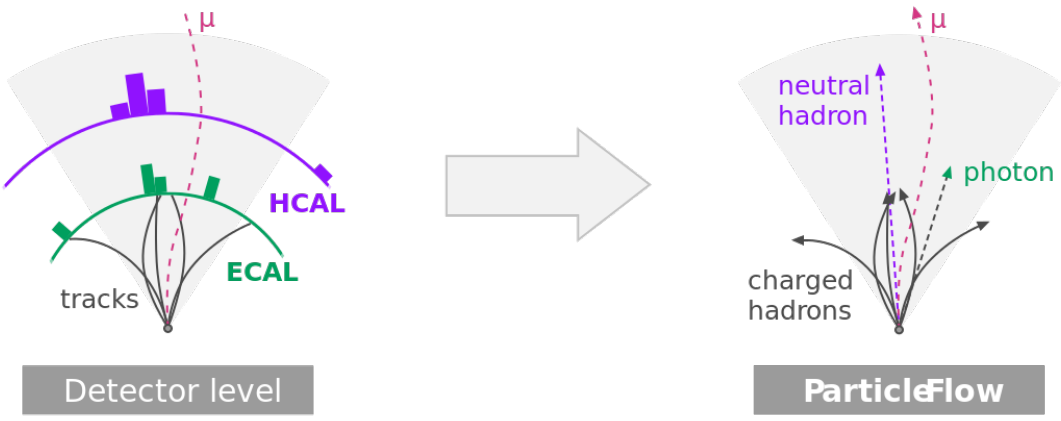

Figure 3.11: Illustration of the PF concept. Photons, electrons, muons, charged hadrons, and neutral hadrons are identified. Figure taken from Ref. [201].

tracks are associated with the interaction vertices. The vertex corresponding to the hardest scattering in the event, evaluated using tracking information alone [202], is defined as the primary vertex (PV). The remaining vertices are considered pileup (PU) vertices. Muon tracks are fitted using information from both the tracking system and the muon chambers. The PF clusters are created by using cluster seeds, the calorimeter cells with energy exceeding a given threshold and larger than the energy of adjacent cells [200]. Non-muon PF tracks and PF clusters are combined into PF blocks, which are subsequently processed to generate PF candidates. The reconstruction of the missing transverse momentum $\vec{p}_{\mathrm{T}}^{\,\mathrm{miss}}$ is also possible, computed as the negative vector sum of the p_{T} of all PF candidates in an event [203]. Particles contributing to $\vec{p}_{\mathrm{T}}^{\,\mathrm{miss}}$ are assumed to be neutrinos or weakly interacting particles escaped from the detector.

The PF algorithm enhances the performance in the identification of leptons, in the determination of $\vec{p}_{\mathrm{T}}^{\,\mathrm{miss}}$, and in the identification of PU tracks [200]. The momentum resolution for electrons with $p_{\mathrm{T}} \approx 45\,\mathrm{GeV}$ from $\mathrm{Z} \to \mathrm{ee}$ decays ranges from 1.6 to 5%. The resolution is generally better in the barrel region than in the endcaps and also depends on the bremsstrahlung energy emitted by the electron as it traverses the material in front of the ECAL [204, 205]. Since the muon momentum can be measured from a charged track with relatively low bremstrahlung, muons are the best measured objects in CMS, with a momentum resolution of 1-3% for muons with p_{T} up to 100 GeV, and better than 7% in the barrel region for muons with p_{T} up to

1 TeV [196]. The resolution of $\vec{p}_{\mathrm{T}}^{\,\mathrm{miss}}$ is typically about 15-30 GeV, increasing with the total sum of hadronic energy in the event [203].

3.3.2 Jet reconstruction and calibration

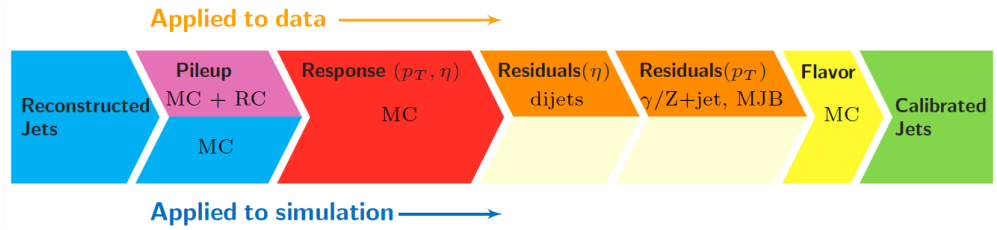

Figure 3.12: Representation of the jet energy calibration procedure in data and MC. Figure taken from Ref. [206].

For each event, hadronic jets are clustered from the PF candidates using the anti-k_{T} algorithm [144, 207] in the FastJet package [207] with a radius distance $R = 0.4$. The typical signature of a jet event in a pp collision consists of energy deposits in both ECAL and HCAL, which point to the corresponding interaction vertex. The PF algorithm associates tracks with calorimeter clusters. Charged hadrons are identified when tracks are successfully matched with clusters in the calorimeters. Once associated, the tracks are excluded from the algorithm input list. When the PF matching is complete, the remaining ECAL clusters are classified as photons, while those in the HCAL are identified as neutral hadrons. Muons and electrons can also be identified within the jet. Finally, the PF candidates are passed as input to the jet clustering algorithm. The momentum and spatial resolution of PF jets are significantly enhanced compared to calorimeter jets, integrating information from the tracking detector and the high granularity of the ECAL, which independently measures charged hadrons and photons within a jet.

The momentum of a jet is calculated as the vectorial sum of the momenta of all PF candidates in the jet and is found from simulation to be, on average, within 5 to 10% of the true momentum over the whole p_{T} spectrum and detector acceptance. The PU can increase the jet momentum by contributing additional tracks and calorimetric energy depositions. Tracks coming from PU vertices are removed prior to the jet clustering to mitigate this effect. One procedure is the *charged hadron subtraction* (CHS) [208], which removes charged-particle candidates associated with a

reconstructed PU vertex. An improved method is the *pileup per particle identification* algorithm (PUPPI) [209, 210], making use of local shape information, event PU properties, and tracking information. In addition, the momenta of the neutral particles are rescaled according to their probability of originating from the primary interaction vertex deduced from the local shape variable. Reconstructed jets with the respective PU mitigation technique are referred to as CHS and PUPPI jets, respectively.

The measured jet energy is corrected to the true energy value, defined at particle level in MC simulations, using jet energy scale (JES) corrections. These corrections are obtained from MC simulations and are applied as a global multiplicative factor to the jet four-momenta, as shown in Figure 3.12. The JES corrections encompass the *offset correction*, which removes the remaining effects from PU and electronic noise. For CHS jets, an event-by-event jet-area-based correction [206, 211, 212] is applied to the jet four-momenta. As a result, the remaining energy due to neutral and charged particles originating from PU vertices is removed. This correction is not required for PUPPI jets. Real and simulated jets are then corrected using an identical *MC calibration* to address the main non-uniformities in η and the non-linearities in p_{T}, as calorimeters typically exhibit a non-linear response. Finally, in situ measurements of the momentum balance in dijet, photon + jet, Z + jet, and multijet events are used to account for any residual differences in the jet energy scale between data and simulation [213] and are only applied to the data (*residual corrections*). The jet energy resolution (JER) is typically 15–20% at 30 GeV, 10% at 100 GeV, and 5% at 1 TeV [206].

3.3.3 Identification of jets originating from b quarks

The identification (tagging) of jets originating from b quarks, referred to as b-jets, play a key role in the measurement of the top quark mass and width, as discussed in Chapter 5. The b-jets have a characteristic signature due to the presence of b hadrons, which have a relatively long lifetime ($\sim$1.5 ps) and a mass of about 5 GeV. As a result, b hadrons typically travel a few millimetres away from the PV before decaying, producing a secondary vertex (SV) with displaced tracks. This feature is leveraged by b tagging algorithms to enhance the separation of b-jets from light-flavour jets (originating from u, d, or s quarks, or gluons) and c jets. An illustration of this phenomenon is provided in Figure 3.13.

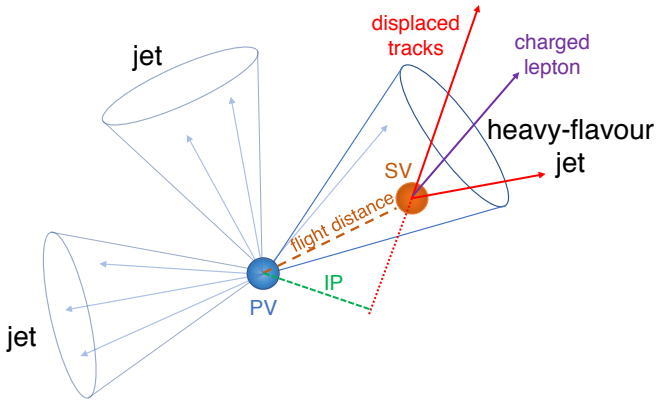

Figure 3.13: Schematic representation of a heavy-flavour jet with an SV from the decay of a b or c hadron that results in displaced tracks (including possibly a soft lepton) with respect to the PV and a large impact parameter (IP) value. Figure taken from Ref. [214].

The displacement of tracks is typically measured by the impact parameter (IP), which is defined as the shortest distance from each track to the PV, as shown in Figure 3.13. By convention, the IP is given a positive sign when the angle between the IP and the jet direction is smaller than $\pi/2$. Otherwise, a negative sign is assigned. Tracks originating from SVs are typically associated with positive IP values, while those originating from the PV exhibit IP values symmetrically distributed around zero. Furthermore, the variable IP significance (IP/σ) is considered, which is the ratio of the IP to its uncertainty. The reconstruction of SVs provides additional valuable information for identifying b-jets. In the CMS experiment, the *inclusive vertex finder* (IVF) algorithm [215] is employed. The efficiency of reconstructing an SV is found to be 75% for b-jets in $\mathrm{t\bar{t}}$ events, for jets with $p_\mathrm{T} > 20$ GeV [214]. Another important variable that helps to discriminate between b and light-flavour jets is the flight distance, which represents the separation between the PV and the SV.

In Chapter 5, the DeepJet b tagging algorithm [216] is used, a machine learning-based classifier which combines the variables described above with other relevant inputs. It uses approximately 650 input features divided into four groups, which contain variables from:

- **Global event-level** (e.g. jet kinematics and PV multiplicity)
- **Charged PF candidates** (e.g. track kinematics, track fit quality or displace-

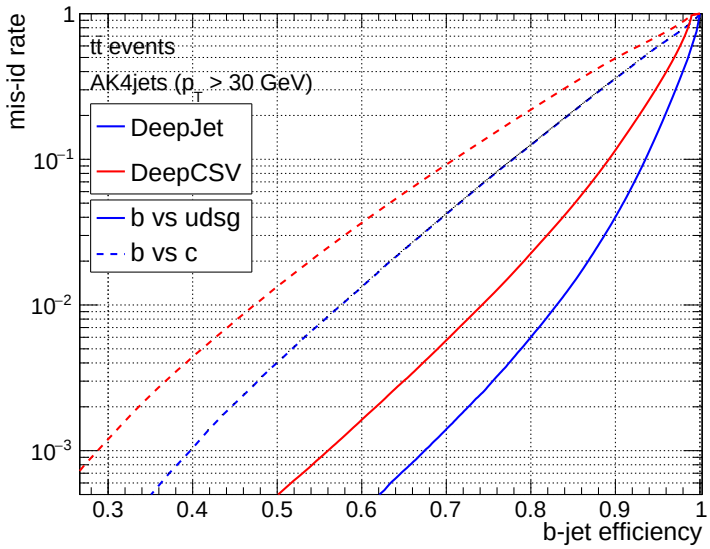

Figure 3.14: Misidentification probability for c and light jets versus b-jet identification efficiency for DeepJet and the previous DeepCSV tagger, obtained using $t\bar{t}$ simulated events. Figure taken from Ref. [216].

ment information with respect to the PV)

- **Neutral PF candidates** (similar to charged PF candidates)
- **Secondary vertices** (e.g. flight distance)

The neural network outputs the probabilities of a jet originating from a specific flavour, allowing for b, c, and light quark/gluon tagging. For b tagging, defined working points correspond to fixed light jet misidentification rates of 10%, 1%, and 0.1% with tagging efficiencies at approximately 92%, 82%, and 65%, respectively [217]. The tagger performs better when the b tagging efficiency is maximised while maintaining low misidentification rates. Therefore, the probability of identifying light-flavour jets as a function of the b-tagging efficiency serves as the performance metric for the tagger. The performance metric of DeepJet and its predecessor DeepCSV [214] are compared in Figure 3.14.

3.4 The High Luminosity LHC upgrade

The HL phase [218] will significantly enhance the LHC capabilities, extending its discovery potential and boosting the precision of its measurements. During this period,

the LHC is expected to reach peak instantaneous luminosities of up to 7.5×10^{34} $\mathrm{cm^{-2}\,s^{-1}}$ at $\sqrt{s} = 14$ TeV. Over the following decade, the ATLAS and CMS experiments will collect more than 3000 fb^{-1} of integrated luminosity, a tenfold increase compared to the currently available 300 fb^{-1}. This amount of data will enable unprecedented precision in testing the SM couplings, including the Higgs-boson couplings, including those to second-generation fermions, and probe rare processes like di-Higgs production and increase sensitivity to new physics by populating the high-momenta distributions of SM processes [219–221].

To achieve the HL–LHC goals, substantial upgrades to the accelerator complex are necessary, including adjustments to beam parameters. These upgrades will feature advanced Nb–Ti and Nb_3Sn superconducting magnets (11-12 T), superconducting radio-frequency cavities for beam steering, and high-power superconducting links with no energy loss. Additionally, novel beam-crossing schemes will enhance collision physics output, and innovative solutions for cryogenics, vacuum and machine protection will address heightened operational demands [222].

As the instantaneous luminosity increases, PU will also grow significantly, potentially reaching up to 200. In Figure 3.15, a special high-pileup run recorded in 2016 is illustrated, showing what a typical HL–LHC event will look like. To deal with the higher PU and radiation levels, the CMS detectors will undergo significant upgrades [192, 224, 225]. The tracker will extend coverage up to $|\eta| = 4$, providing particle momentum information already at the L1 trigger stage [226]. The current HCAL will be substituted with a high-granularity endcap calorimeter (HGCAL) to improve forward-region coverage [227]. Additionally, new muon detectors will expand detection capabilities to $|\eta| < 2.8$ [228]. Furthermore, CMS will include a timing detector for minimum ionising particles (MIP), the MIP Timing Detector (MTD) [220]. The addition of MTD will improve the event reconstruction performance, providing the experiment with a time-aware 4-dimensional vertex reconstruction. As a result, final state particles and observables will be defined using vertices and track collections cleaned of spurious PU tracks through space-time compatibility criteria. Finally, the DAQ and HLT systems will also be upgraded to accommodate all these changes. The L1 trigger rate will increase up to 750 kHz, approximately 7 times higher than in Run2, while the HLT output rate will rise up to 7.5 kHz.

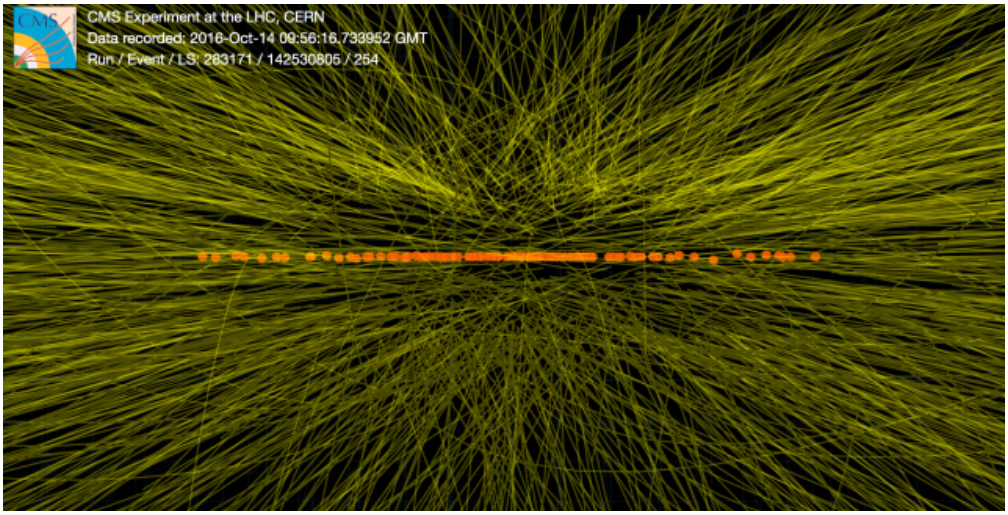

Figure 3.15: A collision recorded by the CMS detector during the 2016 data taking, during a high-pileup run (average PU ∼100). The dots correspond to the reconstructed interaction vertices and the lines represent the reconstructed tracks. Figure taken from Ref. [223].

Another challenge of the HL–LHC will be catching up with the rapid increase in the quantity of data by providing the necessary amount of MC simulated events while addressing the issues of sustainability and computational cost. This topic is addressed in Chapter 4, presenting the solution of this problem, implemented in the frame of this thesis.

3.5 The CPU demand and sustainability

To achieve the physics programme goals of the CERN experiments, large MC-simulated samples with billions of events are required to ensure that the statistical precision of samples has minimal impact on the total uncertainty of data analyses. These simulations come at a high computational cost, with over 75% of the total CPU resources allocated to modelling the detector response and the event reconstruction [15, 16]. At the HL–LHC, the computational demands for producing and storing simulated samples are expected to increase by factors of ten or more [230]. In this scenario, the computing needs exceed those that can be met by scaling up computing facilities if no R&D improvements will be applied, as shown in Figure 3.16. Current projections

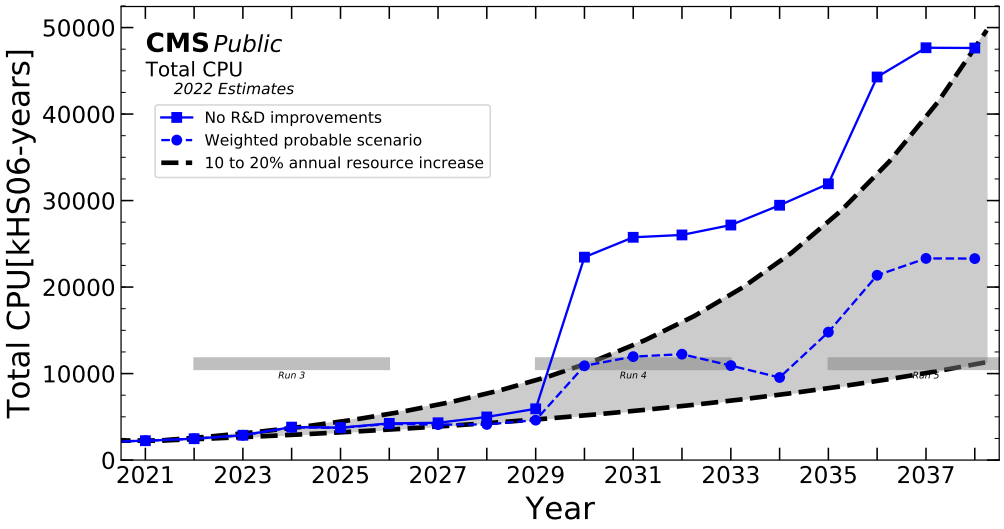

Figure 3.16: Projections of CPU needs into HL–LHC. The projected capacity of the resources within a flat budget (grey band), the *baseline* (solid line) and *weighted probable* (dashed line) scenarios are shown. The effect of GPUs is not included. The legends describe the baseline scenario as "No R&D improvement" and the weighted probable scenario as "R&D most probable outcome". Figure taken from Ref. [229].

indicate that 160 billion fully simulated and reconstructed MC events have to be produced per year after the start of the HL era. This number may further increase by up to 30% due to the presence of events with negative weights in NLO and NNLO simulations, which lower the statistical precision of the simulated samples. Current research and development efforts aim to address these challenges with the strategic goal of minimising CPU and storage requirements. An important part of these efforts is reducing the size and number of simulated samples required for data analyses while maintaining the precision and accuracy of the results. In every physics analysis, additional samples of simulated events are typically generated to evaluate systematic uncertainties connected to model assumptions of the MC event generators. Owing to limited computational resources, these samples are often generated with fewer events than the nominal sample. However, the smaller size of these samples can become a limiting factor in precision analyses, which is currently the case in analyses of Run2 and Run3 data. For instance, in a recent measurement of $t\bar{t}$ pair production cross section

at $\sqrt{s} = 13\,\text{TeV}$, a simultaneous fit of the $\text{t}\bar{\text{t}}$ cross section and m_{t}^{MC} is performed [137]. The primary source of uncertainty in m_{t}^{MC} stems from the limited statistical precision of the simulated samples used for the systematic uncertainty estimation. With the current analysis strategy for the MC simulation, such an analysis based on HL–LHC data would not be possible.

In this thesis, a novel machine-learning-based method to reweight MC simulations to mimic different model parameters or an updated theoretical model has been introduced to decrease CPU demand and enhance the precision of the measurements. The method and its applications to physics analyses will be discussed in Chapter 4.

Chapter 4

ML techniques to reweight simulated events at the LHC

This Chapter introduces a methodology for reweighting MC-simulated samples at the generator level to represent all relevant aspects of an alternative simulation with varied input parameters. The reweighting of the entire event is realised using a machine-learning (ML) algorithm, with the output stored as weights, to be applied to the nominal MC simulation. As a result, the detailed detector simulation is required only for the nominal sample, significantly reducing the computational cost. In this thesis, the ML-based reweighting technique is applied for the case of $t\bar{t}$ production and extensively tested for variations of model parameters of the MC simulation, as well as applying an alternative simulation model.

This Chapter is structured as follows: machine learning and different reweighting techniques are introduced in Section 4.1 and 4.2, respectively. Then, the "deep neural network using classification for tuning and reweighting (DCTR)" [17] method, used in this thesis to reweight MC samples of $t\bar{t}$ pair production, is explained in Section 4.3. This method is applied to mimic variations of two key model parameters, important for the estimation of systematic uncertainties, as detailed in Section 4.4. Further, the reweighting of an NLO simulation to an NNLO simulation of $t\bar{t}$ production is explained in Section 4.5. Finally, the implementation of the method within the CMS analysis software framework is described in Section 4.6. The benefits of the method, future prospects, and the estimated CPU savings are outlined in Section 4.7. This

study was entirely developed for this thesis, following and extending the approach of Ref. [17], for the first time applied in a real analysis scenario at an LHC experiment, and is documented in the corresponding publication [231].

4.1 Machine learning

Machine learning is a method where algorithms learn patterns from data to make predictions or decisions without explicit programming. It is broadly categorised into:

- **Supervised Learning:** The model is trained using labelled data, where each input is paired with a corresponding target output, allowing the algorithm to learn the mapping between inputs and target outputs.
- **Unsupervised Learning:** The model learns patterns exclusively from unlabelled data.
- **Reinforcement Learning:** The model learns by interacting with an environment, making decisions, and receiving feedback in the form of rewards or penalties, used to improve the model decisions over time.

Both *classification* and *regression* problems belong to the category of supervised learning. If the target variable is continuous, the prediction task is a regression problem, while if it is discrete, the task is a classification problem. The study presented in this thesis adopts a classification approach, with the technical details of the classification task outlined below.

Neural network architecture

Machine learning models rely on *neural networks* (NN), which are computational structures inspired by the operation of the human brain. In a *binary classification* task, the NN is trained on two groups of events, each corresponding to a distinct class. Once trained, the network predicts the probability that a new event belongs to one of the two classes, allowing for classification based on the highest probability.

An NN consists of multiple layers of artificial neurons (*nodes*), including an *input layer*, one or more *hidden layers*, and an *output layer*. The input layer contains as many nodes as the input features. A hidden layer encompasses multiple nodes, each associated with a trainable *weight* vector and a *bias* vector. The weight vector comprises one weight for each node of the previous NN layer. Each neuron i computes

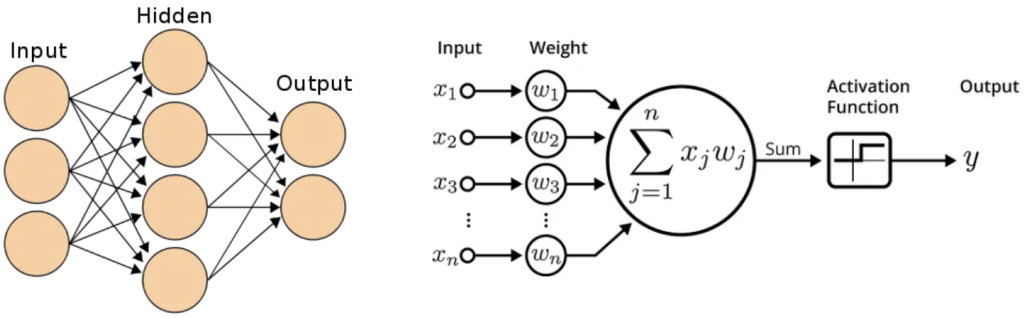

Figure 4.1: Sketch of an NN architecture (left) and how nodes are updated through weights and biases (right). Figures taken from Ref. [232].

a weighted sum of its inputs and adds the bias resulting in z_i, and then applies an activation function to z_i to introduce non-linearity. Mathematically, for a neuron i:

$$z_i = \sum_{j=0}^{N} \hat{w}_{ij} x_j + b_i, \tag{4.1}$$

$$x_i = f(z_i), \tag{4.2}$$

where x_j represents the outputs from the previous layer, $\hat{w}_{ij}$ are the corresponding weights, b_i is the bias term, and f is the activation function. The index j runs over the N nodes of the previous NN layer. In more complicated classification problems, deep NNs are often used, where the term *deep* refers to the presence of many hidden layers. Finally, the output activation function maps the output of the last NN's layer to a probability distribution over the possible classes. In the case of *binary classification*, where inputs are categorised into one of two classes, the output activation function is typically a *sigmoid function* S defined as:

$$S(x) = \frac{1}{1 + e^{-x}}. \tag{4.3}$$

This function ensures that the output is constrained between 0 and 1, as required for probability estimation. A typical NN architecture is illustrated in Figure 4.1.

Training process and optimisation

Neural network training aims to determine the optimal set of weights and biases that minimise the discrepancy between the predicted output $\hat{y} \in [0, 1]$ and the true class labels $y \in \{0, 1\}$, i.e. if the event belongs to class 1 or 2. This optimisation is guided by a *loss function*, which quantifies the discrepancy. The network iteratively updates its parameters (weights and biases) to reduce the mean loss across the training data set. The differentiability of the functions used in the network allows for gradient computation of the mean loss function via the *backpropagation algorithm* [233]. As training progresses, the gradient decreases and approaches zero, leading the model toward a minimum (ideally the global minimum) of the mean loss function. To handle large data sets, training is performed on *batches*—randomly selected subsets of the training data set—over which gradients are averaged to improve computational efficiency. A commonly used optimisation method is the *stochastic gradient descent* [234] or its variants, e.g., the *Adam* algorithm [235].

The training is typically structured into *epochs*, during which the model iterates over the entire data set multiple times, analysing it in every epoch. Each epoch is divided into batches where the *batch size* refers to the number of samples in a batch. At each training step, a batch is passed through the network, and the gradient with respect to all weights and biases is computed and averaged. The model's parameters are then updated using the averaged gradients. The step size at which an optimisation algorithm updates the parameters of the NN model is controlled by the *learning rate*. A higher learning rate accelerates convergence but risks overshooting the optimal solution, while a lower value ensures more precise updates at the cost of slower training. This procedure is repeated over multiple epochs until the model converges.

Validation and overfitting prevention

To prevent overfitting, where the model learns noise or statistical fluctuations specific to the training data rather than generalisable patterns, a separate *validation data set* is employed. At the end of each epoch, the model's performance is evaluated also on the validation data set. If the validation loss remains close to the training loss, it indicates that the model is generalising well. However, if the training loss is significantly lower than the validation loss, this suggests overfitting, meaning the network has memorised the training data rather than learning generalisable patterns. Training

continues until no significant improvement in validation loss is observed over multiple epochs. At this point, the model parameters corresponding to the epoch with the lowest validation loss are retained as the final trained model. Finally, a *test sample*, disjoint from the training and validation data sets, is used to evaluate the goodness of the training.

Optimisation of the NN hyperparameters

Hyperparameters are predefined values that control the training process and model architecture, such as learning rate, batch size, and the number of layers or nodes in the neural network. These values are selected before training and can significantly impact the model's performance. For instance, the choice of batch size plays a crucial role in gradient computation, training stability, and computational efficiency. Larger batch sizes yield smoother gradients by averaging over more samples, leading to more stable but less adaptive updates. However, they require more memory and may overlook finer details in the training data set. On the other hand, smaller batch sizes introduce greater stochasticity in gradient updates, which can help escape local minima but may compromise stability and increase the number of iterations needed for convergence. Finding the right balance between batch size and learning rate is essential for efficient training. Modern optimisers, such as the Adam [235] algorithm, dynamically adjust the learning rate to enhance convergence and overall efficiency. To refine NN training, a hyperparameter scan can be performed, varying the values of the batch size, number of hidden layers and nodes, learning rate, and other factors. The performance of the different configurations is assessed, and the set of hyperparameters that yields the best results is selected. Further, the stability of the training can be evaluated by analysing the consistency of outcomes across different hyperparameter choices.

4.2 Reweighting techniques

As discussed in Section 3.5, the major challenge of the HL-LHC phase will be to sustain the high computational demand to simulate the large MC-simulated samples required by the increased collection of data. To address this issue, reweighting the simulated samples at the generator level can be a solution. Such reweighting can be described in terms of multi-dimensional densities p_i. The conditional densities $p_1(x)$ and $p_2(x)$ describe two densities in a set of given quantities of interest x. The ideal

event weight is given by the density ratio estimate:

$$w(x) = p_1(x)/p_2(x). \tag{4.4}$$

Here, $w(x)$ can be applied as a weight to the density $p_2(x)$ to obtain a conditional density matching $p_1(x)$. In standard reweighting approaches, the density ratio estimate is calculated in intervals of x, by comparing binned distributions at a truth level. Nevertheless, this approach is sensitive to the particular choice of x (binning) and the dimension (number of inputs) could be maximum 2, due to the increasing complexity of the method with the number of dimensions. In contrast, $w(x)$ can be well approximated by training a ML classifier to distinguish between two simulations and reweight one generator-level simulation into another. This method offers a higher flexibility and does not have the limitations of standard reweighting. In particular, all event information can be passed as input to the NN. This enhances the reweighting precision by avoiding binning inaccuracies and accurately reproducing correlations between the elements of x. Additionally, continuous reweighting as a function of any parameter of the simulation is possible.

In modern particle physics analyses, several ML-based reweighting methods are used. For instance, boosted decision trees are employed to derive event weights [236], while NNs are used to learn the likelihood ratio between different simulations [17, 237, 238]. Input convex NNs [239] have been applied to calibrate simulated events [240]. The normalising flows [241,242] can be used to map between the initial and target distributions, e.g. to calibrate the simulation to match the data [243]. Normalising flows can also learn the conditional probability distribution of the initial data, allowing for sampling of events consistent with an alternative conditional distribution [244–246]. In this thesis, the ML-based reweighting method "deep NN using classification for tuning and reweighting (DCTR)" [17] is used and is described in detail in the following.

4.3 Deep neural network using classification for tuning and reweighting (DCTR)

The DCTR method employs a deep NN to reweight MC samples obtained from one simulation to reproduce the features of an alternative simulation, or a simulation with varied model parameters. This method combines a ML architecture designed

to incorporate all the particle information [247] with a parametrised classifier [237, 248]. This approach allows for the full phase-space reweighting, using all the event information such as kinematic and particle type variables. As a consequence, it enables posterior projections onto any desired variable. Additionally, this approach allows for continuous reweighting as a function of any MC parameter. This feature has been exploited in the b quark fragmentation study presented in Section 4.4.2. Full phase-space reweighting is critical for achieving the best precision when evaluating modelling uncertainties arising from parameter variations in the MC simulations. Further, this capability is particularly valuable when reweighting simulations from one model to another (e.g. NLO-based to NNLO-based model). Unlike traditional reweighting methods, which often rely on ratios of observables in discrete bins of two distributions, the DCTR method offers better precision for observables not explicitly considered in the calculation of standard reweighting approaches.

4.3.1 The likelihood ratio trick

The full phase-space reweighting technique involves a prescription to compute event weights. Consider two simulations representing the same phase space Ω and described by the probability densities $p_1(x)$ and $p_2(x)$, with the set of variables $x \in \Omega$. Assuming both densities share the same phase space, the optimal per-event weight to map the second simulation to the first one is defined by the ratio $w(x) = p_1(x)/p_2(x)$. This weight function can be effectively approximated by training a ML classifier to discriminate between the two simulations. For instance, an NN function $f(x)$ can be trained using the binary cross-entropy loss:

$$\text{loss}\big(f(x)\big) = -\sum_{i\in\mathbf{1}} \ln f(x_i) - \sum_{i\in\mathbf{2}} \ln\big(1 - f(x_i)\big), \tag{4.5}$$

where **1** and **2** represent sets of events from the two simulations. Such, the cross-entropy loss is set up to distinguish between the two classes defined by **1** and **2**, respectively. The *likelihood ratio trick* states [17]:

$$f(x)/(1 - f(x)) \approx p_1(x)/p_2(x). \tag{4.6}$$

As a result, the network function $f(x)$ can approximate the weight function $w(x)$, which is the quantity of interest, using the relation $w(x) \approx f(x)/(1 - f(x))$. The representation of $f(x)$ as an NN has the advantage of enabling ML algorithms to

efficiently explore the entire phase space. When dealing with MC events that include weights, for instance, from simulations at NLO or NNLO accuracy, Eq. (4.5) is modified accordingly:

$$\text{loss}(f(x)) = -\frac{1}{N}\sum_i w_i^{\text{MC}} \left(y_i \ln f(x_i) + (1-y_i)\ln(1-f(x_i))\right). \tag{4.7}$$

Here, w_i^{MC} is the MC weight for the event i, the true event label y_i corresponds to 1 (0) if the event belongs to class 1 (2), respectively, and $f(x_i)$ is the network function predicting the class of event i. The specific case of the negative event weights is discussed in Section 4.5.

In a typical reweighting scenario, two classes of events are obtained by using the same simulation but different values θ for an input parameter. In this context, θ serves as the reweighting parameter. For instance, when assessing modelling uncertainties, one may need to transform $p_\theta(x)$ into $p_{\theta+\delta\theta}(x)$. This corresponds to reweight the MC sample obtained with the nominal value of a given parameter to match a sample with a variation in this parameter, $\theta + \delta\theta$. Further, Eq. (4.5) can be extended to the continuous case. This is achieved by parametrising the network function with the parameter θ, which becomes $f(x, \theta)$ [237, 248]. The training data are sampled with a uniform distribution across a range of θ and Eq. (4.5) is modified as:

$$\text{loss}\big(f(x,\theta)\big) = -\sum_{i\in\theta_0} \ln f(x_i,\theta) - \sum_{i\in\Theta} \ln\big(1-f(x_i,\theta)\big). \tag{4.8}$$

Here, the NN is trained to distinguish between the sample generated with the nominal value of the reweighting parameter θ_0 and a sample obtained with a set of values in the parameter θ, denoted by Θ.

4.3.2 Neural network architecture

The DCTR method relies on an NN architecture that can efficiently capture all the relevant aspects of the phase space. The Particle-Flow Network (PFN) [247], based on the deep sets framework [249], is a suitable NN for this task. The PFN is designed to incorporate the full event information, including particle four-momenta and auxiliary information, such as the particle type. Further, the reweighting parameter θ can be used to parametrise the NN with the loss function given in Eq. (4.8). The PFN

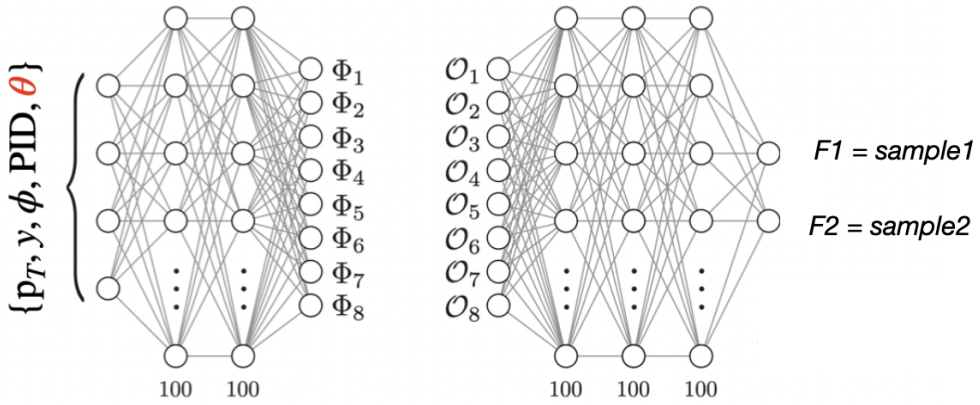

Figure 4.2: The PFN architecture used in the DCTR method. It parametrises the single-particle mapping Φ (left) and the function F (right), shown for the case of a latent space of dimension $l = 8$. The latent observable is $O_n = \sum_i \Phi_n(p_T, y_i, \phi_i, m_i, \mathrm{PID}_i)$ where i is the number of particles in an event and the transverse momentum p_T, rapidity y, azimuthal angle ϕ, mass m, particle ID PID of each particle are given. The output of F is a softmaxed discriminant between two classes. Figure taken from Ref. [247] (modified).

consists of two neural networks, F and Φ, interconnected as:

$$f(p) = F\left(\sum_{i=1}^{N} \Phi(p_i)\right). \tag{4.9}$$

Here, p represents the set of all particles and p_i are the properties of particle i (momentum and type), and θ is the reweighting parameter. The two networks are integrated into a single model, where the output of Φ serves as the input for F. The network Φ processes each particle individually and generates a single-particle internal (latent) representation. The network F takes the sum of these latent representations from all particles and constructs an overall event-level representation. A key hyperparameter is the dimension of the latent space, which is defined by the number of dimensions used to represent the input data in a compressed form within the NN. The input particles are first embedded in an l-dimensional latent space through Φ, while F maps this latent space from $\mathbb{R}^l \to \mathbb{R}$. Finally, the output of F is processed using a SOFTMAX [250] function, which serves as a discriminant to distinguish between the two classes.

The architecture of the PFN is illustrated in Figure 4.2. The network Φ is composed of

two hidden layers, each with 100 nodes. The classifier F includes three hidden layers and two output nodes for binary classification, with each hidden layer comprising 100 nodes. The NN's hyperparameters employed in this project are reported below, corresponding to the default settings of Ref. [247]:

- **Latent space dimension:** $l = 128$.
- **Activation function:** ReLu (rectified linear unit) [251].
- **Classification output function:** SOFTMAX [250].
- **Training and validation loss functions:** cross-entropy loss.
- **Optimiser:** ADAM [235].
- **Learning Rate:** 0.001.
- **Number of epochs**: 100.
- **Early stopping with patience 10:** This technique is used to prevent overfitting during training by stopping the training process if the validation loss does not improve for a certain number of epochs, where the specific number is determined by the patience value. The default patience value of 10 has been used for the two modelling variations, while a value of 30 is preferred for the NLO-to-NNLO model reweighting.

All models are implemented in KERAS [252] with the TensorFlow backend [253], where the data are passed sequentially through both networks. An optimisation of the hyperparameters is performed specifically for each case to determine the size of the training inputs and the batch size. The optimisation of other hyperparameters was explored, but their impact was negligible for the cases under study. This is likely because the PFN has been developed and is already tuned for high-energy physics applications.

4.4 Reweighting of systematics uncertainties

In physics analyses by the LHC experiments, the model uncertainties in the simulation are usually estimated by simulating alternative MC samples where particular input parameters are varied, usually up and down, from their nominal value assuming a Gaussian prior. For instance, in the analyses of $\mathrm{t\bar{t}}$ events in the CMS experiment, the evaluation of systematic model uncertainties involves about ten different sources, each requiring simulation of additional MC samples. Variations of PDF eigenvectors or parameters of initial state and final state radiation are already handled by internal

reweighting methods in most MC generators. To facilitate reweighting of other parameters, alternative approaches are necessary. For the first time, ML-based reweighting for other model parameters is implemented in the realistic scenario of analyses of top quark pair production in CMS. In particular, two parameters of interest were investigated by using the DCTR method. A discrete reweighting to compute the two-sided variations is performed for both cases. In addition, the continuous reweighting of a parameter affecting the fragmentation of b quarks in PYTHIA 8 [129] is studied. This result provides the basis for MC tuning at the detector level, as discussed later in Section 4.4.2.

4.4.1 Parton shower matching uncertainty

Both the ATLAS and CMS experiments use POWHEG+PYTHIA 8 setups to generate their nominal $t\bar{t}$ MC samples. This is done by simulating the hard process of $t\bar{t}$ production with the HVQ program [112] in the POWHEG v2 [110,113] generator, which is interfaced with PYTHIA 8.240 [129] for parton showering (PS) and hadronisation. The POWHEG generator simulates inclusive $t\bar{t}$ production with the matrix element at NLO accuracy in QCD, where the first additional parton is computed at LO. The resummation of the NLO radiation is regulated by the h_{damp} parameter, which controls the matching of the ME with the PS. The h_{damp} parameter enters the simulation in a damping function D, which reduces the real contribution to the Sudakov form factor [254] and is given by:

$$D = \frac{h_{\text{damp}}^2}{p_{\text{T}}^2 + h_{\text{damp}}^2}. \tag{4.10}$$

Here, p_{T} is the transverse momentum of the top quark or antiquark and $h_{\text{damp}} = h m_{\text{t}}$, where h is a real value and m_{t} the top quark mass set to $m_{\text{t}} = 172.5\,\text{GeV}$, consistent with the most precise result [255] obtained from the combined measurements of the ATLAS and CMS collaborations.

In the CMS experiment, the uncertainty related to the h_{damp} parameter is evaluated by considering a two-side variation relative to its nominal value. The nominal value of h_{damp} is set to 1.379 m_{t} [256]. The variations are 2.305 m_{t} (up variation) and 0.8738 m_{t} (down variation), obtained from a tune to data. Since the MC parameter h_{damp} is not a physical quantity, such estimations result in a sizeable uncertainty in h_{damp} [256], which can, in turn, translate into one of the leading systematic uncertain-

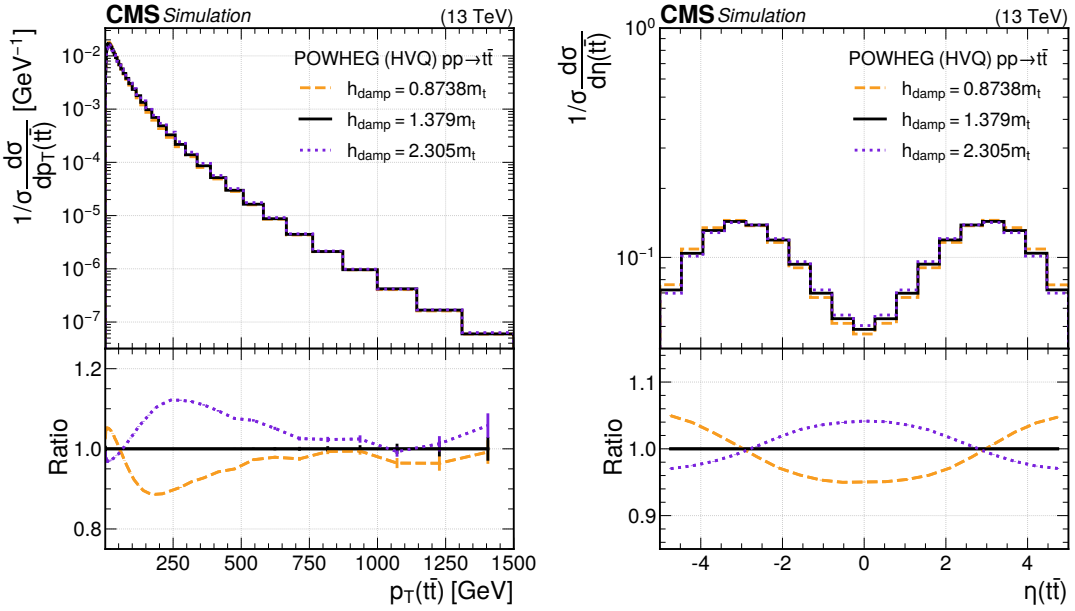

Figure 4.3: The normalised differential cross section of $\mathrm{t\bar{t}}$ production in pp collisions at 13 TeV as a function of the p_{T} (left) and η (right) of the $\mathrm{t\bar{t}}$ system obtained with the POWHEG program. The standard setting of $h_{\mathrm{damp}} = 1.379 m_{\mathrm{t}}$ (black solid lines) is compared to down (orange dashed lines) and up (violet dotted lines) variations in h_{damp}. The ratios of the predictions with the h_{damp} variations to the nominal one are shown in the lower panels. The vertical bars represent the statistical uncertainties in the MC samples. Published in Ref. [231].

ties in precision studies of the top quark. The effect of varying h_{damp} in the MC event generation impacts physical observable distributions, most notably $p_{\mathrm{T}}(\mathrm{t\bar{t}})$ and $\eta(\mathrm{t\bar{t}})$, as shown in Figure 4.3. Differences of up to 10% in the normalised cross sections are observed in the resummation region at $p_{\mathrm{T}}(\mathrm{t\bar{t}}) \sim 250\,\mathrm{GeV}$. The impact diminishes at higher $p_{\mathrm{T}}(\mathrm{t\bar{t}})$ and is expected to become null for $p_{\mathrm{T}}(\mathrm{t\bar{t}}) > 1\,\mathrm{TeV}$ [257]. A variation of around 5% is observed in $\eta(\mathrm{t\bar{t}})$.

Since the h_{damp} parameter cannot be reweighted internally, in practice two additional MC-simulated samples are produced, corresponding to different settings for the value of h_{damp}. To comply with the allocated computational cost, these (and other) model-parameter variation samples are generated with significantly fewer events compared to the nominal samples. The related statistical uncertainty in the MC-simulated samples for the estimate of systematic uncertainty becomes a limiting factor in high-precision CMS analyses. For the full Run2 data set, the nominal $\mathrm{t\bar{t}}$ pair production samples

comprise approximately 2 billion events. In contrast, the two variation samples are produced with approximately 850 million events each, representing a 60% reduction with respect to the nominal sample. Therefore, the h_{damp} parameter is an ideal case for DCTR reweighting, offering a robust alternative to the production of dedicated MC samples and ensuring the high statistical precision of the nominal simulation. The dedicated discussion on CPU saving by implication of the DCTR reweighting method is presented in Section 4.7.

Training setup

Two different NN models have been trained to reweight the MC simulation with nominal h_{damp} setting to the two variations. Each NN model distinguishes between the nominal and up/down variations by using a binary classification output. The parton-level information related to the t and $\bar{\text{t}}$ at the ME level is passed as input to the NN for training. The particles are represented by their four-momenta and type encoded as a particle ID (PID) number. The input variables for each particle are rapidity y, azimuthal angle ϕ, mass m, and the PID. To facilitate the NN learning, the inputs are scaled to be represented by values $\mathcal{O}(1)$ before the training. In particular, the mass m is divided by 244 GeV, corresponding to the maximum in the training sample, and the $\log_{10}(p_{\text{T}})$ is used to mitigate the skewness of the p_{T} distribution. For each h_{damp} setting, 40 million events are used in the training. The resulting 80 million events for each of the two NN models are split into 75% for training and 25% for validation. After a hyperparameter scan, a batch size of 40 000 events is found to give the best results for both variations in h_{damp}. While the batch size significantly affects the reweighting performance, other hyperparameters, such as the number of hidden layers or nodes and the dimension of the latent space, are found to have a negligible impact on the final results.

Results

The performance of the training is assessed by analysing the values of the loss functions on both the training and validation data sets. The training and validation loss curves for the NN models trained with the two variations of h_{damp} are displayed in Figure 4.4. The NN training has been conducted for approximately 40 (30) variations for the down (up) variation. The performance of the reweighting is evaluated using statistically independent test samples of 100 million events each. The weights derived

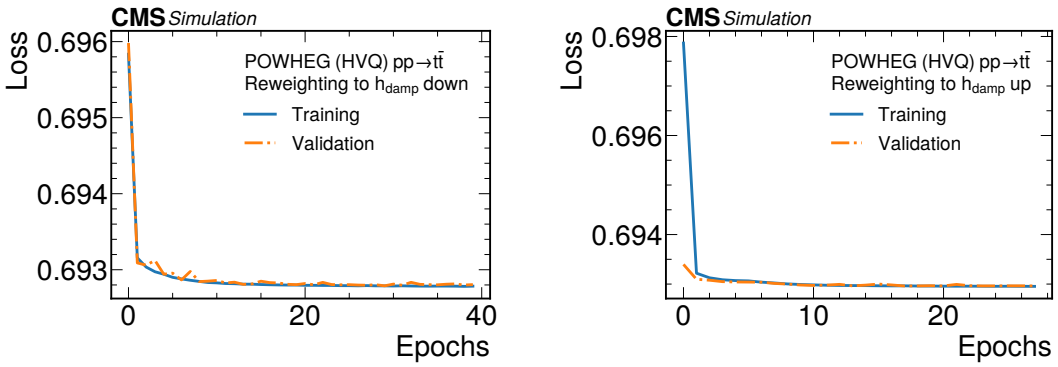

Figure 4.4: The NN histories of the training for the h_{damp} parameter reweighting. Shown are the loss functions for the training data (blue solid line) and the validation data (orange dash-dotted line) for the down (left) and up (right) variations of h_{damp}. Published in Ref. [231].

from the trained model are found to be close to unity with a standard deviation of about 0.1. No weights are observed outside the range from 0.8 to 1.2. These weights are applied to reweight the nominal MC sample to match the up and down variations of h_{damp}. The impact of the reweighting on the distributions of the $\mathrm{t\bar{t}}$ pair, $p_{\text{T}}(\mathrm{t\bar{t}})$ and $\eta(\mathrm{t\bar{t}})$, is shown in Figure 4.5. The accuracy of the reweighting is quantified by the ratio of the reweighted to the nominal sample, shown below each distribution. The target sample, i.e. the sample generated with the variation of h_{damp}, and the reweighted one agree within 1% in $\eta(\mathrm{t\bar{t}})$. Deviations of up to 2% are observed for $p_{\text{T}}(\mathrm{t\bar{t}}) \gtrsim 400\,\text{GeV}$, indicating that the method's closure is within 2%. This closure is excellent, and a 2% deviation is negligible compared to the 10% effect associated with variations of the h_{damp} parameter in $p_{\text{T}}(\mathrm{t\bar{t}})$, where the variations of h_{damp} are used to estimate a systematic uncertainty. The impact of ML reweighting on the p_{T} and y distributions of the additional parton has also been evaluated, achieving a precision comparable to that of the $\mathrm{t\bar{t}}$ system, with the results shown in Figure 4.6.

The NN model is trained using parton-level information under the assumption that the parton shower (PS) and hadronisation do not affect the reweighting of the h_{damp} parameter. To check this assumption, the accuracy of the reweighting is further tested for events at the level of stable particles (particle level). In this case, the PS and hadronisation have been simulated with Pythia 8. The results of the reweighting for distributions obtained at the particle level, such as the jet multiplicity N_{jet}

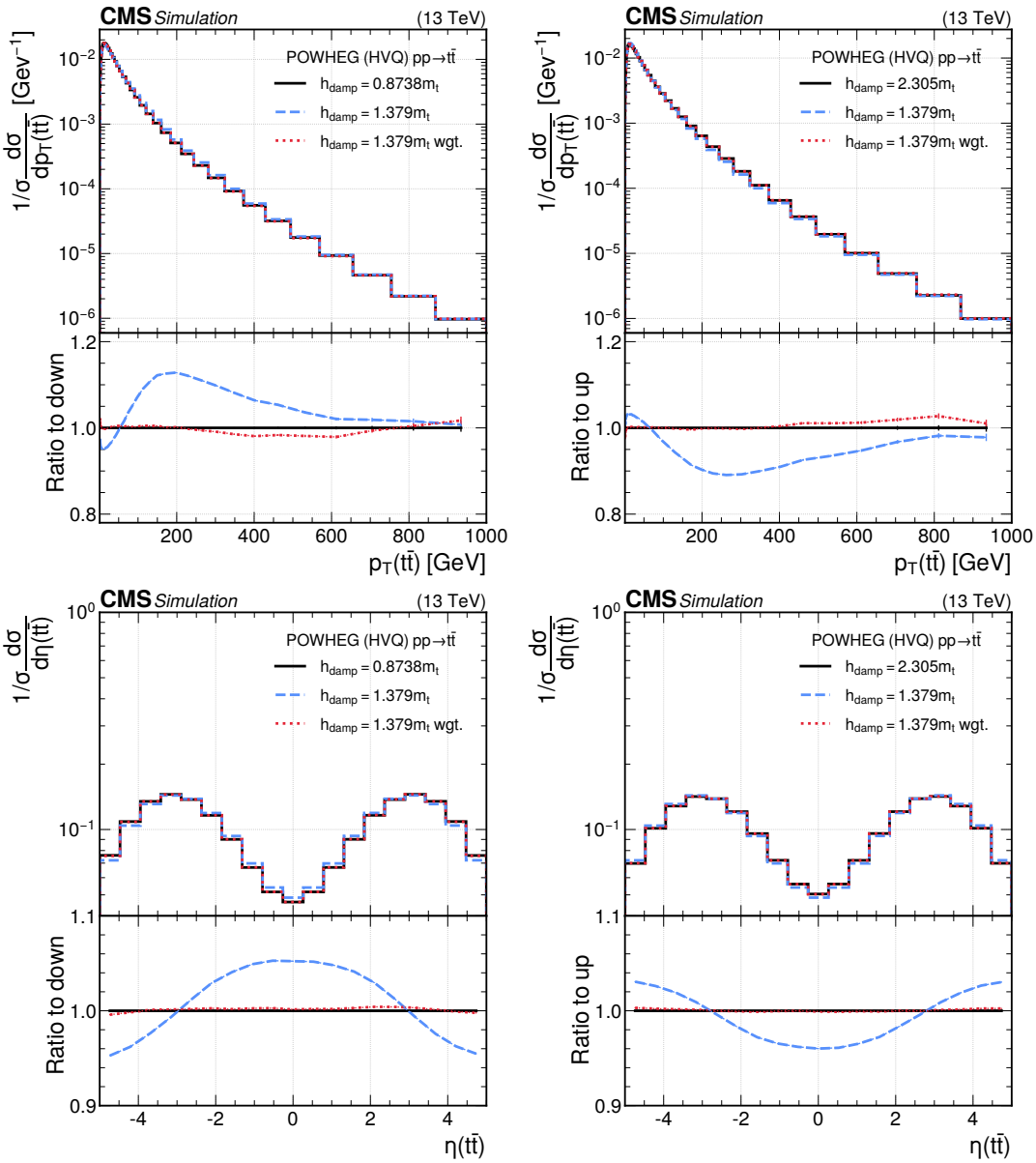

Figure 4.5: The normalised differential cross section as a function of the p_{T} (upper) and η (lower) of the $\mathrm{t\bar{t}}$ system. The black solid line shows the predictions from the down (left) and up (right) variations in h_{damp}, and the blue dashed line presents the prediction from the nominal sample. The red dotted line indicates the nominal sample reweighted to the down (left) and up (right) h_{damp} variations using the DCTR method. The ratios to the samples with the target values of h_{damp} are displayed in the lower panels, together with their almost negligible statistical uncertainties (vertical error bars). Published in Ref. [231].

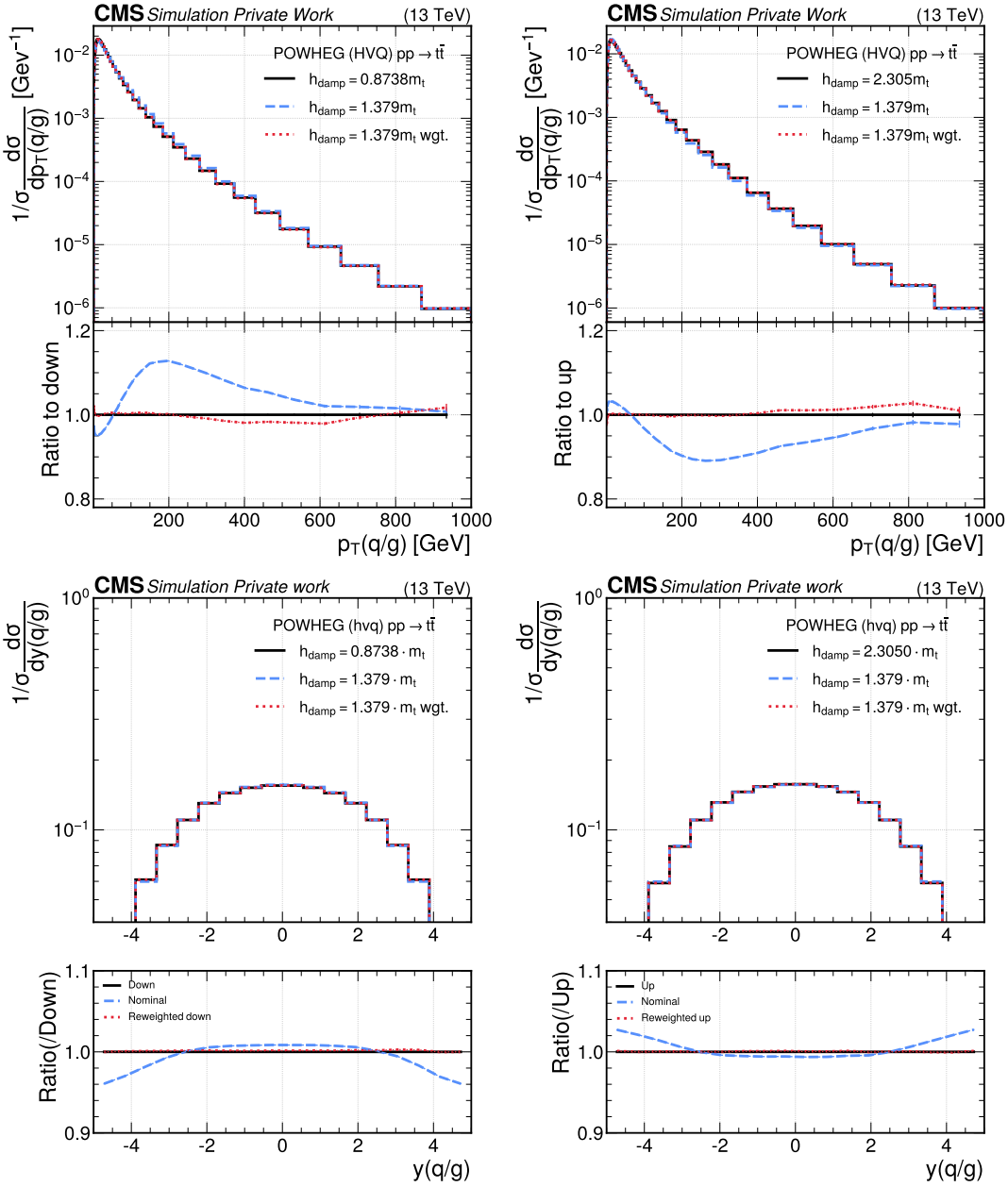

Figure 4.6: Same as Figure 4.5 for the p_{T} (upper) and y (lower) of the additional parton.

and the scalar p_{T} sum of all jets in the event (H_T), are shown in Figure 4.7. The jets are clustered using the anti-k_{T} jet algorithm [144] with a distance parameter of $R = 0.4$, applying kinematics cuts of $p_{\mathrm{T}} > 30\,\mathrm{GeV}$ and $|\eta| < 2.4$. The target distri-

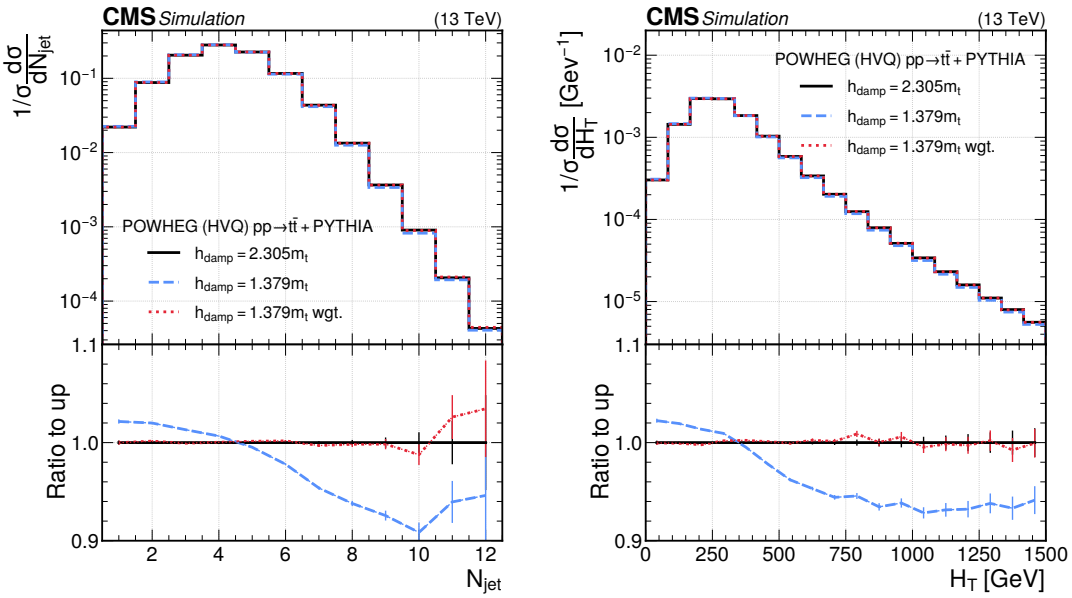

Figure 4.7: The normalised differential cross section as a function of N_{jet} (left) and H_T (right). The black solid line shows the predictions from the up variation in h_{damp} and the blue dashed line presents the prediction from the nominal sample. The red dotted line indicates the nominal sample reweighted to the h_{damp} variation using the DCTR method. The ratios to the target distributions are displayed in the pads below, where the vertical bars represent statistical uncertainties. Published in Ref. [231].

butions obtained from samples generated with the up variation of h_{damp} agree with the reweighted ones within 1% in both observables. Similar results are achieved for the samples generated with the down variation of h_{damp}. This test confirms that the model can be trained at the parton level and successfully applied at the particle or detector levels, since these additional steps of the simulation do not affect the PS matching uncertainty.

4.4.2 The b quark fragmentation

A major source of uncertainty in many precision top quark analyses is the fragmentation of b quarks into hadrons. The b quark from the decay t → Wb fragments into a b hadron. This process is described in PYTHIA by the Lund string model [129], where the probability for the b hadron carrying the momentum fraction z of the b quark's momentum is given by the Lund–Bowler fragmentation function [131, 258]:

$$f_{\mathrm{B}}(z) = \frac{1}{z^{1+br_{\mathrm{b}}m_{\mathrm{b}}^2}}(1-z)^a \exp\left(-\frac{bm_{\mathrm{T}}^2}{z}\right). \tag{4.11}$$

Here, $m_{\mathrm{T}}^2 = m_{\mathrm{B}}^2 + p_{\mathrm{T}}^{\mathrm{B}\,2}$ is the transverse mass of the b hadron and a and b are free parameters treated as universal for all quarks. The values $a = 0.68$ and $b = 0.98\,\mathrm{GeV}^{-2}$ were determined from a fit to data sensitive to light-quark fragmentation in the Monash tune [259], such as charged-particle multiplicities and momentum fractions. The Lund–Bowler parameter r_{b}=0.855 and the b quark mass parameter in the MC simulation $m_{\mathrm{b}} = 4.78\,\mathrm{GeV}$ [259] are set for the Monash tune. Varying the r_{b} parameter in the event simulation influences observables that are sensitive to the b quark fragmentation. One example is the observable x_{b}, which represents the normalised energy fraction of the b hadron and is defined as [260, 261]:

$$x_{\mathrm{b}} = \frac{2p_{\mathrm{B}} \cdot p_{\mathrm{t}}}{m_{\mathrm{t}}^2} \frac{1}{1 - m_{\mathrm{W}}^2/m_{\mathrm{t}}^2}. \tag{4.12}$$

Here, p_{B} and p_{t} are the four-momenta of the b hadron and the top quark, respectively, and m_{W} is the W boson mass. Varying r_{b} in the MC simulation affects the distribution in x_{b}, potentially causing variations in the efficiency of the identification of b-jets. As a result, the choice of this MC parameter can introduce sizeable systematic uncertainties in physics analyses.

In CMS, the CP5 tune [256] is the default underlying event tune for analyses at $\sqrt{s} = 13\,\mathrm{TeV}$. A key difference compared to the Monash tune is the use of a smaller value for the strong coupling parameter in the final-state shower, with $\alpha_S(m_{\mathrm{Z}}) = 0.118$, whereas the Monash tune employs $\alpha_S(m_{\mathrm{Z}}) = 0.1365$. In the CP5 tune, the r_{b} value remains unchanged. However, a re-derivation of the r_{b} parameter on top of the CP5 tune with $\mathrm{e^+e^-}$ data from LEP yields $r_{\mathrm{b}} = 1.056^{+0.196}_{-0.200}$. These values are recommended as the nominal and two-sided variation of the r_{b} parameter for use in CMS analyses. To assess systematic uncertainties related to the b quark fragmentation, CMS analyses use a one-dimensional (1D) traditional reweighting in $\hat{x}_{\mathrm{b}} = p_{\mathrm{T}}^{\mathrm{B}}/p_{\mathrm{T}}^{\mathrm{bjet}}$, where $\hat{x}_{\mathrm{b}}$ approximates the momentum fraction z in Eq. (4.11). Events are generated with the default parameter $r_{\mathrm{b}} = 0.855$ from the Monash tune in Pythia 8. The weights obtained from the 1D reweighting are applied on an event-by-event basis to resemble samples for $r_{\mathrm{b}} = 1.056$ and 1.252. This method is suboptimal because it does not capture all kinematic dependencies of the b quark fragmentation, e.g. the longitudinal component of the four-momentum of the b hadron and b-jet. Additionally, the

choice of binning in $\hat{x}_\mathrm{b}$ can affect the results. The DCTR method is an elegant alternative, as no binning is introduced and the full event information is taken into account.

In this thesis, two NN models are trained to reweight the sample generated with the CP5 tune with $r_\mathrm{b} = 0.855$ to both the new nominal value of $r_\mathrm{b} = 1.056$ and the respective up variation of the r_b parameter 1.252. For the new down variation, the generated value of $r_\mathrm{b} = 0.855$ is used, which closely matches $r_\mathrm{b} = 0.856$ obtained from the reanalysis of LEP data. Further, a continuous reweighting is performed using ten different values of r_b for the training. A single NN model is trained to reweight the generated sample to any arbitrary value of r_b within the range $[0.6, 1.4]$, enabling interpolation between the ten r_b values.

Training setup

The NN is trained using the particle-level information from the events produced with Pythia 8. The input variables to the NN are x_b of t and $\bar{\mathrm{t}}$, as defined in Eq. (4.12). For the continuous reweighting, the value of r_b serves as a reweighting parameter. The observable x_b comprises the information of the entire event, as it contains the four-momenta of the t quarks and the b hadrons in the event. The four-momenta of t and $\bar{\mathrm{t}}$ are taken from the last copies in the Pythia 8 event record before they decay, while the first copies of the b hadrons are used. Since the input variable r_b is close to unity and the variable x_b is defined within the range $[0, 1]$, no normalisation is required in this scenario. Theoretically, the energy of a b hadron cannot exceed that of the parent bare b quark but this constraint no longer holds in a real collision event. In this case, the energy involved in the hadronisation can originate from other components of the final state, including the underlying event, which plays a significant role at the LHC. As a result, while the majority of events fall within the range $x_\mathrm{b} \in [0, 1]$, there are a few instances where x_b exceeds 1.

In the discrete reweighting, approximately one million events for each r_b value are considered in the training. In the case of continuous reweighting, the NN is trained on a total of 5 million events. Out of these 5 millions, 2.5 million events were generated with $r_\mathrm{b} = 0.855$ and another 2.5 million events for ten different r_b values within the interval $[0.6, 1.4]$, i.e. 250 000 events for each value of r_b. In both cases, 90% of the events are reserved for training and 10% for validation. After a hyperparameter scan,

a batch size of 1000 is found to yield the best performance.

Results

The training performance is assessed by analysing the training and validation loss values. In the discrete reweighting, the NN training stopped after about 20 epochs in both cases. Then, the performance of the reweighting is studied with statistically independent samples of about 2 million events. The weights, obtained from the trained model, are found to be in the intervals $[0.6, 1.4]$ for the reweighting to $r_\mathrm{b} = 1.056$ and $[0.2, 2.5]$ for the reweighting to $r_\mathrm{b} = 1.252$. The accuracy of the reweighting is evaluated using the x_b and the transverse momentum of the b hadron (p_T^B) distributions, as shown in Figure 4.8. The reweighted distributions and the distributions simulated with the target r_b values agree within the statistical uncertainties, with a closure of a few percent. The method demonstrates excellent closure as deviations of a few percent are negligible compared to variations of up to 250% in x_b and 40% in p_T^B when varying r_b to estimate a systematic uncertainty.

Similarly, statistically independent samples with 250 000 events are used for the continuous reweighting in r_b to check the goodness of the reweighting. To evaluate the accuracy of the ten distinct r_b values used in the training, a χ^2 test is performed. The results are presented in Figure 4.9. This test quantifies the difference between the target distribution generated with a given value of r_b and the nominal distribution obtained for $r_\mathrm{b} = 0.855$. Prior to reweighting, χ^2 values per number of degrees of freedom (NDF = 50) of about 80 for p_T^B and 650 for x_b are found for the distributions with the largest differences in r_b to the nominal value. After the reweighting, the distributions for both x_b and p_T^B exhibit excellent agreement with the target sample, with χ^2/NDF close to unity across the entire range of r_b values considered in the interval $[0.6, 1.4]$.

Such discrete reweighting of r_b can be applied in any top CMS analyses of $\mathrm{t\bar{t}}$ events, providing an alternative to the traditional (suboptimal) 1D reweighting technique. Moreover, the study of continuous reweighting provides the basis for MC tuning at the detector level. The general idea is to pass the collision data to the model trained with the continuous reweighting. Then, the MC parameter of interest can be extracted at the minimum by gradient descending on a loss function. As a result, the MC

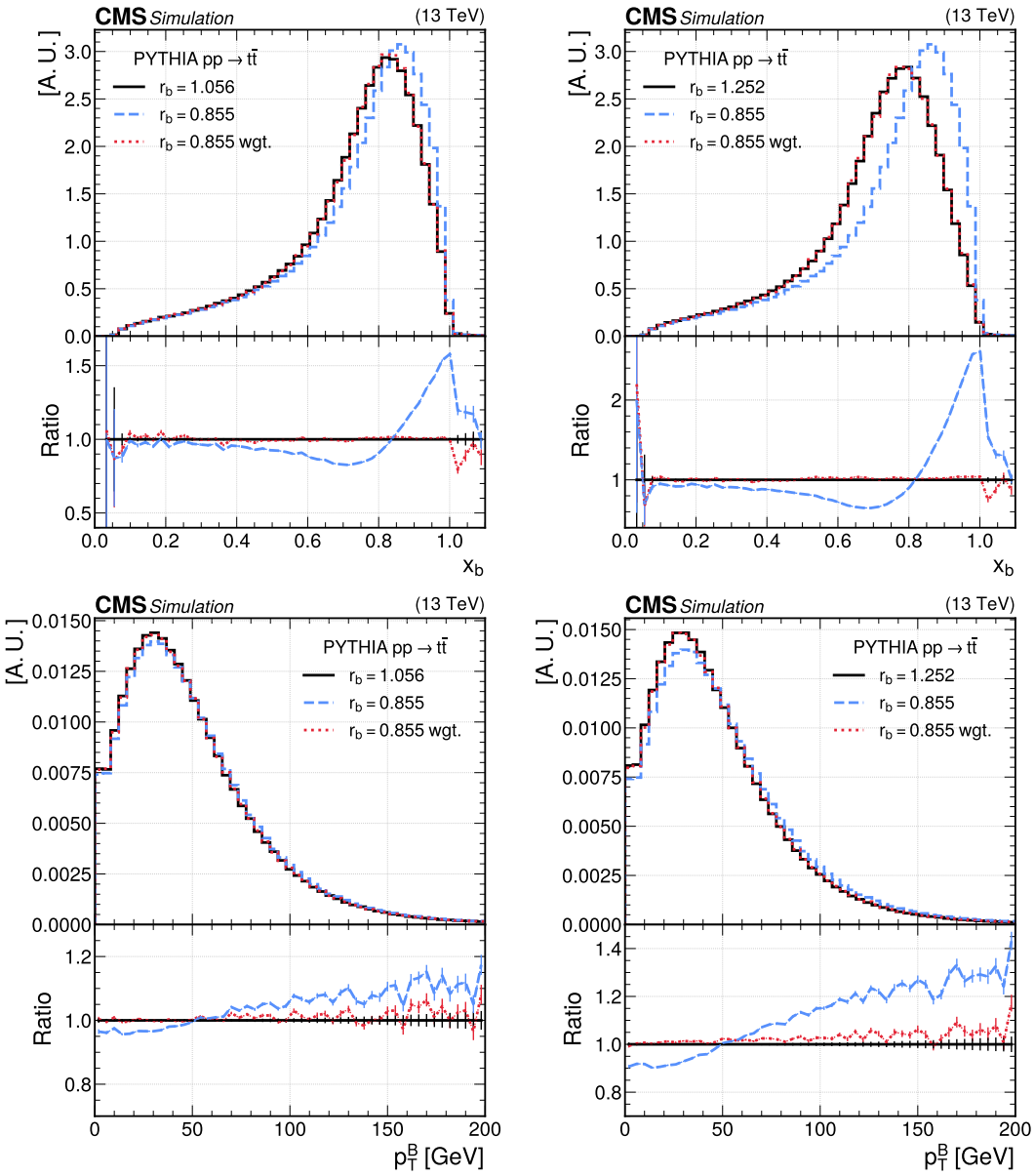

Figure 4.8: Distributions in x_b (upper) and p_T^B (lower) from $\mathrm{t\bar{t}}$ simulations with PYTHIA 8 with value $r_\mathrm{b} = 0.855$ (dashed blue line) and a second value of r_b (solid black line). The nominal sample reweighted to $r_\mathrm{b} = 1.056$ (left) and $r_\mathrm{b} = 1.252$ (right) is shown as red dotted lines. Below each distribution, the ratios to the target distribution are displayed, where the vertical bars represent the statistical uncertainties. Published in Ref. [231].

simulation at the detector level can be directly tuned on data without the need to

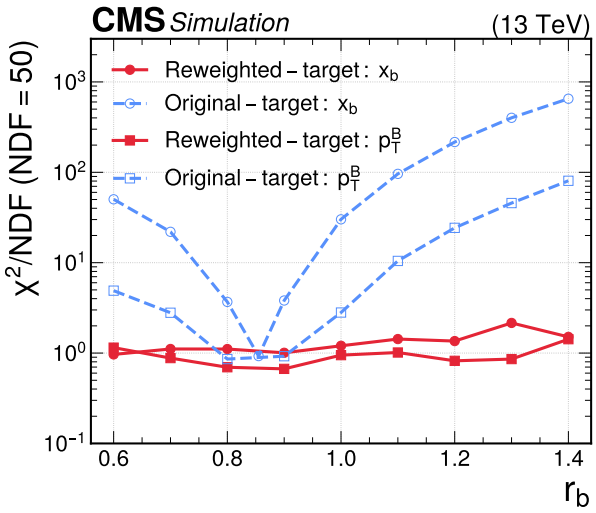

Figure 4.9: Values of χ^2/NDF obtained for distributions in x_b (circles) and p_T^B (squares), where target distributions for events with different r_b values are compared to a distribution with the nominal value of $r_b = 0.855$ before the reweighting (blue dashed line) and after the reweighting to the target value of r_b (red solid line). The lines connecting the markers are shown for illustration purposes only. Published in Ref. [231].

generate numerous templates. This approach could be crucial in the future for tuning parameters of the underlying tune or colour-reconnection models by using data. A more challenging scenario would involve tuning the hadronisation model.

4.4.3 Statistical uncertainty of the method

As mentioned earlier, the DCTR reweighting method implemented in this thesis achieves a closure of the method of about 2% in both the h_{damp} and b fragmentation scenario. To estimate the statistical precision of the reweighting, the training procedure was repeated 50 times [262]. In each iteration, a randomly chosen subset of the generated events was used for the training. The results from 50 different trainings, expressed in ratios of reweighted to target distributions, are compared. Then, the final result is computed as the average of the 50 reweighted distributions, with the statistical uncertainty of the method determined from one standard deviation of these distributions.

The $p_T(t\bar{t})$ and $\eta(t\bar{t})$ distributions for the h_{damp} reweighting scenario are shown in

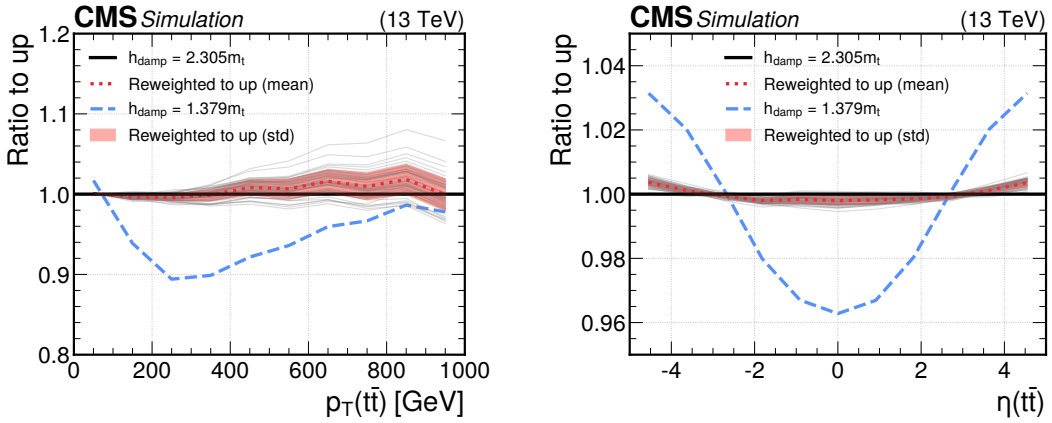

Figure 4.10: Ratios between the h_{damp} target distributions in $p_{\mathrm{T}}(\mathrm{t\bar{t}})$ (left) and $\eta(\mathrm{t\bar{t}})$ (right), and 50 different reweightings (grey solid lines). The ratio to the target before the reweighting is shown as a blue dashed line and the mean of the different reweightings as a red dotted line. The red band represents the statistical uncertainty of the method obtained from the standard deviation of the 50 reweighted samples. Published in Ref. [231].

Figures 4.10. Each training iteration was performed using 80 million events randomly selected from a total sample of 200 million events. Similarly, the x_{b} and $p_{\mathrm{T}}^{\mathrm{B}}$ distributions for the b fragmentation reweighting scenario are illustrated in Figures 4.11. In this case, each training iteration was performed using 2 million events randomly selected from a sample of 26 million events. In both scenarios, the target sample and the average of the 50 reweighted samples are consistent within the statistical uncertainty of the method. In the case of the b fragmentation, this holds when considering the statistical uncertainty of the samples, which, on the other hand, is negligible for the h_{damp} reweighing scenario. The statistical uncertainty of the method, of about few percent, is comparable in magnitude to the deviation observed between the target distribution and the nominal result. A larger statistical uncertainty of up to about 5% is observed only for $x_{\mathrm{b}} > 1$. Therefore, it is concluded that the method closure of 2% is consistent with its statistical uncertainty.

4.5 Reweighting to alternative model

Recent progress in theory enabled precise calculations for $\mathrm{t\bar{t}}$ production in pp collisions using fixed-order computations up to NNLO accuracy in QCD [263–271]. These

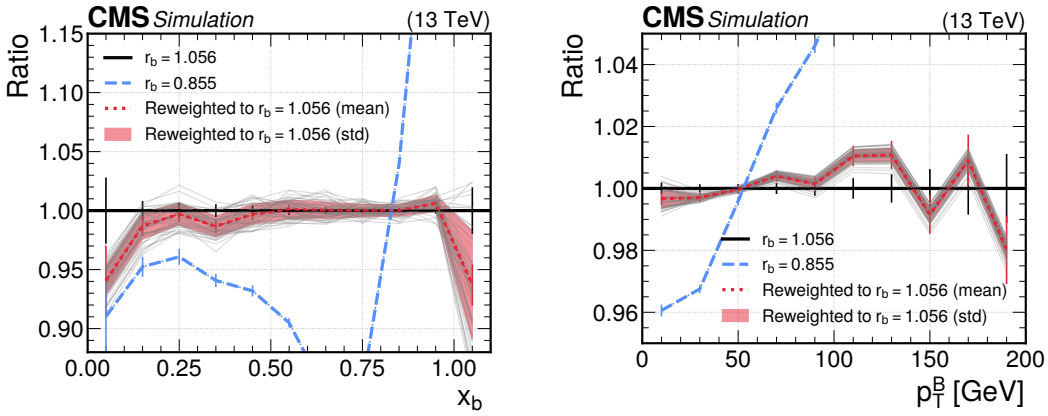

Figure 4.11: Ratios between the r_b target distributions in x_b (left) and p_T^B (right), and 50 different reweightings (grey solid lines). The ratio to the target before the reweighting is shown as a blue dashed line and the mean of the different reweightings as a red dotted line. The red band represents the statistical uncertainty of the method obtained from the standard deviation of the 50 reweighted samples. The vertical bars show the statistical precision of the samples. Published in Ref. [231].

predictions, which are based on an expansion series in the strong coupling constant, show excellent agreement with experimental measurements of $t\bar{t}$ production [96, 136, 272–284]. Nonetheless, certain kinematic regions require an all-order resummation of radiative corrections to achieve reliable perturbative predictions [285–292]. The PS simulation resums the large logarithmic corrections, including the soft and collinear QCD emissions to all orders in perturbation theory. The development of PS algorithms for NLO calculations has significantly improved the theoretical accuracy in describing the LHC data, surpassing the previously available LO calculations matched to PS simulations. Recent progress has also been made in combining NNLO calculations with PS MC generators [293–295]. However, $t\bar{t}$ production remains a challenge due to the presence of coloured particles in both the initial and final states at LO. The MiNNLO$_{PS}$ method [119–122] has been specifically developed to simulate $t\bar{t}$ production with NNLO+PS accuracy. Nevertheless, the event generation at NNLO is computationally more complex and expensive, requiring time to be integrated into the software frameworks of large LHC experiments, e.g. that of CMS. Moreover, the free parameters of the corresponding MC event generator need to be tuned, and the results have to be experimentally validated before large-scale simulations can be considered for use in physics analyses.

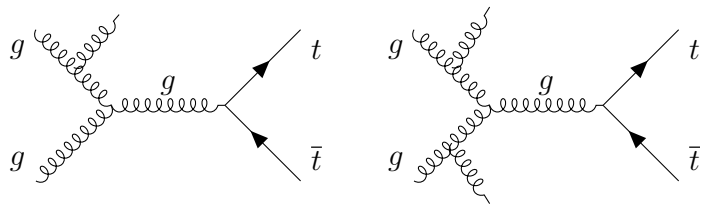

Figure 4.12: One of the most common Feynman diagram representations for $t\bar{t}$ production at NLO (left) and NNLO (right) accuracy produced with the HVQ and MiNNLO generators, respectively.

Meanwhile, corrections for NLO+PS simulations are obtained by comparing them to NNLO calculations using standard reweighting methods. These corrections are defined as a function of a single observable, such as p_{T} of the top quark. While these corrections improve the accuracy of NLO+PS simulations for individual distributions [296–298], they fail to account for the complex higher-order effects across the full phase space of $t\bar{t}$ production. In this thesis, a reweighting of NLO+PS simulations to NNLO+PS predictions with the DCTR method is presented. One of the most important Feynman diagrams of the two matrix-element MC generators at NLO and NNLO is shown in Figure 4.12. The NLO simulation generates a three-particle phase space (t, $\bar{\mathrm{t}}$, and one additional parton), while the NNLO simulation a four-particle phase space (t, $\bar{\mathrm{t}}$, and two additional partons). During training, information from the t and $\bar{\mathrm{t}}$ quarks and the combined $t\bar{t}$ system are used. The four-momenta of additional partons are not included as inputs to the NN, as the PFN architecture is not designed to reweight a 3D phase space to a 4D phase space. Consequently, only events based on the kinematics of the $t\bar{t}$ system can be reweighted, excluding the jets produced by the additional partons.

Dealing with negative event weights

In the POWHEG generator, the divergences of infrared singularities are handled by cancelling soft and collinear real emissions with the corresponding virtual corrections. This process results in a fraction of events with negative weights: around 1% at NLO accuracy and 10% at NNLO accuracy. The definition of the binary cross-entropy in Eq. (4.7) can become unbounded from below for negative event weights and makes the classification task potentially unsolvable [299]. In such cases, the loss function can diverge, particularly when the predicted probabilities are highly confident but incorrect.

For instance, if the true classification of an event is $y_i = 0$, but the model predicts $f(x_i) = 1$, then Eq. (4.7) becomes proportional to $-w_i^{\mathrm{MC}} \log(0) = +|w_i^{\mathrm{MC}}| \log(0) \to -\infty$. This unbounded growth can result in extreme values in the loss function, leading to numerical instability during the NN training and preventing the model from converging to a meaningful solution. One way to mitigate this issue is by using a large batch size, which helps prevent any single event from dominating the loss function. Such a strategy is effective for NLO simulations but encounters challenges when dealing with NNLO calculations, where the fraction of negative-weight events is ten times higher. In this case, a possible solution is to use the mean square error (MSE) as a loss function:

$$\mathrm{loss}(f(x)) = -\frac{1}{N} \sum_i^N w_i^{\mathrm{MC}} \left(f(x_i) - y_i\right)^2 . \tag{4.13}$$

Here, negative event weights still result in a reduction of the loss for wrongly classified events, but the total loss function is not unbounded anymore. As a result, the training is more stable even when considering negative events. Consequently, the MSE loss function has been used instead of the cross-entropy loss in the NLO-to-NNLO reweighting.

Training setup

In this thesis, for the first time, the DCTR method has been applied to reweight the NLO+PS to NNLO+PS calculations. For this task, 10 million $\mathrm{t\bar{t}}$ events at both NLO and NNLO were used, as obtained with the HVQ [112] and MiNNLO [121, 122] package, respectively. Both samples have been interfaced with PYTHIA 8 [129] for the PS. In this case, reweighting must be performed on showered events, as the showering process affects the two generators differently. The training data set is divided into 75% for training and 25% for validation. The event information after PS is used for the NN training. The input variables to the network include p_{T}, y, ϕ, m, PID of the t and $\bar{\mathrm{t}}$ just before decay, obtained from the last copy in the PYTHIA 8 event record, as well as of the $\mathrm{t\bar{t}}$ system. Finally, all input variables are normalised to have comparable magnitudes using the mean and standard deviation of their respective distributions. For p_{T}, the $\log_{10}(p_{\mathrm{T}}/1\,\mathrm{GeV})$ is used instead of p_{T}. In this case, a batch size of $2^{17} = 131072$ events was found to yield the best results.

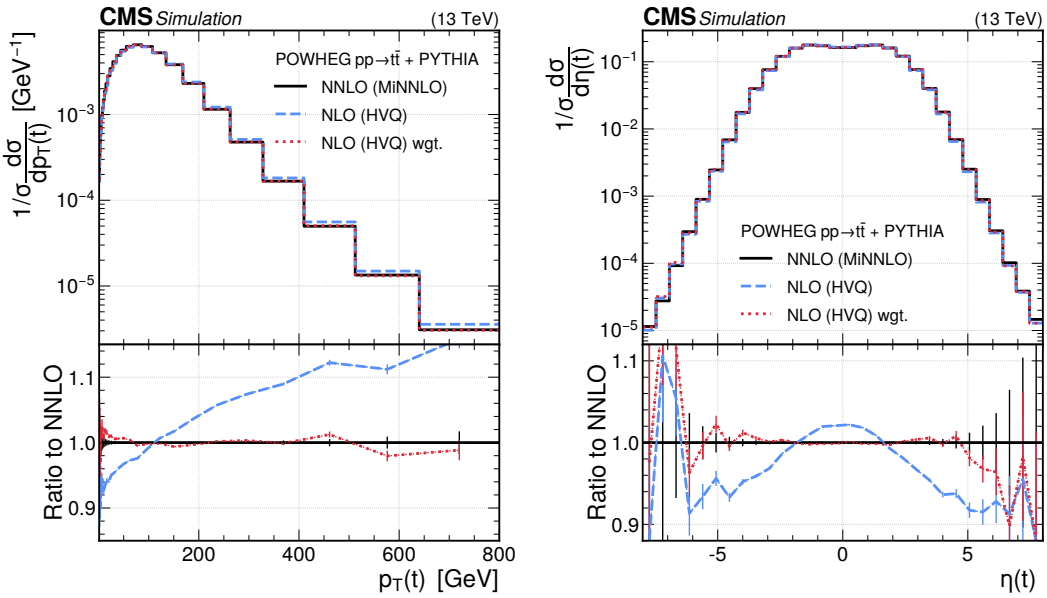

Figure 4.13: Distributions in top quark p_{T} (left) and η (right) obtained from simulations at NNLO accuracy (black solid lines), NLO accuracy (blue dashed lines), and NLO reweighted to NNLO with the DCTR method (red dotted lines). The ratio to the NNLO predictions is shown in the lower panels, where the vertical bars correspond to the statistical uncertainties. Published in Ref. [231].

Results

The accuracy of the NLO-to-NNLO reweighting is evaluated using independent samples with respect to the training ones. For both the NLO and NNLO simulations, 10 million events have been generated. Distributions of the kinematic properties of the t, $\bar{\mathrm{t}}$ and $\mathrm{t\bar{t}}$ system are examined. The distributions in $p_{\mathrm{T}}(\mathrm{t})$ and $\eta(\mathrm{t})$ are shown in Figure 4.13. Before the reweighting, the differences between the NLO and NNLO predictions are less than 10% at low p_{T} and grow to 15% at high p_{T}. The differences between the distributions in η vary from 2% in the central region to about 6% at $|\eta| = 5$. After the reweighting, good agreement is observed between the reweighted NLO sample and the NNLO one within the statistical uncertainties. The NLO, NNLO and NLO-to-NNLO distributions in $p_{\mathrm{T}}(\mathrm{t\bar{t}})$ and $\eta(\mathrm{t\bar{t}})$ are compared in Figure 4.14. While significant differences are observed between the NLO and NNLO predictions across all distributions, the NLO-to-NNLO reweighting is in good agreement with the NNLO predictions within the statistical uncertainties over the full kinematic range of the $\mathrm{t\bar{t}}$ system. It is worth noting that the reweighting method proves effective even for

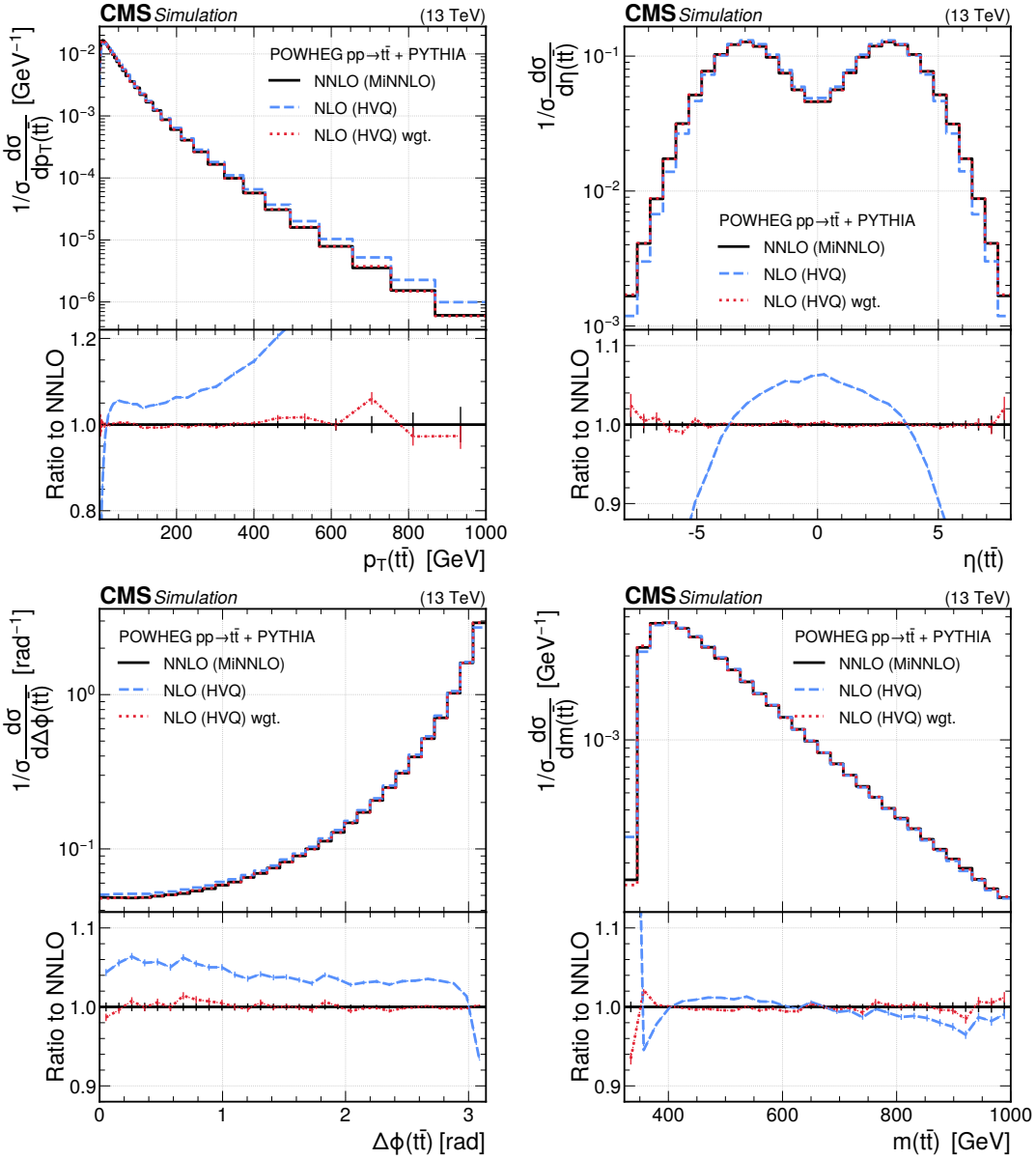

Figure 4.14: Distributions in p_{T} (upper left), η (upper right), $\Delta\phi$ (lower left), and mass (lower right) of the $\mathrm{t\bar{t}}$ system obtained from simulations at NNLO accuracy (black solid lines), NLO accuracy (blue dashed lines), and NLO reweighted to NNLO with the DCTR method (red dotted lines). The ratio to the NNLO predictions is shown in the lower panels, where the vertical bars correspond to the statistical uncertainties. Published in Ref. [231].

observables that were not included in the training, such as $\eta(\mathrm{t\bar{t}})$ or $\Delta\phi$ with the latter

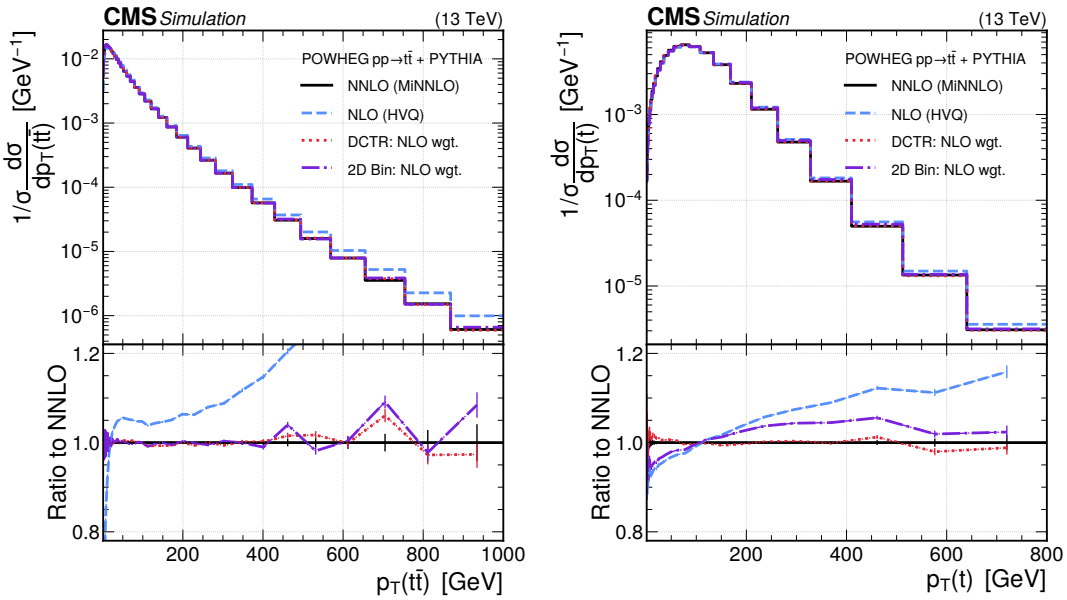

Figure 4.15: Distributions in p_{T} of the $\mathrm{t\bar{t}}$ system and p_{T} of the t obtained from simulations at NNLO accuracy (black solid lines), NLO accuracy (blue dashed lines), NLO reweighted to NNLO with the DCTR method (red dotted lines), and NLO reweighted to NNLO using a two-dimensional reweighting in p_{T} and η of the $\mathrm{t\bar{t}}$ system (violet dash-dotted line). The ratio to the NNLO predictions is shown in the lower panels, where the vertical bars correspond to the statistical uncertainties. Published in Ref. [231].

denoting the difference in azimuthal angle between the t and $\bar{\mathrm{t}}$. This is a consequence of the full phase-space reweighting.

In this scenario, the performance of the DCTR method has been compared to that of a standard two-dimensional (2D) reweighting. The 2D reweighting technique takes $p_{\mathrm{T}}(\mathrm{t\bar{t}})$ and $\eta(\mathrm{t\bar{t}})$ as inputs, with the ratio of NNLO to NLO predictions calculated for sufficiently large bins in these two observables to minimise statistical fluctuations. When considering the $p_{\mathrm{T}}(\mathrm{t\bar{t}})$ distribution, as shown in Figure 4.15 (left), the 2D reweighting works reasonably well over the full kinematic range, with the good closure of about 2%, similar to the DCTR method. However, the 2D reweighting is not as successful as DCTR concerning, e.g., $p_{\mathrm{T}}(\mathrm{t})$ distribution which is not included in the 2D reweighting. Although the 2D-reweighted simulation is closer to the NNLO prediction than the original NLO, there are still differences by up to 6%, as shown in Figure 4.15 (right). This is because the standard reweighting method is not a phase-space reweighting, but depends on the specific observables provided as inputs.

In contrast, the DCTR reweighting applied to the NLO sample accurately matches the NNLO prediction also for observables not included in the reweighting. Therefore, the DCTR NLO-to-NNLO reweighting can be used to correct the kinematics of the $t\bar{t}$ system for higher-order effects in the phase space of $t\bar{t}$ production. The ongoing studies of full NNLO+PS simulation, such as MiNNLO$_{\text{PS}}$, will be crucial for future analyses. Meanwhile, DCTR reweighting offers an intermediate solution until the MiNNLO$_{\text{PS}}$ will be tested and produced in very large samples including hadronisation effects, particle decays, and detector simulation.

4.6 Implementation in CMS software framework

As one of the results achieved in this thesis, the trained DCTR models are provided within the central CMS software framework (CMSSW), making them accessible to all CMSSW users. These models can be seamlessly integrated into physics analyses, enabling fast high-precision evaluation of systematic model uncertainties and the possible impact of higher-order corrections.

The NN models have been stored in the universal Open Neural Network Exchange (ONNX) format [300], an open-source framework designed to facilitate interoperability and portability across different deep learning tools and frameworks. Major frameworks like TensorFlow [253], PyTorch [301], and XGBoost [302] support conversion to and from the ONNX format, enabling seamless integration. The runtime of ONNX for inference with trained models is compatible with CMSSW for GPU-based inference. All the necessary ONNX libraries are already installed in the CMSSW software. The user must implement the following steps to apply the DCTR reweighting within the CMSSW software:

- Read the nominal sample, i.e. the sample to reweight
- Load the pre-trained ONNX model
- Read or compute the inputs based on the reweighting scenario
- Normalise the inputs based on the training and input them to the ONNX model
- Extract the resulting weights and apply them to the nominal sample to obtain the desired variation

An important aspect of this workflow is its flexibility in computing and applying weights at various stages of the analysis pipeline, including the parton, particle, or de-

tector level. In particular, in the latter scenario, the detector simulation is performed only once for the nominal sample. This significantly reduces the computational resource usage, as variations in h_{damp} and b quark fragmentation parameters are handled through reweighting alone. The results of this project are already being used in the CMS experiment. The method will become even more crucial in the HL-LHC, facilitating precision measurements and meeting sustainability requirements.

4.7 Conclusions and prospects

In this thesis, the DCTR method has been tested as a tool for reweighting MC samples used in CMS analyses, offering an elegant solution to address the computational challenges imposed by the production of large MC samples at the LHC. The h_{damp} scenario is an ideal example since CMS generates dedicated samples to address the corresponding systematic uncertainty. Generating one event in CMS requires 33 single-thread CPU-seconds. Based on the estimated number of simulated events for Run2 for the two dedicated h_{damp} samples ($\sim$1773M events, see Section 4.4.1), the DCTR method enables a reduction of 6.2×10^5 single-thread CPU-days. This estimate is based on the current CMS production of variation samples, which corresponds to 60% fewer events compared to the nominal sample. Further, the DCTR method allows for achieving the same statistical precision of the nominal MC samples without requiring additional CPU resources, thereby enhancing the accuracy of physics analyses. Looking ahead to the HL–LHC era, scaling the total number of events produced during Run2 to match the HL–LHC luminosity would result in a nominal $\mathrm{t\bar{t}}$ sample of approximately 45 billion events (to be increased by a factor of 3 considering plane production of variation samples), such that storage and processing is an issue. The DCTR method offers a promising solution to significantly reduce the number of required MC samples, making large-scale simulations more feasible while ensuring that variation samples achieve the same statistical precision as the nominal sample. The resulting CPU savings become increasingly substantial when the method is extended to include additional systematic variations, such as colour reconnection, underlying event, and hadronisation.

Full phase-space reweighting in DCTR is of a significant advantage with respect to currently used e.g. 1-D reweighting, and for the first time allows for using the NLO reweighted to NNLO simulation, which is yet not even available. Furthermore, the case of b-fragmentation demonstrates the applicability of continuous reweighting, paving

the way to MC tuning at the detector level.

In conclusion, the DCTR method facilitates precise measurements while addressing sustainability requirements. The method has shown strong performance across various scenarios, highlighting its potential for broader applications. It could be adapted for other systematic variations or even extended to different areas of physics beyond top quark studies. The results of this work have already been adopted by the CMS experiment for Run2 and Run3 data, and the method is set to become an integral component of the CMSSW software framework.

Chapter 5

Measurement of the top quark mass and width from $\mathrm{t\bar{t}} + \mathrm{tW}$ events

In this Chapter, the measurement of the differential $\mathrm{t\bar{t}}+\mathrm{tW}$ production cross section as a function of the invariant mass of the lepton and b quark from the top quark decay $m_{\ell \mathrm{b}}$ observable is presented. The measured cross section is used to extract the top quark mass employed in the MC generator, $m_{\mathrm{t}}^{\mathrm{MC}}$, and the top quark width Γ_{t}. The decays of the top quarks into leptons are considered. The pp collision data at the LHC at $\sqrt{s} = 13$ TeV are used. The data were collected by the CMS experiment in 2017-2018, corresponding to the integrated luminosity of 101 fb^{-1}. This Chapter is structured as follows. The theoretical predictions for the $\mathrm{t\bar{t}}+\mathrm{tW}$ process are presented in Section 5.1, and the analysis strategy is motivated and explained in Section 5.2. The data sets, the object and event selections and the MC simulations used in this analysis are discussed in Section 5.3. The relevant systematic uncertainties are described in Section 5.4. The measurement of the differential cross section at the particle level is presented in Section 5.5. Finally, the extraction of the top quark mass and width is discussed in Section 5.6.

5.1 Theoretical predictions for $\mathrm{t\bar{t}} + \mathrm{tW}$ process

The differential cross section for $\mathrm{t\bar{t}}$ production has been extensively measured and calculated over a broad kinematic range with high precision. However, most of the theoretical calculations and MC simulations used to unfold the measurements to the

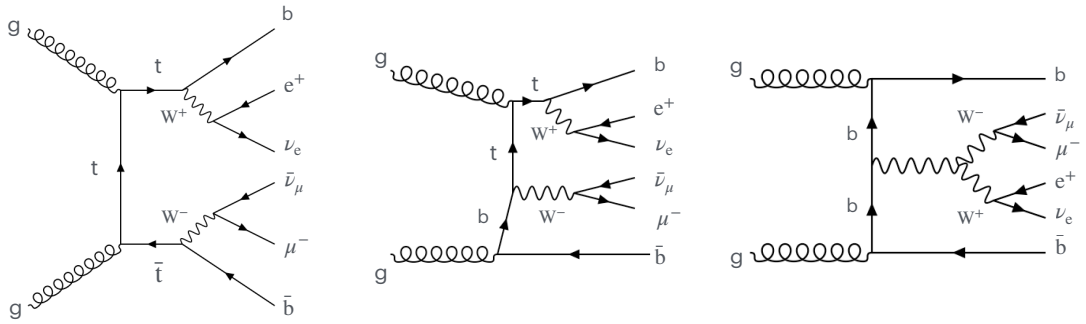

Figure 5.1: Double-, single-, and non-resonant Feynman diagrams representing the $pp \to b\bar{b}l^+l^-\nu\bar{\nu}$ final state.

parton level typically apply the narrow-width approximation for the decay of the top quark into a b quark and a W boson, treating single top-quark production in association with a W boson (tW) as a separate process. However, both processes share identical final states (WWbb) and interfere due to the presence of one or two time-like top-quark propagators, referred to as singly and doubly resonant contributions, respectively.

Conventional approaches for modelling tW and $\mathrm{t\bar{t}}$ interference [8–11] introduce significant uncertainties, which can impact both precision SM measurements and BSM searches. One approach for combining $\mathrm{t\bar{t}}$ and tW processes at NLO is the diagram removal (DR) scheme [8], where all doubly resonant amplitudes are removed from the tW sample. Alternative approaches, such as diagram subtraction (DS) [8], cancel these contributions using gauge-invariant subtraction terms, while the DR2 [9, 11] scheme includes them only in the interference terms. Typically, an uncertainty associated with the difference between the DR and DS schemes is considered, which can become a limiting factor in precision measurements of Γ_t.

A complete description of $\mathrm{t\bar{t}}$ production and decay beyond the narrow-width approximation requires calculating the full set of Feynman diagrams contributing to the WWbb final states, including the W boson decay products. Recent fixed-order calculations of the full NLO $pp \to b\bar{b}l^+l^-\nu\bar{\nu}$ process [303–306] properly account for the interference between $\mathrm{t\bar{t}}$ and tW production. The state-of-the-art predictions are pro-

vided by the bb4l [13, 14] generator, an NLO QCD generator matched to PS effects using Pythia 8 within the Powheg Box Res framework [307]. For the first time, the bb4l generator describes spin correlations and off-shell effects in top-quark decay chains using exact matrix elements for $pp \to b\bar{b}l^+l^-\nu\bar{\nu}$ at NLO QCD, where the leptons can be of different flavour and the b quarks are treated as massive. Consequently, contributions from both $t\bar{t}$ and tW production are fully accounted for along with their quantum interference. Furthermore, it includes non-resonant Feynman diagrams originating from topologies with fewer than two top or W propagators. The double-, single-, and non-resonant Feynman diagrams simulated by bb4l are illustrated in Figure 5.1.

The impact of doubly and singly resonant amplitudes, along with their interference, on the total cross section varies as a function of the $m_{\ell\mathrm{b}}$ observable, as defined in Eq. (2.15). Since there is an ambiguity in associating the correct b-jet to the corresponding lepton, the following convention can be adopted for $m_{\ell\mathrm{b}}$:

$$m_{\ell\mathrm{b}}^{\mathrm{minimax}} = \min(\max(m_{\mathrm{b}_1\ell_1}, m_{\mathrm{b}_2\ell_2}), \max(m_{\mathrm{b}_1\ell_2}, m_{\mathrm{b}_2\ell_1})), \tag{5.1}$$

where the labelling of leptons ℓ and b-jets b is arbitrary. This definition follows the *minimax* procedure employed to construct the transverse mass [308, 309] and measure the top mass [310]. The $m_{\ell\mathrm{b}}^{\mathrm{minimax}}$ observable exhibits a kinematic endpoint at $\sqrt{m_{\mathrm{t}}^2 - m_{\mathrm{W}}^2} \sim 150$ GeV sensitive to the value of m_{t}. For values of $m_{\ell\mathrm{b}}^{\mathrm{minimax}} > \sqrt{m_{\mathrm{t}}^2 - m_{\mathrm{W}}^2}$, the top quark pair process at LO contributes solely through off-shell effects, making tW contributions significant. In a recent ATLAS measurement [311], predictions from the bb4l generator for $pp \to b\bar{b}l^+l^-\nu\bar{\nu}$ are compared to data, alongside $t\bar{t}$+tW predictions using the DR and DS schemes. As shown in Figure 5.2, the tail of the $m_{\ell\mathrm{b}}^{\mathrm{minimax}}$ distribution exhibits sensitivity to interference effects, with bb4l predictions giving a better description of the data and bridging the gap between the DR and DS subtraction schemes for $t\bar{t}$ + tW process.

5.2 Analysis strategy

In this thesis, the differential cross section of $t\bar{t}$+tW production as a function of the $m_{\ell\mathrm{b}}^{\mathrm{minimax}}$ observable has been measured. The latter is sensitive to both m_{t} and Γ_{t}, which are also related to each other (see Eq. (2.13)). The extraction of $m_{\mathrm{t}}^{\mathrm{MC}}$ and Γ_{t} is performed by comparing bb4l predictions to data unfolded to the particle level.

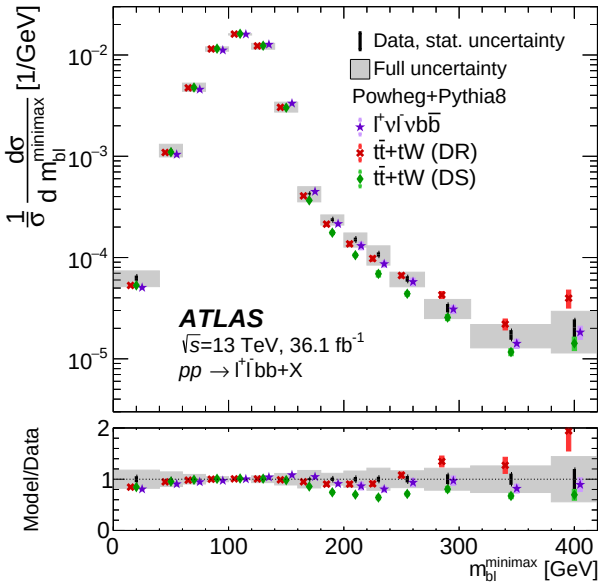

Figure 5.2: The unfolded normalised $m_{\ell\mathrm{b}}^{\mathrm{minimax}}$ distribution along with various MC predictions of the $\mathrm{t\bar{t}}$+tW signal. The uncertainty on the data includes both statistical and systematic sources, while uncertainties for each of the MC predictions comprise variations of μ_{r}, μ_{f}, and PDF set. The data are compared to predictions using the POWHEG+PYTHIA 8 setup with varying treatments of interference effects. Figure taken from Ref. [311].

The idea for such an analysis was introduced in Refs. [177, 178] by using the ATLAS measurement [311]. In the latter, the data were collected in 2016 at $\sqrt{s} = 13$ TeV corresponding to an integrated luminosity of 36.1 fb^{-1}. The simultaneous extraction of $m_{\mathrm{t}}^{\mathrm{MC}}$ and Γ_{t} reached an accuracy of 0.4% and 20%, respectively [178].

The work in this thesis considers WWbb events in pp collisions at the LHC at $\sqrt{s} = 13$ TeV. The data are collected by the CMS experiment and correspond to the integrated luminosity of 101 fb^{-1}, which is a factor 2.8 higher than the integrated luminosity of the ATLAS measurement [311]. Since the extraction of the top quark width is primarily limited by statistical uncertainty, the present measurement offers significant potential for improvement of precision in Γ_{t}. The present analysis, conducted for the first time within the CMS collaboration, is limited to the 2017-18 data-taking periods, as these are the most well-understood datasets from the Run2.

The measurement of the WWbb final state in the dilepton decay channel is performed,

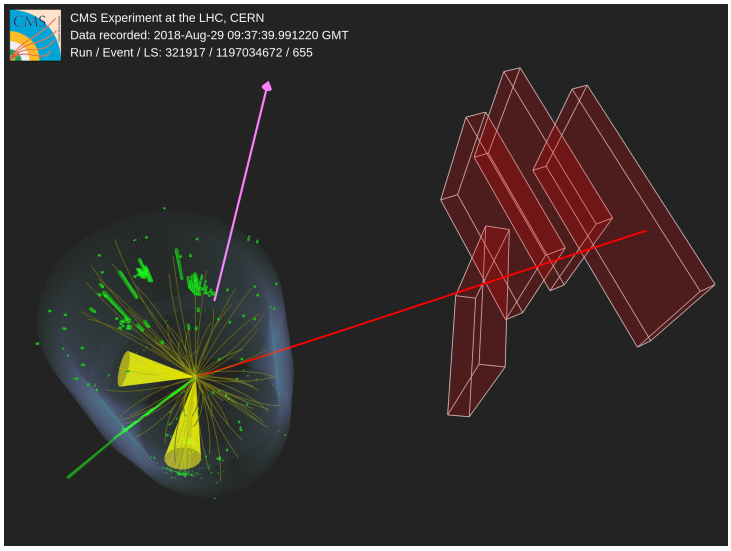

Figure 5.3: Display of one of the selected events in 2018 data-taking. The event comprises one electron (green) and one muon (red) of opposite charge, two b-jets (yellow), and missing transverse energy (violet). Figure taken from Ref. [312].

accounting for combinations of e^+e^-, $\mu^+\mu^-$, and $e^\pm\mu^\pm$. Additionally, events with leptonic W boson decays to τ leptons are treated as signal events if all tau leptons decay further to electrons or muons. The dileptonic final states are chosen because of their clean experimental signature, characterised by two isolated charged leptons (e^+e^-, $\mu^+\mu^-$, $e^\pm\mu^\pm$), two b-jets, and missing transverse energy. An event-display of one of the selected events, as seen by the CMS detector, is shown in Figure 5.3.

The differential cross section is measured within the visible phase space and subsequently extrapolated to the full phase space, as defined at the particle level through a profiled maximum likelihood unfolding method. The visible phase space of the measurement is determined by the geometric acceptance of the detector and the event selection criteria applied to the final-state objects. The absolute differential cross section of WWbb events at the particle level is normalised to the measured inclusive cross section in the corresponding kinematic range. As a result, global systematic uncertainties affecting the normalisation, e.g., uncertainties on the integrated luminosity, cancel out. Finally, the normalised differential cross section is compared to the bb4l predictions generated assuming different values of the top quark mass and width and m_t^{MC} and Γ_t are extracted (yet, individually).

In this thesis, the cross section measurement and extraction of $m_{\mathrm{t}}^{\mathrm{MC}}$ and Γ_{t} are performed using Asimov pseudo-data [313]. The latter is constructed from the expected values of the model under nominal assumptions without incorporating statistical fluctuations. Asimov pseudo-data is employed to evaluate the expected uncertainties in the parameters under investigation. The objective of this work is to assess the sensitivity of the measurement and to develop a robust analysis strategy that can be applied to real data according to the blinding policy of the CMS experiment, which currently reviews the measurement.

5.3 Data set, event selection, and MC simulation

During data taking, events are collected using combinations of dilepton and single-lepton trigger paths. In this analysis, the latter recovers approximately 10% of the dilepton events that would otherwise be excluded by dilepton triggers due to inefficiencies. Leptons must be reconstructed within the acceptance of the tracker to be triggered. The single-lepton trigger requires a muon (electron) with $p_{\mathrm{T}} > 24$ (27) GeV. For the dilepton triggers, the leading muon (electron) must have $p_{\mathrm{T}} > 17$ (23) GeV, while the subleading muon (electron) needs to satisfy $p_{\mathrm{T}} > 8$ (12) GeV. In the electron-muon channel, dilepton triggers require either a muon with $p_{\mathrm{T}} > 23$ GeV and an electron with $p_{\mathrm{T}} > 12$ GeV, or an electron with $p_{\mathrm{T}} > 23$ GeV and a muon with $p_{\mathrm{T}} > 8$ GeV. If an event is selected by the trigger, it must contain at least one well-reconstructed primary vertex (PV).

The events with at least two leptons, two or more jets, and exactly two b-jets are selected. The electron and muon candidates must satisfy the requirements $|\eta| < 2.4$ and $p_{\mathrm{T}} > 25$ (20) GeV for the leading (subleading) lepton. Furthermore, electron candidates within the range $1.4442 < |\eta| < 1.5660$ are excluded because of the poor performance of electron reconstruction in the transition region between the barrel and endcap calorimeters. In events with more than two leptons, the two leptons of opposite charge with the highest p_{T} are chosen.

To minimise the lepton misidentification probability, the selected leptons must also meet identification and isolation criteria. Muons have to pass sequential "tight" quality requirements as defined in Ref. [196], allowing the suppression of fake muons or

muons from in-flight decays and ensuring a selection of prompt muons with high purity. Electrons are identified through a multivariate technique [204], employing a boosted decision tree. Here, a single discriminant variable is built based on multiple input variables, providing separation between signal and background. A working point corresponding to an identification efficiency of approximately 80% has been used. Additionally, a relative lepton isolation variable, I_{rel}, is defined as the ratio of the scalar sum of the p_{T} of the neighbouring particle-flow candidates to the p_{T} of the lepton within a radius of $\Delta R < 0.4$ (0.3) for muons (electrons). For the muon case, $I_{\text{rel}} < 0.15$, whereas for electrons, this parameter is included in the multivariate analysis used for their identification. The event is then classified as e^+e^-, $\mu^+\mu^-$, or $\text{e}^\pm\mu^\pm$, according to the type of the selected lepton pair.

Jet candidates are reconstructed and calibrated as described in Section 3.3.2. In particular, jets are clustered using the anti-k_{T} algorithm with $R = 0.4$, and the PUPPI algorithm [209, 210] is employed for pileup mitigation. A set of "tight" identification criteria are applied to all jet candidates to suppress contributions of jets emerging from noise or reconstruction failures [314]. This approach also helps reduce the occurrence of jets reconstructed from misreconstructed leptons. Jets with $|\eta| < 2.4$, $p_{\text{T}} > 30$ GeV, and a distance $\Delta R > 0.4$ from every isolated lepton are considered in the analysis. The latter condition permits the exclusion of jets overlapping with fully selected leptons. Then, jets are b-tagged using the DeepJet tagger explained in Section 3.3.3. A high purity, i.e. tight working point, is used with a fixed light flavour mistagging rate of 0.1% and a b-tagging efficiency of 65% as determined in $\text{t}\bar{\text{t}}$ events [217].

Finally, the calculation of $p_{\text{T}}^{\text{miss}}$ is based on PF objects, where PUPPI is used for pileup mitigation. Background contributions from Z+jets production are reduced by removing events with $p_{\text{T}}^{\text{miss}} < 40$ GeV.

Once a lepton pair is selected in the event, additional conditions are imposed on the invariant mass of the lepton pair $m_{\ell\ell}$. The $m_{\ell\ell}$ is required to be greater than 20 GeV to suppress contributions from heavy-flavour resonance decay and low-mass Z+jets processes. Additionally, $m_{\ell\ell}$ is vetoed in the Z mass window of $76 < m_{\ell\ell} < 106$ GeV in the same-flavour lepton channels.

5.3.1 Signal definition

If all the above criteria are fulfilled, the event must contain at least two jets and exactly two b-jets and a pair of oppositely charged leptons ($\mathrm{e^+e^-}$, $\mathrm{e^\pm}\mu^\pm$, $\mathrm{e^\pm}\mu^\pm$) to be considered for the analysis. Finally, the invariant mass of the decay products is reconstructed using the $m_{\ell\mathrm{b}}^{\mathrm{minimax}}$ observable defined in Eq. (5.1).

The particle level object definitions, as defined in Refs. [315–317], are implemented:

- **Jets**: Clustering of stable particles using the anti-k_T algorithm ($R = 0.4$), excluding prompt leptons and neutrinos. The b-jets are identified by "ghost" particles and must satisfy the requirements $p_\mathrm{T} > 30$ GeV and $|\eta| < 2.4$
- **Leptons**: Dressed leptons are formed by clustering stable photons around prompt leptons within $\Delta R = 0.1$. They must fulfill the conditions $p_\mathrm{T} > 25\ (20)$ GeV and $|\eta| < 2.4$
- **Invariant mass of the two leptons:** Same cuts as applied at the detector level
- **Signal:** Events which contain exactly two leptons, two jets and two b-jets

The following binning is used in this analysis:

$$m_{\ell\mathrm{b}}^{\mathrm{minimax}} \in [0, 40, 60, 80, 100, 120, 140, 160, 180, 220, 270, \infty] \text{ GeV} \tag{5.2}$$

One additional bin (*Bin0*) is considered for out-of-acceptance signal events. The same binning is also applied at the detector level.

5.3.2 MC simulation

Different MC event generators are used to simulate the hard scattering in the signal and background processes. The $\mathrm{t\bar{t}}$+tW signal is simulated with the bb4l [13,14] generator, where the contributions of W bosons decaying leptonically in the same channels are included [318]. Background events originate dominantly from Drell-Yan events containing a pair of electrons or muons with additional jets (Z+jets) and $\mathrm{t\bar{t}}$ decay channels other than dilepton. Smaller contributions come from W boson production with additional jets (W+jets), $\mathrm{t\bar{t}}$ production in association with a boson (ttW, ttZ, ttH) and diboson production (WW, ZZ, WZ). Finally, a minor background arises from single top quark production in the s-channel and inclusive single top production in the t-channel, which are not included in the bb4l sample. Most of the background

contributions are suppressed by requirements on the isolation of the leptons, the dilepton invariant mass, the missing energy and the number of b-jets in the event. In the plots and tables presented in this thesis, the backgrounds are categorised into three main groups: *Z+jets*, non-dileptonic $\mathrm{t\bar{t}}$ referred to as *$t\bar{t}$ bkg*, and all remaining contributions grouped under *Other*.

The Z+jets and W+jets processes are generated using MG5_AMC@NLO [114] at NLO with up to two additional partons at the ME level. The $\mathrm{t\bar{t}}$ background processes are simulated using the HVQ [112] program of POWHEG v2 [110, 113] at NLO in QCD. The single top quark simulation is performed similarly using HVQ POWHEG v2 for the $t-$channel process, while MG5_AMC@NLO is employed for the $s-$channel process. Samples for associated $\mathrm{t\bar{t}}$ production with Z and W bosons are simulated using MG5_AMC@NLO, while the ttH simulation is performed with HVQ POWHEG v2. Finally, diboson production is simulated with PYTHIA 8 [129].

In the MC generators used for the signal and background predictions, the proton structure is described by the PDF set NNPDF3.1 [319, 320] at NNLO. In POWHEG simulations, the value of the top quark mass is set to $m_{\mathrm{t}}^{\mathrm{MC}} = 172.5\,\mathrm{GeV}$, and the h_{damp} parameter is set to $1.379\,m_{\mathrm{t}}$ [256]. Parton showering and hadronisation are simulated with PYTHIA 8 in all simulated samples, where the underlying event is modelled by the CP5 tune [256]. All predictions are normalised to their theoretical cross section and the corresponding integrated luminosity of the data. The $\mathrm{t\bar{t}}+\mathrm{tW}$ cross section is set to 89.4 pb, corresponding to the $\mathrm{t\bar{t}}$ dileptonic cross section taken from Ref. [321], where it is computed at NNLO with next-to-next-to-leading logarithmic soft-gluon resummation. In the near future, this value will be replaced with the predicted $\mathrm{t\bar{t}}+\mathrm{tW}$ cross section provided by the theorists, which is currently not publicly available. Similarly, the $\mathrm{t\bar{t}}$ background cross section is taken from Ref. [321]. The cross sections for Z+jets and W+jets events used in this thesis are obtained from NLO calculations, while those for diboson production are based on LO calculations.

In all simulated samples, the interaction of the final-state particles with the CMS detector material is modelled using the GEANT4 package [133]. To account for the effects of pileup, additional minimum-bias interactions are included in the simulated events.

5.3.3 Corrections to simulated events

Discrepancies between data and simulated samples can arise due to deficiencies in the event generation/simulation, or detector inefficiencies. To address this issue, various corrections are applied to the simulated samples to improve their agreement with the data. These data-to-MC corrections are typically implemented as event weights, referred to in the following as scale factors (SF). Corrections for efficiency, energy scale, and energy resolution are applied through SFs.

The number of pileup vertices in the simulated events is corrected through event weights to match the one in the data, which is determined from the measured instantaneous luminosity and assuming a total inelastic pp cross section of 69.2 mb [322]. Dedicated trigger SFs are derived as a function of the lepton p_{T} to account for the differences in the efficiency of the trigger selection between data and simulation and applied to the simulated samples. The efficiency for a lepton to pass identification, isolation or reconstruction requirements in simulation is corrected to match the one observed in data. This calibration is performed throug data-to-MC comparison using $Z \to ll$ events, as determined in Refs. [196, 204, 323–325]. These corrections treat the various effects as uncorrelated, and individual efficiencies and SFs for electrons and muons are derived. Additionally, lepton energy-scale and resolution corrections are adopted [204, 326–329]. Similarly, JES and JER corrections are applied as described in Section 3.3.2.

The b-tagging efficiency in simulation is adjusted to be as in the data using flavour-dependent data-to-MC corrections measured as a function of the jet p_{T}. The b-tagging SFs are obtained centrally in the CMS collaboration using data from QCD-enriched regions and dedicated simulated samples [214]. The b-jet multiplicity in simulation is corrected by using event weights defined as the ratio of the probability in data (P_{data}) to the probability in MC (P_{MC}) for a fixed chosen working point. These two quantities can be computed as:

$$P_{\mathrm{MC}} = \prod_{f}^{flavours} \prod_{i}^{tagged} \varepsilon_i^f(p_{\mathrm{T}}) \prod_{j}^{untagged} (1 - \varepsilon_j^f(p_{\mathrm{T}})), \tag{5.3}$$

$$P_{\mathrm{data}} = \prod_{f}^{flavours} \prod_{i}^{tagged} \mathrm{SF}_i^f(p_{\mathrm{T}})\, \varepsilon_i^f(p_{\mathrm{T}}) \prod_{j}^{untagged} (1 - \mathrm{SF}_j^f(p_{\mathrm{T}})\, \varepsilon_j^f(p_{\mathrm{T}})), \tag{5.4}$$

where ε_i^f and SF_i^f represent the b-tagging efficiency and SF in MC for the jet i with a flavour f, dependent on its p_T. The final event weight $P_\mathrm{data}/P_\mathrm{MC}$ is applied to the simulation.

In 2016 and 2017, a timing shift of the ECAL (in the $2 < |\eta| < 3$ region) was not properly propagated to the L1 trigger, causing a significant fraction of triggers to be incorrectly assigned to the previous bunch crossing. Since L1 forbids firing of two consecutive bunch crossings, events can self-veto. This issue is known as *L1 ECAL prefiring*. This effect is not modelled in the simulation, and it is accounted for by applying event weights [197, 330].

5.3.4 Data and MC compatibility

	$\ell\ell$, $N_{\text{b-jet}} = 2$, $N_{\text{jet}} \geq 2$	ee, $N_{\text{b-jet}} = 2$, $N_{\text{jet}} \geq 2$	$e\mu$, $N_{\text{b-jet}} = 2$, $N_{\text{jet}} \geq 2$	$\mu\mu$, $N_{\text{b-jet}} = 2$, $N_{\text{jet}} \geq 2$
$t\bar{t}+tW$ (bb4l) Bin0	5231.88 ± 20.38	830.85 ± 7.77	3152.96 ± 15.92	1248.07 ± 10.08
$t\bar{t}+tW$ (bb4l) Bin1	165.36 ± 3.42	27.02 ± 1.32	96.97 ± 2.63	41.37 ± 1.73
$t\bar{t}+tW$ (bb4l) Bin2	2538.61 ± 14.61	360.33 ± 5.38	1549.29 ± 11.45	628.99 ± 7.30
$t\bar{t}+tW$ (bb4l) Bin3	11901.41 ± 31.52	1637.59 ± 11.21	7310.88 ± 24.64	2952.94 ± 16.14
$t\bar{t}+tW$ (bb4l) Bin4	31497.03 ± 52.53	4433.63 ± 19.17	19209.24 ± 40.44	7854.16 ± 27.50
$t\bar{t}+tW$ (bb4l) Bin5	51621.99 ± 67.86	7317.45 ± 24.68	31504.83 ± 52.39	12799.71 ± 35.38
$t\bar{t}+tW$ (bb4l) Bin6	50168.26 ± 69.33	7144.73 ± 23.98	30741.49 ± 53.93	12282.04 ± 36.39
$t\bar{t}+tW$ (bb4l) Bin7	15471.68 ± 36.60	2208.61 ± 13.03	9527.76 ± 28.84	3735.32 ± 18.39
$t\bar{t}+tW$ (bb4l) Bin8	1691.86 ± 11.77	251.51 ± 4.22	1014.85 ± 9.10	425.50 ± 6.15
$t\bar{t}+tW$ (bb4l) Bin9	834.96 ± 7.95	125.29 ± 2.97	494.34 ± 6.13	215.33 ± 4.10
$t\bar{t}+tW$ (bb4l) Bin10	789.34 ± 7.56	128.27 ± 2.91	455.08 ± 5.76	206.00 ± 3.94
$t\bar{t}+tW$ (bb4l) Bin11	845.96 ± 8.55	138.37 ± 3.38	471.80 ± 6.19	235.80 ± 4.82
$t\bar{t}+tW$ (bb4l) Bin9	546.56 ± 6.35	85.39 ± 2.47	323.46 ± 4.80	137.71 ± 3.33
$t\bar{t}$ (not dileptonic)	449.80 ± 4.12	49.42 ± 1.32	285.74 ± 3.27	114.64 ± 2.13
Z+jets	765.27 ± 66.75	221.74 ± 31.97	79.83 ± 11.88	463.69 ± 57.34
Other	1107.23 ± 6.42	175.64 ± 1.81	637.05 ± 5.60	294.53 ± 2.56
Total ± (stat)	175627.22 ± 141.53	25135.82 ± 54.93	106855.57 ± 97.56	43635.80 ± 86.55
Data	178338	25350	108517	44471
Data / Predictions	1.02 ± 0.01	1.01 ± 0.01	1.02 ± 0.01	1.02 ± 0.01

Table 5.1: Event yields for the signal and background predictions, as well as for the data. The results are shown for each decay channel separately as well as the combined one. In the last line of the table, the ratio between data and predictions is given.

The distributions of the p_T and η for the selected leptons and b-jets, after event selection, are displayed in Figures 5.4 and 5.5 for both data and simulated events. Additionally, Figure 5.5 also includes the jet multiplicity and b-jet multiplicity distributions. The results for the combined 2017 and 2018 datasets are presented. Further control distributions are also included in Appendix A.1 for completeness. Overall, data and simulation agree within systematic uncertainties. The discrepancy between

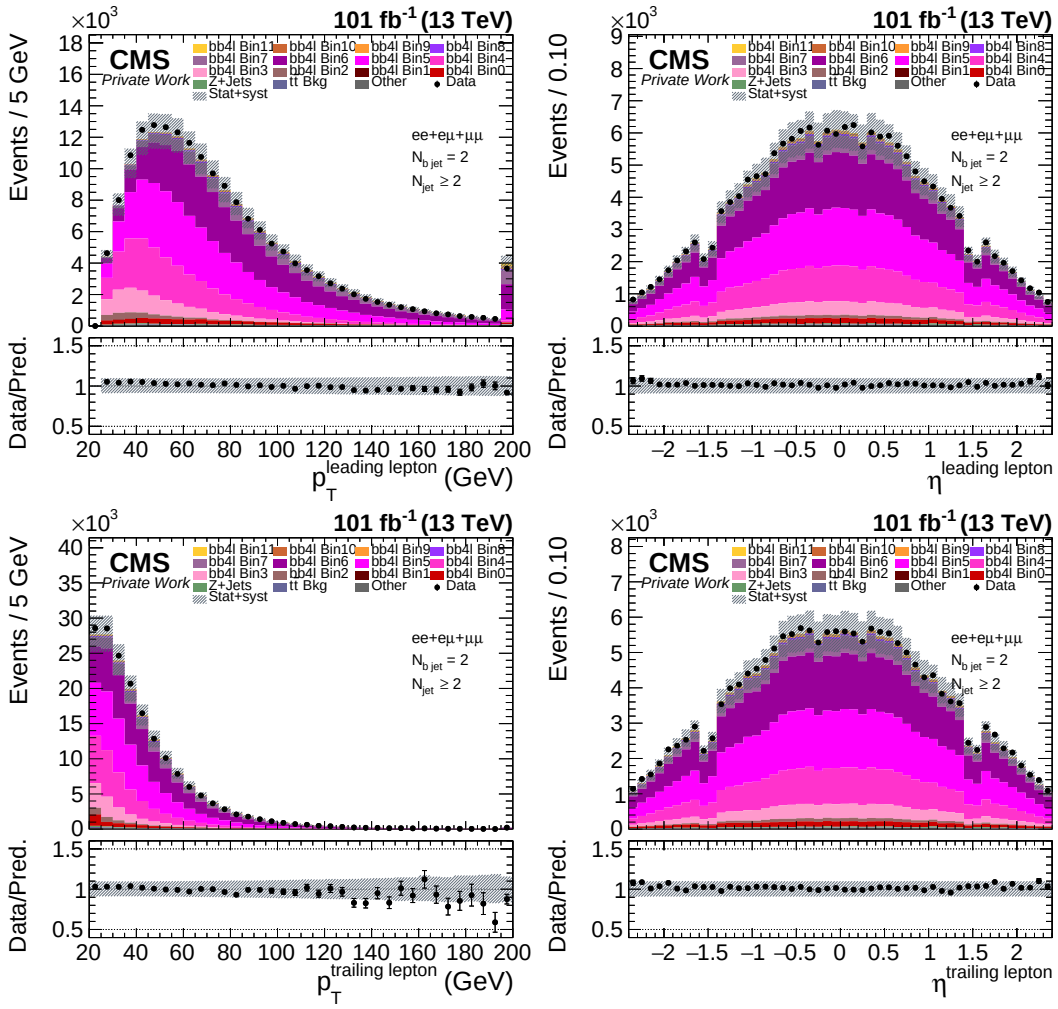

Figure 5.4: Distributions of p_{T} (left) and η (right) of the leading (upper) and subleading (lower) leptons, comparing data (points) with predictions for the signal and various backgrounds (shaded histograms) from simulation. The lower panel of each figure shows the ratio of the data to the sum of the signal and background predictions, where the vertical bars correspond to the statistical uncertainties of the data and the hatched bands represent the combined statistical and systematic uncertainty in the MC predictions.

data and MC predictions in the b-jet multiplicity for $n_{Bjets} > 3$ is expected from the bb4l predictions in this phase-space region and arises from a partially missing contribution of the $q\bar{q}$ splitting from top quarks into heavy-flavour quarks. However, this has no impact on the present analysis since exactly two b-jets are required for this study.

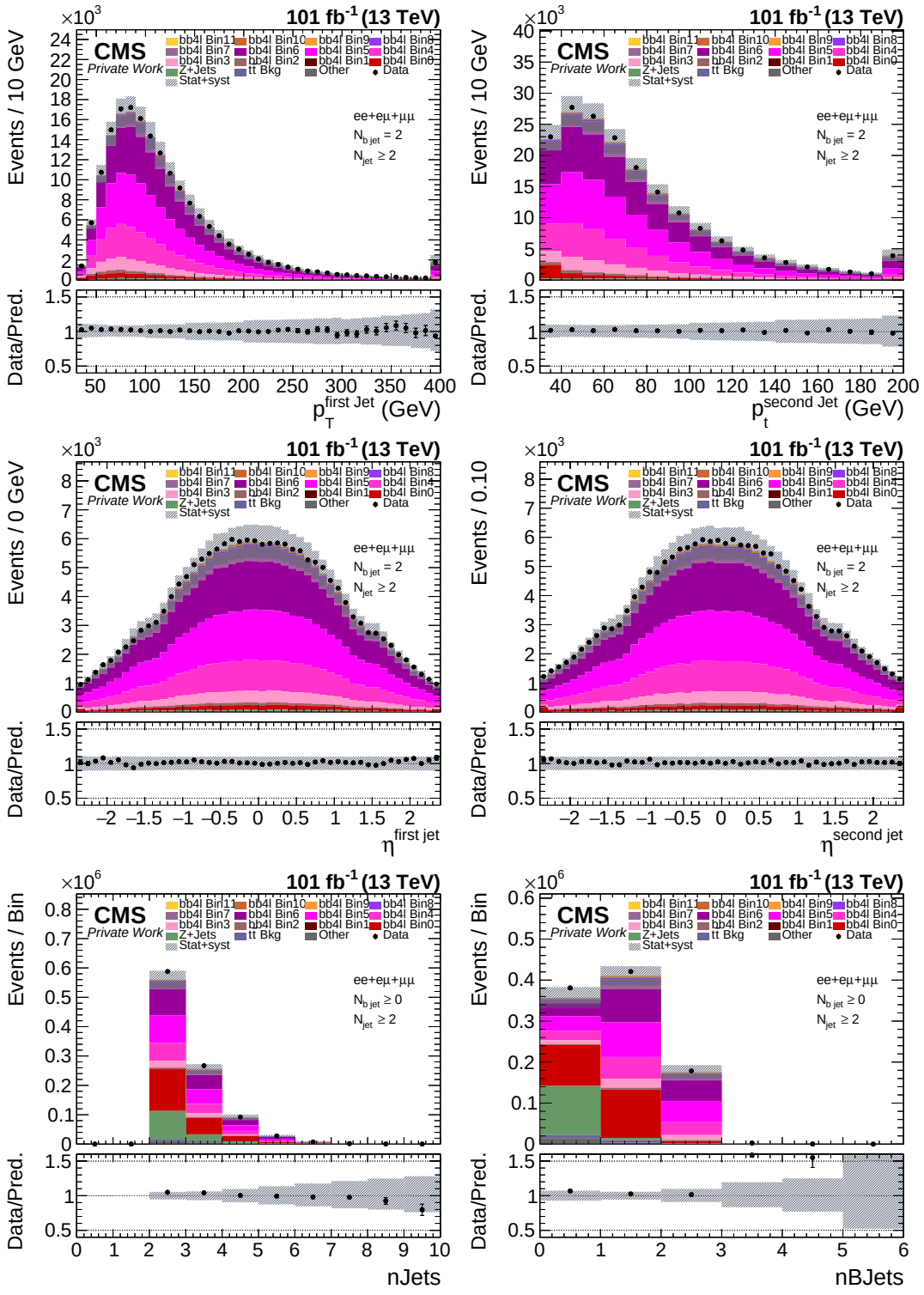

Figure 5.5: Same as Figure 5.4 for the leading (upper row) and trailing (middle row) jets. Additionally, the jet (lower left) and b-jet (lower right) multiplicity distributions are shown.

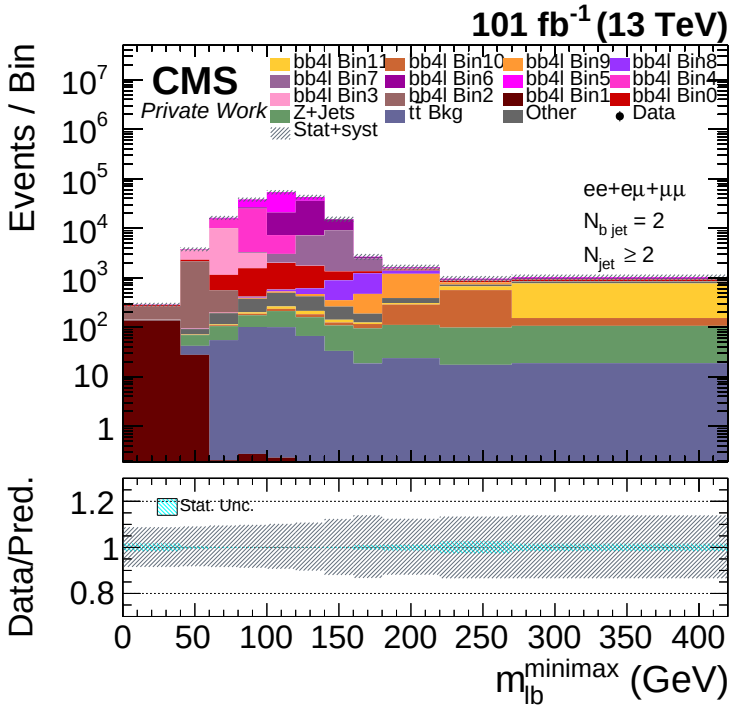

Figure 5.6: The distribution of the $m_{\ell \mathrm{b}}^{\mathrm{minimax}}$ observable for the predictions of the signal and various backgrounds. The hatched bands correspond to the combined statistical and systematic uncertainty in the MC predictions. The lower panel of each figure shows the relative total uncertainty of the predictions, with the hatched light blue band indicating the statistical uncertainty in the simulation.

The agreement is quantified in Table 5.1, which provides a summary of the event yields for the signal and background predictions, as well as for the data. The results are reported for each decay channel separately as well as the combined one. Finally, the observable $m_{\ell \mathrm{b}}^{\mathrm{minimax}}$ is illustrated in Figure 5.6, where the data are not shown due to the CMS blinding procedure. In the blinding procedure, data in the sensitive observable are intentionally hidden to prevent bias in the analysis. Unblinding occurs once the analysis strategy is finalised, allowing the data to be revealed for comparison with predictions.

5.4 Systematic uncertainties

The systematic uncertainties considered in this analysis are categorised into three main groups: experimental uncertainties stemming from the calibration of the final-

state objects, modelling uncertainties associated with assumptions made in the MC simulations, and background normalisation uncertainties. Some uncertainties affect only the normalisation of the MC templates and are evaluated by scaling the entire contribution up or down. These are referred to as *rate* uncertainties. On the other hand, *shape* uncertainties affect the shape of the distributions and are addressed by using alternative MC templates with varied shapes. The various sources of uncertainty and the methods used to evaluate them are outlined below. Table 5.2 provides details on the processes affected by each uncertainty, specifying whether they are considered correlated or uncorrelated across processes. Additionally, it indicates whether each uncertainty is treated as correlated or uncorrelated across data-taking periods (referred to as "years").

Experimental uncertainties

Dedicated measurements are used to derive data-to-simulation SFs for the calibration of final-state objects. The uncertainties associated with these SFs propagate to the total uncertainty in the measured $d\sigma_{\mathrm{t\bar{t}+tW}}/dm_{\ell\mathrm{b}}^{\mathrm{minimax}}$ and, hence, to $m_{\mathrm{t}}^{\mathrm{MC}}$ and Γ_{t}. To estimate the impact of these uncertainties, the event selection is repeated with the SFs varied by $\pm 1\sigma$.

The uncertainty in the JES calibration is split into 24 individual sources [331]. The impact of these uncertainties is assessed by varying the momentum of each reconstructed jet within uncertainties, as a function of jet p_{T} and η. Similarly, the JER uncertainties are assessed across two distinct η regions. Further, uncertainties in the energy scale and resolution are applied to the leptons. The uncertainty associated with unclustered missing energy is determined by propagating the uncertainties of the individual components that contribute to $\vec{p}_T^{\,\mathrm{miss}}$. Finally, an uncertainty related to the L1 prefiring issue is applied to the 2017 year. The SFs are varied according to their uncertainties, shifting the prefiring probabilities by $\pm 1\sigma$.

The uncertainty in the integrated luminosity affects both the signal and background normalisation and is measured to be 2.3% and 2.5% for 2017 and 2018, respectively [332, 333]. The normalisation of the predictions is also affected by the lepton identification and isolation SFs. To assess the corresponding systematic uncertainty, these SFs are varied within their uncertainties in the simulation for each lepton flavour

(electron or muon) and category (identification, isolation, or reconstruction). Since the SF are derived using $Z \to ll$ events, a 0.5% (1%) uncertainty per muon (electron) candidate is added to account for the extrapolation from the Drell–Yan to $t\bar{t}$ phase space. Another source of uncertainty is related to the trigger efficiency, where the derived SFs are varied within their uncertainties. The trigger efficiencies and their uncertainty are shown in Figures A.2 and A.3 in Appendix A.2. Finally, the uncertainties associated with the b-tagging calibration are evaluated by independently varying the b-jet and light jet SFs within their uncertainties. Uncertainties related to heavy flavour (c and b) jets are treated as fully correlated, whereas light and gluon jets uncertainties are assumed to be uncorrelated with b-jets. Further, the uncertainties are split into correlated and uncorrelated parts across the data-taking periods.

Modelling uncertainties

Modelling uncertainties are evaluated based on their source, either by varying MC parameters within the same simulation program or by comparing the default simulation to different models.

The impact of higher-order effects in the ME simulation is estimated by varying μ_r and μ_f scales in the signal, Z+jets, and $t\bar{t}$ background samples. The scales are varied independently by a factor of two up and down [334,335], avoiding cases with $\mu_f/\mu_r = 4$ or 1/4. Similarly, uncertainties in the modelling of the PS are assessed by varying the initial-state radiation (ISR) and the final-state radiation (FSR) scales by a factor of two up and down with respect to their nominal values. This uncertainty is applied only to the signal and $t\bar{t}$ background samples. The uncertainty related to the PDFs is estimated by reweighting the signal and $t\bar{t}$ background samples to the 100 Hessian eigenvector variations in the NNPDF3.1 PDF set. Additionally, the value of $\alpha_S(m_Z)$ is varied within its uncertainty in the PDF set. An uncertainty related to the matching of the ME to PS is evaluated by varying the h_{damp} parameter of POWHEG up and down from its nominal value ($h_{damp} = 1.379^{+0.926}_{-0.5052} m_t$). The ML reweighting method, described in Chapter 4, has been employed. However, this approach was trained on the POWHEG HVQ generator of $t\bar{t}$ production. As a result, it is applied exclusively to $t\bar{t}$ events, with the assumption that its effect on bb4l and HVQ generator is similar. The resulting uncertainty is applied only to the signal and $t\bar{t}$ background samples. Since it is not possible to split the contribution of $t\bar{t}$ and tW in bb4l, dedicated ML

retraining needs to be performed in the future. However, applying the DCTR method is non-trivial, as bb4l is a novel approach, and ongoing studies are being conducted in collaboration with the authors. The fragmentation of a b quark into b hadrons is modelled by the Bowler-Lund function in the nominal CP5 tune of PYTHIA 8 used for $\mathrm{t\bar{t}}$ and single top simulations. The nominal value of the Bowler-Lund parameter is set to 1.056 with variations of $^{+0.196}_{-0.200}$. The corresponding uncertainty is evaluated by a 1D standard reweighting of the relevant transfer function in the signal and $\mathrm{t\bar{t}}$ background samples. In this case, the ML reweighting cannot be performed yet since the information related to the b hadron needed to reconstruct x_{b} is not saved in the bb4l sample. Although this uncertainty is accounted for in the data-to-simulation comparisons, it has not yet been incorporated into the fit, as it will be updated once the ML reweighting can be implemented. Finally, an uncertainty associated with the modelling of the number of pileup interactions is derived by varying the minimum bias cross section by $\pm 4.6\%$ [322].

Owing to the recent large-scale production of bb4l MC samples within CMS, certain dedicated samples required for estimating systematic uncertainties are not yet available. Specifically, the following sources of uncertainties are currently missing for the bb4l samples: underlying event tune, colour reconnection, and b hadron branching fraction. The bb4l is a novel approach introduced in CMS for the first time, and its investigation remains an active area of ongoing and future research. For the sake of completeness, the methods used to compute these uncertainties are outlined below. The uncertainty associated with the UE tuning is assessed by varying the tuning parameters within their uncertainties [123]. In the default CR model implemented in PYTHIA 8 and used for the reference simulations, early resonance decays (ERD) are disabled. To assess the CR uncertainty, additional dedicated samples are generated with ERD enabled, and the resulting difference is treated as a systematic uncertainty. Similarly, an uncertainty derived from the difference of the nominal sample with two alternative CR models is considered: the gluon-move scheme [126] and a QCD-inspired scheme [127]. Another source of uncertainty is related to the assumed b hadron branching fraction, which can affect the momentum of the reconstructed b-jets. This uncertainty can be assessed by varying its value within their uncertainties, as estimated in Ref. [6]. Finally, an empirical uncertainty is introduced based on differential measurements of the $\mathrm{t\bar{t}}$ cross section at $\sqrt{s} = 13$ TeV, which have shown that the $p_{\mathrm{T}}(\mathrm{t})$ spectrum is softer than predicted by the POWHEG sim-

ulation [96, 273, 275, 336]. This uncertainty should be estimated by reweighting the simulation to match the data [272,336–338], but it is a subject of ongoing investigation.

Background normalisation uncertainties

The uncertainties in background normalisation, stemming from the uncertainties in the cross sections of corresponding background processes, are conservatively estimated as follows: $^{+4.20\%}_{-4.84\%}$ for the $\mathrm{t\bar{t}}$ background [321], and 30% for the Z+jets and other backgrounds, respectively.

Other systematic uncertainties

The limited size of the MC simulated samples introduces statistical fluctuations in the templates. This is accounted for using bin-by-bin nuisance parameters with the Barlow-Beeston-lite method [339, 340].

5.5 Unfolding and cross section measurement

The differential cross section, $d\sigma_{\mathrm{t\bar{t}+tW}}/dm_{\ell\mathrm{b}}^{\mathrm{minimax}}$, is measured by means of a maximum likelihood unfolding of multi-differential distributions, following the method of Refs. [321,341]. In order to measure the $\mathrm{t\bar{t}}+\mathrm{tW}$ cross section differentially, the $\mathrm{t\bar{t}}+\mathrm{tW}$ simulation is split into bins of $m_{\ell\mathrm{b}}^{\mathrm{minimax}}$ at the generator level, and each sub-sample is treated as an independent signal process in the likelihood fit while preserving the correlation between the systematic uncertainties. The goal of unfolding is the conclusion on the original distribution corrected for experimental effects, such as resolution, misreconstruction, inefficiencies, and detector acceptance. Unlike other unfolding methods, the maximum likelihood approach allows systematic uncertainties to be constrained together with the parameters of interest by treating them as nuisance parameters (NPs). As a result, any discrepancy between the data and the prior assumptions is corrected by adjusting the central values of the NPs (pulls). If the uncertainty of an NP is determined to be smaller after the fit than initially assumed, the width of its probability distribution is correspondingly reduced (constrained).

The likelihood function $\mathcal{L}$ is based on the assumption that the number of observed

Uncertainty	**Type**	**Process**	**Year**	**Proc. corr.**	**Year corr.**
Luminosity	rate	all	all	yes	partial
$\sigma_{t\bar{t}+tW}$	rate	signal	all	-	yes
σ_{Z+jets}	rate	Z+jets	all	-	yes
$\sigma_{t\bar{t}(non\ dileptonic)}$	rate	$t\bar{t}$ bkg	all	-	yes
σ_{others}	rate	others	all	-	yes
μ_R	shape	signal, $t\bar{t}$ bkg, Z+jets	all	partial	yes
μ_F	shape	signal, $t\bar{t}$ bkg, Z+jets	all	partial	yes
ISR	shape	signal, $t\bar{t}$ bkg	all	yes	yes
FSR	shape	signal, $t\bar{t}$ bkg	all	yes	yes
PDF	shape	signal, $t\bar{t}$ bkg	all	yes	yes
PDF α_s	shape	signal, $t\bar{t}$ bkg	all	yes	yes
h_{damp}	shape	signal, $t\bar{t}$ bkg	all	yes	yes
b fragmentation	shape	signal, $t\bar{t}$ bkg	all	yes	yes
Electron Reco	shape+rate	all	all	yes	yes
Electron ID	shape+rate	all	all	yes	yes
Muon ID	shape+rate	all	all	yes	partial
Muon Isolation	shape+rate	all	all	yes	partial
Muon Scale	shape+rate	all	all	yes	partial
Electron Scale	shape+rate	all	all	yes	yes
Electron Smear	shape+rate	all	all	yes	yes
L1prefire	shape+rate	all	2017	yes	yes
Pileup	shape+rate	all	all	yes	yes
b tagging	shape+rate	all	all	yes	partial
JER	shape+rate	all	all	yes	no
JES	shape+rate	all	all	yes	partial
Unclustered MET	shape+rate	all	all	yes	no
Trigger SFs	shape+rate	all	all	yes	no

Table 5.2: Summary of systematic uncertainties considered in the analysis. The type of uncertainty is labelled as being "rate" (constant normalisation factor) or "shape" (variations that change the shape of the distribution). The processes affected by each uncertainty are listed. The correlations of the systematic uncertainties among processes and years are also reported.

events in each bin follows a Poisson distribution and is expressed as:

$$\mathcal{L} = \prod_i \frac{e^{-v_i} v_i^{n_i}}{n_i!} \prod_m \pi(\lambda_m) \prod_j \pi(w_j), \tag{5.5}$$

where i denotes the index of the bin in the final-state distribution, and v_i and n_i are the expected and observed number of events in bin i, respectively. The terms $\pi(\lambda_m)$ and $\pi(w_j)$ are priors for the nuisance (λ_m) and normalisation (w_j) parameters,

respectively. The expected number of events v_i can be expressed as:

$$v_i = \sum_k s_i^k(\sigma^k_{\mathrm{t\bar{t}}+\mathrm{tW}}, \vec{\lambda}, m_\mathrm{t}^\mathrm{MC}) + \sum_j b_i^j(w_j, \vec{\lambda}, m_\mathrm{t}^\mathrm{MC}), \tag{5.6}$$

where s_i^k denotes the number of expected $\mathrm{t\bar{t}}+\mathrm{tW}$ signal events from the k-th generator-level bin for a reconstructed $m_{\ell\mathrm{b}}^{\mathrm{minimax}}$ value in bin i. The value of s_i^k depends on the total cross section in the k-th bin $\sigma^k_{\mathrm{t\bar{t}}+\mathrm{tW}}$, $\vec{\lambda}$ and m_t^MC. Similarly, b_i^j represents the number of expected events from the background process j, which depends on its normalisation w_j, $\vec{\lambda}$ and m_t^MC in the case of $\mathrm{t\bar{t}}$ background.

For each bin k, a signal strength parameter r^k is introduced and defined as:

$$r^k = \frac{\sigma^k_{\mathrm{t\bar{t}}+\mathrm{tW}}}{\sigma^k_{\mathrm{t\bar{t}}+\mathrm{tW}}(\mathrm{MC})}, \tag{5.7}$$

where the denominator represents the cross section associated with the normalisation of the MC prediction, determined from the nominal bb4l simulation. The signal strength parameters are the parameters of interest (POIs) and they are fitted simultaneously, with each treated as an independent signal. In this way, the bin-to-bin migrations due to smearing or reconstruction inefficiency are taken into account. As a result, the maximum-likelihood fit yields cross section values that are automatically unfolded to the particle level. To reduce the correlation between the fitted r^k and m_t^MC, the latter is included as an additional shape uncertainty in the fit. In this case, no prior is introduced, and the NP is unconstrained. The corresponding predictions are derived from two dedicated MC simulations, where m_t^MC is alternatively varied by ± 3 GeV with respect to the nominal value and scaled by 1/3. A similar approach should be applied to the width predictions for the nominal value of $\Gamma_\mathrm{t} = 1.31$ GeV and the corresponding variations of $\Gamma_\mathrm{t} = 2.0$ GeV and $\Gamma_\mathrm{t} = 0.66$ GeV. However, dedicated detector-level simulated samples for width variations are currently unavailable. While particle-level samples exist [178], they were generated using an earlier version of bb4l [13] rather than the one used in this analysis [14] and do not include detector simulation. As a result, these samples cannot be directly incorporated into the maximum likelihood fit. Instead, they are used later for the extraction of m_t^MC and Γ_t to construct predictions at particle-level with varied top quark widths.

The likelihood is maximised with respect to the POIs, the NPs, and the normalisation parameters. This approach enables the systematic uncertainties to be constrained di-

rectly from the data, thereby reducing the overall uncertainty in $\sigma^{k}_{\mathrm{t\bar{t}+tW}}$. The values of the parameters that maximise the likelihood are obtained by minimising the quantity -2 log $\mathcal{L}$. The MINUIT program [342] is employed for the minimisation, while the MINOS algorithm [342] is then used to estimate the uncertainties. The uncertainties in the POIs are determined by scanning the value of the likelihood function around the minimum. The Higgs Combination Tool [313] is used to perform the fit. Templates of the expected final-state distributions are obtained from the nominal simulation and for each systematic variation (corresponding to $\pm 1\sigma$ shifts). However, a continuous function is necessary for the implementation in the likelihood function. To achieve this, a second-order polynomial is used for interpolation in the case of two-sided variations, whereas a linear function is applied for one-sided variations. This process is known as template morphing [343]. To account for correlations of systematic uncertainties across different data-taking periods, template histograms are generated separately for the two years and they are fitted simultaneously.

Binning definition

The binning of $m_{\ell \mathrm{b}}^{\mathrm{minimax}}$ is chosen to ensure sufficient statistical precision in the tail, which is most sensitive to Γ_{t}. Additional checks were conducted to ensure that the selected binning is appropriate for this analysis. The migrations in and out of the bins are investigated by calculating the purity and stability, defined as:

$$purity = \frac{N_i^{rec\&gen}}{N_i^{gen}}, \quad stability = \frac{N_i^{rec\&gen}}{N_i^{rec}}. \tag{5.8}$$

In an ideal scenario with no bin-to-bin migrations, both metrics would be equal to unity. The purity and stability for the binning employed in this analysis are, on average, 60%. The corresponding response matrix is illustrated in Figure 5.7. The condition number[1] is a function that measures how much the unfolded observables are sensitive to small changes in the generator-level observables. In this analysis, the unfolding problem is found to be well conditioned, with a condition number of the response matrix of about 7. As a result, no regularisation is necessary.

[1]When this value is large, typically greater than 10^4, the problem is considered ill-conditioned, and a technique called regularisation must be applied [344].

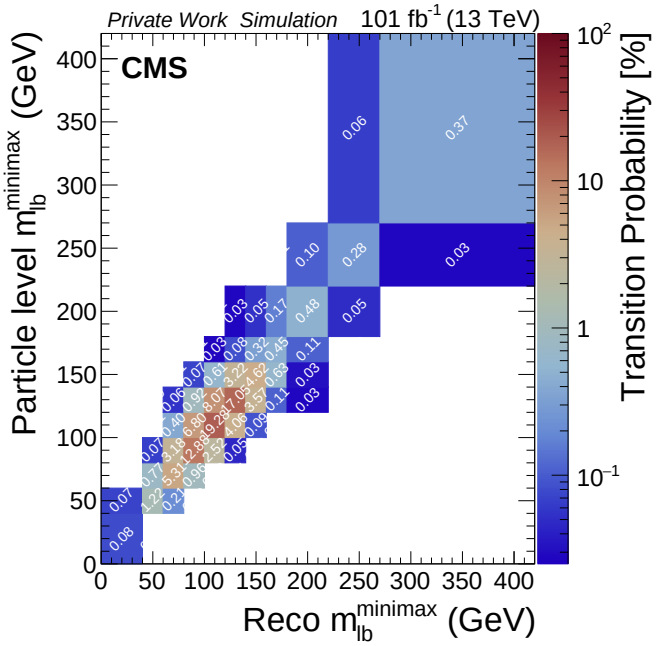

Figure 5.7: The response matrix obtained from the MC simulation.

5.5.1 Results

The differential cross section of the $t\bar{t}+tW$ process as a function of $m_{\ell b}^{\text{minimax}}$ is measured in 11 bins using Asimov pseudo-data. The absolute differential $t\bar{t}+tW$ cross section $d\sigma_{t\bar{t}+tW}/dm_{\ell b}^{\text{minimax}}$ at the particle level is shown in Figure 5.10, together with the bb4l prediction obtained with $m_t^{\text{MC}} = 172.5$, 169.5, and 175.5 GeV.

The fit is repeated with all constrained nuisances fixed to their best fit value to estimate the statistical uncertainty. Then, the systematic uncertainty is extracted by subtracting the statistical uncertainty quadratically from the total uncertainty. The fitted parameter values, expected constraints, and impacts on the signal strength parameters r^k for the 40 most relevant NPs after the fit to data are shown in Figures 5.8 and 5.9, which correspond to Bin7 and Bin11. These bins are the most sensitive to the value of m_t and Γ_t, respectively. Further impact plots are summarised in Appendix A.3. The uncertainties expected to have the most significant impact in Bin7 are related to m_t^{MC} variations, B-tagging, JES, and JER. In Bin11, in addition to B-tagging and m_t^{MC} uncertainties, the muon scale is also expected to play a significant role. Overall, a two-sided behaviour of the NPs is observed, demonstrating good

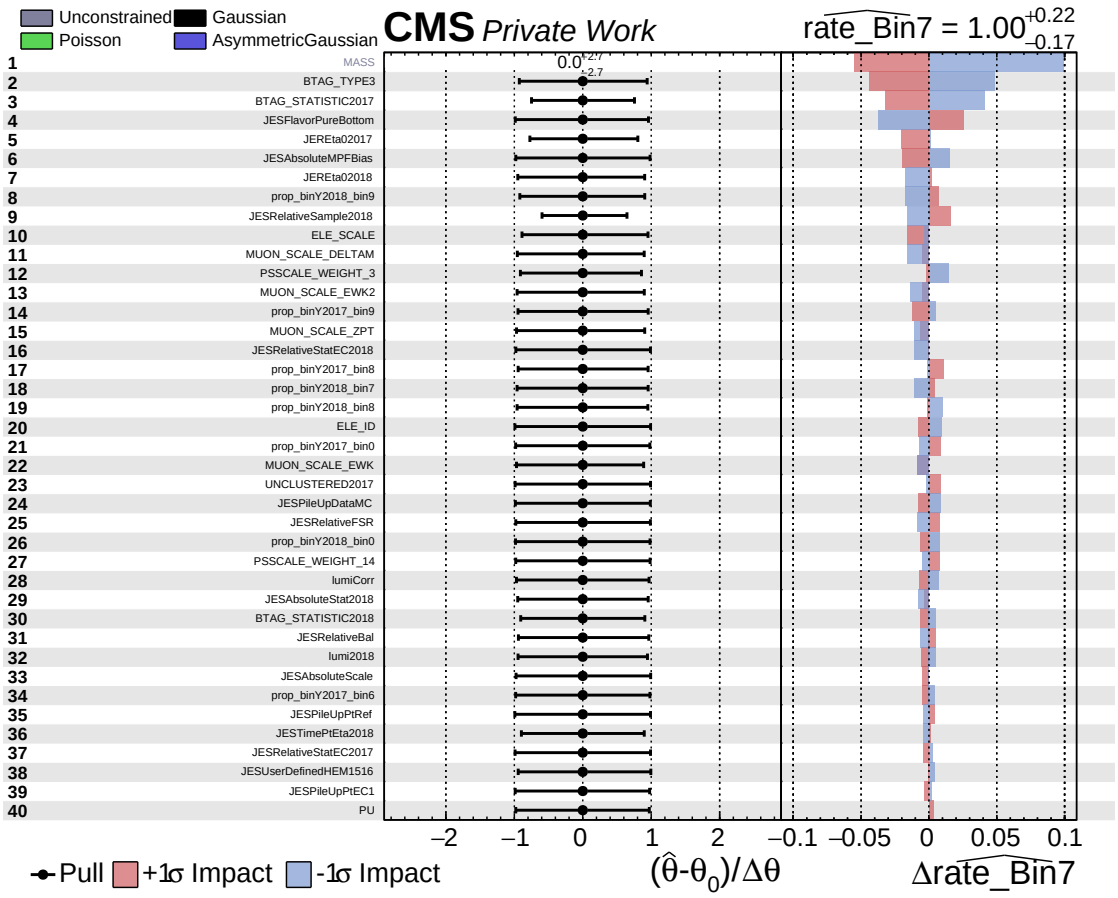

Figure 5.8: Fitted NP values and their expected impacts $\Delta\hat{r}_7$ on the signal strength $\hat{r}_7$ from the fit to the Asimov pseudo-data. Only the 40 highest ranked parameters are shown, ordered by their relative summed impact. The expected uncertainty of $\hat{r}_7$ is also given. The black line shows, for each NP, the relative constraint after the fit. The blue and red shaded areas present the expected impacts of shifting each NP to its $\pm1\sigma$ values in the fits to the Asimov pseudo-data, respectively. For the NP associated with the "MASS", the value after the fit to the Asimov pseudo-data is given because no prior is assigned.

modelling of the systematic uncertainties. Some one-sided variations are observed in Bin11 (particularly for NP indices 2 to 11). This is due to the sensitivity of the last bin to statistical fluctuations, which could explain the unusual behaviour in the MC templates.

The normalised differential cross section is then computed from the absolute cross

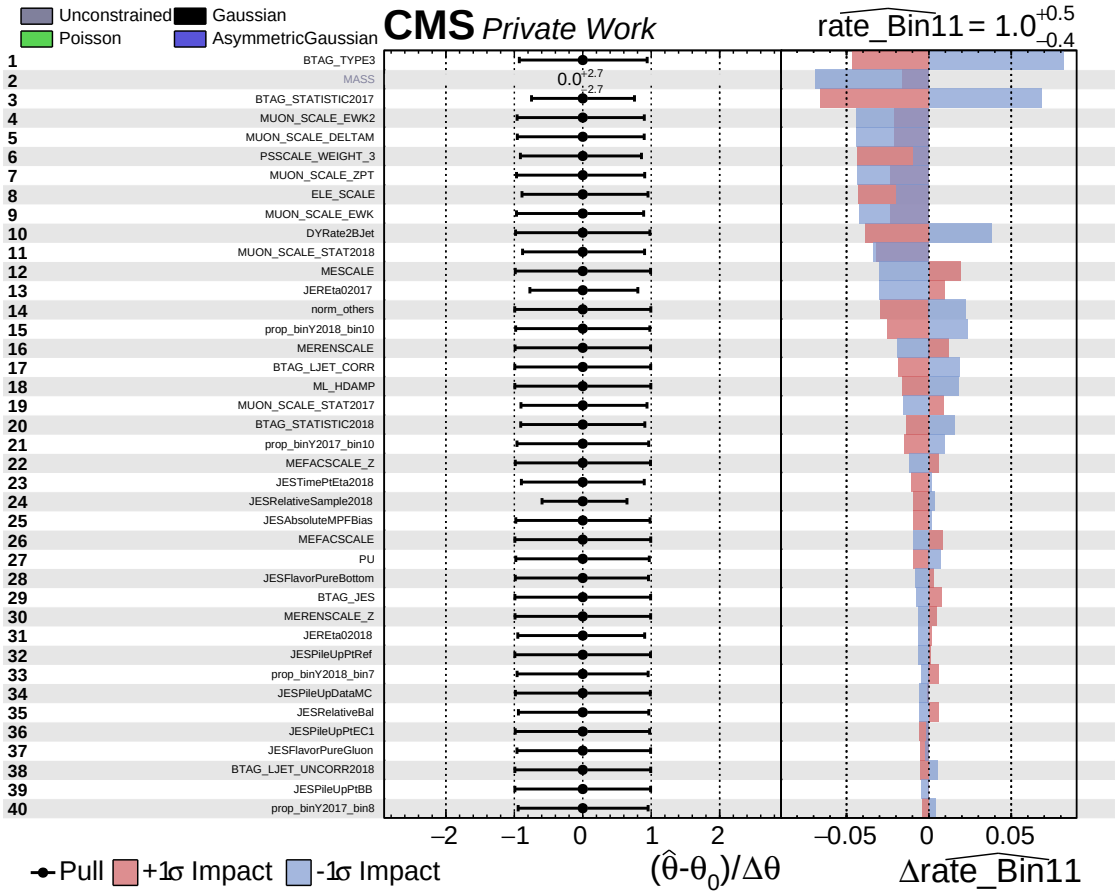

Figure 5.9: Same as Figure 5.8 for Bin11.

section obtained in the fit. This procedure effectively cancels the normalisation uncertainties, significantly reducing the overall uncertainty and allowing for a more precise extraction of $m_{\mathrm{t}}^{\mathrm{MC}}$ and Γ_{t}. To calculate the normalised differential cross section, the absolute differential cross section for each bin is divided by the sum of all bin values. Before the normalisation, the uncertainties are symmetrised as provided by HESSE [342] and they are then propagated to the normalised cross sections using standard error propagation for the statistical and total uncertainties:

$$\sigma_f^2 = |\frac{df}{dx}|^2\sigma_x^2 + |\frac{df}{dy}|^2\sigma_y^2 + 2\frac{df}{dy}\frac{df}{dy}\sigma_{xy}. \tag{5.9}$$

Here, $\sigma_{xy} = \sigma_x\sigma_y\rho_{xy}$ is the covariance between x and y and ρ_{xy} their correlation, and x and y refer to the per-bin cross section or total cross section, respectively.

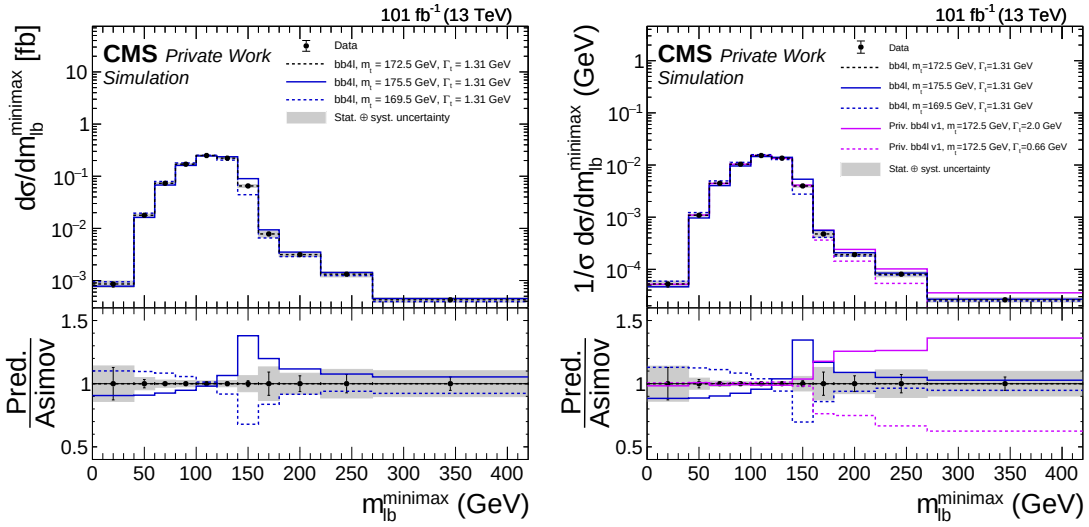

Figure 5.10: Absolute (left) and normalised (right) differential cross sections as a function of $m_{\ell\mathrm{b}}^{\mathrm{minimax}}$. Asimov pseudo-data are shown as black dots with statistical uncertainty, and the total uncertainty of the predictions indicated by the grey band. The standard model expectation is shown for a top quark mass of 172.5 GeV and a top quark width of 1.31 GeV for $\mathrm{t\bar{t}}+\mathrm{tW}$ production using bb4l generator in black and for top quark masses of 169.5 GeV (dashed blue) and 175.5 GeV (solid blue) or top quark width of 0.66 GeV (dashed magenta) and 2.0 GeV (solid magenta). The width variations are shown just for the normalised samples.

The normalised cross section is shown in Figure 5.10 compared to the theoretical predictions. Additional MC templates with $\Gamma_{\mathrm{t}} = 0.66$ or 2.0 GeV and $m_{\mathrm{t}}^{\mathrm{MC}} = 169.5$ or 175.5 GeV are considered. The relative uncertainties of the normalised cross section in each $m_{\ell\mathrm{b}}^{\mathrm{minimax}}$ bin are reported in Table 5.3.

5.6 Extraction of the top quark mass and width

The values and uncertainties of $m_{\mathrm{t}}^{\mathrm{MC}}$ and Γ_{t} are extracted from a χ^2 fit of the normalised measured differential cross section at the particle level to the NLO theoretical predictions from bb4l, assuming different values of $m_{\mathrm{t}}^{\mathrm{MC}}$ and Γ_{t}, respectively. Variations of ± 1 GeV and ± 3 GeV are considered for $m_{\mathrm{t}}^{\mathrm{MC}}$, while Γ_{t} is varied by $+0.69$ GeV and -0.65 GeV. A simultaneous extraction is not yet possible, as theory predictions with variations in both parameters are currently unavailable. The fit is performed using the open-source QCD analysis framework xFitter [345], which implements the χ^2 definition from Ref. [91]. The method involves using the minimum χ^2 for

Bin	Unc. (%)
Bin1	13.857
Bin2	4.413
Bin3	2.051
Bin4	1.509
Bin5	1.187
Bin6	1.337
Bin7	5.748
Bin8	12.855
Bin9	7.879
Bin10	10.898
Bin11	9.742

Table 5.3: Relative uncertainty of the normalised cross section associated with each bin of $m_{\ell\mathrm{b}}^{\mathrm{minimax}}$ distribution.

three-point variations (nominal, upward, and downward variation) of the parameter of interest ($m_{\mathrm{t}}^{\mathrm{MC}}$ or Γ_{t}). The statistical and systematic uncertainties are derived from the maximum-likelihood fit, where the NPs are constrained. The full correlation matrix, containing both statistical and systematic uncertainties, is taken into account. In the χ^2 calculation, the uncertainties are kept fixed to avoid constraining those again, artificially. The χ^2 scans from $m_{\mathrm{t}}^{\mathrm{MC}}$ and Γ_{t} are shown in Figure 5.11. The best fit value for $m_{\mathrm{t}}^{\mathrm{MC}}$ and Γ_{t} are extracted at χ^2_{min}, and the total fit uncertainty at 68% CL is obtained using the tolerance criterion $\Delta\chi^2 = 1$. The best-fit value is 172.61 GeV (1.36 GeV) with a fit uncertainty of 0.37 GeV (0.12 GeV) for $m_{\mathrm{t}}^{\mathrm{MC}}$ (Γ_{t}). The impact of higher-order effects (scale uncertainty) is evaluated by repeating the χ^2 scans with theoretical predictions where μ_{r} and μ_{f} are varied independently by factors of 0.5 and 2, while avoiding cases where $\mu_{\mathrm{f}}/\mu_{\mathrm{r}} = 4$ or 1/4. The total scale uncertainty is then estimated by taking the maximum difference in the $m_{\mathrm{t}}^{\mathrm{MC}}$ and Γ_{t} results with respect to the nominal one. Similarly, the uncertainties associated with the PS, ME-PS matching and the value of $\alpha_S(m_{\mathrm{Z}})$ assumed in the PDFs are estimated. Finally, these modelling uncertainties are summed in quadrature to quantify the theoretical uncertainty, which is dominated by the scale uncertainty. The final results are:

$$\begin{aligned} m_{\mathrm{t}}^{\mathrm{MC}} &= 172.61 \pm 0.37_{(\mathrm{fit})}{}^{+0.18}_{-0.24(\mathrm{theory})} \ \mathrm{GeV} \\ \Gamma_{\mathrm{t}} &= 1.36 \pm 0.12_{(\mathrm{fit})}{}^{+0.17}_{-0.22(\mathrm{theory})} \ \mathrm{GeV} \end{aligned} \tag{5.10}$$

where the total uncertainties are $^{+0.41}_{-0.44}$ GeV and $^{+0.24}_{-0.28}$ GeV for $m_{\mathrm{t}}^{\mathrm{MC}}$ and Γ_{t}, re-

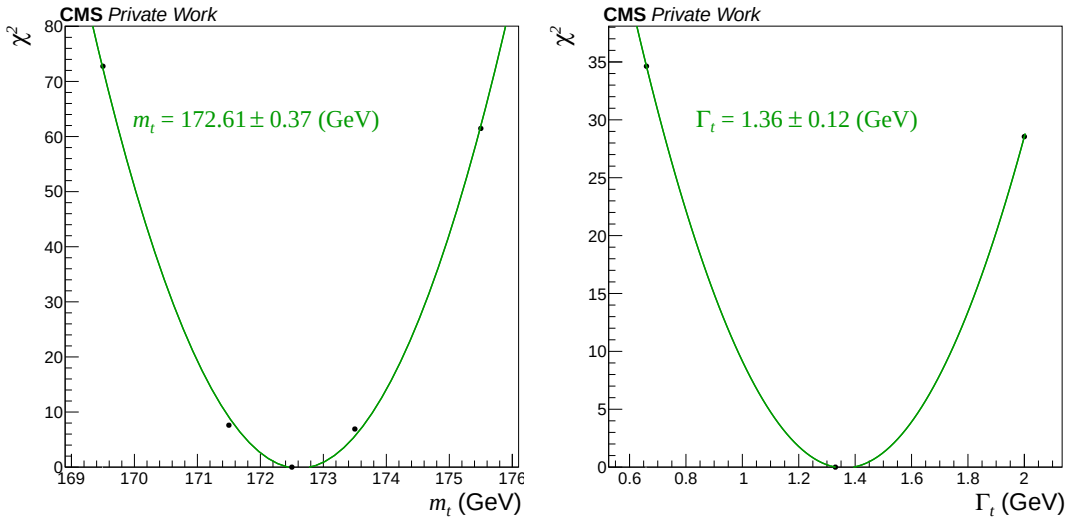

Figure 5.11: A 2nd order polynomial fitted to the χ^2 resulting from comparing the the normalised $t\bar{t}$+tW differential cross sections using Asimov pseudo-data to theory predictions of bb4l assuming different values of m_t^{MC} (left) and Γ_t (right). The m_t^{MC} (left) and Γ_t (right) extracted from the polynomial fit at χ^2_{min} value and the uncertainty at 68% CL are given.

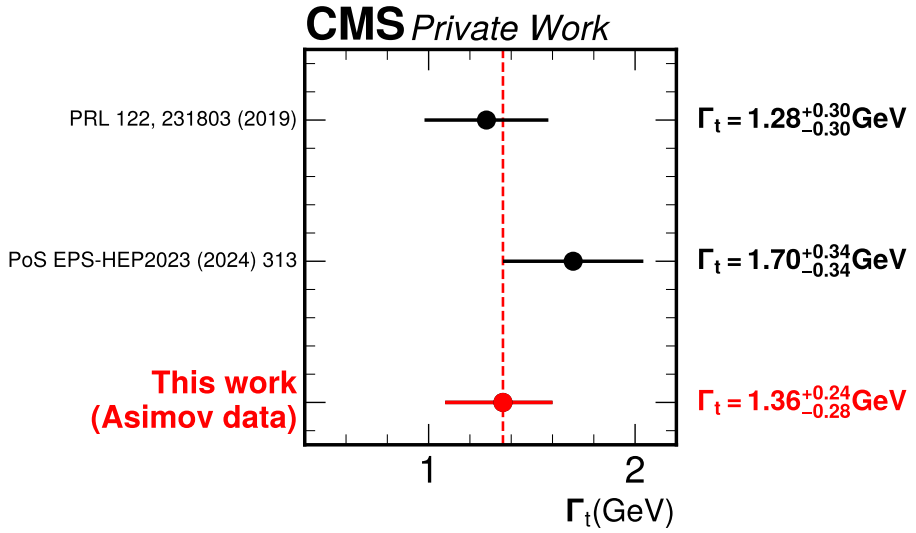

Figure 5.12: Summary of direct determinations of Γ_t using the bb4l MC generator.

spectively. The summary of Γ_t determinations using bb4l method is given in Fig-

ure 5.12. This measurement (currently with Asimov pseudo-data) promises significantly improved precision as compared to other direct measurements obtained with bb4l method [177, 178]. The $m_{\mathrm{t}}^{\mathrm{MC}}$ result is as precise as the most precise single-experiment direct $m_{\mathrm{t}}^{\mathrm{MC}}$ measurement [168] and represents the first determination of m_{t} from the combined $\mathrm{t\bar{t}}$ and tW cross section in the CMS collaboration. The prospects for this measurement are very promising. The analysis is in the CMS review and the unblinding is imminent.

Chapter 6

Extraction of α_S and illustration of its running by using inclusive jet production

This Chapter presents the QCD analysis of the CMS inclusive jet measurements used together with the electron-proton DIS cross section data collected at HERA. The analysis has been developed within the PhD project and is documented in the CMS publication [346].

The QCD analysis is performed using the open-source framework xFitter, described in Section 6.1. Details on the experimental data employed in the QCD analysis are described in Section 6.2, while the theory predictions for inclusive jet production are outlined in Section 6.3. The general strategy is discussed in Section 6.4. Finally, the results of the simultaneous fit of $\alpha_S(m_Z)$ and PDFs at NNLO in QCD are presented in Section 6.5 and the illustration of α_S running is given in Section 6.6.

6.1 The xFitter framework for QCD analyses

The xFitter framework [347–349], which originated from HERAfitter [345], is an open-source tool developed for performing QCD analyses, where the PDFs and the fundamental parameters of the SM are extracted: e.g. α_S, quark masses, EW mixing angle. The framework supports experimental data from a wide range of experiments,

including the Tevatron, HERA, LHC, and fixed-target experiments, thus covering a broad range of x. The xFitter QCD analysis platform is highly versatile and offers a wide set of theoretical calculations, schemes for treatment of heavy flavours and variants in χ^2 calculations. As a result, it has been used in many previous analyses in CMS [54, 95–97, 99–101, 104, 106–108, 137, 350] and ATLAS [141, 351–354]. Furthermore, it enables SMEFT studies through an interface with CIJET [355–357], allowing for the simultaneous extraction of SMEFT and SM parameters.

The xFitter platform is primarily based on the collinear factorisation foundation. The theoretical predictions for a particular process are obtained by convolving the PDFs with the partonic cross sections. For DIS processes, different mass schemes can be used to account for heavy quark (i.e. b and c quark) contributions. These include the *zero mass variable flavour number* (ZM-VFN) [358], the *fixed-flavour number* (FFN) [359–361], and the *general mass variable flavour number* (GM-VFN) schemes. In the FFN scheme, only gluons and light quarks appear in the PDFs, while heavy quarks are treated as massive and are produced only perturbatively. The number of active flavours, n_f, is set to either 3, 4, or 5 and remains unchanged even at energy scales exceeding the mass thresholds of heavy quarks. This scheme is applicable at scales around $\mu^2 \approx m_Q^2$. The GM-VFN scheme ensures a smooth transition between the ZM-VFN and FFN approaches by treating heavy quarks in the FFN scheme near the production threshold ($\mu^2 \sim m_Q^2$) and as massless at higher scales ($\mu^2 \gg m_Q^2$). Various implementations exist for this transition, and this thesis employs the *Thorne-Roberts* GM-VFN scheme [362–364].

The comparison between theory predictions and experimental data permits the determination of PDFs and other parameters through an iterative χ^2 minimisation process that incorporates both correlated and uncorrelated uncertainties across the measurements. Since in the collinear factorisation the x-dependence of the PDFs cannot currently be derived from first principles, it has to be parametrised at a certain starting scale Q_0^2. In xFitter, different predefined functional forms and flavour decompositions can be used, each offering various levels of flexibility in capturing the x-dependence. One of the most common functional forms for parametrising the gluon g, valence u- and d-quark, and $\overline{\mathrm{u}}$ and $\overline{\mathrm{d}}$ antiquark densities is given by:

$$xq_i(x) = A_i x^{B_i}(1-x)^{C_i} P_i(x), \tag{6.1}$$

where A_i are normalisation constants and $P_i(x) = (1 + D_i x + E_i x^2)$ are polynomials that interpolate between the small- and large-x behaviour governed by the B_i and C_i parameters. The parameters A_{u_v} and A_{d_v} are determined during the fit from the valence-quark number sum rule, while the value of A_g is obtained from the momentum sum rule. Finally, the D_i and E_i parameters assess the sensitivity of new datasets in a QCD analysis to the chosen functional form. In the fit, the parametrised distributions of the PDFs are evolved to the energy scale of the measurement using the DGLAP equations, as implemented in the QCDNUM [365] program. A schematic overview of the general workflow of a QCD analysis in xFitter is presented in Figure 6.1.

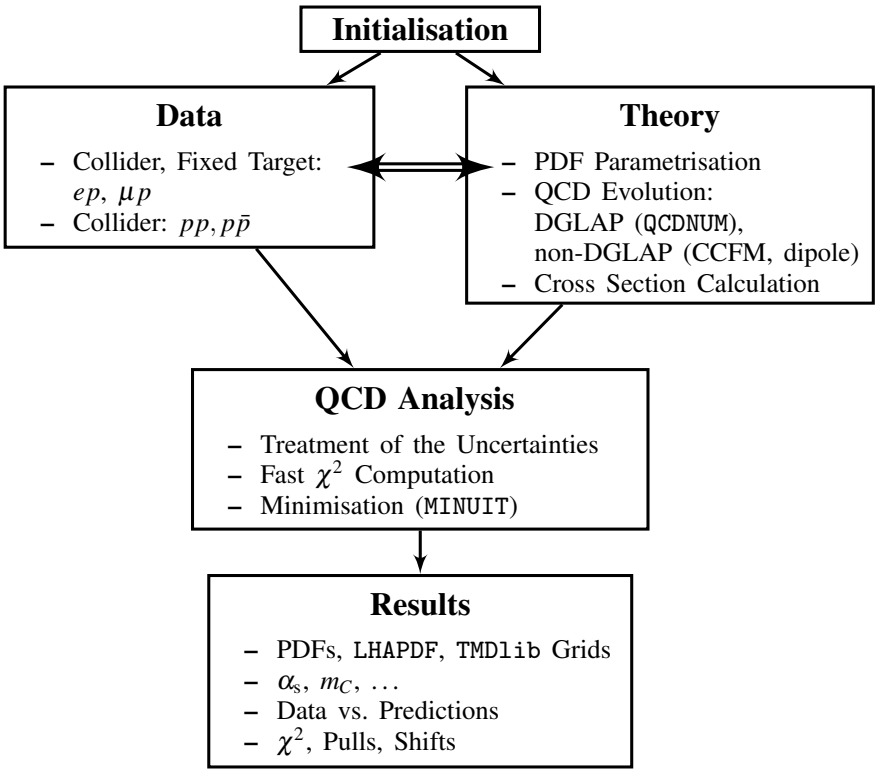

Figure 6.1: Schematic overview of a QCD analysis in xFitter. Figure taken from Ref. [345].

Minimisation algorithm and uncertainties

The default minimisation algorithm used by xFitter is an extended version of the Fortran program MINUIT [342]. This allows for the fitting of a larger number of parameters and supports uncertainty analysis with both asymmetric and symmetric

error bands using the Hessian method. xFitter offers multiple options for incorporating experimental uncertainties into the χ^2 definition. Correlated uncertainties can be treated either as nuisance parameters or via a covariance matrix. In this thesis, the former method is adopted, and the χ^2 goodness-of-fit function reads:

$$\chi^2(\mathbf{T}, \mathbf{b}_{\text{exp}}) = \sum_{i=1}^{N_{\text{data}}} \frac{\left[M_i - T_i(1 - \sum_j \gamma_{ij}^{\text{exp}} b_{j,\text{exp}})\right]^2}{\delta_{i,\text{uncor}}^2 T_i^2 + \delta_{i,\text{stat}}^2 M_i T_i (1 - \sum_j \gamma_{ij}^{\text{exp}} b_{j,\text{exp}})} + \sum_{j=1}^{N_{\text{exp.sys}}} b_{j,\text{exp}}^2, \quad (6.2)$$

where the index i is an individual measurement from all measurements (N_{data}). Here, M_i represents the measured values, while T_i are the theory predictions, respectively. The statistical and uncorrelated systematic uncertainties associated with each measurement i are denoted by $\delta_{i,\text{stat}}$ and $\delta_{i,\text{uncor}}$, respectively. Correlated experimental uncertainties are incorporated through the nuisance parameters $b_{j,\text{exp}}$, with their impact on the theoretical prediction T_i described by the matrices γ_{ij}^{exp}. The nuisance parameters b_j are determined through the χ^2 minimisation process. Asymmetric uncertainties in the PDF parameters are obtained from a $\Delta\chi^2 = \chi^2 - \chi^2_{\text{min}} = 1$ criterion using an iterative Hessian approach, following the prescription of Ref. [366]. These uncertainties correspond to 68% confidence level (CL).

Profiling procedure

The profiling technique allows for evaluating the impact of a new dataset on a global PDF set [367–370] and conducting sensitivity studies on $\alpha_S(m_{\text{Z}})$ while keeping the PDFs fixed. In this case, the χ^2 function of Eq. (6.2) is modified as:

$$\chi^2(\mathbf{b}_{\text{exp}}, \mathbf{b}_{\text{th}}) = \sum_{i=1}^{N_{\text{data}}} \frac{\left(M_i + \gamma_{ij}^{\text{exp}} b_{j,\text{exp}} - T_i - \gamma_{ij}^{\text{th}} b_{j,\text{th}}\right)^2}{\Delta_i^2} + \sum_{j=1}^{N_{\text{exp.sys}}} b_{j,\text{exp}}^2 + \sum_{j=1}^{N_{\text{th.sys}}} b_{j,\text{th}}^2, \quad (6.3)$$

where the nuisance parameter $\mathbf{b}^{\text{exp}}$ and $\mathbf{b}^{\text{th}}$ comprise the correlated experimental and theoretical uncertainties, while the uncorrelated experimental uncertainties are included in Δ_i. This technique has the advantage of fast investigation of the possible impact of a new data set on the existing PDFs; however, it disregards the correlations between PDFs and further parameters, e.g. α_S. In the QCD analysis presented in this thesis, the profiling procedure was used to estimate the sensitivity of each individual CMS measurement to $\alpha_S(m_{\text{Z}})$ from the global PDF sets, by using the $\alpha_S(m_{\text{Z}})$ series

from the global PDF sets, typically spanning $\alpha_S(m_Z)$ from 0.111 to 0.122.

PDF parametrisation scan

New datasets can introduce additional constraints on the PDF shape, which would lead to a more flexible parameterisation form. To investigate the impact of a new data set on the parametrisation, a parametrisation scan is performed, starting with D and E parameters of Eq. (6.1) set to zero. Successively, they are included in the fit, one at a time. The process is monitored using the *Bayesian Information Criterion* (BIC) [371], which takes into account both the χ^2 fit quality, the number of degrees of freedom, and the number of free parameters. The procedure is terminated once no further improvement is observed.

Interpolation grids

In QCD analyses, fits often require recalculating the cross section multiple times, but computing full perturbative QCD (pQCD) predictions at NLO or higher orders is computationally expensive. This issue is addressed through fast interpolation grid techniques, where perturbative cross sections are computed once, stored in tables, and represented as grids based on fractional momenta (x_1, x_2) and QCD scales (μ_f, μ_r). These precomputed values enable fast and precise predictions without needing to repeat the full NLO (or higher orders) calculation in every iteration. Interpolation grids are currently available for processes such as jets, $t\bar{t}$, and Drell-Yan. For jet-related observables, xFitter uses interpolation grids, such as those from ApplGrid [372], fastNLO [146], or PineAppl [373].

6.2 Data used in the QCD analysis

As described in Section 2.2, the PDF fits are primarily based on measurements of CC and NC DIS cross sections from $e^{\pm}p$ collisions at HERA. The HERA data sets used in this study are the combination of inclusive DIS cross sections measured by H1 and ZEUS experiments in HERA 1 and HERA 2 running periods [91]. The NC cross sections cover the kinematic range $6 \cdot 10^{-7} \leq x \leq 0.65$, while the CC cross sections are measured in the range $1.3 \cdot 10^{-2} \leq x \leq 0.40$. In the original HERAPDF2.0 analysis [91], inclusive DIS data with $Q^2 < 3.5\,\mathrm{GeV}^2$ were excluded from the PDF

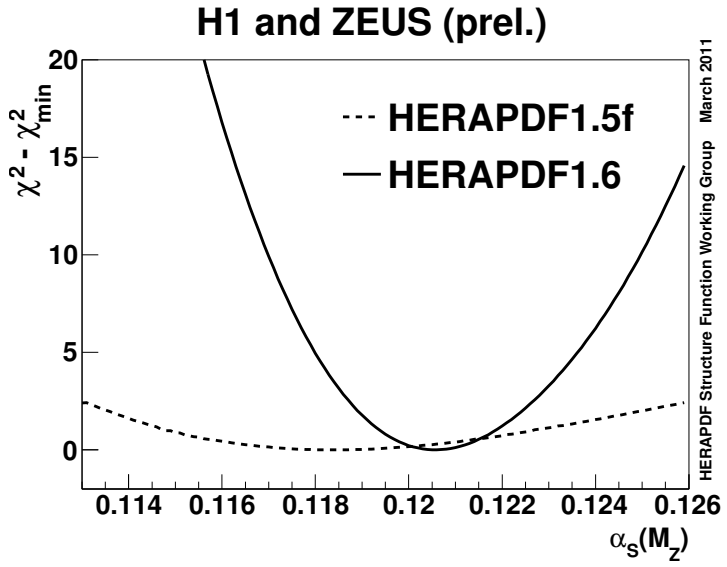

Figure 6.2: The χ^2 profiling of $\alpha_S(m_Z)$, using inclusive DIS data (dashed line) and inclusive DIS data combined with HERA jet data (solid line). Figure taken from Ref. [374].

fit. In the present analysis, a higher Q^2 cut is imposed on HERA data, to improve the general quality of the fit. The published DIS cross sections have already been corrected for the dominant EW effects.

The sensitivity of HERA DIS data to $\alpha_S(m_Z)$ was investigated by the HERA combination group. In Figure 6.2 [374], the χ^2 values are shown as a function of $\alpha_S(m_Z)$, obtained in the simultaneous QCD analyses of PDFs and $\alpha_S(m_Z)$ in the GM-VFN scheme by using inclusive DIS data or, alternatively, inclusive and HERA DIS jet measurements. The very shallow minimum in χ^2 for inclusive DIS alone demonstrates a fair sensitivity to $\alpha_S(m_Z)$ in the GM-VFN scheme. Enhanced sensitivity is achieved only when including also HERA jet data.

The CMS inclusive jet measurements use jets clustered with the anti-k_T [144] algorithm as implemented in the FastJet [207] program with a distance parameter of $R = 0.4$ or $R = 0.7$. The QCD analysis presented in this thesis includes the CMS inclusive jet measurements[1] at $\sqrt{s} = 2.76$ [148], 7 [103,104], 8 [105], and 13 [106] TeV,

[1]The CMS measurement at 5.02 TeV [149] is also available but not included in this study, as it uses jets clustered with $R = 0.4$, which are known to exhibit discrepancies with QCD predictions in the forward region.

obtained with $R = 0.7$. The choice of this radius parameter minimises out-of-cone radiation effects and improves the agreement between theoretical predictions and experimental data [106]. Furthermore, as stated in Refs. [375–377], using $R = 0.7$ rather than $R = 0.4$ improves the stability of NNLO calculations. The measurements are performed double-differentially in rapidity y and p_{T}, where the cross section is defined as:

$$\frac{d^2\sigma}{dp_{\mathrm{T}}dy} = \frac{N_{\mathrm{jets}}}{\mathcal{L}\Delta p_{\mathrm{T}}\Delta y}. \tag{6.4}$$

Here, N_{jets} represents the number of jets per bin after applying corrections for detector effects. $\mathcal{L}$ denotes the integrated luminosity, while Δp_{T} and Δy refer to the bin widths in jet p_{T} and y, respectively [106]. The measurements themselves were not performed in this thesis, but the general strategy for conducting an inclusive jet measurement and a brief overview of each measurement is outlined below.

In each of the measurements, events are selected using a combination of HLT single-jet triggers, each covering exclusive intervals of the leading jet's p_{T} to ensure an efficiency of approximately 99%. The triggers are prescaled, except for the one with the highest p_{T} threshold. Additionally, selected events must have at least one well-reconstructed primary vertex, and the jets are required to satisfy quality criteria based on their constituents to reduce the impact of detector noise. Jet reconstruction and calibration are performed as described in Section 3.3.2. Corrections are then applied to simulated events to reduce discrepancies between data and MC samples, including trigger efficiency and pileup corrections. Finally, detector effects are corrected through an unfolding procedure, and the double-differential cross-section at the particle level is extracted. While the overall strategy is consistent across measurements, different unfolding techniques have been applied in each case.

The measurements were accompanied by a comprehensive QCD analysis for the 7, 8, and 13 TeV datasets, although such interpretation was not performed for the 2.76 TeV dataset. However, the 13 TeV analysis is the only one carried out at NNLO in QCD, since the NNLO predictions for inclusive jet production in pp collisions became available at the time of this measurement. Prior to the study presented in this thesis, the inclusive jet measurement at 13 TeV provided the most precise determination of $\alpha_S(m_{\mathrm{Z}})$ from jet measurements, with $\alpha_S(m_{\mathrm{Z}}) = 0.1166 \pm 0.0017$ [106]. In the following, the most relevant details of each measurement are briefly summarised.

6.2.1 Measurement at 2.76 TeV

The CMS measurement of the double-differential inclusive jet cross section in pp collisions at $\sqrt{s} = 2.76$ TeV is based on data taken in 2010 at low pileup and corresponding to an integrated luminosity of 0.0054 fb^{-1}. It is detailed in Ref. [148]. The cross sections are measured as functions of p_{T} in the range 74–592 GeV in 6 bins in $|y|$ in the range 0.0–3.0. Events are selected using prescaled single-jet triggers with jet p_{T} thresholds of 40, 60, and 80 GeV, except for the highest threshold trigger, which remains unprescaled. To compare the measurements with the theoretical predictions, the jet p_{T} spectrum is corrected for detector effects. The detector response is described by a function that defines the probability density for reconstructing a jet with transverse momentum p_T^{det} given a corresponding particle-level jet transverse momentum p_T^{part}. The response function is extracted from multijet events simulated using the PYTHIA 6 (v.6.4, tune Z2) [378, 379] event generator. A kernel density estimation technique is used to model the response function, ensuring an accurate description of the tails of the distributions. The response matrix is obtained by convolving the response function with the p_T^{part} spectrum predicted by NLO QCD calculations [380] and the CT10 PDF set [381]. The measured distributions are unfolded using the D'Agostini iterative method [382], as implemented in the ROOUNFOLD package [383]. Regularisation is achieved by limiting the number of iterations to four in each rapidity bin.

The dominant sources of the experimental uncertainties in this measurement are JES, JER, and the integrated luminosity (3.7%) [384]. The uncertainty associated with JES consists of 22 independent contributions, described in detail in Ref. [385]. The corresponding cross section uncertainty is 5–22% for $|y| < 2.5$, increasing to 78% at the highest rapidity of $2.5 \leq |y| < 3.0$. The JER uncertainty is 2–3% for $|y| < 2.5$, increasing to 22% for the highest rapidity. For this data set, the energy offset due pileup (PU) is small and no PU corrections are applied. The uncertainty associated with possible mismodelling of trigger and jet selection criteria is determined to be 1%.

6.2.2 Measurement at 7 TeV

The CMS measurement of the double-differential inclusive jet cross section in pp collisions at $\sqrt{s} = 7$ TeV is based on data collected in 2011 and corresponding to an integrated luminosity of 5.0 fb^{-1}. The measurement is detailed in Ref. [148]. The data cover a jet p_{T} range 114–2000 GeV and the cross section is measured in five $|y|$

bins in the range 0.0–2.5. The events are selected using single-jet triggers with jet p_{T} thresholds of 60, 110, 190, 240, or 370 GeV, respectively, in the corrected jet p_{T}. To avoid any trigger bias, the jets are additionally required to have $p_{\mathrm{T}} > 110$, 200, 300, 360, and 510 GeV. The observed spectra are unfolded to correct for detector effects. The response matrix is obtained from the detector simulation and corrected for the measured differences in the resolution between data and simulation [385]. The unfolding is performed by using the D'Agostini method [382, 383].

Several categories of experimental systematic uncertainties are defined: the JES, the JER, the luminosity, the corrections for detector response and resolution. The JES uncertainty is split into 20 different sources and amounts to 1–2% [386], which translates into a 5–25% uncertainty in the cross section, depending on p_{T} and $|y|$. The uncertainty in the integrated luminosity is 2.2% [387] and translates into a normalisation uncertainty that is fully correlated across $|y|$ and p_{T}. The effect of JER is corrected for using the D'Agostini method [382]. The unfolding uncertainty accounts for the modelling of the jet p_T resolution and the jet p_T spectrum in the simulation. To assess the sensitivity of the correction to these factors, the jet p_T resolution is varied by $\pm 10\%$, reflecting the observed discrepancies between data and simulation in the JER [385]. Further, the jet spectrum slope is adjusted by $\pm 5\%$, which is a conservative estimate based on comparisons between the theoretical and measured p_T spectrum shapes. Finally, a constant 2% uncertainty is introduced to account for the dependence on the unfolding method. Overall, the unfolding uncertainty is about 3–4%. Remaining effects are collected into an uncorrelated uncertainty of about 1%.

6.2.3 Measurement at 8 TeV

The CMS measurement of the double-differential inclusive jet cross section in pp collisions at $\sqrt{s} = 8$ TeV is based on data collected in 2012 and corresponding to an integrated luminosity of 19.7 fb^{-1}. The measurement is detailed in Ref. [105]. The data cover a jet p_{T} range 74–2500 GeV and the cross section is measured in six $|y|$ bins in the range 0.0–3.0. The events are selected using HLT single-jet triggers with jet p_{T} thresholds of 40, 80, 140, 200, 260, and 320 GeV, respectively. All triggers are prescaled except the highest threshold trigger. To correct for detector effects, the unfolding procedure following the same strategy as in the measurement at $\sqrt{s} = 7$ TeV is applied.

The dominant contribution to the experimental systematic uncertainty is associated with JES, which is decomposed into 24 independent sources corresponding to different components of the corrections. An uncertainty of 1%, uncorrelated across all jet p_{T} and $|y|$ bins, is assigned to account for the residual effects of inefficiencies in the trigger performance and jet identification. The uncertainty in the integrated luminosity is 2.6% [388] and translates into a normalisation uncertainty that is fully correlated across $|y|$ and p_{T}. The unfolding depends on the uncertainties in the JER parametrisation, which are obtained from the simulation. The JER parameters are varied by one standard deviation, and the corresponding response matrices are then used to unfold the observed spectra. The uncertainty induced by the JER ranges from 1–5%. Finally, the uncertainty associated with the jet angular resolution and the model dependence of the unfolding, stemming from the theoretical p_T spectrum used to calculate the response matrix, contributes less than 1% to the cross section.

6.2.4 Measurement at 13 TeV

The CMS measurement of the double-differential inclusive jet cross section in pp collisions at $\sqrt{s} = 13$ TeV is based on data collected in 2016 and corresponding to an integrated luminosity of 33.5 fb^{-1}. The measurement is detailed in Ref. [106]. The data cover a jet p_{T} range 97–3103 GeV and the cross section is measured in four $|y|$ bins in the range 0.0–2.0. The events are selected using single-jet triggers with jet p_{T} threshold of 40, 60, 80, 140, 200, 260, 320, 400, 450 GeV, respectively. All triggers are prescaled except for the highest trigger threshold. Jets reconstructed in regions of the detector corresponding to defective zones in the calorimeters are excluded from the measurement and recovered later in the unfolding procedure, together with any other type of inefficiency.

Compared to the previous measurements, the analysis strategy for $\sqrt{s}$ =13 TeV has significantly improved, accounting for non linearity in the trigger rate as a function of the instantaneous luminosity and variation of the JES corrections with time and pileup conditions. Further, a smoothing technique is applied to the JES corrections to ensure the cross sections remain smooth. The detector-level p_{T} distribution is rescaled to match the JER between the simulated samples and the data. Additionally, a matching procedure is performed between the particle-level and detector-level

jets for each event, and the JER fitting procedure is refined.

The measured detector-level distribution is unfolded to the particle level via a two-dimension unfolding in p_{T} and $|y|$ using corrections derived from the simulated events. The unfolding is performed by using the matrix inversion method as implemented in the TUnfold package [389], version 17. Additionally, corrections for the migrations, background and inefficiencies are considered. The jets that are successfully matched between detector and particle level are considered to derive the response matrix. On the other hand, unmatched jets at the particle (detector) level are used to estimate the inefficiencies (background). The background contribution is about 1–2%-level at low p_{T} and becomes negligible at medium and high p_{T}, while the inefficiency reaches a maximum of 2–5% at both low and high p_{T}.

The dominant contribution to the experimental systematic uncertainty is associated with JES, which is decomposed into 22 independent sources. The uncertainty in the integrated luminosity is 2.2% [390] and translates into a normalisation uncertainty that is fully correlated across $|y|$ and p_{T}. Variations of the JES, JER and PU profile corrections are applied to the simulated sample and propagated to the particle level by repeating the unfolding process. The estimates for inefficiencies and backgrounds, derived from the MC simulation, are normalised and varied independently within a conservative 5% margin. This accounts for potential model dependencies in phase space migrations and the influence of the matching algorithm in the unfolding procedure. The model uncertainty in the unfolding for p_{T} and $|y|$ is evaluated by comparing the nominal cross section, obtained from the original Pythia 8 simulation, with a modified version in which the inclusive jet spectrum is adjusted to align with the data. To mitigate bin-to-bin fluctuations in the systematic variations, a smoothing technique using Chebyshev polynomials is applied, as described in [391]. Finally, uncorrelated and partially correlated uncertainties across p_T and y bins have been considered. The primary source of uncorrelated uncertainty arises from the inclusive jet measurement, which is based on multiple jets recorded in each event. Another source of uncertainty comprises the statistical fluctuations of the simulated distributions. Finally, an additional uncorrelated systematic uncertainty of 0.2% is introduced prior to unfolding to address variations between different methods for determining trigger efficiency.

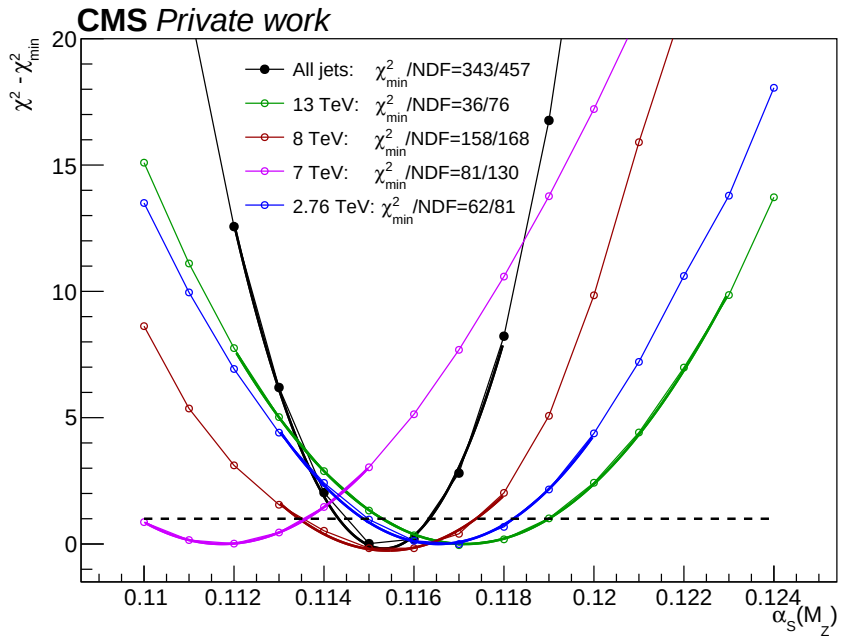

Figure 6.3: The χ^2 profiling of $\alpha_S(m_Z)$, using measurements and NNLO QCD predictions for CMS inclusive jet production at various $\sqrt{s}$, performed separately for the individual measurements (markers of different colours) and considering all the jet measurements together (black markers). The CT18NNLO [88] PDF set is used.

6.2.5 Estimate of $\alpha_S(m_Z)$ sensitivity for individual CMS jet measurements

The jet production measurements at the LHC provide significant constraints on $\alpha_S(m_Z)$. An illustration of the sensitivity of $\alpha_S(m_Z)$ for each of the CMS jet measurements used is presented in Figure 6.3, obtained with the profiling technique using the CT18NNLO PDF set [88]. Profiling is performed separately for each PDF member in the $\alpha_S(m_Z)$ series and a χ^2 corresponding to each member of the series is recorded. The optimal $\alpha_S(m_Z)$ value is obtained from the minimum of the resulting (parabolic) χ^2 distribution and the 68% confidence level (CL) uncertainty is obtained by using the criterion $\Delta\chi^2 = 1$. While the position of the parabola's minimum is not meaningful in this context, as it depends on the chosen PDF set, the associated 68% CL uncertainty provides an estimate of the measurement sensitivity. Among all the measurements, the one at $\sqrt{s} = 13$ TeV exhibits the highest sensitivity, as indicated by the narrowest parabola. Further improvement is expected from the inclusion of all the CMS jet

data in the fit. For each measurement, the corresponding integrated luminosity $\mathcal{L}$, the number of data points N_{dp}, and the ranges in p_T and $|y|$ considered in the QCD analysis are listed in Table 6.1.

Table 6.1: The CMS inclusive jet measurements used in this analysis. The columns show the centre-of-mass energy, the integrated luminosity, the number of measured data points, and the ranges of individual jet p_T and $|y|$.

$\sqrt{s}$ [TeV]	$\mathcal{L}$ [fb^{-1}]	N_{dp}	p_T[GeV]	$\lvert y\rvert$
2.76	0.0054	80	74–592	0.0–3.0
7	5.0	130	114–2116	0.0–2.5
8	20	165	74–1784	0.0–3.0
13	33.5	78	97–3103	0.0–2.0

6.2.6 Systematic correlations in CMS jet data

The leading experimental systematic uncertainty in jet measurements originates from the calibration of the JES and JER. Other major sources of uncertainty are related to luminosity, trigger and unfolding. As an example, the uncertainty contributions for the 13 TeV measurement are shown in Figure 6.4, where the colour bands represent fully correlated uncertainties between bins, while the vertical error bars show the uncorrelated uncertainties.

In this thesis, the correlations of JES and JER uncertainties across p_T and $|y|$ intervals, within and across the individual measurements at different $\sqrt{s}$, are investigated in detail. These correlations are incorporated into the QCD analysis, enhancing the precision and accuracy of $\alpha_S(m_Z)$ and offering valuable recommendations for future global QCD analyses of CMS inclusive jet measurements.

A comprehensive discussion of the JES calibration and its associated uncertainties can be found in Refs. [331,392]. A brief overview is provided below to aid in understanding the JES correlation scheme described later. The exact same convention is used in the publication [346], which is based on the work presented in this thesis. The JES uncertainties are categorised into eight main types:

- Uncertainties related to the absolute scale are associated with the JES correction within the barrel region, corresponding to pseudorapidities $|\eta| < 1.3$. This

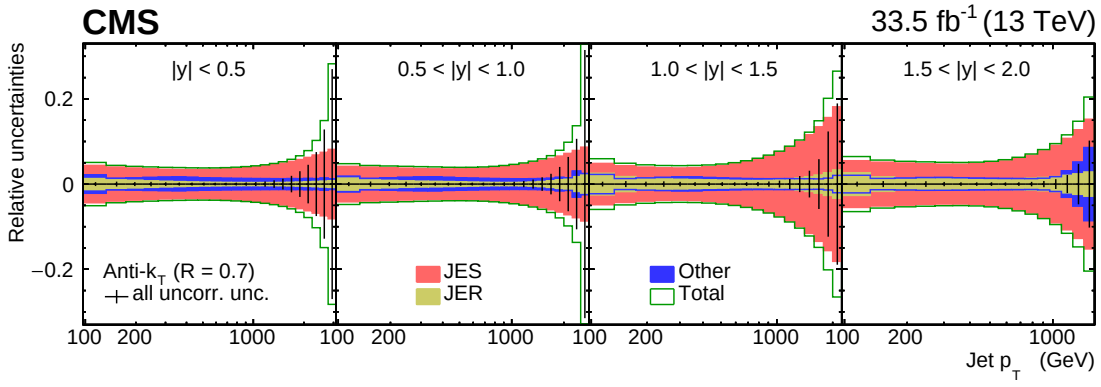

Figure 6.4: Relative uncertainties in the double-differential cross section, as functions of jet p_{T} (horizontal axis) and y (quadrants). The systematic uncertainties are shown in different noncumulative bands: JES uncertainties (red), JER uncertainties (yellow), and all other sources (blue), including the integrated luminosity uncertainty and unfolding related uncertainties. The error bars account for statistical uncertainties from both the data and the MC sample used in the unfolding procedure, as well as the binwise systematic uncertainties, all summed in quadrature. The total uncertainty (green) represents the sum of all statistical and systematic uncertainties, added in quadrature. Taken from Ref. [106].

correction (*AbsoluteScale*) is obtained from a global fit using Z+jet, γ+jet, and multijet data. It includes a correction for initial-state (ISR) and final-state radiation (FSR) (*AbsoluteMPFBias*). Extrapolations to high p_{T} beyond the reach of the measurements are performed by using MC simulations. Additional uncertainties arise from the response variations of different MC event generators (*Fragmentation*) and the single-particle response in the ECAL and HCAL (*SinglePionECAL, SinglePionHCAL*).

- Relative JER uncertainties represent the η-dependent uncertainty of the JES from the JER corrections (*RelativeJER*).
- The relative η correction of the JES calibration ensures a uniform detector response across different detector regions. In addition, it includes a log-linear p_{T} dependence. An uncertainty associated with the choice of the p_{T}-dependent shape is included. (*RelativePt*).
- The relative contribution *RelativeFSR* corresponds to an uncertainty in the η-dependent corrections for ISR and FSR.
- The statistical uncertainties in the determination of the relative corrections in various regions of η for multiple uncertainty sources are merged into one uncer-

tainty (*RelativeStat*).

- Differences in the simulated detector response to jets from different quark flavours and gluons result in the *FlavourQCD* uncertainty. It is derived from differences between data and MC simulations when the corresponding corrections are applied to various mixtures of jet flavours. The uncertainty is based on response differences to jets from uds/c/b quarks and gluons between PYTHIA [129] and HERWIG [393].
- Two time-dependent uncertainties address the JES variation over time during the data-taking periods (*TimePt* and *TimeEta*).
- Uncertainties associated with the pileup corrections are included.

Additional uncertainties specific to each individual measurement are discussed in the original publications [103–106, 148].

The correlation scheme for JES-related uncertainties across the various CMS measurements used in this analysis is outlined below. Uncertainties related to pileup, the relative statistical contribution (*RelativeStat*), and the time-dependent sources (*TimePt* and *TimeEta*) are treated as uncorrelated across measurements, as they depend on specific data-taking periods. For the measurement at $\sqrt{s} = 7$ TeV [103], a reanalysis of the JES and JER systematic uncertainties was conducted as part of the QCD analysis [104]. The correlation scheme for JES-related uncertainties, as defined in the reanalysis, is applied. Specifically, the *SinglePionECAL* and *SinglePionHCAL* uncertainty sources are decorrelated as a function of η [104]. The correlations in the remaining JES uncertainties between different measurements are implemented and described below following the exact same convention used in the publication [346], which is based on the work presented in this thesis.

- The *AbsoluteMPFBias* uncertainty is fully correlated between the 2.76, 8, and 13 TeV measurements. In the 7 TeV analysis, a combined source of uncertainty is used by including uncertainties from the *AbsoluteScale*, ISR and FSR, and a statistical component associated with the *AbsoluteScale* correction [104]. This combined source of uncertainty in the 7 TeV analysis is uncorrelated with uncertainties in the other measurements.
- The *AbsoluteScale*, *SinglePionECAL*, *SinglePionHCAL*, and *RelativeJER* uncertainties are fully correlated between the 2.76 and 8 TeV measurements, since the corresponding corrections were obtained using 8 TeV data and applied to

both measurements. These uncertainties are uncorrelated with other data sets for which the corrections were specifically derived.

- The *RelativeFSR* and *Fragmentation* uncertainties are fully correlated between the 2.76, 7, and 8 TeV measurements, but uncorrelated with the 13 TeV measurement, because of the use of different MC tunes and event generators.
- The *RelativePt* uncertainties are uncorrelated across the measurements, since these account for the differences between linear and logarithmic fits in the p_{T} extrapolation of the residual corrections, which vary across data-taking periods.
- The *FlavorQCD* uncertainty is treated as fully correlated between the 7 and 8 TeV measurements, but uncorrelated with the 2.76 and 13 TeV ones.

While the JER uncertainties are considered uncorrelated across the measurements at different $\sqrt{s}$, the correlations of these uncertainties within each measurement have been investigated. In particular, the JER uncertainties have been decorrelated in $|y|$ for the measurements at 2.76, 7, and 8 TeV, because a residual $|y|$ dependence of these data sets was not fully accounted for. A further uncorrelated component of 1.5% is added to the JER uncertainty in the 2.76 TeV measurement to account for a statistical contribution to the JER uncertainty.

6.3 Theoretical predictions for inclusive jets

Theoretical predictions for inclusive jet production in pp collisions are available at NNLO via the NNLOJet program [394–396]. These calculations assume five active massless quark flavours in the leading-colour (LC) and leading-flavour-number approximation. The subleading colour contributions to the NNLO corrections, which were neglected in Ref. [394], have been recently calculated [397]. These contributions have been shown to have a very small impact on inclusive jet production with $R = 0.7$. The scales μ_{r} and μ_{f} are set to the individual jet p_{T}, which was found to be a better scale choice than the leading-jet transverse momentum p_{T}^{max} in Ref. [395].

The predictions for the jet cross section across different intervals of p_{T} and $|y|$ are encoded as interpolation grids in the APPLfast [145] format. This format enables fast evaluation of the predictions when varying α_S, PDFs, or the μ_{r} and μ_{f} scales. The associated numerical uncertainty in the grids is generally below 1% for most intervals, increasing to approximately 5% in the forward region at high p_{T}, which remains con-

siderably smaller than the statistical uncertainties of the measurements. However, in the forward region, certain intervals at the highest p_{T} values exhibit grid uncertainties greater than 10%, and these are excluded from the QCD interpretation. Further, following the recommendations from the NNLOJet authors, the statistical uncertainties in the theory predictions are doubled to account for point-to-point fluctuations. However, their impact in the QCD analysis is negligible.

The pQCD predictions are corrected multiplicatively for the electroweak contributions, stemming from the virtual exchange of soft or collinear massive weak gauge bosons, computed at NLO precision [398]. The impact of EW effects becomes more pronounced at high jet p_{T}. These effects reach 11% at the highest p_{T} probed in the 13 TeV measurement and rise to 25% at the highest p_{T} reached by the 7 TeV measurement. Subleading EW effects from the emissions of real weak gauge bosons have been evaluated in the 13 TeV measurement and found to be less than 1% at high p_{T}. The EW corrections for the CMS inclusive jet production cross sections are illustrated in Figure 6.5. For the 13 TeV measurement, these corrections are taken from the original publication [106], while for the 7 and 8 TeV measurements, they have been recently updated by the authors of Ref. [398] using the latest PDF sets. For the 2.76 TeV measurement, EW corrections are not calculated, as their effect is negligible for $p_{\mathrm{T}} < 600$ GeV, which is the maximum p_{T} reached in this measurement.

Finally, to compare the fixed-order predictions to the measured particle-level cross sections, the former are corrected for the nonperturbative (NP) effects from hadronisation (HAD) and the multiparton interactions (MPI). The NP corrections have been derived as ratios of the cross sections, simulated with the same MC generator+PS, where NP effects are switched on and off, respectively:

$$\mathrm{NP} = \frac{\sigma^{\mathrm{MC}}(\mathrm{PS}\ \&\ \mathrm{MPI}\ \&\ \mathrm{HAD})}{\sigma^{\mathrm{MC}}(\mathrm{PS})}. \tag{6.5}$$

At low p_{T}, the NP corrections are mainly driven by MPI, which increase the radiation in the jet cone by a constant offset. This effect is particularly significant for large R, relevant for the presented analysis. On the other hand, hadronisation effects become more important at smaller R.

The pQCD predictions are corrected by NP effects through p_{T}- and $|y|$-dependent correction factors, as provided in the original publications of the individual measure-

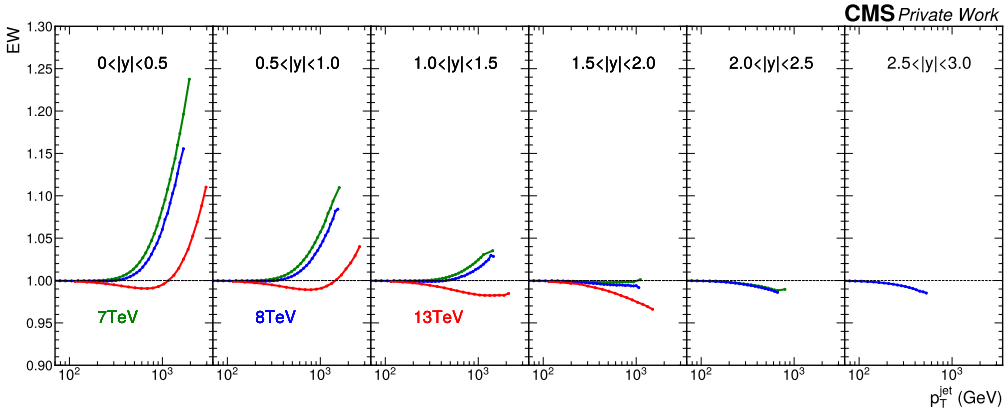

Figure 6.5: The EW corrections for the different inclusive jet measurements.

ments. In each measurement, the NP corrections are derived using the generator tune that best matches the data. In the measurement at 2.76 TeV, the NP effects are derived using PYTHIA 6 (v.6.4, tune Z2) [378, 379], and, alternatively, HERWIG ++ (v.2.5.0, tune UE EE 3C) [393,399] and averaging the results. In the measurement at 7 TeV, the NP corrections are estimated similarly using the event generators PYTHIA 6 (tune Z2) and HERWIG ++ (v.2.4.2) [393]. In the measurement at 8 TeV, the NP effects are determined using LO and NLO event generators and averaging the results. At LO, the NP correction is evaluated by averaging results obtained by using PYTHIA 6 (v.4.26, tune Z2*) [378] and HERWIG ++ (v.2.4.2, tune UE) [393,400]. The NLO NP correction is derived using POWHEG [110,111,113,401], interfaced with PYTHIA 6 with tunes Z2* and P11 [402] and averaging the results. The NP uncertainty is taken as half the width of the envelope of NP values obtained using LO and NLO generators. In the measurement at $\sqrt{s} = 13$ TeV, the NP effects are derived using PYTHIA 8 (CP1 tune) [123] and HERWIG ++ (EE5C tune) [403] and fitting them with a smooth p_T-dependent function. The final correction is obtained from the resulting envelope with the central value taken as the average of the envelope and the uncertainties from its edges. The NP corrections for the CMS inclusive jet production cross sections at the different $\sqrt{s}$ are illustrated in Figure 6.6. These corrections vary between 5 and 20% at low p_T, with their effect decreasing as p_T rises. The related uncertainties vary between 1 and 5% at low p_T, depending on $|y|$, and become negligible at high p_T.

The uncertainties related to the NP corrections are treated as correlated bin-to-bin

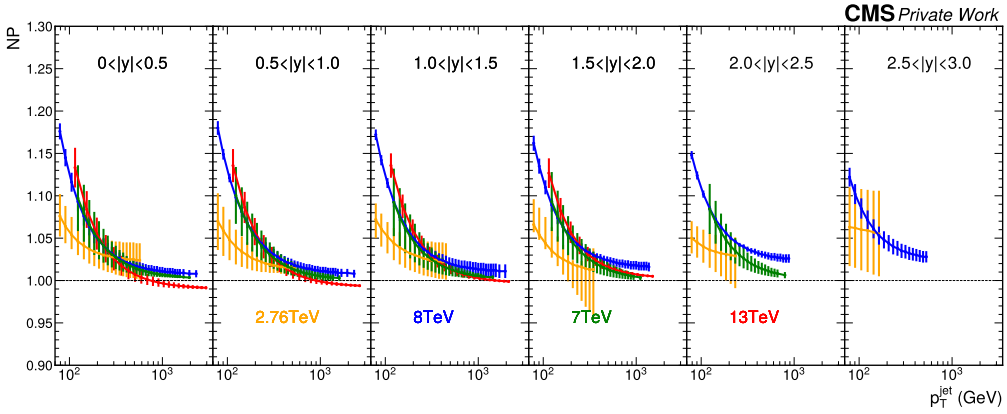

Figure 6.6: The NP corrections for the different inclusive jet measurements.

and uncorrelated across the measurements. Despite slight differences in the way the NP corrections were derived for each measurement, the impact of the NP corrections in the $\alpha_S(m_Z)$ determination is insignificant when the associated uncertainties are considered. To evaluate the impact of the NP corrections on the QCD analysis, individual fits were performed using subsets of measurements with jet p_T values greater than 150, 200, and 300 GeV. This approach allows for probing kinematic ranges where the importance of NP corrections decreases. The resulting differences are found to be negligible.

Finally, the CMS jet data used in the present QCD analysis are compared to the theoretical predictions at NNLO corrected by NP and EW effects in Figure 6.7.

6.4 QCD analysis

In the QCD analysis, the inclusive DIS NC and CC cross sections and the CMS jet data, described in the Section 6.2, are used together to constrain simultaneously the proton PDFs and $\alpha_S(m_Z)$. Theoretical predictions for the DIS cross sections are computed at fixed order in QCD at NNLO accuracy using the QCDNUM code [365], with μ_r and μ_f set to the squared four-momentum transfer Q^2. The NNLO predictions for jet productions, described in Section 6.3 are used, with the scales $\mu_f = \mu_r$ set to the individual jet p_T. The contribution of heavy c and b quarks to the DIS cross sections is treated in the Thorne–Roberts GM–VFN scheme [362–364]. The pole masses of c

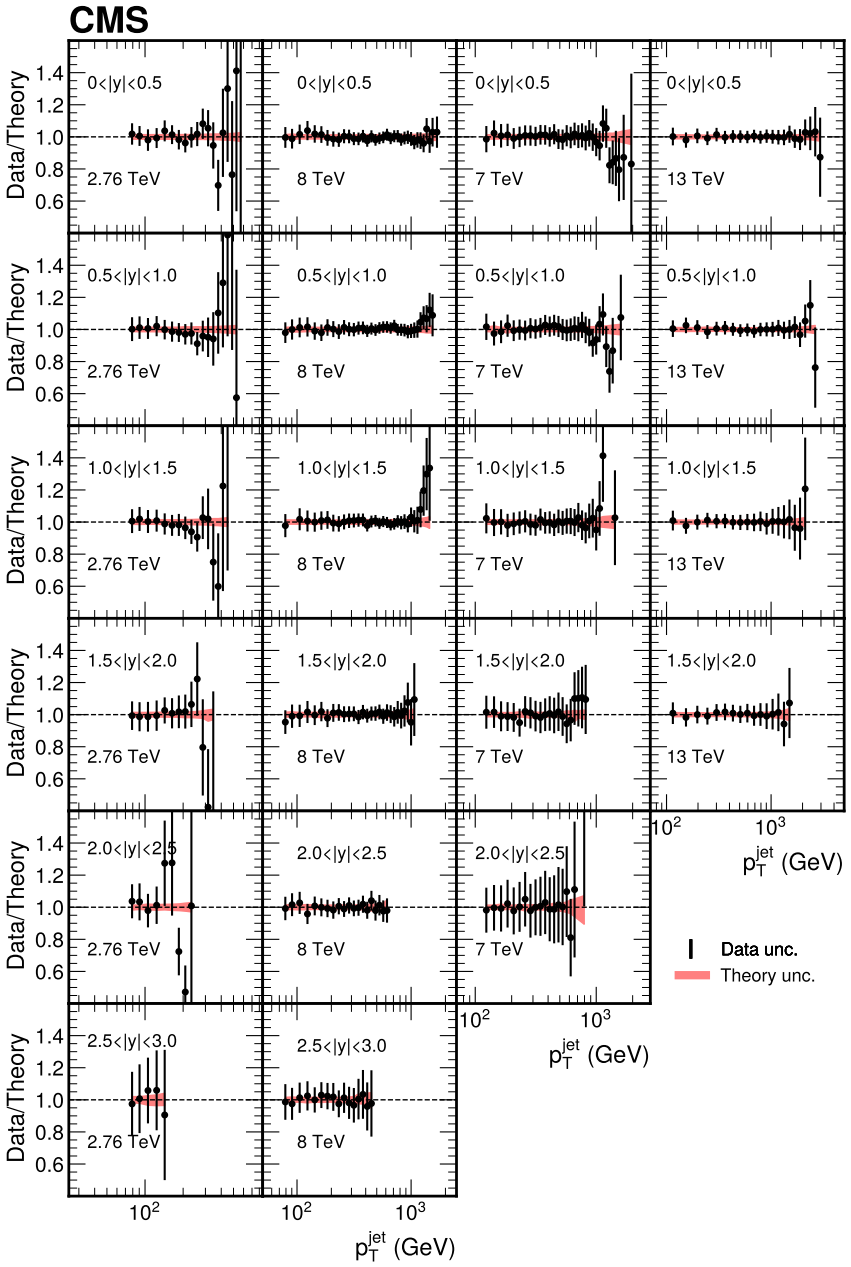

Figure 6.7: Cross section ratios between data and theory for inclusive jet production in pp collisions as measured by CMS at $\sqrt{s}$ of 2.76, 8, 7, and 13 TeV, using the anti-k_T clustering algorithm with $R = 0.7$, as functions of individual jet p_T in intervals of absolute rapidity $|y|$. Shown is the total uncertainty of every data point (vertical bar). Predictions correspond to the NNLO LC QCD calculations corrected for NP and EW effects. The total theory uncertainty (red shaded band) includes the PDF and scale variation uncertainties. Published in Ref. [346].

and b quarks are fixed to $m_{\mathrm{c}} = 1.47$ GeV and $m_{\mathrm{b}} = 4.5$ GeV, respectively, as given in Table 6.2. To avoid tension between the low-Q^2 and high-Q^2 region as shown in the original publication [91], only DIS data with $Q^2 > 10\,\mathrm{GeV}^2$ are included in the fit.

The parametrisation from the latest NNLO QCD analysis [106] of the CMS inclusive jet production measurement at 13 TeV is used since these data are most precise and access the highest jet p_{T}, thereby having the highest sensitivity to α_S, as shown in Figure 6.3. At the starting scale $Q_0^2 = 1.9\,\mathrm{GeV}^2$, the functional forms of the PDFs are:

$$xg(x) = A_{\mathrm{g}} x^{B_{\mathrm{g}}}(1-x)^{C_{\mathrm{g}}}(1 + D_{\mathrm{g}}x + E_{\mathrm{g}}x^2), \tag{6.6}$$

$$x\mathrm{u}_v(x) = A_{\mathrm{u}_v} x^{B_{\mathrm{u}_v}}(1-x)^{C_{\mathrm{u}_v}}(1 + E_{\mathrm{u}_v}x^2), \tag{6.7}$$

$$x\mathrm{d}_v(x) = A_{\mathrm{d}_v} x^{B_{\mathrm{d}_v}}(1-x)^{C_{\mathrm{d}_v}}, \tag{6.8}$$

$$x\overline{\mathrm{u}}(x) = A_{\overline{\mathrm{u}}} x^{B_{\overline{\mathrm{u}}}}(1-x)^{C_{\overline{\mathrm{u}}}}(1 + D_{\overline{\mathrm{u}}}x), \tag{6.9}$$

$$x\overline{\mathrm{d}}(x) = A_{\overline{\mathrm{d}}} x^{B_{\overline{\mathrm{d}}}}(1-x)^{C_{\overline{\mathrm{d}}}}(1 + E_{\overline{\mathrm{d}}}x^2), \tag{6.10}$$

where the relations $x\overline{\mathrm{U}}(x) = x\overline{\mathrm{u}}(x)$ and $x\overline{\mathrm{D}}(x) = x\overline{\mathrm{d}}(x) + x\overline{\mathrm{s}}(x)$ are assumed for the up, down, and strange antiquarks $x\overline{\mathrm{u}}(x)$, $x\overline{\mathrm{d}}(x)$, and $x\overline{\mathrm{s}}(x)$. The sea quark distribution is defined by the relation $x\Sigma(x) = 2x\overline{\mathrm{u}}(x) + x\overline{\mathrm{d}}(x) + x\overline{\mathrm{s}}(x)$. Following Ref. [91], the normalisations of $x\overline{\mathrm{u}}$ and $x\overline{\mathrm{d}}$ in the limit $x \to 0$ are assumed to be the same by imposing the conditions $B_{\overline{\mathrm{U}}} = B_{\overline{\mathrm{D}}}$ and $A_{\overline{\mathrm{U}}} = A_{\overline{\mathrm{D}}}(1 - f_{\mathrm{s}})$. Here, $f_{\mathrm{s}} = \overline{\mathrm{s}}/(\overline{\mathrm{d}} + \overline{\mathrm{s}})$ is the strangeness fraction and is assumed to be 0.4 as in Ref. [91] and as given in Table 6.2, which is in agreement with the CMS measurement of W+c production at 8 and 13 TeV [100,101].

Following the HERAPDF [91] approach, the uncertainties outlined below are considered in the full QCD fit:

- The *fit uncertainties* in $\alpha_S(m_{\mathrm{Z}})$ and the PDF parameters correspond to the statistical and experimental uncertainties in the measurements. The fit uncertainties are estimated through the Hessian method [366] implying the tolerance criterion $\Delta\chi^2 = 1$, which corresponds to the 68% confidence level (CL).
- The *scale uncertainty* stems from an estimate of missing higher-order corrections. It is obtained by varying the renormalisation and factorisation scales up and down independently by a factor of 2, avoiding cases with $\mu_{\mathrm{f}}/\mu_{\mathrm{r}} = 4$ or $1/4$. For each scale choice, an individual fit is performed where the scale variations are applied only to the jet data, and the maximum difference with respect to

the central result is considered as an uncertainty.

- The *model uncertainties* are determined by varying the fit input parameters, such as the heavy quark masses m_b and m_c, the strangeness fraction f_s, the minimum Q^2_min imposed on the HERA data, and the starting scale Q^2_0, within their uncertainties. The central values and variation ranges of the model input parameters are summarised in the Table 6.2. The total model uncertainty is obtained by summing the different contributions in quadrature.

Table 6.2: The central value and the corresponding upper and lower limits of the variations used to determine model uncertainties.

Parameter	Central value	Lower limit	Upper limit
m_b	4.50 GeV	4.25 GeV	4.75 GeV
m_c	1.47 GeV	1.41 GeV	1.53 GeV
Q^2_min	10 GeV^2	7.5 GeV^2	12.5 GeV^2
Q^2_0	1.9 GeV^2	1.7 GeV^2	2.1 GeV^2
f_s	0.40	0.32	0.48

- The *parametrisation uncertainty* is assessed by extending the functional form of the PDFs with additional parameters, D and E, added one at a time. The uncertainty is then determined from the envelope of the results obtained from the corresponding fits.

Finally, the *total uncertainty* is then estimated by summing the fit, model and scale uncertainties in quadrature and the parametrisation uncertainty linearly.

6.5 Results on PDFs and $\alpha_S(m_\mathrm{Z})$

The comparison between data and theory predictions after the fit is shown in Figure 6.7. Overall, a very good agreement is observed. The consistency of all the experimental data is quantified by the goodness of the fit χ^2 from Eq. (6.2). The values of χ^2 per $\mathrm{N_{dp}}$ are reported for the individual data sets (partial $\chi^2/\mathrm{N_{dp}}$) in Table 6.3, along with the total χ^2 per number of degrees of freedom $\mathrm{N_{dof}}$, which is 1680/1453. These values demonstrate a good agreement among all the data sets. The sum of partial $\chi^2/\mathrm{N_{dp}}$ for all CMS jet measurements is 427/453, further indicating good compatibility among the jet data. A slightly higher partial $\chi^2/\mathrm{N_{dp}}$ for the HERA DIS data has been examined in detail in the original study [91], which identified tensions between measurements at low and high Q^2.

Table 6.3: The values of χ^2 per N_{dp} for each individual data set as obtained in the fit to HERA and CMS jet data, together with the contribution to the χ^2 from correlated uncertainty sources. In the last line, the total χ^2 per number of degrees of freedom, N_{dof}, is reported.

Data set	Partial χ^2/N_{dp}
HERA I+II neutral current	1036/935
HERA I+II charged current	112/81
CMS jets 2.76 TeV	63/80
CMS jets 7 TeV	81/130
CMS jets 8 TeV	206/165
CMS jets 13 TeV	77/78
Correlated χ^2	125
Total χ^2/N_{dof}	1680/1453

The impact of the CMS jet data on the PDF determination fit (*HERA+CMS fit*) is illustrated in Figure 6.8. The Hessian fit uncertainties in the PDFs are compared to the results of an alternative fit, where only the HERA data are included (*HERA-only fit*). In the HERA-only fit, because of poor sensitivity of the DIS data to $\alpha_S(m_Z)$, its value is fixed to that of the HERA+CMS fit. The PDFs are shown at the factorisation scale $Q^2 = m_t^2$, where m_t is the top quark mass. A notable reduction in the uncertainties in all PDFs is achieved when CMS jet measurements are used.

Additionally, the PDF uncertainties of the present QCD analysis are compared to those from the previous QCD analysis based solely on the 13 TeV measurement in Figure 6.9. While the previous QCD studies based on individual jet measurement have already observed improved precision in the gluon PDF, the inclusion of all available CMS inclusive jet measurements at different $\sqrt{s}$ provides further improved constraints in the d_v distribution, as shown in Figure 2.8.

In Figure 6.10, the PDFs obtained in the present analysis (HERA+CMS fit) are compared with results of different PDF groups HERAPDF20 [91], NNPDF40 [89], CT18NNLO [88], and MSHT20 [87]. Among the data explored in the global PDF fits NNPDF40, CT18NNLO, MSHT20, the HERA data are always used as a backbone. Furthermore, the PDF sets NNPDF40, CT18NNLO, MSHT20 use also the CMS jet data at $\sqrt{s} = 8$ TeV, $\sqrt{s} = 7,\ 8$ TeV, $\sqrt{s} = 2.76,\ 7,\ 8$ TeV, respectively. By def-

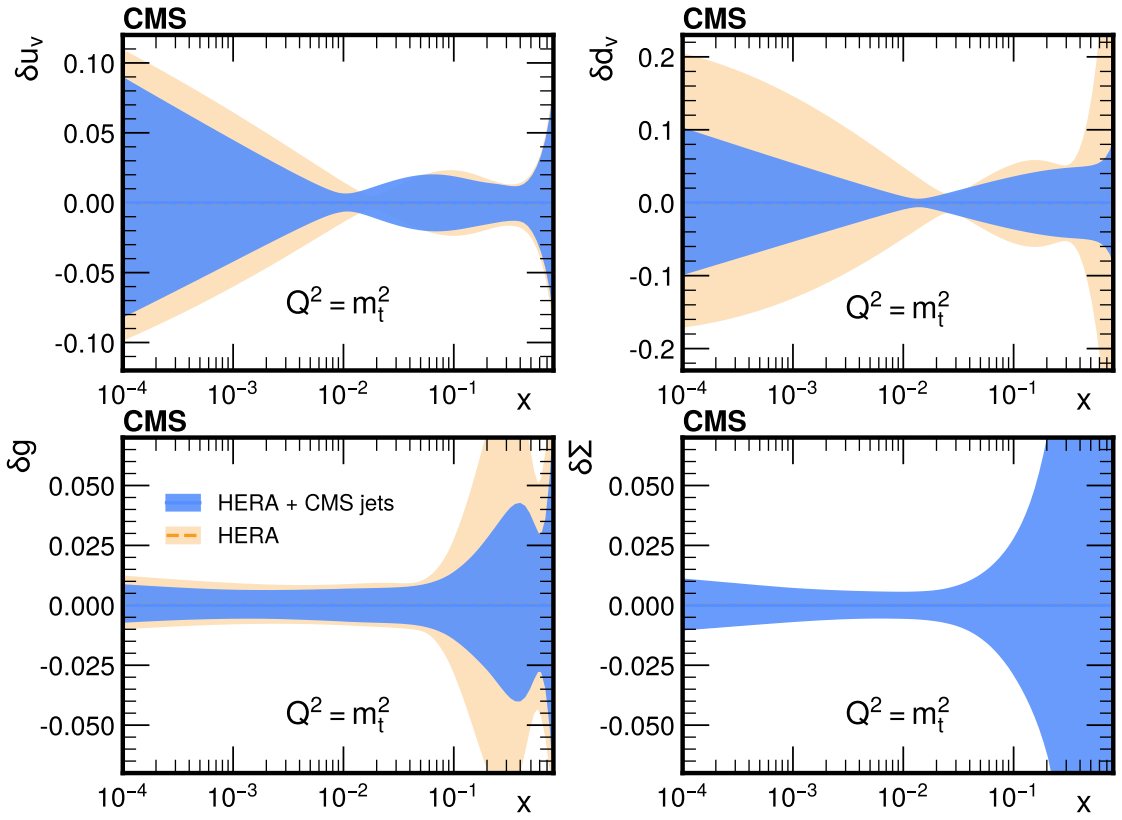

Figure 6.8: The fit uncertainties in the valence u quark (u_v) (upper left), valence d quark (d_v) (upper right), gluon g (lower left), and sea quark Σ (lower right) distributions, shown as a function of x at the factorisation scale $Q^2 = m_t^2$. The results of the HERA+CMS fit (blue shaded area) are compared with the results of the HERA-only fit (orange shaded area). In the HERA-only fit, because of the poor sensitivity of the DIS data to $\alpha_S(m_Z)$, its value is fixed to that of the HERA+CMS fit. The uncertainties are given at 68% CL. Published in Ref. [346].

inition, HERAPDF2.0 is based exclusively on HERA DIS data. Overall, the PDFs extracted in this analysis are in reasonable agreement with the global PDF sets in the x range probed by the CMS jet data. As compared to the HERAPDF2.0, the present fit results in significantly improved agreement with the global PDFs, in particular, in the valence quark distribution, which is expected since jet production in pp collisions (in particular at lower $\sqrt{s}$) probes not only the gluon, but also the light quark distributions, see Figure 2.8.

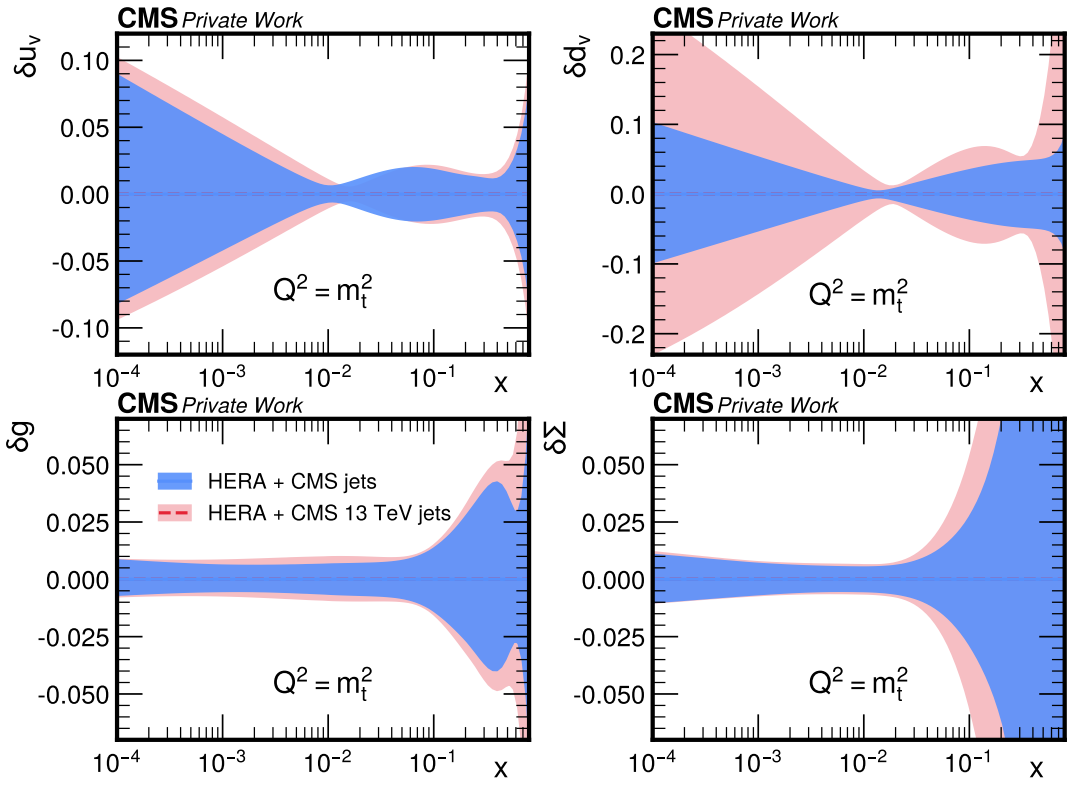

Figure 6.9: Same as Figure 6.8, where the HERA+CMS fit (blue shaded area) is compared to the HERA+CMS 13 TeV fit (red shaded area).

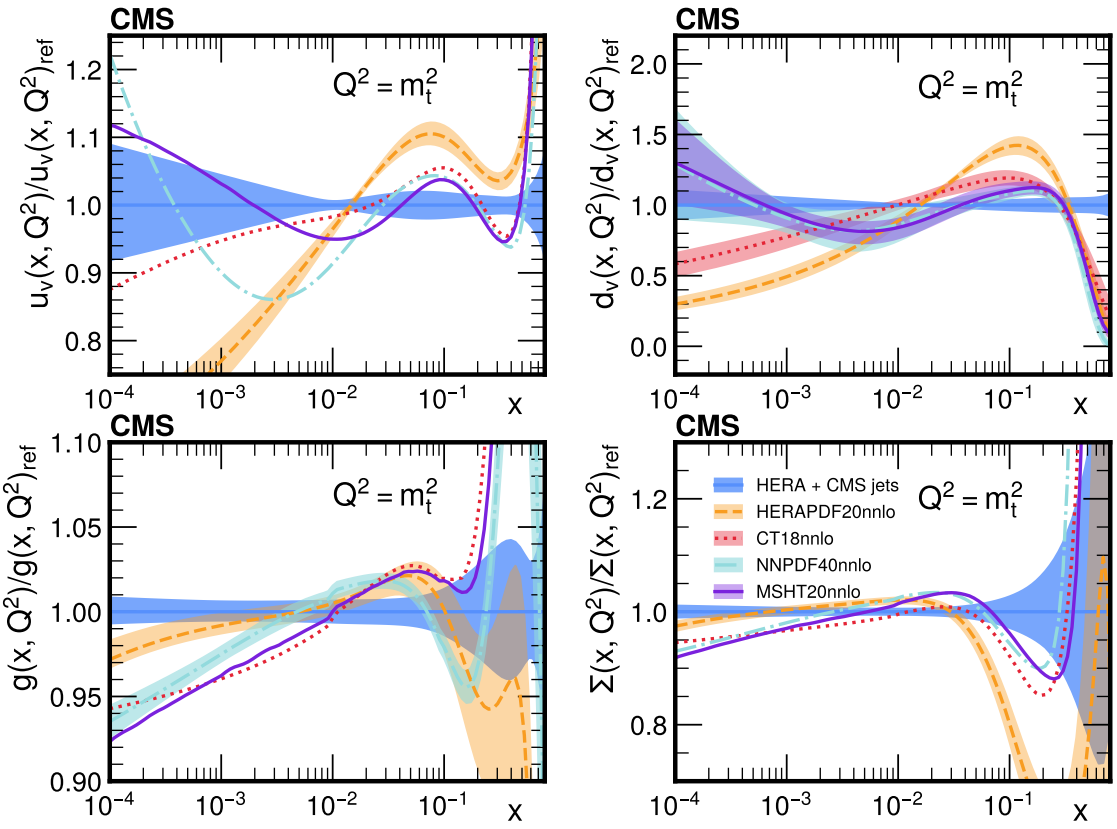

Figure 6.10: Ratios of different global PDF sets at NNLO, namely HERAPDF20 [91], CT18 [88], NNPDF4 [89], and MSHT20 [87], to the result of the present study. The valence u quark (u_v) (upper left), valence d quark (d_v) (upper right), gluon g (lower left), and sea quark Σ (lower right) distributions are shown as functions of x at the factorisation scale $Q^2 = m_t^2$. Only the Hessian PDF uncertainties at 68% CL are shown, where the width of the band represents the uncertainty in the numerator by keeping the denominator constant. Published in Ref. [346].

The strong coupling constant, extracted simultaneously with the PDFs, results in

$$\alpha_S(m_Z) = 0.11759^{+0.0009}_{-0.0009}\,(\text{fit})^{+0.0006}_{-0.0004}\,(\text{model})^{+0.0009}_{-0.0012}\,(\text{scale})^{+0.}_{-0.00004}\,(\text{param.}), \quad (6.11)$$

corresponding to the total uncertainty of $^{+0.0014}_{-0.0016}$ (tot). This value is in good agreement with the PDG world average of $\alpha_S(m_Z) = 0.1180 \pm 0.0009$ [59] and with previous CMS results obtained at NNLO [106, 107, 137–139], as shown in Figure 6.11. While

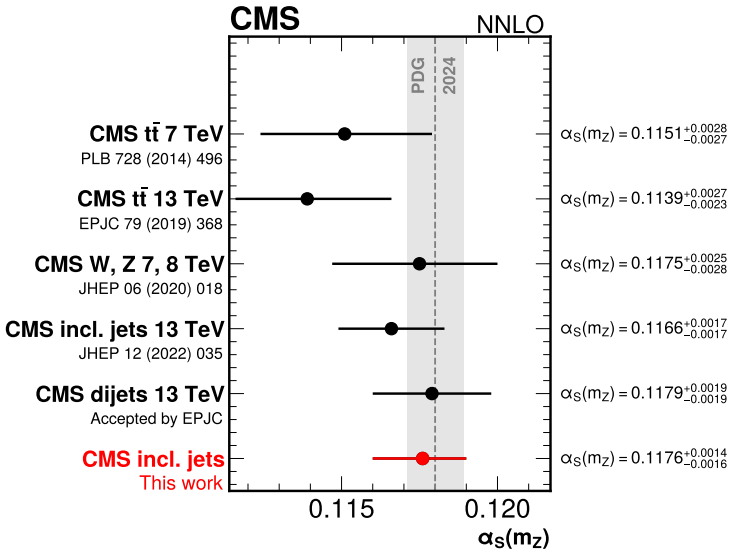

Figure 6.11: The value of $\alpha_S(m_Z)$ obtained in this analysis (red marker), compared with all CMS results obtained at NNLO by using different methods (black markers) with their total uncertainties (horizontal error bars). The PDG world average (dashed line) together with its uncertainty (shaded band) is also shown. Published in Ref. [346].

the $\alpha_S(m_Z)$ result of 13 TeV measurement was dominated by the fit uncertainty [106], including data from multiple $\sqrt{s}$ improves precision by reducing the fit uncertainty by approximately 35%. This result is the most precise determination of $\alpha_S(m_Z)$ from jet measurements, to date, and is limited by the missing higher-order corrections for $\sqrt{s} < 13$ TeV.

6.6 Running of α_S

Using the approach outlined in Section 6.4, the value of α_S is extracted in five distinct intervals of $\mu_r = p_T$, demonstrating its scale dependence, $\alpha_S(\mu_r)$, at NNLO. The CMS measurements of inclusive jet production are divided into exclusive p_T intervals

of individual jet p_{T}. For each p_{T} range, a simultaneous fit of PDFs and $\alpha_S(m_{\mathrm{Z}})$ is performed. Each extracted value of $\alpha_S(m_{\mathrm{Z}})$ is subsequently evolved to $\alpha_S(\mu_{\mathrm{r}})$ via the five-loop, five-flavour renormalisation group equation (RGE) as implemented in CRunDec [404], version 0.5.2, which is also used to determine the associated uncertainties. The fit, model, scale, and parametrisation uncertainties are evaluated following the procedure applied in Eq. (6.11). For every p_{T} interval, μ_{r} is computed at NNLO QCD as a cross section-weighted mean $\langle p_{\mathrm{T}} \rangle$, where the contribution of each measurement is weighted by the corresponding luminosity. The results are presented in Table 6.4 and Figure 6.12, where the extracted $\alpha_S(\mu_{\mathrm{r}})$ values are compared to the five-loop QCD evolution of the world-average $\alpha_S(m_{\mathrm{Z}})$, as obtained using CRunDec. The observed running of α_S is in agreement with the prediction of the QCD renormalisation group equation and is tested up to energy scales of 1.6 TeV.

Table 6.4: The determined $\alpha_S(m_{\mathrm{Z}})$ and the corresponding $\alpha_S(Q)$ values for each p_{T} range with their total uncertainties. For $\alpha_S(Q)$, the individual uncertainty contributions (fit, scale, model, parametrisation) are listed.

p_{T}(GeV)	$\langle Q \rangle$	$\alpha_S(m_{\mathrm{Z}})$ (tot)	$\alpha_S(Q)$	(fit)	(scale)	(model)	(param.)	(tot)
74–220	103.06	$0.1182\ ^{+0.0014}_{-0.0013}$	0.1160	$^{+0.0011}_{-0.0011}$	$^{+0.0007}_{-0.0005}$	$^{+0.0006}_{-0.0004}$	$^{+0.0}_{-0.0}$	$^{+0.0014}_{-0.0012}$
220–395	266.63	$0.1184\ ^{+0.0011}_{-0.0012}$	0.1019	$^{+0.0007}_{-0.0007}$	$^{+<0.0001}_{-0.0004}$	$^{+0.0004}_{-0.0003}$	$^{+0.0}_{-<0.0001}$	$^{+0.0008}_{-0.0009}$
395–638	464.31	$0.1179\ ^{+0.0013}_{-0.0012}$	0.0947	$^{+0.0007}_{-0.0007}$	$^{+0.0003}_{-<0.0001}$	$^{+0.0004}_{-0.0003}$	$^{+0.0}_{-<0.0001}$	$^{+0.0009}_{-0.0008}$
638–1410	753.66	$0.1184\ ^{+0.0014}_{-0.0012}$	0.0898	$^{+0.0006}_{-0.0006}$	$^{+0.0003}_{-<0.0001}$	$^{+0.0004}_{-0.0003}$	$^{+<0.0001}_{-0.0}$	$^{+0.0008}_{-0.0007}$
1410–3103	1600.5	$0.1170\ ^{+0.0021}_{-0.0016}$	0.0821	$^{+0.0007}_{-0.0007}$	$^{+0.0004}_{-0.0}$	$^{+0.0005}_{-0.0003}$	$^{+<0.0001}_{-0.0}$	$^{+0.0010}_{-0.0008}$

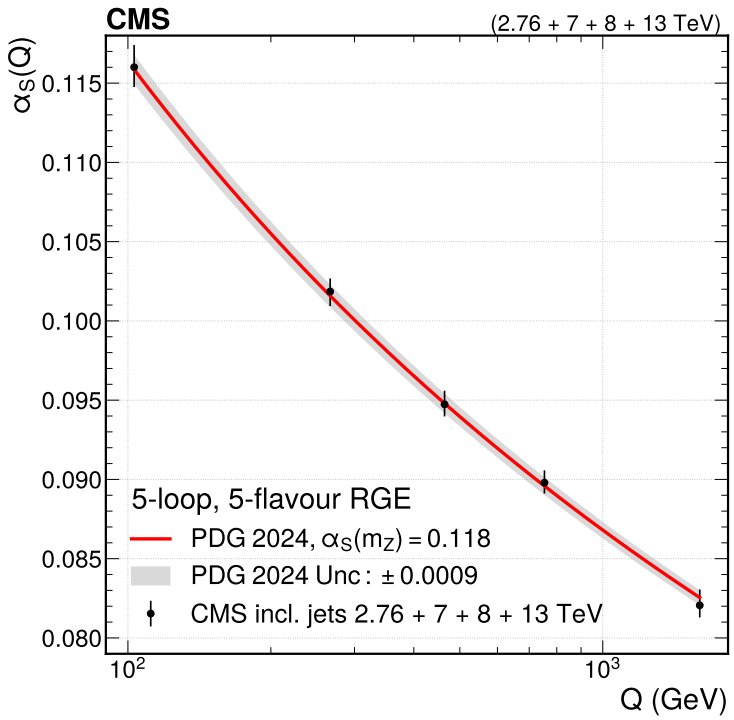

Figure 6.12: Values of α_S as extracted from different jet p_{T} ranges in the present QCD analysis at NNLO, each translated to a single scale $\langle Q \rangle$, as indicated in Table 6.4. The results (black markers) are shown with their total uncertainties (vertical error bars). For comparison, the RGE at 5 loops is shown using the current world-average value $\alpha_S(m_{\mathrm{Z}}) = 0.1180 \pm 0.0009$ [59] (red line) together with its associated total uncertainty (shaded band). Published in Ref. [346].

Chapter 7

Summary and conclusions

This thesis presents a precise determination of $\alpha_S(m_Z)$ and lays the foundation for a precise measurement of m_t and Γ_t that promises significant constraints on the stability of the vacuum. The extraction of $\alpha_S(m_Z)$ from jet rates is the most precise, to date, and has been achieved through a comprehensive QCD analysis at NNLO. The running of α_S up to an energy scale of 1.6 TeV is demonstrated. The measurement of m_t^{MC} and Γ_t is performed using $t\bar{t}+tW$ events, taking into account the interference between $t\bar{t}$ and tW processes.

For the first time, the CMS inclusive jet measurements obtained in pp collisions at $\sqrt{s} = 2.76,\ 7,\ 8$, and 13 TeV have been analysed together, assessing the correlations among the different data sets. The simultaneous extraction of $\alpha_S(m_Z)$ and PDFs has been performed through a comprehensive NNLO QCD analysis, combining CMS jet data with HERA deep inelastic scattering measurements. This approach properly accounts for the correlation between PDFs and $\alpha_S(m_Z)$, in contrast to many determinations of $\alpha_S(m_Z)$ at the LHC suffering from the dependence on the choice of the PDF set. The resulting value, $\alpha_S(m_Z) = 0.1176^{+0.0014}_{-0.0016}$, is the most precise obtained from the jet rates, to date. In addition, the reevaluated systematic correlations among the CMS jet measurements is recommended for future use of these data in global PDF fits. The results presented in this part of the thesis were published in the *Physics Letters B* [346], and the author of this thesis is the contact person for the publication.

The determination of m_t^{MC} and Γ_t from the differential cross section of $t\bar{t}+tW$ pro-

cess as a function of the $m_{\ell \mathrm{b}}$ unfolded to the particle level has been performed using an Asimov pseudo-data as a precursor to a measurement with data that will soon be unblinded. This analysis is based on data obtained in the LHC pp collision at $\sqrt{s} = 13$ TeV, collected by the CMS experiment during 2017–2018. The values of $m_{\mathrm{t}}^{\mathrm{MC}} = 172.61^{+0.41}_{-0.44}$ GeV and $\Gamma_{\mathrm{t}} = 1.36^{+0.24}_{-0.28}$ GeV are obtained. Therefore, are expected improved precision in Γ_{t} compared to direct measurements obtained with the bb4l method [177, 178]. The $m_{\mathrm{t}}^{\mathrm{MC}}$ result is as precise as the most accurate single-experiment direct $m_{\mathrm{t}}^{\mathrm{MC}}$ measurement [168] and represents the first determination of $m_{\mathrm{t}}^{\mathrm{MC}}$ from the combined $\mathrm{t\bar{t}}$ and tW cross sections within the CMS Collaboration. This analysis is the first of its kind within the CMS experiment, employing the state-of-the-art event generator bb4l and is currently under review by the collaboration.

In the HL–LHC era, the integrated luminosity is expected to increase by a factor of 10 or more compared to its current value. As a result, the volume of data, and consequently, the number of events to be simulated will rise, to ensure that the statistics of the simulated samples do not become a limiting factor in precision analyses. As a result, the major challenge of the HL–LHC will be to manage the high computational demand. This is already an issue for ongoing high-precision analyses since various simulated samples need to be generated to estimate the modelling uncertainties. In this thesis, a ML-based method has been applied to reweight the MC simulations to account for variations in model parameters and the simulation model itself. The excellent performance of the method was show-cased using $\mathrm{t\bar{t}}$ production scenario in the environment of the CMS experiment. As a result, the number of MC samples can be significantly reduced, decreasing CPU usage by up to 75% for each MC variation [15, 16]. This result of the thesis was published in the *European Physical Journal C* [231], and the author of this thesis is the contact person for the publication.

In conclusion, this thesis has addressed the extraction of the α_S, proton PDFs, and top quark mass $m_{\mathrm{t}}^{\mathrm{MC}}$, and width Γ_{t}. The impact of the results on prediction for the Higgs quartic coupling λ as a function of the energy scale, and in turn on the stability of the electroweak vacuum, is demonstrated in Figure 7.1, obtained by using the open-source program of Ref. [406]. To account for the relation between $m_{\mathrm{t}}^{\mathrm{MC}}$ and $m_{\mathrm{t}}^{\mathrm{pole}}$, an additional uncertainty of 0.5 GeV is considered [169, 405]. The value of the Higgs boson mass has been set to the world average $m_{\mathrm{H}} = 125.20$ GeV [6]. The precision of λ is comparable to that of the results based on the world average values of $\alpha_S(m_{\mathrm{Z}})$

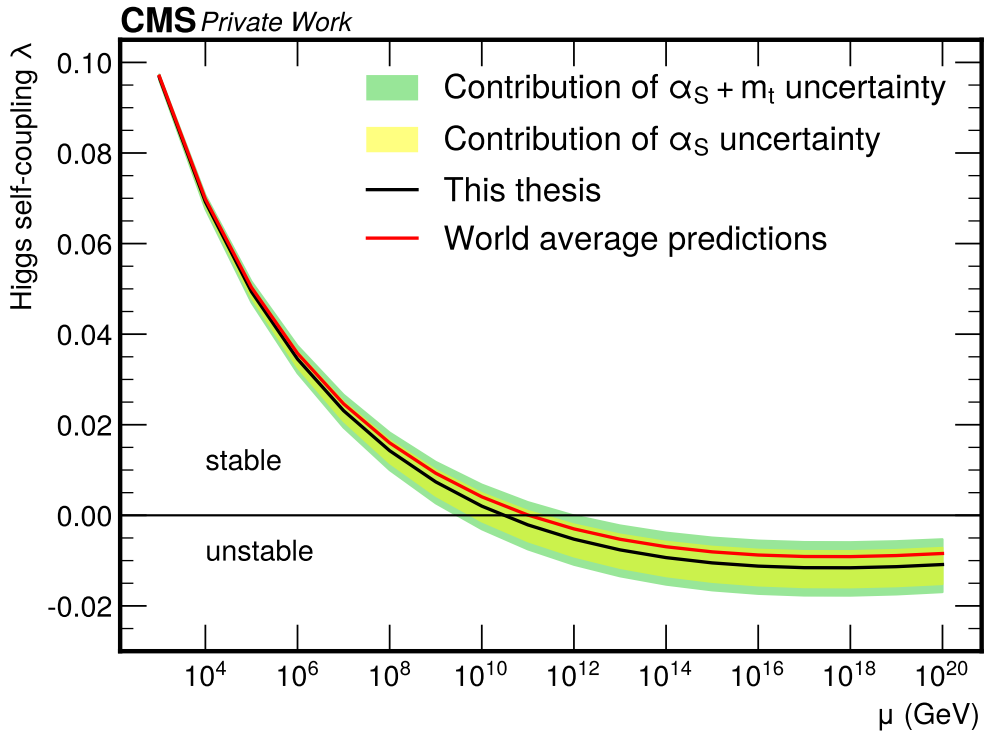

Figure 7.1: The evolution of the Higgs quartic coupling λ as a function of the scale μ. The results of $\alpha_S(m_Z)$ and m_t^{MC} obtained in this thesis are used, including their $\pm 1\sigma$ uncertainty. To account for the relation between m_t^{MC} and m_t^{pole}, an additional uncertainty of 0.5 GeV is considered [169, 405]. The prediction is obtained by using the open-source program mr [406].

and m_t^{pole}. The value of $\alpha_S(m_Z)$ obtained in this thesis will soon be included in the Particle Data Group (PDG) review [59], contributing to an improved precision of the world average of $\alpha_S(m_Z)$ and superseding the previous result obtained using only CMS inclusive jets at $\sqrt{s} = 13$ TeV [106]. Regarding m_t, the result presented in this work will enhance the accuracy on m_t by including, for the first time, contributions from the $t\bar{t}+tW$ processes. Further studies using larger data sets from the HL–LHC will be crucial for a definitive conclusion on the vacuum stability and possibly unveiling signatures of new physics. Should vacuum stability be ruled out, alternative new physics scenarios would need to be explored, such as various singlet scalar field extensions using the Higgs portal mechanism, as discussed in Ref. [76]. Finally, in the context of the future running of HL–LHC, a sustainable method for the reduction of

the computational cost of MC simulations has been developed, which will facilitate high-precision measurements.

Acknowledgements

I would like to express my sincere gratitude to my supervisors, Katerina Lipka and Simone Amoroso, for their guidance and support throughout these years. I am also grateful to the DESY-CMS group for fostering a positive and stimulating working environment, and in particular to the DESY Top group for their collaboration and for making this research journey truly inspiring. Last but not least, I warmly thank all my colleagues, many of whom have become friends and some even like family, as well as everyone who has accompanied and supported me over these four years.

Bibliography

[1] O. S. Brüning et al., "LHC Design Report". CERN Yellow Reports: Monographs. CERN, Geneva, 2004.

[2] J. Yan et al., "Improved analysis of the decay width of t → Wb up to N3LO QCD corrections", *Phys. Rev. D* **109** (2024), no. 11, 114026, doi:10.1103/PhysRevD.109.114026, arXiv:2404.11133.

[3] A. Czarnecki and K. Melnikov, "Two loop QCD corrections to top quark width", *Nucl. Phys. B* **544** (1999) 520–531, doi:10.1016/S0550-3213(98)00844-X, arXiv:hep-ph/9806244.

[4] K. G. Chetyrkin, R. Harlander, T. Seidensticker, and M. Steinhauser, "Second order QCD corrections to Γ(t → Wb)", *Phys. Rev. D* **60** (1999) 114015, doi:10.1103/PhysRevD.60.114015, arXiv:hep-ph/9906273.

[5] I. R. Blokland, A. Czarnecki, M. Slusarczyk, and F. Tkachov, "Heavy to light decays with a two loop accuracy", *Phys. Rev. Lett.* **93** (2004) 062001, doi:10.1103/PhysRevLett.93.062001, arXiv:hep-ph/0403221.

[6] P. D. Group, "Review of Particle Physics", 2024. Accessed: 2024-11-07.

[7] CMS Collaboration, "Measurement of the ratio $\mathcal{B}(t \to Wb)/\mathcal{B}(t \to Wq)$ in pp collisions at $\sqrt{s} = 8$ TeV", *Phys. Lett. B* **736** (2014) 33–57, doi:10.1016/j.physletb.2014.06.076, arXiv:1404.2292.

[8] S. Frixione et al., "Single-top hadroproduction in association with a W boson", *JHEP* **07** (2008) 029, doi:10.1088/1126-6708/2008/07/029, arXiv:0805.3067.

[9] W. Hollik, J. M. Lindert, and D. Pagani, "NLO corrections to squark-squark production and decay at the LHC", *JHEP* **03** (2013) 139, doi:10.1007/JHEP03(2013)139, arXiv:1207.1071.

[10] F. Demartin et al., "tWH associated production at the LHC", *Eur. Phys. J. C* **77** (2017), no. 1, 34, doi:10.1140/epjc/s10052-017-4601-7, arXiv:1607.05862.

[11] ATLAS Collaboration, "Studies on top-quark Monte Carlo modelling for Top2016", technical report, CERN, Geneva, 2016.

[12] S. Biswas, K. Melnikov, and M. Schulze, "Next-to-leading order QCD effects and the top quark mass measurements at the LHC", *JHEP* **08** (2010) 048, doi:10.1007/JHEP08(2010)048, arXiv:1006.0910.

[13] T. Ježo et al., "An NLO+PS generator for $t\bar{t}$ and Wt production and decay including non-resonant and interference effects", *Eur. Phys. J. C* **76** (2016), no. 12, 691, doi:10.1140/epjc/s10052-016-4538-2, arXiv:1607.04538.

[14] T. Ježo, J. M. Lindert, and S. Pozzorini, "Resonance-aware NLOPS matching for off-shell $t\bar{t}$ + tW production with semileptonic decays", *JHEP* **10** (2023) 008, doi:10.1007/JHEP10(2023)008, arXiv:2307.15653.

[15] ATLAS Collaboration, "ATLAS software and computing HL-LHC roadmap", ATLAS Technical Proposal CERN-LHCC-2022-005, 2022.

[16] CMS Offline Software and Computing Group, "CMS Phase 2 computing model: update document", CMS Note CMS-NOTE-2022-008, 2022.

[17] A. Andreassen and B. Nachman, "Neural networks for full phase-space reweighting and parameter tuning", *Phys. Rev. D* **101** (2020) 091901, doi:10.1103/PhysRevD.101.091901, arXiv:1907.08209.

[18] F. Mandl and G. Shaw, "Quantum Field Theory". John Wiley & Sons, 2010.

[19] P. W. Higgs, "Broken Symmetries and the Masses of Gauge Bosons", *Phys. Rev. Lett.* **13** (Oct, 1964) 508–509, doi:10.1103/PhysRevLett.13.508.

[20] F. Englert and R. Brout, "Broken Symmetry and the Mass of Gauge Vector Mesons", *Phys. Rev. Lett.* **13** (1964) doi:10.1103/PhysRevLett.13.321.

[21] W. C. the free media repository, "Standard model of elementary particles", 03, 2025. Accessed: 2025-03-05.

[22] G. Bachy et al., "The LEP collider: construction, project status and outlook", *Part. Accel.* **26** (1990) 19–32.

[23] C. N. Yang and R. L. Mills, "Conservation of Isotopic Spin and Isotopic Gauge Invariance", *Phys. Rev.* **96** (10, 1954) doi:10.1103/PhysRev.96.191.

[24] M. Gell-Mann, "A Schematic Model of Baryons and Mesons", *Phys. Lett.* **8** (1964) 214–215, doi:10.1016/S0031-9163(64)92001-3.

[25] G. Zweig, "An SU(3) model for strong interaction symmetry and its breaking. Version 1", doi:10.17181/CERN-TH-401.

[26] G. Zweig, "An SU(3) model for strong interaction symmetry and its breaking. Version 2", pp. 22–101. 2, 1964. doi:10.17181/CERN-TH-412.

[27] TASSO Collaboration, "Evidence for Planar Events in e^+e^- Annihilation at High-Energies", *Phys. Lett. B* **86** (1979) doi:10.1016/0370-2693(79)90830-X.

[28] JADE Collaboration, "Observation of planar three-jet events in e^+e^- annihilation and evidence for gluon bremsstrahlung", *Phys. Lett. B* **91** (1980) 142–147, doi:10.1016/0370-2693(80)90680-2.

[29] PLUTO Collaboration, "Evidence for Gluon Bremsstrahlung in e+ e- Annihilations at High-Energies", *Phys. Lett. B* **86** (1979) 418–425, doi:10.1016/0370-2693(79)90869-4.

[30] D. P. Barber et al., "Discovery of Three Jet Events and a Test of Quantum Chromodynamics at PETRA Energies", *Phys. Rev. Lett.* **43** (1979) 830, doi:10.1103/PhysRevLett.43.830.

[31] I. Aitchison and T. Hey, "Gauge theories in particle physics: A practical introduction. Vol. 1: From relativistic quantum mechanics to QED". 2003.

[32] G. 't Hooft and M. J. G. Veltman, "Regularization and renormalization of gauge fields", *Nucl. Phys. B* **44** (1972) 189–213, doi:10.1016/0550-3213(72)90279-9.

[33] R. K. Ellis, W. J. Stirling, and B. R. Webber, "QCD and collider physics". Cambridge monographs on particle physics, nuclear physics, and cosmology. Cambridge University Press, Cambridge, 2003. Photography by S. Vascotto.

[34] D. J. Gross and F. Wilczek, "Ultraviolet Behavior of Nonabelian Gauge Theories", *Phys. Rev. Lett.* **30** (1973) 1343–1346, doi:10.1103/PhysRevLett.30.1343.

[35] D. J. Gross and F. Wilczek, "Asymptotically Free Gauge Theories - I", *Phys. Rev. D* **8** (1973) 3633–3652, doi:10.1103/PhysRevD.8.3633.

[36] M. D. Schwartz, "Quantum Field Theory and the Standard Model". Cambridge University Press, 3, 2014.

[37] K. G. Wilson, "Confinement of Quarks", *Phys. Rev. D* **10** (1974) 2445–2459, doi:10.1103/PhysRevD.10.2445.

[38] W. A. Bardeen, A. J. Buras, D. W. Duke, and T. Muta, "Deep inelastic scattering beyond the leading order in asymptotically free gauge theories", *Phys. Rev. D* **18** (1978) 3998, doi:10.1103/PhysRevD.18.3998.

[39] CMS Collaboration, "Review of top quark mass measurements in CMS", arXiv:2403.01313.

[40] R. Tarrach, "The Pole Mass in Perturbative QCD", *Nucl. Phys. B* **183**

(1981) 384–396, doi:10.1016/0550-3213(81)90140-1.

[41] A. S. Kronfeld, "The Perturbative pole mass in QCD", *Phys. Rev. D* **58** (1998) 051501, doi:10.1103/PhysRevD.58.051501, arXiv:hep-ph/9805215.

[42] I. I. Y. Bigi, M. A. Shifman, N. G. Uraltsev, and A. I. Vainshtein, "The Pole mass of the heavy quark. Perturbation theory and beyond", *Phys. Rev. D* **50** (1994) 2234–2246, doi:10.1103/PhysRevD.50.2234, arXiv:hep-ph/9402360.

[43] M. Beneke and V. M. Braun, "Heavy quark effective theory beyond perturbation theory: Renormalons, the pole mass and the residual mass term", *Nucl. Phys. B* **426** (1994) 301–343, doi:10.1016/0550-3213(94)90314-X, arXiv:hep-ph/9402364.

[44] M. C. Smith and S. S. Willenbrock, "Top quark pole mass", *Phys. Rev. Lett.* **79** (1997) 3825–3828, doi:10.1103/PhysRevLett.79.3825, arXiv:hep-ph/9612329.

[45] M. Beneke, P. Marquard, P. Nason, and M. Steinhauser, "On the ultimate uncertainty of the top quark pole mass", *Phys. Lett. B* **775** (2017) 63–70, doi:10.1016/j.physletb.2017.10.054, arXiv:1605.03609.

[46] A. H. Hoang, C. Lepenik, and M. Preisser, "On the Light Massive Flavor Dependence of the Large Order Asymptotic Behavior and the Ambiguity of the Pole Mass", *JHEP* **09** (2017) 099, doi:10.1007/JHEP09(2017)099, arXiv:1706.08526.

[47] A. H. Hoang et al., "The MSR mass and the $\mathcal{O}(\Lambda_{\rm QCD})$ renormalon sum rule", *JHEP* **04** (2018) 003, doi:10.1007/JHEP04(2018)003, arXiv:1704.01580.

[48] S. L. Glashow, "Partial Symmetries of Weak Interactions", *Nucl. Phys.* **22** (1961) 579–588, doi:10.1016/0029-5582(61)90469-2.

[49] A. Salam, "Weak and Electromagnetic Interactions", *Conf. Proc. C* **680519** (1968) 367–377, doi:10.1142/9789812795915_0034.

[50] S. Weinberg, "A Model of Leptons", *Phys. Rev. Lett.* **19** (Nov, 1967) 1264–1266, doi:10.1103/PhysRevLett.19.1264.

[51] C. S. Wu et al., "Experimental Test of Parity Conservation in β Decay", *Phys. Rev.* **105** (1957) 1413–1414, doi:10.1103/PhysRev.105.1413.

[52] T. Nakano and K. Nishijima, "Charge Independence for V-particles", *Progress of Theoretical Physics* **10** (11, 1953) 581–582, doi:10.1143/PTP.10.581.

[53] ALEPH, DELPHI, L3, OPAL, SLD, LEP Electroweak Working Group, SLD Electroweak Group, SLD Heavy Flavour Group Collaboration, "Precision electroweak measurements on the Z resonance", *Phys. Rept.* **427** (2006)

257–454, doi:10.1016/j.physrep.2005.12.006, arXiv:hep-ex/0509008.

[54] CMS Collaboration, "Measurement of the Drell–Yan forward-backward asymmetry and of the effective leptonic weak mixing angle in proton-proton collisions at $\sqrt{s} = 13$ TeV", arXiv:2408.07622.

[55] D0 Collaboration, "Measurement of the forward-backward charge asymmetry and extraction of $\sin^2\theta_W^{\text{eff}}$ in $p\bar{p} \to Z/\gamma* + X \to e^+e^- + X$ events produced at $\sqrt{s} = 1.96$", *Phys. Rev. Lett.* **101** (2008) 191801, doi:10.1103/PhysRevLett.101.191801, arXiv:0804.3220.

[56] CMS Collaboration, "Measurement of the weak mixing angle using the forward-backward asymmetry of Drell-Yan events in pp collisions at 8 TeV", *Eur. Phys. J. C* **78** (2018), no. 9, 701, doi:10.1140/epjc/s10052-018-6148-7, arXiv:1806.00863.

[57] J. Lykken and M. Spiropulu, "The future of the Higgs boson", *Physics Today* **66** (Dec, 2013) 28–33, doi:10.1063/PT.3.2212.

[58] G. Degrassi et al., "Higgs mass and vacuum stability in the Standard Model at NNLO", *JHEP* **08** (2012) 098, doi:10.1007/JHEP08(2012)098, arXiv:1205.6497.

[59] Particle Data Group Collaboration, "Review of particle physics", *Phys. Rev. D* **110** (2024) 030001, doi:10.1103/PhysRevD.110.030001.

[60] ATLAS Collaboration, "Observation of a new particle in the search for the Standard Model Higgs boson with the ATLAS detector at the LHC", *Phys. Lett. B* **716** (2012) 1–29, doi:10.1016/j.physletb.2012.08.020, arXiv:1207.7214.

[61] CMS Collaboration, "Observation of a New Boson at a Mass of 125 GeV with the CMS Experiment at the LHC", *Phys. Lett. B* **716** (2012) 30–61, doi:10.1016/j.physletb.2012.08.021, arXiv:1207.7235.

[62] CMS Collaboration, "A portrait of the Higgs boson by the CMS experiment ten years after the discovery.", *Nature* **607** (2022), no. 7917, 60–68, doi:10.1038/s41586-022-04892-x, arXiv:2207.00043. [Erratum: Nature 623, (2023)].

[63] ATLAS Collaboration, "A detailed map of Higgs boson interactions by the ATLAS experiment ten years after the discovery", *Nature* **607** (2022), no. 7917, 52–59, doi:10.1038/s41586-022-04893-w, arXiv:2207.00092. [Erratum: Nature 612, E24 (2022)].

[64] Super-Kamiokande Collaboration, "Evidence for oscillation of atmospheric

neutrinos", *Phys. Rev. Lett.* **81** (1998) 1562–1567, doi:10.1103/PhysRevLett.81.1562, arXiv:hep-ex/9807003.

[65] SNO Collaboration, "Direct evidence for neutrino flavor transformation from neutral current interactions in the Sudbury Neutrino Observatory", *Phys. Rev. Lett.* **89** (2002) 011301, doi:10.1103/PhysRevLett.89.011301, arXiv:nucl-ex/0204008.

[66] OPERA Collaboration, "Final Results of the OPERA Experiment on ν_τ Appearance in the CNGS Neutrino Beam", *Phys. Rev. Lett.* **120** (2018), no. 21, 211801, doi:10.1103/PhysRevLett.120.211801, arXiv:1804.04912. [Erratum: Phys.Rev.Lett. 121, 139901 (2018)].

[67] IceCube Collaboration, "Measurement of atmospheric neutrino oscillation parameters using convolutional neural networks with 9.3 years of data in IceCube DeepCore", arXiv:2405.02163.

[68] S. Cao, "Long Baseline Neutrino Oscillation Results (T2K and NOvA)", 10, 2023. arXiv:2310.09855.

[69] Z. Maki, M. Nakagawa, and S. Sakata, "Remarks on the unified model of elementary particles", *Prog. Theor. Phys.* **28** (1962) 870–880, doi:10.1143/PTP.28.870.

[70] B. Pontecorvo, "Inverse beta processes and nonconservation of lepton charge", *Zh. Eksp. Teor. Fiz.* **34** (1957) 247.

[71] KATRIN Collaboration, "Direct neutrino-mass measurement with sub-electronvolt sensitivity", *Nature Phys.* **18** (2022), no. 2, 160–166, doi:10.1038/s41567-021-01463-1, arXiv:2105.08533.

[72] S. Alekhin, A. Djouadi, and S. Moch, "The top quark and Higgs boson masses and the stability of the electroweak vacuum", *Phys. Lett. B* **716** (2012) 214–219, doi:10.1016/j.physletb.2012.08.024, arXiv:1207.0980.

[73] F. Bezrukov, M. Y. Kalmykov, B. A. Kniehl, and M. Shaposhnikov, "Higgs Boson Mass and New Physics", *JHEP* **10** (2012) 140, doi:10.1007/JHEP10(2012)140, arXiv:1205.2893.

[74] A. V. Bednyakov, B. A. Kniehl, A. F. Pikelner, and O. L. Veretin, "Stability of the Electroweak Vacuum: Gauge Independence and Advanced Precision", *Phys. Rev. Lett.* **115** (2015), no. 20, 201802, doi:10.1103/PhysRevLett.115.201802, arXiv:1507.08833.

[75] A. Andreassen, W. Frost, and M. D. Schwartz, "Scale Invariant Instantons and the Complete Lifetime of the Standard Model", *Phys. Rev. D* **97** (2018),

no. 5, 056006, doi:10.1103/PhysRevD.97.056006, arXiv:1707.08124.

[76] G. Hiller, T. Höhne, D. F. Litim, and T. Steudtner, "Vacuum stability in the Standard Model and beyond", *Phys. Rev. D* **110** (2024), no. 11, 115017, doi:10.1103/PhysRevD.110.115017, arXiv:2401.08811.

[77] J. C. Collins, D. E. Soper, and G. F. Sterman, "Factorization of Hard Processes in QCD", *Adv. Ser. Direct. High Energy Phys.* **5** (1989) 1–91, doi:10.1142/9789814503266_0001, arXiv:hep-ph/0409313.

[78] V. N. Gribov and L. N. Lipatov, "Deep inelastic ep scattering in perturbation theory", *Sov. J. Nucl. Phys.* **15** (1972) 438.

[79] G. Altarelli and G. Parisi, "Asymptotic freedom in parton language", *Nucl. Phys. B* **126** (1977) 298, doi:10.1016/0550-3213(77)90384-4.

[80] G. Curci, W. Furmanski, and R. Petronzio, "Evolution of parton densities beyond leading order: The non-singlet case", *Nucl. Phys. B* **175** (1980) 27, doi:10.1016/0550-3213(80)90003-6.

[81] W. Furmanski and R. Petronzio, "Singlet parton densities beyond leading order", *Phys. Lett. B* **97** (1980) 437, doi:10.1016/0370-2693(80)90636-X.

[82] S. Moch, J. A. M. Vermaseren, and A. Vogt, "The Three-loop splitting functions in QCD: The Nonsinglet case", *Nucl. Phys. B* **688** (2004) 101, doi:10.1016/j.nuclphysb.2004.03.030, arXiv:hep-ph/0403192.

[83] A. Vogt, S. Moch, and J. A. M. Vermaseren, "The Three-loop splitting functions in QCD: The Singlet case", *Nucl. Phys. B* **691** (2004) 129, doi:10.1016/j.nuclphysb.2004.04.024, arXiv:hep-ph/0404111.

[84] M. D. Schwartz, "Quantum Field Theory and the Standard Model". Cambridge University Press, March, 2014. ISBN 978-1-107-03473-0.

[85] M. E. Peskin and D. V. Schroeder, "An Introduction to quantum field theory". 1995.

[86] S. Alekhin, J. Bluemlein, S.-O. Moch, and R. Placakyte, "The new ABMP16 PDF", *PoS* **DIS2016** (2016) 016, doi:10.22323/1.265.0016, arXiv:1609.03327.

[87] S. Bailey et al., "Parton distributions from LHC, HERA, Tevatron and fixed target data: MSHT20 PDFs", *Eur. Phys. J. C* **81** (2021) 341, doi:10.1140/epjc/s10052-021-09057-0, arXiv:2012.04684.

[88] T.-J. Hou et al., "New CTEQ global analysis of quantum chromodynamics with high-precision data from the LHC", *Phys. Rev. D* **103** (2021) 014013, doi:10.1103/PhysRevD.103.014013, arXiv:1912.10053.

[89] NNPDF Collaboration, "The path to proton structure at 1% accuracy", *Eur. Phys. J. C* **82** (2022) 428, doi:10.1140/epjc/s10052-022-10328-7, arXiv:2109.02653.

[90] CMS Collaboration, "High-precision measurement of the W boson mass with the CMS experiment at the LHC", arXiv:2412.13872.

[91] H1, ZEUS Collaboration, "Combination of measurements of inclusive deep inelastic $e^{\pm}p$ scattering cross sections and QCD analysis of HERA data", *Eur. Phys. J. C* **75** (2015), no. 12, 580, doi:10.1140/epjc/s10052-015-3710-4, arXiv:1506.06042.

[92] H1, ZEUS Collaboration, "HERA Inclusive Neutral and Charged Current Cross Sections and a New PDF Fit, HERAPDF 2.0", *Acta Phys. Polon. Supp.* **8** (2015) 957, doi:10.5506/APhysPolBSupp.8.957, arXiv:1511.05402.

[93] PROSA Collaboration, "Impact of heavy-flavour production cross sections measured by the LHCb experiment on parton distribution functions at low x", *Eur. Phys. J. C* **75** (2015), no. 8, 396, doi:10.1140/epjc/s10052-015-3618-z, arXiv:1503.04581.

[94] PROSA Collaboration, "Improved constraints on parton distributions using LHCb, ALICE and HERA heavy-flavour measurements and implications for the predictions for prompt atmospheric-neutrino fluxes", *JHEP* **04** (2020) 118, doi:10.1007/JHEP04(2020)118, arXiv:1911.13164.

[95] CMS Collaboration, "Measurement of $\mathrm{t\bar{t}}$ normalised multi-differential cross sections in pp collisions at $\sqrt{s} = 13\,\mathrm{TeV}$, and simultaneous determination of the strong coupling strength, top quark pole mass, and parton distribution functions", *Eur. Phys. J. C* **80** (2020) 658, doi:10.1140/epjc/s10052-020-7917-7, arXiv:1904.05237.

[96] CMS Collaboration, "Measurement of double-differential cross sections for top quark pair production in pp collisions at $\sqrt{s} = 8\,\mathrm{TeV}$ and impact on parton distribution functions", *Eur. Phys. J. C* **77** (2017) 459, doi:10.1140/epjc/s10052-017-4984-5, arXiv:1703.01630.

[97] CMS Collaboration, "Measurement of the inclusive $\mathrm{t\bar{t}}$ cross section in pp collisions at $\sqrt{s} = 5.02$ TeV using final states with at least one charged lepton", *JHEP* **03** (2018) 115, doi:10.1007/JHEP03(2018)115, arXiv:1711.03143.

[98] M. Guzzi, K. Lipka, and S.-O. Moch, "Top-quark pair production at hadron colliders: differential cross section and phenomenological applications with DiffTop", *JHEP* **01** (2015) 082, doi:10.1007/JHEP01(2015)082,

arXiv:1406.0386.

[99] CMS Collaboration, "Measurement of the muon charge asymmetry in inclusive $pp \to W + X$ production at $\sqrt{s} = 7$ TeV and an improved determination of light parton distribution functions", *Phys. Rev. D* **90** (2014), no. 3, 032004, doi:10.1103/PhysRevD.90.032004, arXiv:1312.6283.

[100] CMS Collaboration, "Measurement of the differential cross section and charge asymmetry for inclusive pp $\to$ W$^{\pm} + X$ production at $\sqrt{s} = 8$ TeV", *Eur. Phys. J. C* **76** (2016), no. 8, 469, doi:10.1140/epjc/s10052-016-4293-4, arXiv:1603.01803.

[101] CMS Collaboration, "Measurement of associated production of a W boson and a charm quark in proton-proton collisions at $\sqrt{s} = 13$ TeV", *Eur. Phys. J. C* **79** (2019), no. 3, 269, doi:10.1140/epjc/s10052-019-6752-1, arXiv:1811.10021.

[102] S. Alekhin et al., "Determination of strange sea quark distributions from fixed-target and collider data", *Phys. Rev. D* **91** (2015), no. 9, 094002, doi:10.1103/PhysRevD.91.094002, arXiv:1404.6469.

[103] CMS Collaboration, "Measurements of Differential Jet Cross Sections in Proton-Proton Collisions at $\sqrt{s} = 7$ TeV with the CMS detector", *Phys. Rev. D* **87** (2013) 112002, doi:10.1103/PhysRevD.87.112002, arXiv:1212.6660. [Erratum: 10.1103/PhysRevD.87.119902].

[104] CMS Collaboration, "Constraints on parton distribution functions and extraction of the strong coupling constant from the inclusive jet cross section in pp collisions at $\sqrt{s} = 7$ TeV", *Eur. Phys. J. C* **75** (2015) 288, doi:10.1140/epjc/s10052-015-3499-1, arXiv:1410.6765.

[105] CMS Collaboration, "Measurement and QCD analysis of double-differential inclusive jet cross sections in pp collisions at $\sqrt{s} = 8$ TeV and cross section ratios to 2.76 and 7 TeV", *JHEP* **03** (2017) 156, doi:10.1007/JHEP03(2017)156, arXiv:1609.05331.

[106] CMS Collaboration, "Measurement and QCD analysis of double-differential inclusive jet cross sections in proton-proton collisions at $\sqrt{s} = 13$ TeV", *JHEP* **02** (2022) 142, doi:10.1007/JHEP02(2022)142, arXiv:2111.10431. [Addendum: JHEP 12, 035 (2022)].

[107] CMS Collaboration, "Measurement of multidifferential cross sections for dijet production in proton–proton collisions at $\sqrt{s} = 13\,\text{TeV}$", *Eur. Phys. J. C* **85** (2025), no. 1, 72, doi:10.1140/epjc/s10052-024-13606-8,

arXiv:2312.16669.

[108] CMS Collaboration, "Measurement of the triple-differential dijet cross section in proton-proton collisions at $\sqrt{s} = 8\,\text{TeV}$ and constraints on parton distribution functions", *Eur. Phys. J. C* **77** (2017), no. 11, 746, doi:10.1140/epjc/s10052-017-5286-7, arXiv:1705.02628.

[109] S. Höche, "Introduction to parton-shower event generators", in *Theoretical Advanced Study Institute in Elementary Particle Physics: Journeys Through the Precision Frontier: Amplitudes for Colliders*, pp. 235–295. 2015. arXiv:1411.4085. doi:10.1142/9789814678766_0005.

[110] S. Frixione, P. Nason, and C. Oleari, "Matching NLO QCD computations with parton shower simulations: the POWHEG method", *JHEP* **11** (2007) 070, doi:10.1088/1126-6708/2007/11/070, arXiv:0709.2092.

[111] P. Nason, "A New method for combining NLO QCD with shower Monte Carlo algorithms", *JHEP* **11** (2004) 040, doi:10.1088/1126-6708/2004/11/040, arXiv:hep-ph/0409146.

[112] S. Frixione, G. Ridolfi, and P. Nason, "A positive-weight next-to-leading-order Monte Carlo for heavy flavour hadroproduction", *JHEP* **09** (2007) 126, doi:10.1088/1126-6708/2007/09/126, arXiv:0707.3088.

[113] S. Alioli, P. Nason, C. Oleari, and E. Re, "A general framework for implementing NLO calculations in shower Monte Carlo programs: the POWHEG BOX", *JHEP* **06** (2010) 043, doi:10.1007/JHEP06(2010)043, arXiv:1002.2581.

[114] J. Alwall et al., "The automated computation of tree-level and next-to-leading order differential cross sections, and their matching to parton shower simulations", *JHEP* **07** (2014) 079, doi:10.1007/JHEP07(2014)079, arXiv:1405.0301.

[115] A. Buckley et al., "General-purpose event generators for LHC physics", *Phys. Rept.* **504** (2011) 145–233, doi:10.1016/j.physrep.2011.03.005, arXiv:1101.2599.

[116] J. C. Collins, "Sudakov form-factors", *Adv. Ser. Direct. High Energy Phys.* **5** (1989) 573–614, doi:10.1142/9789814503266_0006, arXiv:hep-ph/0312336.

[117] T. Ježo, J. M. Lindert, N. Moretti, and S. Pozzorini, "New NLOPS predictions for $t\bar{t} + b$ -jet production at the LHC", *Eur. Phys. J. C* **78** (2018), no. 6, 502, doi:10.1140/epjc/s10052-018-5956-0, arXiv:1802.00426.

[118] R. Frederix and S. Frixione, "Merging meets matching in MC@NLO", *JHEP*

12 (2012) 061, doi:10.1007/JHEP12(2012)061, arXiv:1209.6215.

[119] P. F. Monni et al., "MiNNLO$_{\rm PS}$: a new method to match NNLO QCD to parton showers", *JHEP* **05** (2020) 143, doi:10.1007/JHEP05(2020)143, arXiv:1908.06987. [Erratum: 10.1007/JHEP02(2022)031].

[120] P. F. Monni, E. Re, and M. Wiesemann, "MiNNLO$_{\rm PS}$: optimizing $2 \to 1$ hadronic processes", *Eur. Phys. J. C* **80** (2020) 1075, doi:10.1140/epjc/s10052-020-08658-5, arXiv:2006.04133.

[121] J. Mazzitelli et al., "Next-to-next-to-leading order event generation for top-quark pair production", *Phys. Rev. Lett.* **127** (2021) 062001, doi:10.1103/PhysRevLett.127.062001, arXiv:2012.14267.

[122] J. Mazzitelli et al., "Top-pair production at the LHC with MINNLO$_{\rm PS}$", *JHEP* **04** (2022) 079, doi:10.1007/JHEP04(2022)079, arXiv:2112.12135.

[123] CMS Collaboration, "Extraction and validation of a new set of CMS PYTHIA8 tunes from underlying-event measurements", *Eur. Phys. J. C* **80** (2020), no. 1, 4, doi:10.1140/epjc/s10052-019-7499-4, arXiv:1903.12179.

[124] G. Gustafson, U. Pettersson, and P. M. Zerwas, "Jet Final States in W W Pair Production and Color Screening in the QCD Vacuum", *Phys. Lett. B* **209** (1988) 90–94, doi:10.1016/0370-2693(88)91836-9.

[125] T. Sjostrand and M. van Zijl, "A Multiple Interaction Model for the Event Structure in Hadron Collisions", *Phys. Rev. D* **36** (1987) 2019, doi:10.1103/PhysRevD.36.2019.

[126] S. Argyropoulos and T. Sjöstrand, "Effects of color reconnection on $t\bar{t}$ final states at the LHC", *JHEP* **11** (2014) 043, doi:10.1007/JHEP11(2014)043, arXiv:1407.6653.

[127] J. R. Christiansen and P. Z. Skands, "String Formation Beyond Leading Colour", *JHEP* **08** (2015) 003, doi:10.1007/JHEP08(2015)003, arXiv:1505.01681.

[128] B. Andersson, G. Gustafson, G. Ingelman, and T. Sjostrand, "Parton Fragmentation and String Dynamics", *Phys. Rept.* **97** (1983) 31–145, doi:10.1016/0370-1573(83)90080-7.

[129] T. Sjöstrand et al., "An introduction to PYTHIA 8.2", *Comput. Phys. Commun.* **191** (2015) 159, doi:10.1016/j.cpc.2015.01.024, arXiv:1410.3012.

[130] G. Marchesini et al., "HERWIG: A Monte Carlo event generator for simulating hadron emission reactions with interfering gluons. Version 5.1 - April 1991",

Comput. Phys. Commun. **67** (1992) 465–508, doi:10.1016/0010-4655(92)90055-4.

[131] M. G. Bowler, "e^+e^- production of heavy quarks in the string model", *Z. Phys. C* **11** (1981) 169, doi:10.1007/BF01574001.

[132] C. Peterson, D. Schlatter, I. Schmitt, and P. M. Zerwas, "Scaling Violations in Inclusive e^+e^- Annihilation Spectra", *Phys. Rev. D* **27** (1983) 105, doi:10.1103/PhysRevD.27.105.

[133] GEANT4 Collaboration, "GEANT4–a simulation toolkit", *Nucl. Instrum. Meth. A* **506** (2003) 250–303, doi:10.1016/S0168-9002(03)01368-8.

[134] R. Brandelik et al., "Evidence for planar events in e^+e^- annihilation at high energies", *Physics Letters B* **86** (1979), no. 2, 243–249, doi:https://doi.org/10.1016/0370-2693(79)90830-X.

[135] OPAL Collaboration, "A Simultaneous measurement of the QCD color factors and the strong coupling", *Eur. Phys. J. C* **20** (2001) 601–615, doi:10.1007/s100520100699, arXiv:hep-ex/0101044.

[136] CMS Collaboration, "Measurement of $\mathrm{t\bar{t}}$ normalised multi-differential cross sections in pp collisions at $\sqrt{s} = 13$ TeV, and simultaneous determination of the strong coupling strength, top quark pole mass, and parton distribution functions", *Eur. Phys. J. C* **80** (2020), no. 7, 658, doi:10.1140/epjc/s10052-020-7917-7, arXiv:1904.05237.

[137] CMS Collaboration, "Measurement of the $\mathrm{t\bar{t}}$ production cross section, the top quark mass, and the strong coupling constant using dilepton events in pp collisions at $\sqrt{s} = 13$ TeV", *Eur. Phys. J. C* **79** (2019), no. 5, 368, doi:10.1140/epjc/s10052-019-6863-8, arXiv:1812.10505.

[138] CMS Collaboration, "Determination of the Top-Quark Pole Mass and Strong Coupling Constant from the $t\bar{t}$ Production Cross Section in pp Collisions at $\sqrt{s}$ = 7 TeV", *Phys. Lett. B* **728** (2014) 496–517, doi:10.1016/j.physletb.2013.12.009, arXiv:1307.1907. [Erratum: Phys.Lett.B 738, 526–528 (2014)].

[139] CMS Collaboration, "Determination of the strong coupling constant $\alpha_S(m_\mathrm{Z})$ from measurements of inclusive $\mathrm{W}^\pm$ and Z boson production cross sections in proton-proton collisions at $\sqrt{\mathrm{s}} = 7$ and 8 TeV", *JHEP* **06** (2020) 018, doi:10.1007/JHEP06(2020)018, arXiv:1912.04387.

[140] D. d'Enterria and A. Poldaru, "Extraction of the strong coupling $\alpha_s(\mathrm{m}_Z)$ from a combined NNLO analysis of inclusive electroweak boson cross sections at

hadron colliders", *JHEP* **06** (2020) 016, doi:10.1007/JHEP06(2020)016, arXiv:1912.11733.

[141] ATLAS Collaboration, "A precise determination of the strong-coupling constant from the recoil of Z bosons with the ATLAS experiment at $\sqrt{s} = 8$ TeV", arXiv:2309.12986.

[142] S. Catani, Y. L. Dokshitzer, M. H. Seymour, and B. R. Webber, "Longitudinally invariant K_t clustering algorithms for hadron hadron collisions", *Nucl. Phys. B* **406** (1993) 187–224, doi:10.1016/0550-3213(93)90166-M.

[143] Y. Dokshitzer, G. Leder, S. Moretti, and B. Webber, "Better jet clustering algorithms", *Journal of High Energy Physics* **1997** (8, 1997) 001–001, doi:10.1088/1126-6708/1997/08/001.

[144] M. Cacciari, G. P. Salam, and G. Soyez, "The anti-k_{T} jet clustering algorithm", *JHEP* **04** (2008) 063, doi:10.1088/1126-6708/2008/04/063, arXiv:0802.1189.

[145] D. Britzger et al., "NNLO interpolation grids for jet production at the LHC", *Eur. Phys. J. C* **82** (2022) 930, doi:10.1140/epjc/s10052-022-10880-2, arXiv:2207.13735.

[146] fastNLO Collaboration, D. Britzger, K. Rabbertz, F. Stober, and M. Wobisch, "New features in version 2 of the fastNLO project", in *20th International Workshop on Deep-Inelastic Scattering and Related Subjects*, p. 217. 2012. arXiv:1208.3641. doi:10.3204/DESY-PROC-2012-02/165.

[147] T. Kluge, K. Rabbertz, and M. Wobisch, "FastNLO: Fast pQCD calculations for PDF fits", in *14th International Workshop on Deep Inelastic Scattering*, pp. 483–486. 9, 2006. arXiv:hep-ph/0609285. doi:10.1142/9789812706706_0110.

[148] CMS Collaboration, "Measurement of the inclusive jet cross section in pp collisions at $\sqrt{s} = 2.76$ TeV", *Eur. Phys. J. C* **76** (2016) 265, doi:10.1140/epjc/s10052-016-4083-z, arXiv:1512.06212.

[149] CMS Collaboration, "Measurement of the double-differential inclusive jet cross section in proton-proton collisions at $\sqrt{s} = 5.02$ TeV", (2024). arXiv:2401.11355. Submitted to JHEP.

[150] ATLAS Collaboration, "Measurement of inclusive jet and dijet cross sections in proton-proton collisions at 7 TeV centre-of-mass energy with the ATLAS detector", *Eur. Phys. J. C* **71** (2011) 1512,

doi:10.1140/epjc/s10052-010-1512-2, arXiv:1009.5908.

[151] ATLAS Collaboration, "Measurement of inclusive jet and dijet production in pp collisions at $\sqrt{s} = 7$ TeV using the ATLAS detector", *Phys. Rev. D* **86** (2012) 014022, doi:10.1103/PhysRevD.86.014022, arXiv:1112.6297.

[152] ATLAS Collaboration, "Measurement of the inclusive jet cross section in pp collisions at $\sqrt{s} = 2.76$ TeV and comparison to the inclusive jet cross section at $\sqrt{s} = 7$ TeV using the ATLAS detector", *Eur. Phys. J. C* **73** (2013) 2509, doi:10.1140/epjc/s10052-013-2509-4, arXiv:1304.4739.

[153] ATLAS Collaboration, "Measurement of the inclusive jet cross-section in proton-proton collisions at $\sqrt{s} = 7$ TeV using 4.5 fb^{-1} of data with the ATLAS detector", *JHEP* **02** (2015) 153, doi:10.1007/JHEP02(2015)153, arXiv:1410.8857. [Erratum: 10.1007/JHEP09(2015)141].

[154] ATLAS Collaboration, "Measurement of the inclusive jet cross-sections in proton-proton collisions at $\sqrt{s} = 8$ TeV with the ATLAS detector", *JHEP* **09** (2017) 020, doi:10.1007/JHEP09(2017)020, arXiv:1706.03192.

[155] ATLAS Collaboration, "Measurement of inclusive jet and dijet cross-sections in proton-proton collisions at $\sqrt{s} = 13$ TeV with the ATLAS detector", *JHEP* **05** (2018) 195, doi:10.1007/JHEP05(2018)195, arXiv:1711.02692.

[156] ZEUS Collaboration, "Measurement of jet production in deep inelastic scattering and NNLO determination of the strong coupling at ZEUS", *Eur. Phys. J. C* **83** (2023), no. 11, 1082, doi:10.1140/epjc/s10052-023-12180-9, arXiv:2309.02889.

[157] A. A. Petrov and A. E. Blechman, "Effective Field Theories". World Scientific, 2016.

[158] J. Gao, C. S. Li, and C. P. Yuan, "NLO QCD Corrections to dijet Production via Quark Contact Interactions", *JHEP* **07** (2012) 037, doi:10.1007/JHEP07(2012)037, arXiv:1204.4773.

[159] M. Kobayashi and T. Maskawa, "CP Violation in the Renormalizable Theory of Weak Interaction", *Prog. Theor. Phys.* **49** (1973) 652–657, doi:10.1143/PTP.49.652.

[160] S. W. Herb et al., "Observation of a Dimuon Resonance at 9.5 GeV in 400-GeV Proton-Nucleus Collisions", *Phys. Rev. Lett.* **39** (Aug, 1977) 252–255, doi:10.1103/PhysRevLett.39.252.

[161] CDF Collaboration, "Observation of top quark production in $\bar{p}p$ collisions", *Phys. Rev. Lett.* **74** (1995) 2626–2631, doi:10.1103/PhysRevLett.74.2626,

arXiv:hep-ex/9503002.

[162] D0 Collaboration, "Observation of the top quark", *Phys. Rev. Lett.* **74** (1995) 2632–2637, doi:10.1103/PhysRevLett.74.2632, arXiv:hep-ex/9503003.

[163] M. Jezabek and J. H. Kuhn, "QCD Corrections to Semileptonic Decays of Heavy Quarks", *Nucl. Phys. B* **314** (1989) 1–6, doi:10.1016/0550-3213(89)90108-9.

[164] P. de Jong, "Top Physics at the LHC", arXiv:0902.4798.

[165] LHC Top Working Group, "LHC Top Working Group Summary Plots", 2024. [Accessed: 21-November-2024].

[166] Particle Data Group Collaboration, "Review of Particle Physics", *PTEP* **2022** (2022) 083C01, doi:10.1093/ptep/ptac097.

[167] D0 Collaboration Collaboration, "Useful Diagrams of Top Signals and Backgrounds", 10, 2011. Accessed: 2022-07-19.

[168] CMS Collaboration, "Measurement of the top quark mass using a profile likelihood approach with the lepton + jets final states in proton–proton collisions at $\sqrt{s} = 13\,\text{TeV}$", *Eur. Phys. J. C* **83** (2023), no. 10, 963, doi:10.1140/epjc/s10052-023-12050-4, arXiv:2302.01967.

[169] A. H. Hoang, "What is the Top Quark Mass?", *Ann. Rev. Nucl. Part. Sci.* **70** (2020) 225–255, doi:10.1146/annurev-nucl-101918-023530, arXiv:2004.12915.

[170] A. H. Hoang, S. Plätzer, and D. Samitz, "On the cutoff dependence of the quark mass parameter in angular ordered parton showers", *JHEP* **10** (2018) 200, doi:10.1007/JHEP10(2018)200, arXiv:1807.06617.

[171] S. Alioli et al., "A new observable to measure the top-quark mass at hadron colliders", *Eur. Phys. J. C* **73** (2013) 2438, doi:10.1140/epjc/s10052-013-2438-2, arXiv:1303.6415.

[172] CMS Collaboration, "Search for anomalous single top quark production in association with a photon in pp collisions at $\sqrt{s} = 8$ TeV", *JHEP* **04** (2016) 035, doi:10.1007/JHEP04(2016)035, arXiv:1511.03951.

[173] ATLAS Collaboration, "Search for flavour-changing neutral-current couplings between the top-quark and the photon with the ATLAS detector at $\sqrt{s} = 13$ TeV", *ATLAS-CONF-2022-003* (2022).

[174] CDF Collaboration, "Direct Measurement of the Total Decay Width of the Top Quark", *Phys. Rev. Lett.* **111** (2013), no. 20, 202001, doi:10.1103/PhysRevLett.111.202001, arXiv:1308.4050.

[175] ATLAS Collaboration, "Direct top-quark decay width measurement in the $t\bar{t}$ lepton+jets channel at $\sqrt{s}$=8 TeV with the ATLAS experiment", *Eur. Phys. J. C* **78** (2018), no. 2, 129, doi:10.1140/epjc/s10052-018-5595-5, arXiv:1709.04207.

[176] CMS Collaboration, "Bounding the top quark width using final states with two charged leptons and two jets at $\sqrt{s} = 13$ TeV", CMS Physics Analysis Summary CMS-PAS-TOP-16-019, CERN, Geneva, 2016.

[177] C. Herwig, T. Ježo, and B. Nachman, "Extracting the Top-Quark Width from Nonresonant Production", *Phys. Rev. Lett.* **122** (2019), no. 23, 231803, doi:10.1103/PhysRevLett.122.231803, arXiv:1903.10519.

[178] S. Amoroso, D. Britzger, S. Kluth, and L. Scyboz, "NLOPS off-shell effects in precise determinations of the top-quark mass and width at the LHC", *PoS* **EPS-HEP2023** (2024) 313, doi:10.22323/1.449.0313.

[179] A. Collaboration, "The ATLAS Experiment at the CERN Large Hadron Collider", *JINST* **3** (8, 2008) S08003–S08003, doi:10.1088/1748-0221/3/08/s08003.

[180] CMS Collaboration, "The CMS experiment at the CERN LHC", *JINST* **3** (2008) S08004, doi:10.1088/1748-0221/3/08/S08004.

[181] A. Collaboration, "The ALICE experiment at the CERN LHC", *JINST* **3** (8, 2008) S08002–S08002, doi:10.1088/1748-0221/3/08/s08002.

[182] L. Collaboration, "The LHCb Detector at the LHC", *JINST* **3** (8, 2008) S08005–S08005, doi:10.1088/1748-0221/3/08/s08005.

[183] C. Lefèvre, "The CERN accelerator complex", (12, 2008).

[184] W. Herr and B. Muratori, "Concept of luminosity", in *Intermediate accelerator physics. Proceedings, CERN Accelerator School.* Zeuthen, Germany, September 15-26, 2003, 2003. doi:10.5170/CERN-2006-002.361.

[185] CMS Collaboration, "Public CMS luminosity information". https://twiki.cern.ch/twiki/bin/view/CMSPublic/LumiPublicResults. Accessed: November 2024.

[186] High Luminosity LHC Project, "High Luminosity LHC Project". https://hilumilhc.web.cern.ch/content/hl-lhc-project. Accessed: December 2024.

[187] CMS Collaboration, "CMS Physics: Technical Design Report Volume 2: Physics Performance", *J. Phys. G* **34** (2007) 995–1579, doi:10.1088/0954-3899/34/6/S01. revised version submitted on 2006-09-22

17:44:47.

[188] CMS Collaboration, "CMS Physics: Technical Design Report Volume 1: Detector Performance and Software". Technical design report. CMS. CERN, Geneva, 2006.

[189] T. Sakuma and T. McCauley, "Detector and Event Visualization with SketchUp at the CMS Experiment", *J. Phys. Conf. Ser.* **513** (2014) 022032, doi:10.1088/1742-6596/513/2/022032, arXiv:1311.4942.

[190] CMS Collaboration, "Description and performance of track and primary-vertex reconstruction with the CMS tracker", *JINST* **9** (2014) P10009, doi:10.1088/1748-0221/9/10/P10009, arXiv:1405.6569.

[191] CMS Collaboration, "CMS Technical Design Report for the Pixel Detector Upgrade", doi:10.2172/1151650.

[192] CMS Collaboration, "The Phase-2 Upgrade of the CMS Tracker", doi:10.17181/CERN.QZ28.FLHW.

[193] CMS Collaboration, "The CMS ECAL performance with examples", *JINST* **9** (2014) C02008, doi:10.1088/1748-0221/9/02/C02008.

[194] CMS Collaboration, "The CMS experiment at the CERN LHC", *JINST* **3** (2008) S08004, doi:10.1088/1748-0221/3/08/S08004.

[195] CMS Collaboration Collaboration, "Performance of CMS hadron calorimeter timing and synchronization using test beam, cosmic ray, and LHC beam data", *JINST* **5** (Nov, 2009) doi:10.1088/1748-0221/5/03/T03013, arXiv:0911.4877.

[196] CMS Collaboration, "Performance of the CMS muon detector and muon reconstruction with proton-proton collisions at $\sqrt{s} = 13$ TeV", *JINST* **13** (2018) P06015, doi:10.1088/1748-0221/13/06/P06015, arXiv:1804.04528.

[197] CMS Collaboration, "Performance of the CMS Level-1 trigger in proton-proton collisions at $\sqrt{s} = 13$ TeV", *JINST* **15** (2020), no. 10, P10017, doi:10.1088/1748-0221/15/10/P10017, arXiv:2006.10165.

[198] CMS Collaboration, "CMS Physics: Technical Design Report Volume 1: Detector Performance and Software", *CERN-LHCC-2006-001, CMS-TDR-8-1, CERN-LHCC-2006-001, CMS-TDR-8-1* (2006).

[199] A. S. et al., "Particle-flow reconstruction and global event description with the CMS detector", doi:10.1088/1748-0221/12/10/p10003.

[200] CMS Collaboration, "Particle-flow reconstruction and global event description with the CMS detector", *JINST* **12** (2017) P10003,

doi:10.1088/1748-0221/12/10/P10003, arXiv:1706.04965.

[201] S. Wuchterl, "Top quark pole mass from tt+jet using a machine learning based reconstruction for tt kinematics". Phd thesis, Universität Hamburg, 2022.

[202] CMS Collaboration, "Technical proposal for the Phase-II upgrade of the Compact Muon Solenoid", CMS Technical Proposal CERN-LHCC-2015-010, CMS-TDR-15-02, 2015.

[203] CMS Collaboration, "Performance of missing transverse momentum reconstruction in proton-proton collisions at $\sqrt{s} = 13$ TeV using the CMS detector", *JINST* **14** (2019), no. 07, P07004, doi:10.1088/1748-0221/14/07/P07004, arXiv:1903.06078.

[204] CMS Collaboration, "Electron and photon reconstruction and identification with the CMS experiment at the CERN LHC", *JINST* **16** (2021), no. 05, P05014, doi:10.1088/1748-0221/16/05/P05014, arXiv:2012.06888.

[205] CMS Collaboration, "ECAL 2016 refined calibration and Run2 summary plots", CMS Detector Performance Summary CMS-DP-2020-021, 2020.

[206] CMS Collaboration, "Jet energy scale and resolution in the CMS experiment in pp collisions at 8 TeV", *JINST* **12** (2017), no. 02, P02014, doi:10.1088/1748-0221/12/02/P02014, arXiv:1607.03663.

[207] M. Cacciari, G. P. Salam, and G. Soyez, "FastJet User Manual", *Eur. Phys. J. C* **72** (2012) 1896, doi:10.1140/epjc/s10052-012-1896-2, arXiv:1111.6097.

[208] CMS Collaboration, "Pileup removal algorithms", CMS Physics Analysis Summary CMS-PAS-JME-14-001, CERN, Geneva, 2014.

[209] CMS Collaboration, "Pileup mitigation at CMS in 13 TeV data", *JINST* **15** (2020) P09018, doi:10.1088/1748-0221/15/09/p09018, arXiv:2003.00503.

[210] D. Bertolini, P. Harris, M. Low, and N. Tran, "Pileup Per Particle Identification", *JHEP* **10** (2014) 059, doi:10.1007/JHEP10(2014)059, arXiv:1407.6013.

[211] M. Cacciari, G. P. Salam, and G. Soyez, "The Catchment Area of Jets", *JHEP* **04** (2008) 005, doi:10.1088/1126-6708/2008/04/005, arXiv:0802.1188.

[212] M. Cacciari and G. P. Salam, "Pileup subtraction using jet areas", *Phys. Lett. B* **659** (2008) 119–126, doi:10.1016/j.physletb.2007.09.077, arXiv:0707.1378.

[213] CMS Collaboration, "Jet energy scale and resolution in the CMS experiment in pp collisions at 8 TeV", *JINST* **12** (2017) P02014,

doi:10.1088/1748-0221/12/02/P02014, arXiv:1607.03663.

[214] CMS Collaboration, "Identification of heavy-flavour jets with the CMS detector in pp collisions at 13 TeV", *JINST* **13** (2018), no. 05, P05011, doi:10.1088/1748-0221/13/05/P05011, arXiv:1712.07158.

[215] T. Müller, C. Piasecki, G. Quast, and C. Weiser, "Inclusive Secondary Vertex Reconstruction in Jets", technical report, CERN, Geneva, 2006.

[216] E. Bols et al., "Jet Flavour Classification Using DeepJet", *JINST* **15** (2020), no. 12, P12012, doi:10.1088/1748-0221/15/12/P12012, arXiv:2008.10519.

[217] CMS Collaboration, "Performance of the DeepJet b tagging algorithm using 41.9/fb of data from proton-proton collisions at 13TeV with Phase 1 CMS detector", CMS Detector Performance Note CMS-DP-2018-058, 2018.

[218] I. Zurbano Fernandez et al., "High-Luminosity Large Hadron Collider (HL-LHC): Technical design report", doi:10.23731/CYRM-2020-0010.

[219] CMS Collaboration, "CMS Phase II Upgrade Scope Document", technical report, CERN, Geneva, 2015.

[220] CMS Collaboration, "A MIP Timing Detector for the CMS Phase-2 Upgrade", technical report, CERN, Geneva, 2019.

[221] D. Contardo et al., "Technical Proposal for the Phase-II Upgrade of the CMS Detector", technical report, Geneva, 2015. doi:10.17181/CERN.VU8I.D59J.

[222] "High-Luminosity Large Hadron Collider (HL-LHC): Technical design report". CERN Yellow Reports: Monographs. CERN, Geneva, 2020.

[223] T. M. Cauley, "Collisions recorded by the CMS detector on 14 Oct 2016 during the high pile-up fill". CMS-PHO-EVENTS-2016-008, 2016. https://cds.cern.ch/record/2231915.

[224] CMS Collaboration, "The Phase-2 Upgrade of the CMS Endcap Calorimeter", doi:10.17181/CERN.IV8M.1JY2.

[225] CMS Collaboration, "The Phase-2 Upgrade of the CMS Muon Detectors", *CERN-LHCC-2017-012, CMS-TDR-016* (9, 2017).

[226] CMS Collaboration, "The Phase-2 Upgrade of the CMS Tracker", technical report, CERN, Geneva, 2017. doi:10.17181/CERN.QZ28.FLHW.

[227] CMS Collaboration, "The Phase-2 Upgrade of the CMS Endcap Calorimeter", technical report, CERN, Geneva, 2017. doi:10.17181/CERN.IV8M.1JY2.

[228] CMS Collaboration, "The Phase-2 Upgrade of the CMS Muon Detectors", technical report, CERN, Geneva, 2017.

[229] CMS Collaboration, "CMS Offline and Computing Public Results", 2024.

[Accessed: 5-December-2024].

[230] HEP Software Foundation, J. Albrecht et al., "A roadmap for HEP software and computing R&D for the 2020s", *Comput. Softw. Big Sci.* **3** (2019) 7, doi:10.1007/s41781-018-0018-8, arXiv:1712.06982.

[231] CMS Collaboration, "Reweighting simulated events using machine-learning techniques in the CMS experiment", *Eur. Phys. J. C* **85** (2025) 495, doi:10.1140/epjc/s10052-025-14097-x, arXiv:2411.03023.

[232] H. Ghorbel, "Machine Learning - Activation Function in Neural Network". Medium, 2024. Accessed: 2024-03-05.

[233] D. E. Rumelhart, G. E. Hinton, and R. J. Williams, "Learning representations by back-propagating errors", *Nature* **323** (1986), no. 6088, 533–536, doi:10.1038/323533a0.

[234] H. Robbins and S. Monro, "A stochastic approximation method", *The Annals of Mathematical Statistics* **22** (1951), no. 3, 400–407, doi:10.1214/aoms/1177729586.

[235] D. P. Kingma and J. Ba, "ADAM: a method for stochastic optimization", in *Proc. 3rd Int. Conf. on Learning Representations (ICLR 2015): San Diego CA, USA, May 7–9, 2015*. 2015. arXiv:1412.6980.

[236] A. Rogozhnikov, "Reweighting with boosted decision trees", in *Proc. 17th International Workshop on Advanced Computing and Analysis Techniques in Physics Research (ACAT 2016): Valparaiso, Chile, January 18–22, 2016*. 2016. arXiv:1608.05806. [J. Phys. Conf. Ser. 762 (2016) 012036]. doi:10.1088/1742-6596/762/1/012036.

[237] K. Cranmer, J. Pavez, and G. Louppe, "Approximating likelihood ratios with calibrated discriminative classifiers", (2015). arXiv:1506.02169.

[238] B. Nachman and J. Thaler, "Neural conditional reweighting", *Phys. Rev. D* **105** (2022) 076015, doi:10.1103/PhysRevD.105.076015, arXiv:2107.08979.

[239] B. Amos, L. Xu, and J. Zico Kolter, "Input convex neural networks", in *Proc. 34th International Conference on Machine Learning (ICML 2017): Sydney, Australia, August 6–11, 2017*. 2017. arXiv:1609.07152. [PMLR 70 (2017) 146].

[240] C. Pollard and P. Windischhofer, "Transport away your problems: Calibrating stochastic simulations with optimal transport", *Nucl. Instrum. Meth. A* **1027** (2022) 166119, doi:10.1016/j.nima.2021.166119, arXiv:2107.08648.

[241] E. G. Tabak and C. V. Turner, "A family of nonparametric density estimation

algorithms", *Commun. Pure Appl. Math.* **66** (2013) 145, doi:10.1002/cpa.21423.

[242] E. G. Tabak and E. Vanden-Eijnden, "Density estimation by dual ascent of the log-likelihood", *Comm. Math. Sci.* **8** (2010) 217, doi:10.4310/CMS.2010.v8.n1.a11.

[243] T. Golling, S. Klein, R. Mastandrea, and B. Nachman, "Flow-enhanced transportation for anomaly detection", *Phys. Rev. D* **107** (2023) 096025, doi:10.1103/PhysRevD.107.096025, arXiv:2212.11285.

[244] J. A. Raine, S. Klein, D. Sengupta, and T. Golling, "CURTAINs for your sliding window: Constructing unobserved regions by transforming adjacent intervals", *Front. Big Data* **6** (2023) 899345, doi:10.3389/fdata.2023.899345, arXiv:2203.09470.

[245] A. Hallin et al., "Classifying anomalies through outer density estimation", *Phys. Rev. D* **106** (2022) 055006, doi:10.1103/PhysRevD.106.055006, arXiv:2109.00546.

[246] M. Algren et al., "Flow away your differences: Conditional normalizing flows as an improvement to reweighting", (2023). arXiv:2304.14963. Submitted to *SciPost Phys.*

[247] P. Komiske, E. Metodiev, and J. Thaler, "Energy flow networks: deep sets for particle jets", *JHEP* **01** (2019) 121, doi:10.1007/JHEP01(2019)121, arXiv:1810.05165.

[248] P. Baldi et al., "Parameterized neural networks for high-energy physics", *Eur. Phys. J. C* **76** (2016) 235, doi:10.1140/epjc/s10052-016-4099-4, arXiv:1601.07913.

[249] M. Zaheer et al., "Deep sets", in *Proc. 31st Conference on Neural Information Processing Systems (NIPS 2017): Long Beach CA, USA, December 04–09, 2017*, p. 3391. 2017. arXiv:1703.06114.

[250] C. M. Bishop, "Pattern Recognition and Machine Learning". Springer, New York, 2006.

[251] A. F. Agarap, "Deep learning using rectified linear units (ReLU)", (2018). arXiv:1803.08375.

[252] F. Chollet et al., "KERAS", 2015. Software available from https://keras.io.

[253] M. Abadi et al., "TensorFlow: Large-scale machine learning on heterogeneous systems", 2015. Software available from http://tensorflow.org. doi:10.5281/zenodo.4724125.

[254] S. Alioli, P. Nason, C. Oleari, and E. Re, "NLO Higgs boson production via gluon fusion matched with shower in POWHEG", *JHEP* **04** (2009) 002, doi:10.1088/1126-6708/2009/04/002, arXiv:0812.0578.

[255] ATLAS and CMS Collaborations, "Combination of measurements of the top quark mass from data collected by the ATLAS and CMS experiments at $\sqrt{s} = 7$ and 8 TeV", *Phys. Rev. Lett.* **132** (2024) 261902, doi:10.1103/PhysRevLett.132.261902, arXiv:2402.08713.

[256] CMS Collaboration, "Extraction and validation of a new set of CMS PYTHIA 8 tunes from underlying-event measurements", *Eur. Phys. J. C* **80** (2020) 4, doi:10.1140/epjc/s10052-019-7499-4, arXiv:1903.12179.

[257] S. Amoroso et al., "Standard model working group report", in *Proc. 11th Les Houches Workshop on Physics at Colliders (PhysTeV 2019): Les Houches, France, June 10–28, 2019*. 2020. arXiv:2003.01700.

[258] C. Bierlich et al., "A comprehensive guide to the physics and usage of PYTHIA 8.3", *SciPost Phys. Codeb.* **8** (2022) doi:10.21468/SciPostPhysCodeb.8, arXiv:2203.11601.

[259] P. Skands, S. Carrazza, and J. Rojo, "Tuning PYTHIA 8.1: the Monash 2013 tune", *Eur. Phys. J. C* **74** (2014) 3024, doi:10.1140/epjc/s10052-014-3024-y, arXiv:1404.5630.

[260] G. Corcella and A. D. Mitov, "Bottom-quark fragmentation in top-quark decay", *Nucl. Phys. B* **623** (2002) 247, doi:10.1016/S0550-3213(01)00639-3, arXiv:hep-ph/0110319.

[261] M. Cacciari, G. Corcella, and A. D. Mitov, "Soft gluon resummation for bottom fragmentation in top quark decay", *JHEP* **12** (2002) 015, doi:10.1088/1126-6708/2002/12/015, arXiv:hep-ph/0209204.

[262] B. Efron, "Bootstrap methods: Another look at the jackknife", in *Breakthroughs in statistics*, S. Kotz and N. Johnson, eds., p. 569. Springer-Verlag New York, New York, 1992. doi:10.1007/978-1-4612-4380-9_41.

[263] P. Bärnreuther, M. Czakon, and A. Mitov, "Percent level precision physics at the Tevatron: Next-to-next-to-leading order QCD corrections to $q\bar{q} \to t\bar{t} + $ ", *Phys. Rev. Lett.* **109** (2012) 132001, doi:10.1103/PhysRevLett.109.132001, arXiv:1204.5201.

[264] M. Czakon and A. Mitov, "NNLO corrections to top-pair production at hadron colliders: the all-fermionic scattering channels", *JHEP* **12** (2012) 054,

doi:10.1007/JHEP12(2012)054, arXiv:1207.0236.

[265] M. Czakon and A. Mitov, "NNLO corrections to top pair production at hadron colliders: the quark-gluon reaction", *JHEP* **01** (2013) 080, doi:10.1007/JHEP01(2013)080, arXiv:1210.6832.

[266] M. Czakon, P. Fiedler, and A. Mitov, "Total top-quark pair-production cross section at hadron colliders through $O(\alpha_S^4)$", *Phys. Rev. Lett.* **110** (2013) 252004, doi:10.1103/PhysRevLett.110.252004, arXiv:1303.6254.

[267] M. Czakon, D. Heymes, and A. Mitov, "High-precision differential predictions for top-quark pairs at the LHC", *Phys. Rev. Lett.* **116** (2016) 082003, doi:10.1103/PhysRevLett.116.082003, arXiv:1511.00549.

[268] M. Czakon, P. Fiedler, D. Heymes, and A. Mitov, "NNLO QCD predictions for fully-differential top-quark pair production at the Tevatron", *JHEP* **05** (2016) 034, doi:10.1007/JHEP05(2016)034, arXiv:1601.05375.

[269] S. Catani et al., "Top-quark pair hadroproduction at next-to-next-to-leading order in QCD", *Phys. Rev. D* **99** (2019) 051501, doi:10.1103/PhysRevD.99.051501, arXiv:1901.04005.

[270] S. Catani et al., "Top-quark pair production at the LHC: fully differential QCD predictions at NNLO", *JHEP* **07** (2019) 100, doi:10.1007/JHEP07(2019)100, arXiv:1906.06535.

[271] S. Catani et al., "Top-quark pair hadroproduction at NNLO: differential predictions with the $\overline{\text{MS}}$ mass", *JHEP* **08** (2020) 027, doi:10.1007/JHEP08(2020)027, arXiv:2005.00557.

[272] CMS Collaboration, "Measurement of differential cross sections for top quark pair production using the lepton+jets final state in proton-proton collisions at 13 TeV", *Phys. Rev. D* **95** (2017), no. 9, 092001, doi:10.1103/PhysRevD.95.092001, arXiv:1610.04191.

[273] CMS Collaboration, "Measurement of normalized differential $\mathrm{t\bar{t}}$ cross sections in the dilepton channel from pp collisions at $\sqrt{s} = 13$ TeV", *JHEP* **04** (2018) 060, doi:10.1007/JHEP04(2018)060, arXiv:1708.07638.

[274] CMS Collaboration, "Measurements of differential cross sections of top quark pair production as a function of kinematic event variables in proton-proton collisions at $\sqrt{s} = 13\,\text{TeV}$", *JHEP* **06** (2018) 002, doi:10.1007/JHEP06(2018)002, arXiv:1803.03991.

[275] CMS Collaboration, "Measurements of $\mathrm{t\bar{t}}$ differential cross sections in proton-proton collisions at $\sqrt{s} = 13$ TeV using events containing two leptons",

JHEP **02** (2019) 149, doi:10.1007/JHEP02(2019)149, arXiv:1811.06625.

[276] CMS Collaboration, "Measurement of the top quark mass in the all-jets final state at $\sqrt{s} = 13\,\text{TeV}$ and combination with the lepton+jets channel", *Eur. Phys. J. C* **79** (2019) 313, doi:10.1140/epjc/s10052-019-6788-2, arXiv:1812.10534.

[277] CMS Collaboration, "Measurement of differential $\mathrm{t\bar{t}}$ production cross sections in the full kinematic range using lepton+jets events from proton-proton collisions at $\sqrt{s} = 13\,\text{TeV}$", *Phys. Rev. D* **104** (2021) 092013, doi:10.1103/PhysRevD.104.092013, arXiv:2108.02803.

[278] ATLAS Collaboration, "Measurements of top-quark pair differential cross-sections in the lepton+jets channel in pp collisions at $\sqrt{s} = 8\,\text{TeV}$ using the ATLAS detector", *Eur. Phys. J. C* **76** (2016) 538, doi:10.1140/epjc/s10052-016-4366-4, arXiv:1511.04716.

[279] ATLAS Collaboration, "Measurement of top quark pair differential cross-sections in the dilepton channel in pp collisions at $\sqrt{s} = 7$ and $8\,\text{TeV}$ with ATLAS", *Phys. Rev. D* **94** (2016) 092003, doi:10.1103/PhysRevD.94.092003, arXiv:1607.07281. [Addendum: 10.1103/PhysRevD.101.119901].

[280] ATLAS Collaboration, "Measurements of top-quark pair differential cross-sections in the e channel in *pp* collisions at $\sqrt{s} = 13\,\text{TeV}$ using the ATLAS detector", *Eur. Phys. J. C* **77** (2017) 292, doi:10.1140/epjc/s10052-017-4821-x, arXiv:1612.05220.

[281] ATLAS Collaboration, "Measurements of top-quark pair differential cross-sections in the lepton+jets channel in pp collisions at $\sqrt{s} = 13\,\text{TeV}$ using the ATLAS detector", *JHEP* **11** (2017) 191, doi:10.1007/JHEP11(2017)191, arXiv:1708.00727.

[282] ATLAS Collaboration, "Measurement of lepton differential distributions and the top quark mass in $\mathrm{t\bar{t}}$ production in pp collisions at $\sqrt{s} = 8\,\text{TeV}$ with the ATLAS detector", *Eur. Phys. J. C* **77** (2017) 804, doi:10.1140/epjc/s10052-017-5349-9, arXiv:1709.09407.

[283] ATLAS Collaboration, "Measurements of top-quark pair differential and double-differential cross-sections in the ℓ+jets channel with pp collisions at $\sqrt{s} = 13\,\text{TeV}$ using the ATLAS detector", *Eur. Phys. J. C* **79** (2019) 1028, doi:10.1140/epjc/s10052-019-7525-6, arXiv:1908.07305. [Erratum: 10.1140/epjc/s10052-020-08541-3].

[284] ATLAS Collaboration, "Measurement of the $t\bar{t}$ production cross-section and lepton differential distributions in e dilepton events from pp collisions at $\sqrt{s} = 13\,\text{TeV}$ with the ATLAS detector", *Eur. Phys. J. C* **80** (2020) 528, doi:10.1140/epjc/s10052-020-7907-9, arXiv:1910.08819.

[285] M. Beneke, P. Falgari, S. Klein, and C. Schwinn, "Hadronic top-quark pair production with NNLL threshold resummation", *Nucl. Phys. B* **855** (2012) 695, doi:10.1016/j.nuclphysb.2011.10.021, arXiv:1109.1536.

[286] M. Beneke et al., "Inclusive top-pair production phenomenology with TOPIXS", *JHEP* **07** (2012) 194, doi:10.1007/JHEP07(2012)194, arXiv:1206.2454.

[287] H. X. Zhu et al., "Transverse-momentum resummation for top-quark pairs at hadron colliders", *Phys. Rev. Lett.* **110** (2013) 082001, doi:10.1103/PhysRevLett.110.082001, arXiv:1208.5774.

[288] H. T. Li et al., "Top quark pair production at small transverse momentum in hadronic collisions", *Phys. Rev. D* **88** (2013) 074004, doi:10.1103/PhysRevD.88.074004, arXiv:1307.2464.

[289] S. Catani, M. Grazzini, and A. Torre, "Transverse-momentum resummation for heavy-quark hadroproduction", *Nucl. Phys. B* **890** (2014) 518, doi:10.1016/j.nuclphysb.2014.11.019, arXiv:1408.4564.

[290] S. Catani, M. Grazzini, and H. Sargsyan, "Transverse-momentum resummation for top-quark pair production at the LHC", *JHEP* **11** (2018) 061, doi:10.1007/JHEP11(2018)061, arXiv:1806.01601.

[291] W.-L. Ju et al., "Top quark pair production near threshold: single/double distributions and mass determination", *JHEP* **06** (2020) 158, doi:10.1007/JHEP06(2020)158, arXiv:2004.03088.

[292] S. Alioli, A. Broggio, and M. A. Lim, "Zero-jettiness resummation for top-quark pair production at the LHC", *JHEP* **01** (2022) 066, doi:10.1007/JHEP01(2022)066, arXiv:2111.03632.

[293] K. Hamilton, P. Nason, C. Oleari, and G. Zanderighi, "Merging H/W/Z + 0 and 1 jet at NLO with no merging scale: a path to parton shower + NNLO matching", *JHEP* **05** (2013) 082, doi:10.1007/JHEP05(2013)082, arXiv:1212.4504.

[294] S. Alioli et al., "Matching fully differential NNLO calculations and parton showers", *JHEP* **06** (2014) 089, doi:10.1007/JHEP06(2014)089, arXiv:1311.0286.

[295] S. Höche, Y. Li, and S. Prestel, "Drell–Yan lepton pair production at NNLO

QCD with parton showers", *Phys. Rev. D* **91** (2015) 074015, doi:10.1103/PhysRevD.91.074015, arXiv:1405.3607.

[296] CMS Collaboration, "Search for a heavy resonance decaying to a top quark and a W boson at $\sqrt{s} = 13\,\text{TeV}$ in the fully hadronic final state", *JHEP* **12** (2021) 106, doi:10.1007/JHEP12(2021)106, arXiv:2104.12853.

[297] CMS Collaboration, "Search for a heavy resonance decaying into a top quark and a W boson in the lepton+jets final state at $\sqrt{s} = 13\,\text{TeV}$", *JHEP* **04** (2022) 048, doi:10.1007/JHEP04(2022)048, arXiv:2111.10216.

[298] ATLAS Collaboration, "Measurements of differential cross-sections in top-quark pair events with a high transverse momentum top quark and limits on beyond the standard model contributions to top-quark pair production with the ATLAS detector at $\sqrt{s} = 13\,\text{TeV}$", *JHEP* **06** (2022) 063, doi:10.1007/JHEP06(2022)063, arXiv:2202.12134.

[299] B. Nachman and J. Thaler, "Neural resampler for Monte Carlo reweighting with preserved uncertainties", *Phys. Rev. D* **102** (2020) 076004, doi:10.1103/PhysRevD.102.076004, arXiv:2007.11586.

[300] "Open neural network exchange (ONNX)". Software available at https://onnx.ai.

[301] A. Paszke et al., "PyTorch: An imperative style, high-performance deep learning library", in *Proc. 33rd Conference on Neural Information Processing Systems (NeurIPS 2019): Vancouver, Canada, December 08–14, 2019*. 2019. arXiv:1912.01703.

[302] T. Chen and C. Guestrin, "XGBoost: A scalable tree boosting system", in *Proc. 22nd ACM SIGKDD International Conference on Knowledge Discovery and Data Mining: San Francisco CA, USA, August 13–17, 2016*. 2016. arXiv:1603.02754. doi:10.1145/2939672.2939785.

[303] A. Denner, S. Dittmaier, S. Kallweit, and S. Pozzorini, "NLO QCD corrections to WWbb production at hadron colliders", *Phys. Rev. Lett.* **106** (2011) 052001, doi:10.1103/PhysRevLett.106.052001, arXiv:1012.3975.

[304] G. Bevilacqua et al., "Complete off-shell effects in top quark pair hadroproduction with leptonic decay at next-to-leading order", *JHEP* **02** (2011) 083, arXiv:1012.4230.

[305] F. Cascioli, S. Kallweit, P. Maierhöfer, and S. Pozzorini, "A unified NLO description of top-pair and associated Wt production", *Eur. Phys. J. C* **74** (2014) 2783, arXiv:1312.0546.

[306] R. Frederix, "Top quark induced cackgrounds to Higgs production in the $WW^{(*)} \to ll\nu\nu$ decay channel at next-to-leading-order in QCD", *Phys. Rev. Lett.* **112** (2014), no. 8, 082002, doi:10.1103/PhysRevLett.112.082002, arXiv:1311.4893.

[307] T. Ježo and P. Nason, "On the treatment of resonances in next-to-leading order calculations matched to a parton shower", *JHEP* **12** (2015) 065, doi:10.1007/JHEP12(2015)065, arXiv:1509.09071.

[308] C. G. Lester and D. J. Summers, "Measuring masses of semiinvisibly decaying particles pair produced at hadron colliders", *Phys. Lett. B* **463** (1999) 99–103, doi:10.1016/S0370-2693(99)00945-4, arXiv:hep-ph/9906349.

[309] A. Barr, C. Lester, and P. Stephens, "m(T2): The Truth behind the glamour", *J. Phys. G* **29** (2003) 2343–2363, doi:10.1088/0954-3899/29/10/304, arXiv:hep-ph/0304226.

[310] CMS Collaboration, "Measurement of Masses in the $t\bar{t}$ System by Kinematic Endpoints in pp Collisions at $\sqrt{s} = 7$ TeV", *Eur. Phys. J. C* **73** (2013) 2494, doi:10.1140/epjc/s10052-013-2494-7, arXiv:1304.5783.

[311] ATLAS Collaboration, "Probing the quantum interference between singly and doubly resonant top-quark production in pp collisions at $\sqrt{s} = 13$ TeV with the ATLAS detector", *Phys. Rev. Lett.* **121** (2018), no. 15, 152002, doi:10.1103/PhysRevLett.121.152002, arXiv:1806.04667.

[312] C. Collaboration, "Display of a dileptonic top quark pair event seen in CMS", (2024). CMS Collection.

[313] G. Cowan, K. Cranmer, E. Gross, and O. Vitells, "Asymptotic formulae for likelihood-based tests of new physics", *Eur. Phys. J. C* **71** (2011) 1554, doi:10.1140/epjc/s10052-011-1554-0, arXiv:1007.1727. [Erratum: Eur.Phys.J.C 73, 2501 (2013)].

[314] CMS Collaboration, "Jet algorithms performance in 13 TeV data",.

[315] https://github.com/cms-sw/cmssw/blob/CMSSW_10_6_X/GeneratorInterface/RivetInterface/python/particleLevel_cfi.py.

[316] CMS Collaboration, "Object definitions for top quark analyses at the particle level", technical report, CERN, Geneva, 2017.

[317] https://cms.cern.ch/iCMS/analysisadmin/cadilines?line=TOP-20-010.

[318] CMS Collaboration, "Simulation of on- and off-shell $t\bar{t}$ production with the Monte Carlo generator b_bbar_4l at CMS", technical report, CERN, Geneva, 2023.

[319] NNPDF Collaboration, "Unbiased global determination of parton distributions and their uncertainties at NNLO and LO", *Nucl. Phys. B* **855** (2012) 153, doi:10.1016/j.nuclphysb.2011.09.024, arXiv:1107.2652.

[320] The NNPDF Collaboration and Richard D. Ball and Valerio Bertone and Stefano Carrazza and Luigi Del Debbio and Stefano Forte and Patrick Groth-Merrild and Alberto Guffanti and Nathan P. Hartland and Zahari Kassabov and José I. Latorre and Emanuele R. Nocera and Juan Rojo and Luca Rottoli and Emma Slade and Maria Ubiali, "Parton distributions from high-precision collider data", arXiv:1706.00428.

[321] CMS Collaboration, "Measurement of the top quark pole mass using $\mathrm{t\bar{t}}$+jet events in the dilepton final state in proton-proton collisions at $\sqrt{s} = 13$ TeV", *JHEP* **07** (2023) 077, doi:10.1007/JHEP07(2023)077, arXiv:2207.02270.

[322] ATLAS Collaboration, "Measurement of the Inelastic Proton-Proton Cross Section at $\sqrt{s} = 13$ TeV with the ATLAS Detector at the LHC", *Phys. Rev. Lett.* **117** (2016), no. 18, 182002, doi:10.1103/PhysRevLett.117.182002, arXiv:1606.02625.

[323] CMS Collaboration, "Electron and photon performance in CMS with the full 2016 data sample", CMS Detector Performance Note CMS-DP-2017-004, CERN, 2017.

[324] CMS Collaboration, "Performance of muon reconstruction including Alignment Position Errors for 2016 Collision Data", Technical Report CMS-DP-2016-067, CERN, 2016.

[325] CMS Collaboration, "Muon Identification and Isolation efficiency on full 2016 dataset", CMS Detector Performance Note CMS-DP-2017-007, CERN, 2017.

[326] A. Bodek et al., "Extracting Muon Momentum Scale Corrections for Hadron Collider Experiments", *Eur. Phys. J. C* **72** (2012) 2194, doi:10.1140/epjc/s10052-012-2194-8, arXiv:1208.3710.

[327] CMS Collaboration, "Muon Reconstruction and Identification Performance with Run-2 data", CMS Detector Performance Note CMS-DP-2020-040, CERN, 2020.

[328] CMS Collaboration, "Muon reconstruction performance during Run II", CMS Detector Performance Note CMS-DP-2019-022, CERN, 2019.

[329] CMS Collaboration, "Performance of electron and photon reconstruction in Run 2 with the CMS experiment", CMS Detector Performance Note CMS-DP-2020-037, 2020.

[330] CMS Collaboration, "Performance of the CMS muon trigger system in proton-proton collisions at $\sqrt{s} = 13$ TeV", *JINST* **16** (2021) P07001, doi:10.1088/1748-0221/16/07/P07001, arXiv:2102.04790.

[331] CMS Collaboration, "Jet energy scale and resolution in the CMS experiment in pp collisions at 8 TeV", *JINST* **12** (2017) P02014, doi:10.1088/1748-0221/12/02/P02014, arXiv:1607.03663.

[332] CMS Collaboration, "CMS luminosity measurement for the 2017 data-taking period at $\sqrt{s} = 13$ TeV", CMS Physics Analysis Summary CMS-PAS-LUM-17-004, CERN, Geneva, 2018.

[333] CMS Collaboration, "CMS luminosity measurement for the 2018 data-taking period at $\sqrt{s} = 13$ TeV", CMS Physics Analysis Summary CMS-PAS-LUM-18-002, CERN, Geneva, 2019.

[334] M. Cacciari et al., "The t anti-t cross-section at 1.8-TeV and 1.96-TeV: A Study of the systematics due to parton densities and scale dependence", *JHEP* **04** (2004) 068, doi:10.1088/1126-6708/2004/04/068, arXiv:hep-ph/0303085.

[335] S. Catani, D. de Florian, M. Grazzini, and P. Nason, "Soft gluon resummation for Higgs boson production at hadron colliders", *JHEP* **07** (2003) 028, doi:10.1088/1126-6708/2003/07/028, arXiv:hep-ph/0306211.

[336] CMS Collaboration, "Measurement of the differential cross section for top quark pair production in pp collisions at $\sqrt{s} = 8\,\text{TeV}$", *Eur. Phys. J. C* **75** (2015), no. 11, 542, doi:10.1140/epjc/s10052-015-3709-x, arXiv:1505.04480.

[337] CMS Collaboration, "Measurement of the $\mathrm{t\bar{t}}$ production cross section in the all-jets final state in pp collisions at $\sqrt{s} = 8$ TeV", *Eur. Phys. J. C* **76** (2016), no. 3, 128, doi:10.1140/epjc/s10052-016-3956-5, arXiv:1509.06076.

[338] CMS Collaboration, "Measurement of the differential cross section for $\mathrm{t\bar{t}}$ production in the dilepton final state at $\sqrt{s} = 13$ TeV", CMS Physics Analysis Summary CMS-PAS-TOP-16-011, CERN, Geneva, 2016.

[339] R. J. Barlow and C. Beeston, "Fitting using finite Monte Carlo samples", *Comput. Phys. Commun.* **77** (1993) 219–228, doi:10.1016/0010-4655(93)90005-W.

[340] J. S. Conway, "Incorporating Nuisance Parameters in Likelihoods for Multisource Spectra", in *PHYSTAT 2011*, pp. 115–120. 2011.

arXiv:1103.0354. doi:10.5170/CERN-2011-006.115.

[341] CMS Collaboration, "Running of the top quark mass from proton-proton collisions at $\sqrt{s} = 13$TeV", *Phys. Lett. B* **803** (2020) 135263, doi:10.1016/j.physletb.2020.135263, arXiv:1909.09193.

[342] F. James and M. Roos, "Minuit: a system for Function Minimization and Analysis of the Parameter Errors and Correlations", *Comput. Phys. Commun.* **10** (1975) 343, doi:10.1016/0010-4655(75)90039-9.

[343] M. Baak, S. Gadatsch, R. Harrington, and W. Verkerke, "Interpolation between multi-dimensional histograms using a new non-linear moment morphing method", *Nucl. Instrum. Meth. A* **771** (2015) 39–48, doi:10.1016/j.nima.2014.10.033, arXiv:1410.7388.

[344] F. Spano, "Unfolding in particle physics: a window on solving inverse problems", *EPJ Web Conf.* **55** (2013) 03002, doi:10.1051/epjconf/20135503002.

[345] S. Alekhin et al., "HERAFitter, open source QCD fit project", *Eur. Phys. J. C* **75** (2015) 304, doi:10.1140/epjc/s10052-015-3480-z, arXiv:1410.4412.

[346] CMS Collaboration, "Determination of the strong coupling and its running from measurements of inclusive jet production", *Phys. Lett. B* **868** (2025) 139651, doi:10.1016/j.physletb.2025.139651, arXiv:2412.16665.

[347] V. Bertone, M. Botje, D. Britzger et al., "xFitter 2.0.0: An Open Source QCD Fit Framework", *PoS* **DIS2017** (2018) 203, doi:10.22323/1.297.0203, arXiv:1709.01151.

[348] xFitter Collaboration, H. Abdolmaleki et al., "xFitter: An Open Source QCD Analysis Framework. A resource and reference document for the Snowmass study", 6, 2022. arXiv:2206.12465.

[349] xFitter Developers' Team, "https://www.xfitter.org/xFitter/".

[350] CMS Collaboration, "Measurement and QCD analysis of double-differen-tial inclusive jet cross sections in pp collisions at $\sqrt{s} = 8$ TeV and cross section ratios to 2.76 and 7 TeV", *JHEP* **03** (2017) 156, doi:10.1007/JHEP03(2017)156, arXiv:1609.05331.

[351] ATLAS Collaboration, "Determination of the parton distribution functions of the proton from ATLAS measurements of differential $W^{\pm}$ and Z boson production in association with jets", *JHEP* **07** (2021) 223, doi:10.1007/JHEP07(2021)223, arXiv:2101.05095.

[352] ATLAS Collaboration, "Determination of the parton distribution functions of the proton using diverse ATLAS data from pp collisions at $\sqrt{s} = 7$, 8 and 13 TeV", *Eur. Phys. J. C* **82** (2022), no. 5, 438, doi:10.1140/epjc/s10052-022-10217-z, arXiv:2112.11266.

[353] ATLAS Collaboration, "Determination of the parton distribution functions of the proton from ATLAS measurements of differential W and Z/γ^* and $t\bar{t}$ cross sections", ATLAS Note ATL-PHYS-PUB-2018-017, 2018.

[354] ATLAS Collaboration, "Precision measurement and interpretation of inclusive W^+ , W^- and Z/γ^* production cross sections with the ATLAS detector", *Eur. Phys. J. C* **77** (2017), no. 6, 367, doi:10.1140/epjc/s10052-017-4911-9, arXiv:1612.03016.

[355] J. Gao, "CIJET: A program for computation of jet cross sections induced by quark contact interactions at hadron colliders", *Comput. Phys. Commun.* **184** (2013) 2362, doi:10.1016/j.cpc.2013.05.019, arXiv:1301.7263.

[356] X. Shen et al., "A framework for simultaneous fit of QCD and BSM parameters with xFitter", *Eur. Phys. J. C* **84** (2024), no. 11, 1235, doi:10.1140/epjc/s10052-024-13585-w, arXiv:2407.16061.

[357] H. Abdolmaleki et al., "Exploring SMEFT couplings using the forward–backward asymmetry in neutral current Drell–Yan production at the LHC", *Eur. Phys. J. C* **84** (2024), no. 12, 1277, doi:10.1140/epjc/s10052-024-13480-4, arXiv:2310.19638.

[358] J. C. Collins and W.-K. Tung, "Calculating heavy quark distributions", *Nuclear Physics B* **278** (1986), no. 4, 934–950, doi:https://doi.org/10.1016/0550-3213(86)90425-6.

[359] E. Laenen, S. Riemersma, J. Smith, and W. van Neerven, "Complete $\mathcal{O}(\alpha_S)$ corrections to heavy-flavour structure functions in electroproduction", *Nuclear Physics B* **392** (1993), no. 1, 162–228, doi:https://doi.org/10.1016/0550-3213(93)90201-Y.

[360] E. Laenen, S. Riemersma, J. Smith, and W. van Neerven, "On the heavy-quark content of the nucleon", *Physics Letters B* **291** (1992), no. 3, 325–328, doi:https://doi.org/10.1016/0370-2693(92)91053-C.

[361] S. Riemersma, J. Smith, and W. van Neerven, "Rates for inclusive deep-inelastic electroproduction of charm quarks at HERA", *Physics Letters B* **347** (1995), no. 1, 143–151, doi:https://doi.org/10.1016/0370-2693(95)00036-K.

[362] R. S. Thorne and R. G. Roberts, "Ordered analysis of heavy flavor production in deep inelastic scattering", *Phys. Rev. D* **57** (1998) 6871, doi:10.1103/PhysRevD.57.6871, arXiv:hep-ph/9709442.

[363] R. S. Thorne, "Variable-flavor number scheme for NNLO", *Phys. Rev. D* **73** (2006) 054019, doi:10.1103/PhysRevD.73.054019, arXiv:hep-ph/0601245.

[364] R. S. Thorne, "Effect of changes of variable flavor number scheme on parton distribution functions and predicted cross sections", *Phys. Rev. D* **86** (2012) 074017, doi:10.1103/PhysRevD.86.074017, arXiv:1201.6180.

[365] M. Botje, "QCDNUM: Fast QCD Evolution and Convolution", *Comput. Phys. Commun.* **182** (2011) 490, doi:10.1016/j.cpc.2010.10.020, arXiv:1005.1481.

[366] J. Pumplin et al., "Uncertainties of predictions from parton distribution functions. 2. The Hessian method", *Phys. Rev. D* **65** (2001) 014013, doi:10.1103/PhysRevD.65.014013, arXiv:hep-ph/0101032.

[367] H. Paukkunen and P. Zurita, "PDF reweighting in the Hessian matrix approach", *JHEP* **12** (2014) 100, doi:10.1007/JHEP12(2014)100, arXiv:1402.6623.

[368] C. Schmidt, J. Pumplin, C. P. Yuan, and P. Yuan, "Updating and optimizing error parton distribution function sets in the Hessian approach", *Phys. Rev. D* **98** (2018) 094005, doi:10.1103/PhysRevD.98.094005, arXiv:1806.07950.

[369] R. Abdul Khalek et al., "Towards ultimate parton distributions at the high-luminosity LHC", *Eur. Phys. J. C* **78** (2018) 962, doi:10.1140/epjc/s10052-018-6448-y, arXiv:1810.03639.

[370] HERAFitter developers' team Collaboration, "QCD analysis of W- and Z-boson production at Tevatron", *Eur. Phys. J. C* **75** (2015), no. 9, 458, doi:10.1140/epjc/s10052-015-3655-7, arXiv:1503.05221.

[371] G. Schwarz, "Estimating the Dimension of a Model", *The Annals of Statistics* **6** (1978), no. 2, 461–464, doi:10.1214/aos/1176344136.

[372] T. Carli et al., "A posteriori inclusion of parton density functions in NLO QCD final-state calculations at hadron colliders: The APPLGRID Project", *Eur. Phys. J. C* **66** (2010) 503–524, doi:10.1140/epjc/s10052-010-1255-0, arXiv:0911.2985.

[373] S. Carrazza, E. R. Nocera, C. Schwan, and M. Zaro, "PineAPPL: combining EW and QCD corrections for fast evaluation of LHC processes", *JHEP* **12** (2020) 108, doi:10.1007/JHEP12(2020)108, arXiv:2008.12789.

[374] H1 and ZEUS Collaborations, HERAPDF1.6, "HERA Combined H1 and ZEUS Results: Jets, PDFs, and α_s", 2024. Accessed: 2024-03-11.

[375] M. Cacciari et al., "Single-jet inclusive cross section and its definition", *Phys. Rev. D* **100** (2019) 114015, doi:10.1103/PhysRevD.100.114015, arXiv:1906.11850.

[376] M. Dasgupta, F. A. Dreyer, G. P. Salam, and G. Soyez, "Inclusive jet spectrum for small-radius jets", *JHEP* **06** (2016) 057, doi:10.1007/JHEP06(2016)057, arXiv:1602.01110.

[377] J. Bellm et al., "Jet cross sections at the LHC and the quest for higher precision", *Eur. Phys. J. C* **80** (2020) 93, doi:10.1140/epjc/s10052-019-7574-x, arXiv:1903.12563.

[378] T. Sjostrand, S. Mrenna, and P. Z. Skands, "PYTHIA 6.4 Physics and Manual", *JHEP* **05** (2006) 026, doi:10.1088/1126-6708/2006/05/026, arXiv:hep-ph/0603175.

[379] R. Field, "Min-Bias and the Underlying Event at the LHC", *Acta Phys. Polon. B* **42** (2011) 2631–2656, doi:10.5506/APhysPolB.42.2631, arXiv:1110.5530.

[380] Z. Nagy, "Three jet cross-sections in hadron hadron collisions at next-to-leading order", *Phys. Rev. Lett.* **88** (2002) 122003, doi:10.1103/PhysRevLett.88.122003, arXiv:hep-ph/0110315.

[381] H.-L. Lai et al., "New parton distributions for collider physics", *Phys. Rev. D* **82** (2010) 074024, doi:10.1103/PhysRevD.82.074024, arXiv:1007.2241.

[382] G. D'Agostini, "A Multidimensional unfolding method based on Bayes' theorem", *Nucl. Instrum. Meth. A* **362** (1995) 487–498, doi:10.1016/0168-9002(95)00274-X.

[383] T. Adye, "Unfolding algorithms and tests using RooUnfold", in *PHYSTAT 2011*, pp. 313–318. CERN, Geneva, 2011. arXiv:1105.1160. doi:10.5170/CERN-2011-006.313.

[384] CMS Collaboration, "Luminosity Calibration for the 2013 Proton-Lead and Proton-Proton Data Taking", CMS Physics Analysis Summary CMS-PAS-LUM-13-002, CERN, 2014.

[385] CMS Collaboration, "Determination of Jet Energy Calibration and Transverse Momentum Resolution in CMS", *JINST* **6** (2011) P11002, doi:10.1088/1748-0221/6/11/P11002, arXiv:1107.4277.

[386] CMS Collaboration, "Jet Energy Scale performance in 2011", CMS Detector

Performance Note CMS-DP-2012-006, CERN-CMS-DP-2012-006, CERN, 5, 2012.

[387] CMS Collaboration, "Absolute Calibration of the Luminosity Measurement at CMS: Winter 2012 Update", CMS Physics Analysis Summary CMS-PAS-SMP-12-008, CERN, Geneva, 2012.

[388] CMS Collaboration, "CMS Luminosity Based on Pixel Cluster Counting - Summer 2013 Update", CMS Physics Analysis Summary CMS-PAS-LUM-13-001, CERN, Geneva, 2013.

[389] S. Schmitt, "TUnfold: an algorithm for correcting migration effects in high energy physics", *JINST* **7** (2012) T10003, doi:10.1088/1748-0221/7/10/T10003, arXiv:1205.6201.

[390] CMS Collaboration, "Precision luminosity measurement in proton-proton collisions at $\sqrt{s} = 13$ TeV in 2015 and 2016 at CMS", *Eur. Phys. J. C* **81** (2021), no. 9, 800, doi:10.1140/epjc/s10052-021-09538-2, arXiv:2104.01927.

[391] P. L. S. Connor and R. Žlebčík, "STEP: A tool to perform tests of smoothness on differential distributions based on expansion of polynomials", *SciPost Phys. Core* **6** (2023) 040, doi:10.21468/SciPostPhysCore.6.2.040.

[392] CMS Collaboration, "Determination of Jet Energy Calibration and Transverse Momentum Resolution in CMS", *JINST* **6** (2011) P11002, doi:10.1088/1748-0221/6/11/P11002, arXiv:1107.4277.

[393] M. Bahr et al., "Herwig++ Physics and Manual", *Eur. Phys. J. C* **58** (2008) 639–707, doi:10.1140/epjc/s10052-008-0798-9, arXiv:0803.0883.

[394] J. Currie, E. W. N. Glover, and J. Pires, "Next-to-Next-to Leading Order QCD Predictions for Single Jet Inclusive Production at the LHC", *Phys. Rev. Lett.* **118** (2017) 072002, doi:10.1103/PhysRevLett.118.072002, arXiv:1611.01460.

[395] J. Currie et al., "Infrared sensitivity of single jet inclusive production at hadron colliders", *JHEP* **10** (2018) 155, doi:10.1007/JHEP10(2018)155, arXiv:1807.03692.

[396] T. Gehrmann et al., "Jet cross sections and transverse momentum distributions with NNLOJET", *PoS* **RADCOR2017** (2018) 074, doi:10.22323/1.290.0074, arXiv:1801.06415.

[397] X. Chen et al., "NNLO QCD corrections in full colour for jet production observables at the LHC", *JHEP* **09** (2022) 025,

doi:10.1007/JHEP09(2022)025, arXiv:2204.10173.

[398] S. Dittmaier, A. Huss, and C. Speckner, "Weak radiative corrections to dijet production at hadron colliders", *JHEP* **11** (2012) 095, doi:10.1007/JHEP11(2012)095, arXiv:1210.0438.

[399] S. Gieseke, C. Rohr, and A. Siodmok, "Colour reconnections in Herwig++", *Eur. Phys. J. C* **72** (2012) 2225, doi:10.1140/epjc/s10052-012-2225-5, arXiv:1206.0041.

[400] M. H. Seymour and A. Siodmok, "Constraining MPI models using σ_{eff} and recent Tevatron and LHC Underlying Event data", *JHEP* **10** (2013) 113, doi:10.1007/JHEP10(2013)113, arXiv:1307.5015.

[401] S. Alioli et al., "Jet pair production in POWHEG", *JHEP* **04** (2011) 081, doi:10.1007/JHEP04(2011)081, arXiv:1012.3380.

[402] P. Z. Skands, "Tuning Monte Carlo Generators: The Perugia Tunes", *Phys. Rev. D* **82** (2010) 074018, doi:10.1103/PhysRevD.82.074018, arXiv:1005.3457.

[403] CMS Collaboration, "Event generator tunes obtained from underlying event and multiparton scattering measurements", *Eur. Phys. J. C* **76** (2016), no. 3, 155, doi:10.1140/epjc/s10052-016-3988-x, arXiv:1512.00815.

[404] F. Herren and M. Steinhauser, "Version 3 of RunDec and CRunDec", *Comput. Phys. Commun.* **224** (2018) 333, doi:10.1016/j.cpc.2017.11.014, arXiv:1703.03751.

[405] A. H. Hoang, S. Plätzer, and D. Samitz, "On the Cutoff Dependence of the Quark Mass Parameter in Angular Ordered Parton Showers", *JHEP* **10** (2018) 200, doi:10.1007/JHEP10(2018)200, arXiv:1807.06617.

[406] B. A. Kniehl, A. F. Pikelner, and O. L. Veretin, "mr: a C++ library for the matching and running of the Standard Model parameters", *Comput. Phys. Commun.* **206** (2016) 84–96, doi:10.1016/j.cpc.2016.04.017, arXiv:1601.08143.

Appendices

A.1 Additional control plots

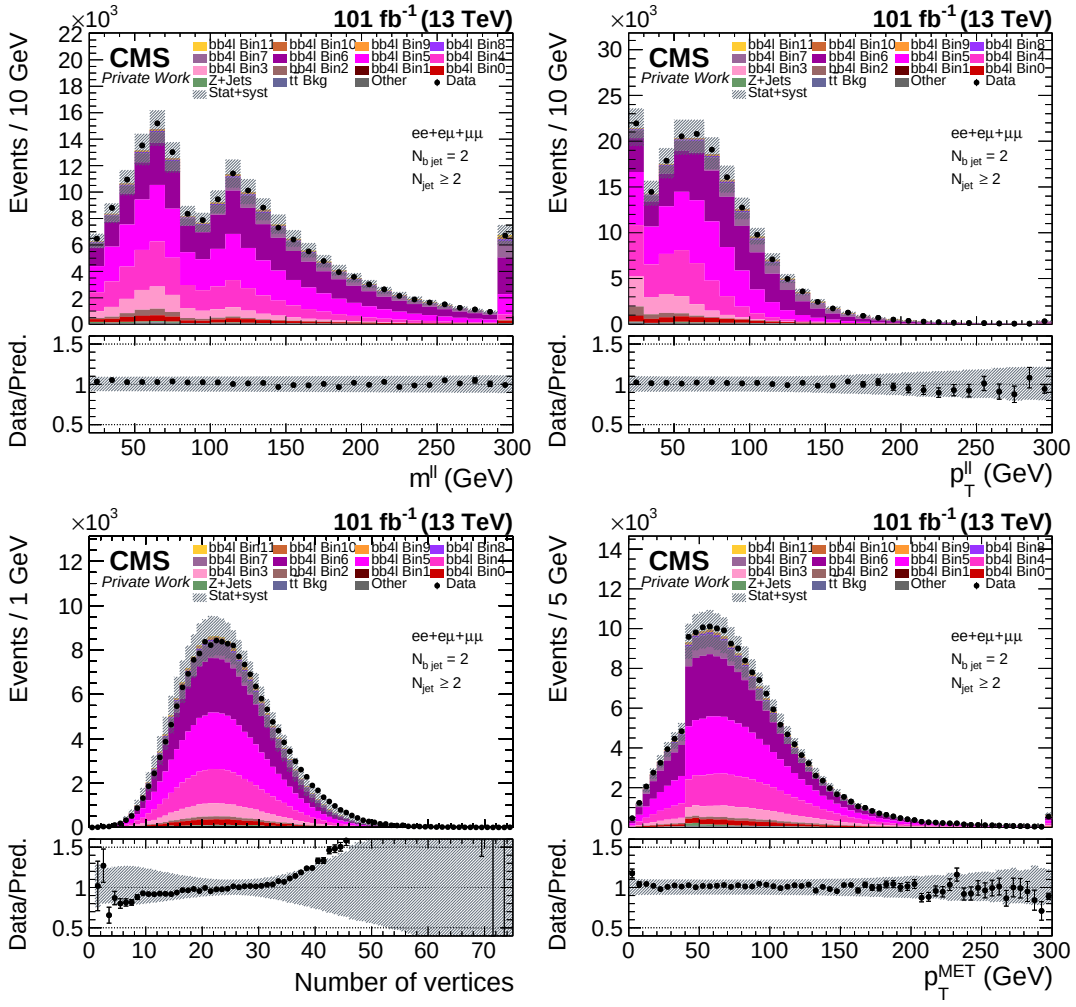

Figure A.1: Distributions of mass (upper left) and p_{T} (upper right) of selected dilepton pair, number of vertices (lower left), and transverse missing energy (lower right.)

A.2 Trigger efficiencies

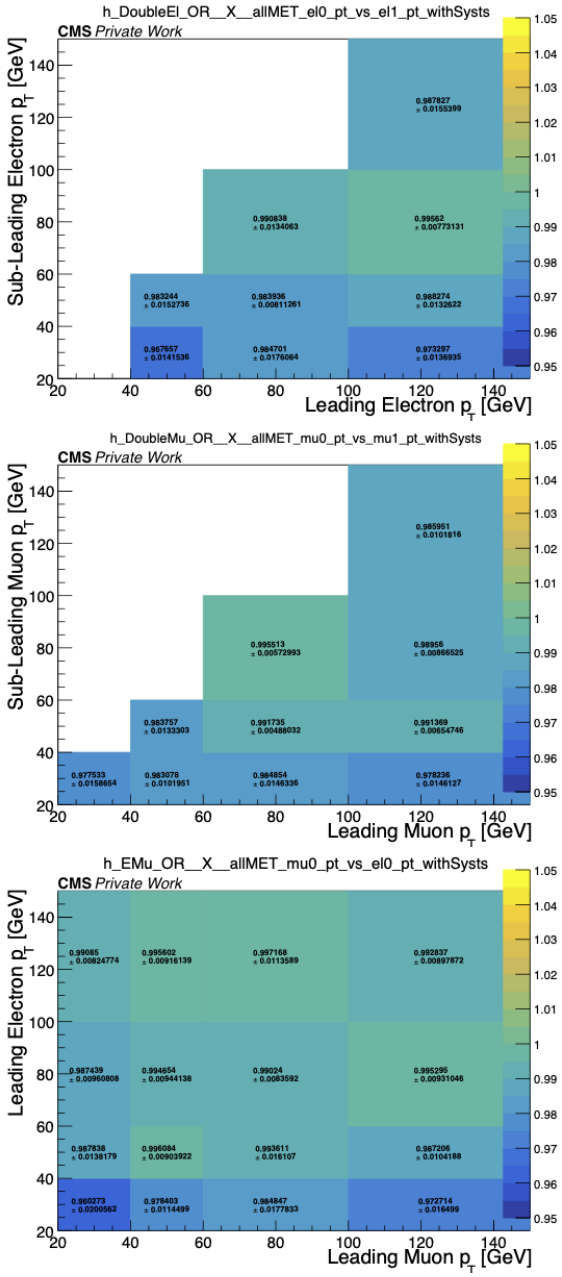

Figure A.2: Trigger scale factors (2017 data-taking) measured differentially as a function of p_{T} for $\mathrm{e^{+}e^{-}}$(top), $\mu^{+}\mu^{-}$(middle) and $\mathrm{e^{\pm}}\mu^{\pm}$(bottom) channels. The given uncertainties correspond to the statistical uncertainty added in quadratures to the additional systematic uncertainty on the measured value.

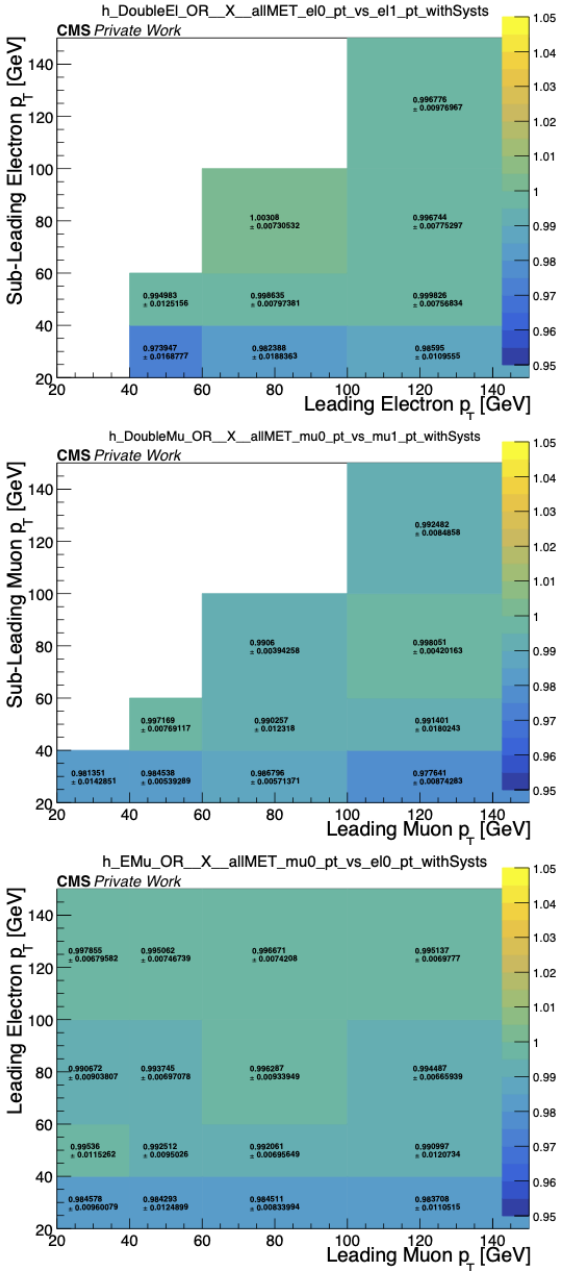

Figure A.3: Same as Figure A.2 for 2018 data-taking.

A.3 Impact plots

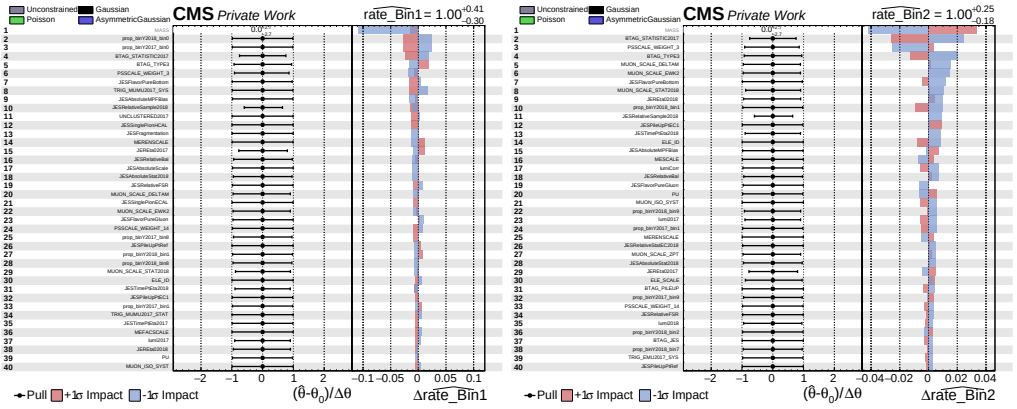

Figure A.4: Impact plots using Asimov pseudo-data for Bin1 (left) and Bin2 (right).

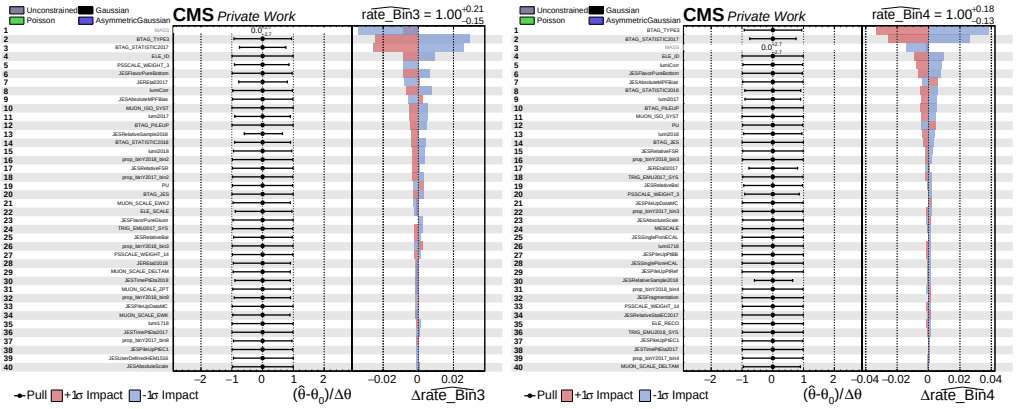

Figure A.5: Impact plots using Asimov pseudo-data for Bin3 (left) and Bin4 (right).

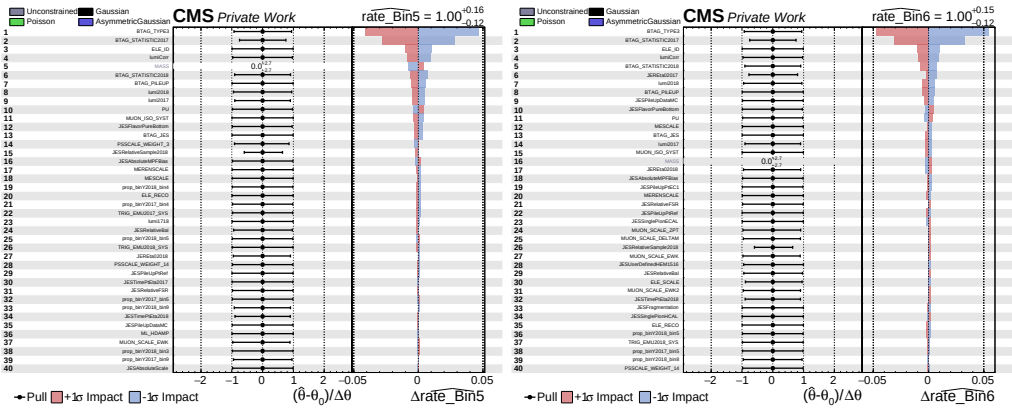

Figure A.6: Impact plots using Asimov pseudo-data for Bin5 (left) and Bin6 (right).

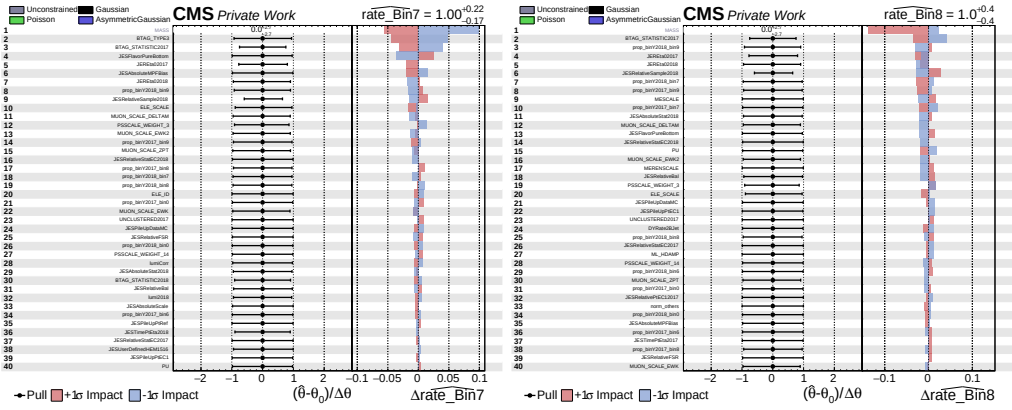

Figure A.7: Impact plots using Asimov pseudo-data for Bin7 (left) and Bin8 (right).

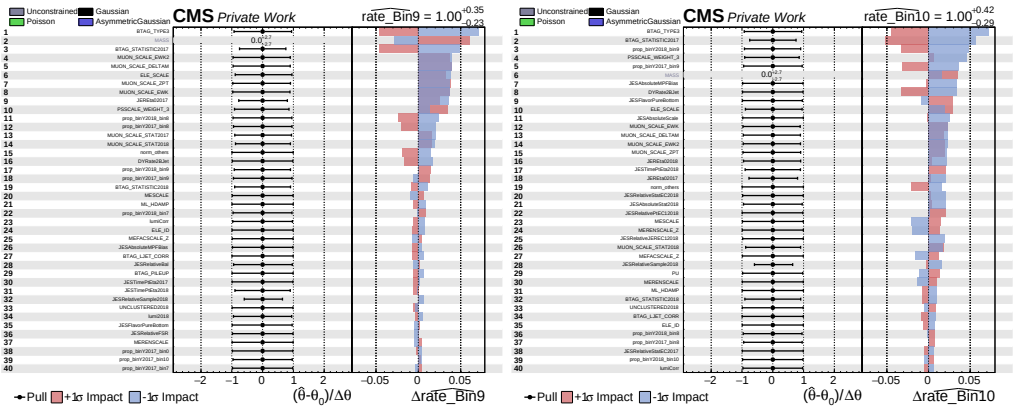

Figure A.8: Impact plots using Asimov pseudo-data for Bin9 (left) and Bin10 (right).

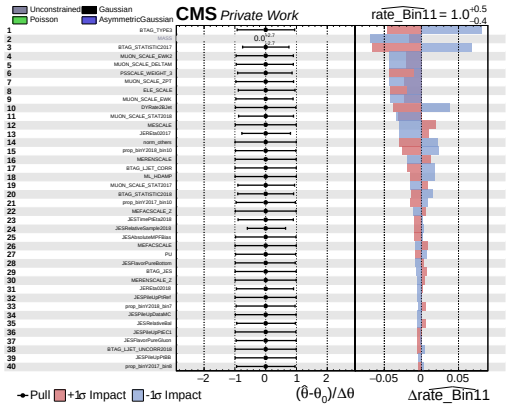

Figure A.9: Impact plots using Asimov pseudo-data for Bin11.